



Max-Planck-Institut für Metallforschung
Stuttgart

Phase Transformations of the NbCr₂ and HfCr₂ Laves Phases

Jochen Marc Aufrecht

Dissertation
an der
Universität Stuttgart

Bericht Nr. 231
November 2010

Phase Transformations of the NbCr₂ and HfCr₂ Laves Phases

Von der Fakultät Chemie der Universität Stuttgart zur
Erlangung der Würde eines Doktors der Naturwissenschaften (Dr. rer. nat.)
genehmigte Abhandlung

vorgelegt von

Jochen Marc Aufrecht

aus Göppingen

Hauptberichter: Prof. Dr. Ir. E.J. Mittemeijer

Mitberichter: Prof. Dr. J. Bill

Prüfungsvorsitzender: Prof. Dr. Th. Schleid

Tag der Einreichung: 11.10.2010

Tag der mündlichen Prüfung 18.11.2010

MAX-PLANCK-INSTITUT FÜR METALLFORSCHUNG, STUTTGART
INSTITUT FÜR MATERIALWISSENSCHAFT DER UNIVERSITÄT STUTTGART
STUTTGART, 2010

Table of contents

1.	General introduction	7
1.1	Laves phases	7
1.2	Polytypism of Laves phases.....	8
1.2.1	The building principles of Laves phase polytypes: the classical and a modified notation	8
1.2.2	Polytypism of Laves-phase	14
1.2.3	Occurrence of different polytypes within one system	16
1.2.4	Polytypic phase transformations in Laves phases: Synchroshear.....	16
1.3	Scope of the thesis	17
1.4	Experimental strategy	18
1.4.1	General remarks	18
1.4.2	Structure identification and evaluation of defect and microstructure.....	18
1.4.3	Selection of model systems.....	19
1.4.4	Control of high-temperatures, sample composition and contamination level.....	21
1.5	Outline of the thesis	26
1.6	References.....	27
2.	The absence of a stable hexagonal Laves phase modification (NbCr₂) in the Nb-Cr system.....	29
2.1	Introduction.....	30
2.2	Experimental details and results	31
2.3	Conclusions.....	37
2.4	References.....	38
3.	Metastable hexagonal modifications of the NbCr₂ Laves phase as function of cooling rate	41
3.1	Introduction.....	42
3.2	Experiment.....	43
3.3	Results.....	44
3.4	Discussion.....	47
3.5	Conclusions.....	50

3.6	Acknowledgements.....	50
3.7	References.....	51
4.	Layer-stacking irregularities in C36-type Nb-Cr and Ti-Cr Laves phases and their relation with polytypic phase transformations	53
4.1	Introduction.....	54
4.1.1	Laves phases; layer-stacking rules.....	54
4.1.2	Partial-dislocation dipole mechanism for polymorphic transformations in Laves phases	57
4.1.3	Diffraction from layered hexagonal structures containing stacking irregularities	63
4.2	Experimental.....	66
4.2.1	Preparation of alloys	66
4.2.2	High resolution transmission electron microscopy (HRTEM).....	68
4.2.3	X-ray powder diffraction (XRPD).....	68
4.3	Results.....	69
4.3.1	Nb-Cr	69
4.3.2	TiCr ₂	74
4.3.3	NbCo ₂	77
4.4	Discussion.....	78
4.4.1	Stacking irregularities and associated displacement vectors	78
4.4.2	Relation with phase-transformation mechanism.....	79
4.5	Conclusions.....	91
4.6	Acknowledgements.....	91
4.7	References.....	92
5.	Transformation-dislocation dipoles in Laves phases: a high-resolution transmission electron microscopy analysis.....	95
5.1	Introduction.....	96
5.2	Theoretical considerations: layer-stacking sequences and their changes by glide of synchro-Shockley partial dislocations	97
5.3	Experimental.....	107
5.4	Results and discussion	108

5.4.1	Stacking faults and the structure of a single synchro-Shockley partial dislocation dipole	108
5.4.2	“Anti-phase boundary”, constituted by a synchro-Shockley partial dislocation dipole configuration	118
5.5	Conclusions.....	124
5.6	Acknowledgements.....	124
5.7	References.....	125
6.	Polytypic transformations of the HfCr₂ Laves phase – Structural evolution as a function of temperature, time and composition	127
6.1	Introduction.....	128
6.2	Theoretical background	130
6.2.1	Laves-phase polytypes	130
6.2.2	Diffraction patterns and distinction between polytypes.....	133
6.3	Experimental procedures	139
6.4	Results.....	142
6.4.1	C14-HfCr ₂	142
6.4.2	Structural evolution upon annealing of C14-HfCr ₂ as function of temperature	144
6.4.3	Structural evolution upon annealing of C14-HfCr ₂ as function of composition.....	149
6.4.4	Structural evolution upon annealing of C14-HfCr ₂ as function of time .	152
6.5	Discussion.....	160
6.5.1	The initial structure: C14-HfCr ₂	160
6.5.2	Structural changes upon annealing; phase map for HfCr ₂	160
6.5.3	The degree of transformation.....	163
6.6	Conclusions.....	164
6.7	Acknowledgements.....	165
6.8	References.....	165
7.	Polytypic transformations of the HfCr₂ Laves phase - Kinetics of the polymorphic C14 → C15 transformation	169
7.1	Introduction.....	170

7.2	Theory	171
7.2.1	Polytypic transformations of the HfCr ₂ Laves phase.....	171
7.2.2	Evaluation of phase-transformation kinetics by XRPD.....	172
7.3	Experimental.....	176
7.4	Results.....	176
7.5	Discussion.....	183
7.6	Conclusions.....	185
7.7	Acknowledgements.....	186
7.8	Literature.....	186
8.	Summary.....	189
9.	Zusammenfassung.....	195
	List of publications.....	203
	Danksagung	205
	Curriculum Vitae	207

1. General introduction

1.1 Laves phases

Laves phases form the largest group of intermetallic phases with currently more than 1400 known representatives [1]. They belong to the family of the Frank-Kasper phases [2, 3]. The general building principle has been revealed by F. Laves and J.B. Friauf [4-7], where the term Laves phases has been introduced by G.E.R. Schulze [8]. Laves phases are characterized by an ideal composition of AB_2 , where the atomic radius of A is about 1.225 times larger than the atomic radius of B. This enables a close packing of the atoms with a space filling of 71%. The building principle of Laves phases allows for a theoretically infinite number of polytypes (the phenomenon of polytypism in Laves phases is described in detail from a crystallographic point of view and from a thermodynamic point of view in the following section), the three most prominent are the hexagonal C14 (MgZn₂-type) and C36 (MgNi₂-type) modifications and the cubic C15 (MgCu₂-type) modification (Fig. 1.1).

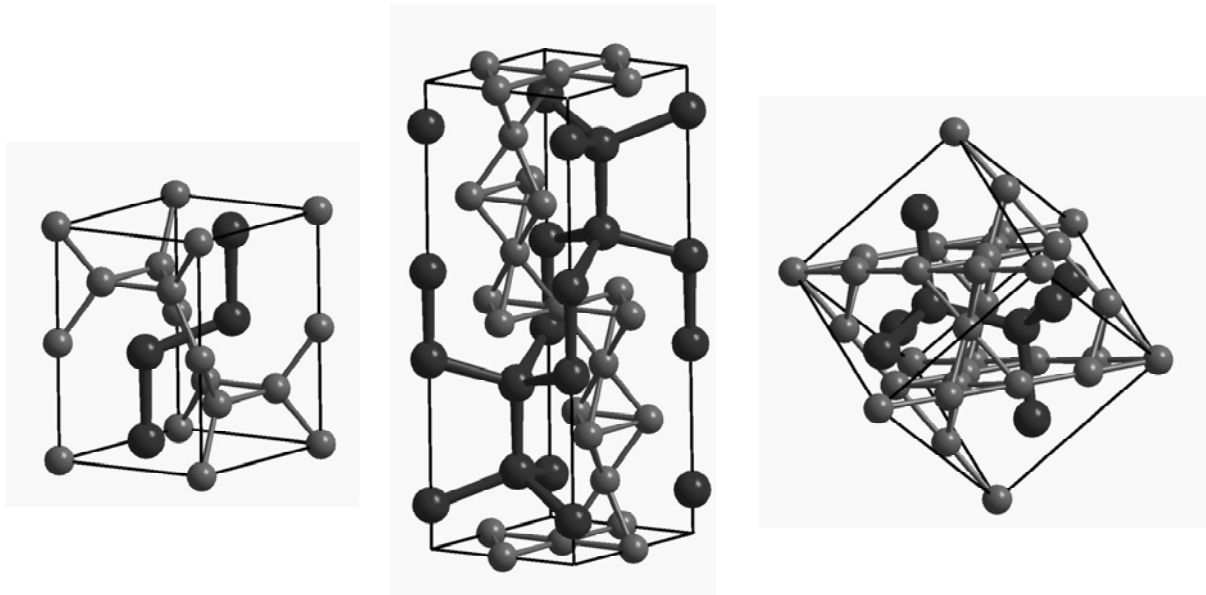


Fig. 1.1: Structure models of the (a) C14, (b) C36 and (c) C15 polytypic crystal structures of Laves phases. Black: A atoms, grey: B atoms.

A and B must not necessarily symbolize only one type of atoms, the corresponding sites in the crystal structure can also be occupied by different atoms so that multinary Laves phases result. Especially in transition-metal Laves phases, also deviations from the ideal AB_2 composition are possible, allowing for considerable homogeneity ranges also in binary systems. This is associated with the occurrence of constitutional point defects as anti-site atoms or structural vacancies.

The chemical bonding in Laves phases is predominately of metallic character, there are however also ionic and covalent contributions to different extend depending on the constituting atoms.

1.2 Polytypism of Laves phases

1.2.1 The building principles of Laves phase polytypes: the classical and a modified notation

Laves phases can be conceived as layered structures; the polytypes differ in stacking sequence of the layers building up the crystal structures (see the introduction to chapter 4 for a more detailed crystallographic description). Always four layers are stacked on top of each other repeatedly (Fig. 1.2):

- (1) A Kagomé-layer constituted by small B atoms,
- (2) A layers consisting of large atoms A which are positioned at the holes of the Kagomé layer.
- (3) A layer consisting of small B atoms positioned at the gaps left between two layer-sandwich units built up as indicated above.
- (4) Another layer consisting of large A atoms, which are located at the holes of the successive Kagomé layer.

For each of these layers, three stacking positions are available (subject to some restrictions, see below) within a two-dimensional, hexagonal unit mesh: $A(0,0)$, $B(1/3,2/3)$ and $C(2/3,1/3)$.

The most detailed notation for a stacking sequence is to denote the stacking position of each of these layers by an own symbol [9]:

- A, B, C for the positions of the holes of the Kagomé layer,
- α , β , γ for positions of the atoms of the two layers consisting of large A atoms,
- a, b, c for the atoms of the layer consisting of small B atoms positioned between the two A layers.

The stacking sequences of Laves phases are thus described by a letter sequence consisting repeatedly of (1) a capital letter, (2) a Greek letter, (3) a lower case letter and (4) a Greek letter.

The following structural requirements have to be fulfilled, restricting the possible stacking variants:

- i. The layers consisting of large A atoms have to be at the same position as the holes of the Kagomé layer, which is embraced by them, i.e. adjacent Greek and capital letters may not be different,
- ii. The layer consisting of small B atoms, which is situated between two layer consisting of large A atoms and those two adjacent layers must all be at different positions, i.e. in a sequence consisting of a Greek letter followed by a lower case letter, followed again by a Greek letter all these three letters have to be different.

An example for this notation is given for the C36 polytype in Fig. 1.3. To reduce this notation, usually the layers (2) – (4), are embraced into so-called ‘triple-layers’ or ‘triplets’ [9-12]. The Kagomé layer is correspondingly named ‘single layer’. Because of rule (ii) mentioned above, there are only six triple layers possible: $\alpha\beta$, $\beta\alpha\gamma$, $\gamma\beta\alpha$, $\beta\alpha$, $\gamma\alpha\beta$, $\alpha\beta\gamma$. Because of rule (i), the first greek letter is determined by the preceding capital letter (i.e. the position (the holes) of the preceding single (Kagomé) layer). A single layer at position A can thus only be followed by the triple layers $\alpha\beta$ or $\alpha\beta\gamma$. The stacking position of the next single layer is, however, determined by the last Greek letter of the triple layer: B in case of $\alpha\beta$, C in case of $\alpha\beta\gamma$. The triple layers thus determine whether the transition between two single (Kagomé) layers belongs to the sequence $\dots A \rightarrow B \rightarrow C \dots$ or the twin sequence $\dots C \rightarrow B \rightarrow A \dots$. Members of the group of triple layers which establish the sequence $A \rightarrow B \rightarrow C$ are abbreviated by t, members of the second group of triple layers, which establish the sequence $C \rightarrow B \rightarrow A$ are abbreviated by t’. To describe

the stacking sequence of a Laves phase polytype, it is in principle sufficient to give only the sequence of triple layers, e.g. C14 can be denoted by ...tt'..., C36 by ...ttt't'... and C15 by ...ttt... or ...t't't'.... However, usually a single layer and its succeeding triple layer are embraced into a so-called 'quadruple layer', which is denoted by the stacking position of the single layer (X if it is on position A, Y if it is on position B and Z if it is on position C) and a prime, if the triple layer is of t' type (if it is of t type, the prime is omitted). C14 would thus be for example denoted by ...XY'..., C36 by ...XY'X'Z... and C15 by ...XYZ... or ...Z'Y'X'....

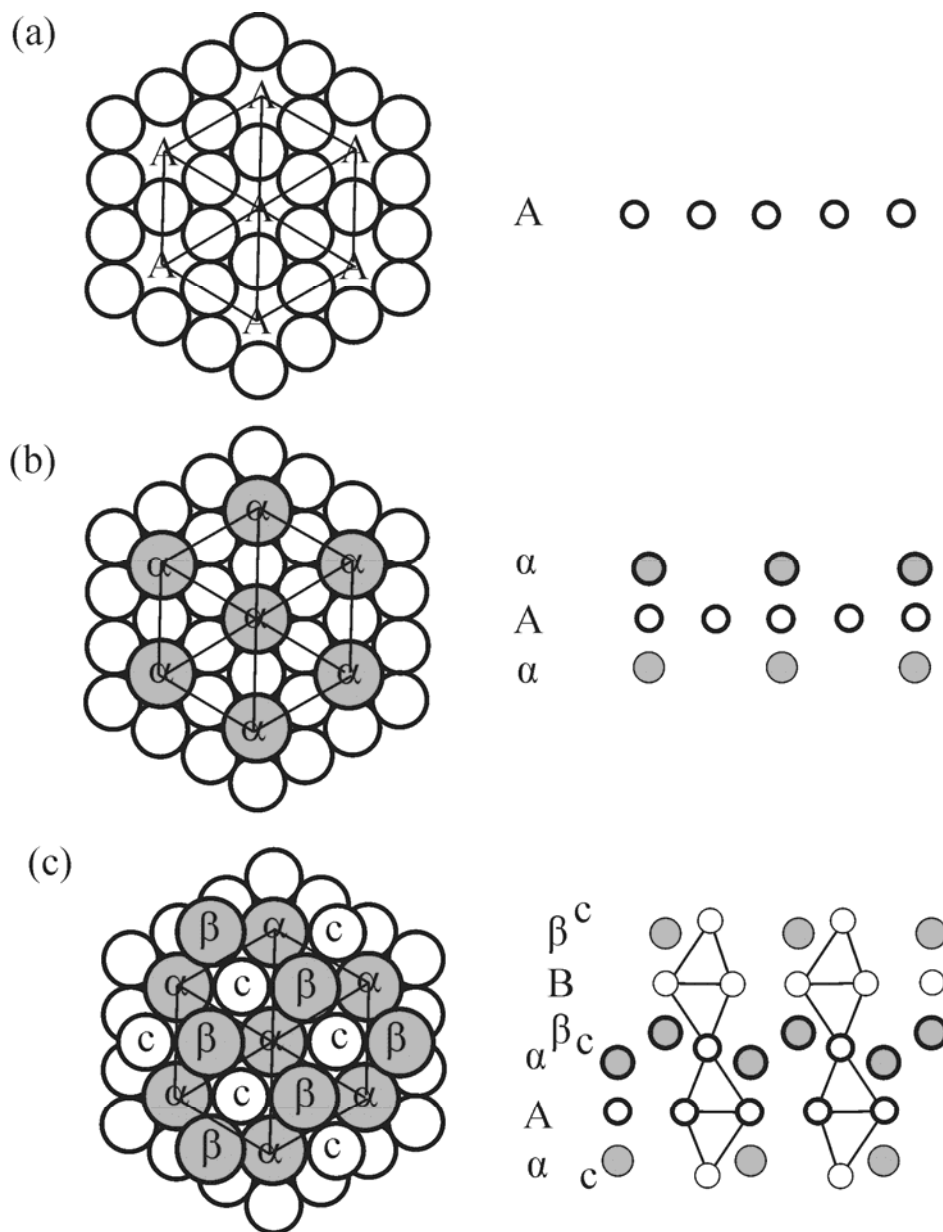


Fig. 1.2: Elements of the classical notation of the stacking sequence of Laves phases, left row: top view $[0001]$ direction and right row: view in $[11\bar{2}0]$ direction. Atoms shown in the top view on the left are indicated by the thick outlines on the right. (a) Kagomé layer of B atoms, (b) Kagomé layer with large A atoms positioned in the holes, (c) small atoms B added within the gaps. For illustration of the alternative notation, see Fig. 5.2 in chapter 5.

The “classical” notation described above has been used in a couple of publications dealing with Laves-phase polytypes or polytypic transformations of Laves phases. It emphasizes the complex structure and building principles of Laves phases compared to other structures, where the same polytype phenomena occur, e.g. simple-closest packed metals as e.g. cobalt. By comparing the stacking-sequence notation of e.g. the hcp structure (...AB...) or the fcc structure (...ABC... or ...CBA...) with the notations given at the end of the preceding paragraph, it becomes clear that, formally, only the primes mark the difference between the stacking principles of the two structures. If, e.g. during a polytypic phase transformation, the stacking sequence is locally changed, i.e. from X'Z to XY, this is associated with a change of a t' layer into a t layer (by synchroshear, see section. 1.2.3). This image, although valid, suggests some kind of “transformation” of the triple layer and also suggests that stacking sequences of Laves phase polytypes can not be as freely changed as in simple-close packed structures. In fact, the information contained in the primes of the A, B and C positions is redundant in terms of stacking sequence notation, the stacking sequences can be unambiguously notated by using only the position of the Kagomé layers (the single layers in the above described view) also by omitting the primes in general, because if the transition between two adjacent quadruple layers is part of the sequence $X \rightarrow Y \rightarrow Z$, then the first quadruple layer must always comprise a t layer (und thus be “unprimed”), while in case of the transition between two adjacent quadruple layers being part of the twin sequence $Z \rightarrow Y \rightarrow X$, the first quadruple layer must always comprise a t' layer (und thus be primed). An additional drawback of this “classical” notation is that the quadruple layers are not symmetric with respect to the Kagomé layer. The Kagomé layer with the two adjacent layers of large atoms, which is a rigid, compact building block, is split-up by the “classic” notation, what causes the apparent special role of the triple layers. A somehow unnatural and inconvenient concept of stacking sequences, which are changed not by change of the position of rigid building blocks but by structural changes of the building blocks themselves is evoked.

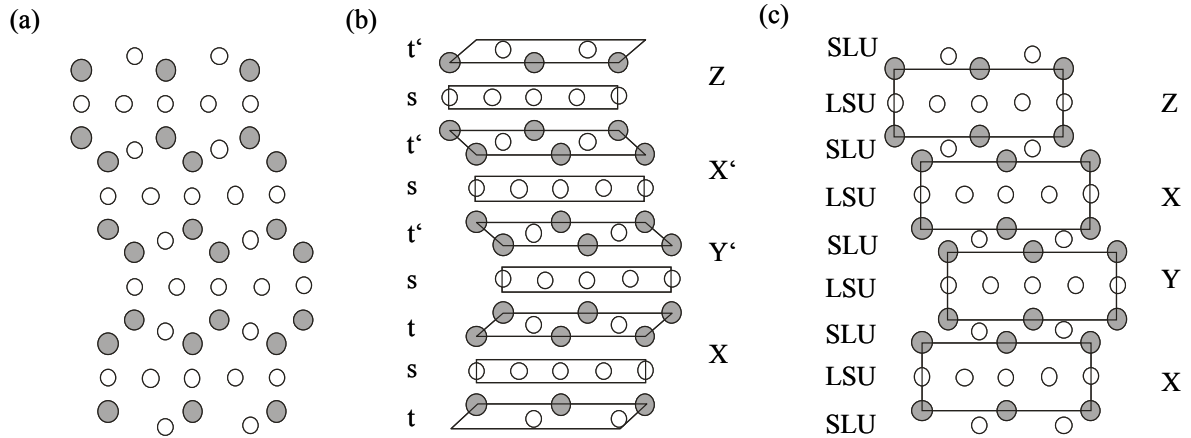


Fig. 1.3: (a) Crystal structure of a C36-Laves phase in an $[11\bar{2}0]$ projection. (b) classical subdivision of this crystal structure into triple (t , t') and single layers (s). Each, a single layer and a successive triple layer form a quadruple layer indicated by its stacking position X, Y and Z , where a prime indicates that a quadruple layer contains a t' layer. (c) Alternative subdivision of the crystal structure into layer-sandwich units (LSU) and single-layer units (SLU). The stacking sequence is indicated by the position X, Y and Z of the layer-sandwich units. No primes are needed. (cf. also Fig. 1.2 and Fig. 4.1 of chapter 4).

In this work, an alternate view (see Fig. 1.3 and Fig. 4.1 of chapter 4) on the stacking sequences of Laves phases will be introduced and used for the description of (changes of) Laves-phase stacking sequences, using the rigid building blocks of the Kagomé layers with the adjacent two layers consisting of large A atoms as basic units (called layer-sandwich units in the present work, $\alpha A\alpha$, $\beta B\beta$ and $\gamma C\gamma$ in the detailed notation), which are alternately stacked with the layers consisting of small B atoms (called single-layer units in the present work). The introduction of these building blocks is justified, because, as already discussed, the layer-sandwich units represent rigid building blocks, which remain unchanged if the stacking sequence is modified. The image of the compact, rigid layer sandwich units, which are alternately stacked with the single-layer units positioned in-between appears to be closer to the nature of the stacking principle of Laves phases. The positions of the layer-sandwich units are indicated by capital letters, the positions of the single-layer units by lower-case letters. The two rules

regarding allowed stacking sequences given above can be adapted to this notation. Rule (1) is covered by introduction of the rigid layer-sandwich units. Rule (2) can be written in terms of two new rules:

- (1) Two adjacent layer-sandwich units must not be located at the same stacking position, i.e. a capital letter may not be followed by the same capital letter (same rule exists for the layers of simple close-packed structures),
- (2) A single-layer unit must not be located at the same position as the adjacent layer-sandwich units, i.e. a lower case letter has to be different from both adjacent capital letters.

C14 would thus be denoted by ...XzYz..., C36 by ...XzYzXyZy... and C15 by ...XzYxZy... or ...ZxYzXy.... It is obvious that the only difference to the stacking sequences formed for simple closest packed structures is rule (2) and the lower-case letter in the notation of the stacking sequences, i.e. the presence of the single layer units. On the other hand, because of rules (1) and (2), the position of the single-layer unit is fixed by the positions of the layer-sandwich units. Hence the lower-case letter is given by the two adjacent capital letters, and it can thus be omitted, which is done in this work. The formal analogy between Laves phases and other layered structures is thus clear and not hidden behind use of the prime. The difference to other layered structures is the mechanism by which polytypic phase transformations, i.e. changes on stacking sequence, proceed (see section on synchroshear).

1.2.2 Polytypism of Laves-phase

1.2.2.1 Approaches towards a systematic understanding of the phenomenon

Several approaches have been undertaken to understand the occurrence of Laves phases in a binary or multinary system and especially to identify the factors which determine which of the different polytypes is stable. It has been shown that there is no correlation between the atomic size ratio and the structure type formed [13]. A dependence of the stable structure type of the valence electron concentration has been only observed within particular series of Laves phase structure, but not in general [1].

Also, so-called structure maps have been assessed, giving the stable structure type as a function of two different structure-controlling factors, e.g. the valence electron concentration and the atom-size ratio (Fig. 1.4, [14]) or the Mendeleev numbers of the two elements A and B constituting binary Laves phases. Although in these phase maps, fields can be identified, which are crowded predominately by one particular structure type, also exceptions are present.

The observed role of the valence electron concentration in the control of the stable polytype has given rise to some calculations of the electron density-of-states by the Extended Hückel method [15]. The results indicate a complex, cyclic change of the stable structure type as a function of the valence electron concentration. Such calculations, however, are restricted to stoichiometric compositions and 0 K. A general understanding of the structure-controlling factors for all compound systems, temperatures and compositions is still lacking.

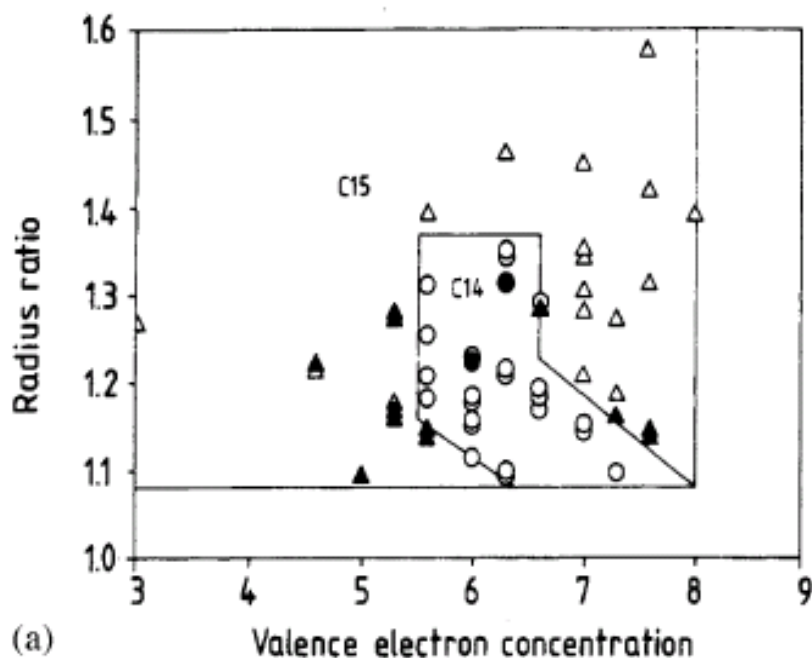


Fig. 1.4: Example of a structure map, showing the stable structure type of several Laves phases as a function of valence electron concentration and the atomic radius ratio. The triangles indicate the C15 polytype, the circles the C14 polytype. Filled symbols indicate a temperature-dependent phase transformation [14].

1.2.3 Occurrence of different polytypes within one system

Different Laves-phase polytypes may exist within one binary or multinary alloy system, either as a function of temperature or as a function of composition or even as a function of pressure. The following systematic observations can be made [16]:

- If two or more polytypes occur for the same composition, but at different temperatures, then the cubic C15 modification is the low-temperature modification and the hexagonal C14 and C36 are high-temperature phases.
- If two or more polytypes occur at the same temperature, but at different compositions, for binary Laves phases the C15 phase is always the modification situated around the stoichiometric composition, whereas the the C14 or C36 modifications have off-stoichiometric compositions.
- Laves phases which occur in ternary systems, but do not occur in one of the binary boundary systems have the C14 structure.

1.2.4 Polytypic phase transformations in Laves phases: Synchronshear

Polytypic transformations between Laves-phase polytypes occur by changes in the layer-stacking sequence. It requires displacement of the layer-sandwich units, and, different from similar transformations in simple-close packed structures, simultaneous displacement of the single layer units into a crystallographic direction different from the displacement of the layer-sandwich units due to the crystallographic restrictions concerning the stacking sequences as described in section 1.2.1. The concept of such “simultaneous shear of sub-layers into different directions”, called synchronshear has been introduced for the first time for sapphire [17]. Allen et al. [9] have proposed that this concept should also be applicable to Laves phases. It is postulated that this shear is established by passage of partial dislocations with a core spread over two adjacent atomic layers associated with two different Burgers vectors, called synchro-Shockley dislocations. Glide of this type of dislocations is also proposed as the microscopic mechanism for plastic deformation of Laves phase crystals by shear and twinning [11, 18-20]. The existence of this type of dislocations has been proven by direct observation recently [21]. For a detailed introduction into the concept of synchronshear in Laves phases, see the introduction and theory sections of chapters 4 and 5 of this work.

The polytypic phase transformation of Laves phases is thus a shear transformation, involving a layer-wise change of atom positions. The symmetry of the individual layers is not changed by the transformation. Similar transformations occur e.g. in elementary Co [22] or the Co-Fe system [23, 24] and are addressed as martensitic transformation. In contrast to the martensitic transformations occurring e.g. in the Fe-C system, the polytypic phase transformations in Laves phases are thermally activated transformations, which can be suppressed e.g. by fast cooling [12, 25, 26], see chapters 2 and 6.

1.3 Scope of the thesis

The present work aims at understanding the polytypic phase transformations in Laves phases. The structural changes during such phase transformation are investigated; the validity of the concept of synchroshear is evaluated and further elaborated. Because of the questionable reliability of the literature data concerning phase stability and occurrence of different polytypes in Laves phases, also the field of thermodynamics and phase stability has been covered.

This work has been performed in the framework of the inter-institutional research initiative “The Nature of Laves Phases” funded by the Max Planck society, which aimed at improving the data basis and the fundamental understanding on transition-metal Laves phase systems.

1.4 Experimental strategy

1.4.1 General remarks

Experiment-based work on, especially the transition-metal, Laves-phase systems has to face some distinct challenges, which are the main reason that the experimental data basis especially on phase transformations is still extremely scarce and the data on thermodynamics and phase stability is often incomplete, contradictory or erroneous. This is on the one hand result of the difficult sample preparation for the high-melting point transition-metal Laves-phases (see section 1.4.4 and chapter 2), but also can be attributed to the difficult structure identification with respect to distinction between different Laves phase polytypes. Additionally, as also shown in the present work (chapters 4, 5 and 6), two-phased microstructures consisting of two different Laves-phase polytypes usually exhibit these polytypes not as well-separated phases, but as a common intergrowth structure, which can be conceived as a single Laves phase with a stacking sequence which varies between the sequences associated with the two constituting polytype.

Consequently, in the present work, literature data has been always verified by own experiments. An amount of work has been spent on investigations of phase stability, occurrence of different polytypes as a function of temperature and composition and on the microstructure and defect structure of the investigated Laves phases subject to polytypic transformations. This effort has been the essential requirement for the investigations concerning phase transformations

1.4.2 Structure identification and evaluation of defect and microstructure

The often erroneous or contradictory data on stability of Laves phase polytypes can be in most cases attributed to the fact that especially X-ray diffraction patterns, but also electron-diffraction patterns of different Laves phases are often very similar for different polytypes. The broadening of reflections, occurring due to layer-stacking faults, which may be introduced by polytypic phase transformations, often hides reflections which are characteristic for a particular modification. Especially the C36 modification is often erroneously identified as C14. Consequently, in the present work, emphasis has been laid on thorough structural investigations: High-quality X-ray powder diffraction employing

monochromatic $\text{CuK}_{\alpha 1}$ radiation has been performed, the X-ray diffraction patterns have been carefully evaluated, not only concerning structure identification but also revealing layer-defect structures; the findings from X-ray diffraction have been verified and complemented by high-resolution electron microscopy (see Chapters 4, 5 and 6).

1.4.3 Selection of model systems

To investigate the mechanism and kinetics of polytypic phase transformations in Laves phases, model systems have to be selected, where the different polytypes occur depending on temperature at the same composition, because only in this case the kinetics will be determined by the synchroshear mechanism itself and not by long-range diffusion. To keep the model systems under investigation as simple as possible, only binary Laves phases were considered as candidate systems for the present investigations. An overview of the candidate Laves phases is provided by Table 1.1.

Table 1.1: Binary systems including Laves phases AB_2 with temperature-dependent transitions between different Laves-phase modifications. RT: room-temperature modification, HT1, HT2: high-temperature modifications. Data from [27], except for Ta-V [28]. In case of Hf-Fe, the data refer to Hf-rich $HfFe_2$, stoichiometric $HfFe_2$ is reported to be C14 for all temperatures.

System <i>A-B</i>	RT	transition temperature (°C)	HT1	transition temperature (°C)	HT2	Melting temperature or transition temperature to other structure
Nb-Cr	C15	1585-1620	C14			1770 [27] or 1730 [29] (congruent melting) ^a
Ta-Cr	C15	1660-1695	C14			2020 (congruent melting)
Ti-Cr	C15	800-1220	C36	1270	C14	1370 (transition to bcc)
Zr-Cr	C15	1532-1592	C36	1622	C14	1673 (congruent melting)
Hf-Cr	C15	1335	C14			1825 (congruent melting)
Ta-V	C15	1125-1280	C14			1430 (transition to bcc)
Hf-Mo	C15	1783-1858	C36			2170 (incongruent melting)
Hf-Fe	C15	1200	C36			1640 (incongruent melting)
Sc-Fe	C14	1310	C15	1510	C36	1600 (congruent melting) ^b
Mg-Th	C36	750	C15			812 (incongruent melting) ^b

^a The data on $NbCr_2$ will be discussed in chapter 2. It will be shown in particular that C14 is no stable modification and no equilibrium phase transformation exists.

^b The occurrence of polytypes as a function of temperature is obviously in contrast to the observation mentioned in section 2.2.2, that C15 is usually the low-temperature modification, whereas C14/C36 are the high-temperature modifications. This data is thus questionable.

To ensure experimental accessibility of the polytypic transformations and manageability of sample production, systems were excluded with too high transformation/melting temperatures, this affects Ta-Cr and Hf-Mo. The systems Ta-V, Hf-Fe, Sc-Fe and Mg-Th have been declined due to questionable and insufficient data basis regarding the phase diagrams and the polytypic transformations. In case of Zr-Cr,

the temperature ranges of the stability fields of the high-temperature polytypes are very narrow, which induces experimental difficulties. Moreover, the temperature of the eutectic on the Zr-rich side of the Laves phase is lower than the phase transformation temperatures, which additionally limits the handling of the samples at the phase transformation temperatures (see discussion in section 5.3). In general, systems were avoided, where the Laves Phase melts incongruently, because this turns preparation of single-phase, compositionally homogenous samples in a melting process very difficult.

Hence, the systems Nb-Cr, Ti-Cr and Hf-Cr are identified as candidate systems. The present work puts a focus on Nb-Cr and Hf-Cr. For Ti-Cr see [30].

1.4.4 Control of high-temperatures, sample composition and contamination level

Many transition metal Laves phases occur in systems with at least one refractory element, thus high-melting element and have in most cases a high melting point (substantially higher than 1000°C) themselves. Diffusivity is restricted at least in the lower and intermediate temperature range and phase transformations are often very sluggish. Production of well-defined homogeneous samples with respect to composition and establishing of phase equilibria is thus very difficult and requires long-term heat treatments at high temperatures. This leads to some severe problems: many transition metals forming Laves phases are very reactive, at least when exposed to high temperatures, and the danger of sample contamination, e.g. by light elements, is very high. As it will be shown in chapter 2 of the present thesis, this can lead to erroneous conclusions on phase stability.

A problem can also be the selective evaporation of one constituent during sample preparation from the liquid state or extensive heat treatments at high temperatures, associated with considerable changes in sample composition. This in particular affects the Laves phases containing chromium, which has a comparably high vapour pressure. The liquid state is especially sensitive on this issue, due to fast transport of the evaporating element to the surface. Also powders with a high surface-to-volume ratio suffer from this problem. It should, however be noted that also in case of massive samples, the region directly beneath the surface experiences chromium loss, what can lead to partial melting of the sample if a eutectic is situated next to the Laves phase in the

direction of decreasing chromium content and if the sample is heated above the eutectic temperature. As a last point, proper control and measurement of high temperatures is a non-trivial task.

The Laves-phase systems Nb-Cr and Hf-Cr investigated in the present study are sensitive to all experimental challenges mentioned above. The melting point of NbCr₂ is 1730°C [29], the sample homogenization treatment has been conducted at 1500°C and experiments were conducted in a temperature range from 1500°C to the melting point. The melting point of HfCr₂ is 1825°C [27], the homogenization treatment has been performed at 1420°C and further heat treatments have been conducted in a temperature range from 1050°C to 1300°C. The measures taken to prevent sample contamination, evaporation of chromium and to ensure proper temperature control were as follows.

The preparation of the initial alloy ingots has been conducted using an arc-melting furnace under a high-purity argon atmosphere. Immediately before melting of the samples, a titanium ingot has been molten in order to getter away the remaining oxygen and nitrogen impurities from the atmosphere. To ensure chemical homogeneity of the as-cast ingots, they have been flipped and remolten several times. Selective chromium evaporation during this step can not be prevented. By composition analysis after sample preparation (chemical analysis, wave-length dispersive X-ray spectroscopy) and by determination of the weight difference between the as-cast ingots and the initial element material, an empirical value on chromium loss can be determined based on several produced samples, which can be accounted for during successive sample preparation. However, establishing of a certain sample composition is only possible in a range of about ± 0.2 at.% for NbCr₂ and HfCr₂.

Heat treatments above 1150°C have been performed using an inductive furnace, originally intended for casting purposes (Fig. 1.5 and 1.6). This furnace basically consists of a tiltable induction coil within gas-tight container, within which a vacuum in the order of 10^{-7} Pa can be established. By repeated evacuation of the container and backfilling with argon of purity 5N, a high-purity atmosphere could be established. The sample itself was placed in an alumina crucible within a molybdenum susceptor. The crucible and the susceptor itself each were covered by a zirconium getter sheet. Temperature measurement

has been complicated especially during the heat treatments of NbCr_2 and HfCr_2 . Evaporized chromium reacted with the platinum (type B) thermocouple resulting in failure of the thermocouple. During extensive trials, it has been realized that also use of a protective cover for the thermocouple was not appropriate, because this lead to false (too low) temperature values. As a solution, before each heat treatment, the thermocouple has been placed at the location of the sample (in the absence of the sample itself) and the susceptor was heated to the targeted temperature. The induction voltage used to establish this temperature subsequently has been used also for annealing of the sample, with the thermocouple being removed from the furnace.



Fig. 1.5: Furnace for homogenization and annealing treatments under protective atmosphere.



Fig. 1.6: Interior of the furnace showing the induction coil, the susceptor and the zirconium cover sheets.

In the high-temperature neutron diffraction measurements (chapter 2), a vacuum furnace has been used with type C tungsten thermocouples, which were located directly above the sample. Although it was possible to establish high-purity conditions within this furnace, selective evaporation of chromium has been a severe problem during the first set of experiments (see chapter 2). This problem has been addressed by using tantalum sample containers, within which the sample has been encapsulated by welding under a high-purity inert atmosphere.

The high-temperature differential thermal analysis (chapter 2) has been performed using a Netzsch DTA 409 CD apparatus (Fig. 1.7). The samples have been placed in tungsten crucibles coated with Y_2O_3 . The crucibles have been covered by relatively thick (2.5 mm) cover plates. Within the sample room, a high-purity atmosphere has been established by repeatedly evacuating and backfilling with 6N argon. Because the cover plates were not fixed to the crucibles at this stage, also within the crucibles itself a high-purity argon atmosphere has been established. During the experiments, an argon flow has been established. As an additional measure, the initially used polymeric tubes for argon supply have been replaced by stainless steel tubes. Upon heating, the tungsten covers

adhered to the crucibles, which on the one hand protected the sample material from the argon flow (which although being of high purity provides a steady flow of residual impurities to the sample room), on the other hand restricted chromium evaporation to an acceptable level.



Fig. 1.7: Experimental setup for high-temperature DTA measurements. The inset shows the measuring head with the tungsten crucibles and tungsten covers.

1.5 Outline of the thesis

In chapter 2, results of high-temperature neutron diffraction and high-temperature differential thermal analysis on NbCr₂ will be presented. Based on these results, it will be demonstrated that the reversible C14/C15 polytypic phase transformation, which is taken for granted in many works [29, 31-35] although it has never been directly observed, does not occur and the C14 phase, which actually has been observed in arc-melted ingots, is metastable.

In chapter 3, such arc-melted ingots will be inspected in detail by X-ray powder diffraction, electron-backscatter diffraction and high-resolution transmission electron microscopy. It will be shown, that the ingots consist mainly of the C15 modification. In the top-part of the ingots, remote from the cooling plate, however, also the C14, and to a major extent, a C36 modification containing large amounts of stacking defects are identified.

In chapter 4, this faulted C36 structure is examined further, using high-quality X-ray powder diffraction measurements and high-resolution transmission microscopy. A relation is established between the layer-fault structure of this C36 structure and selective reflection broadening in the X-ray powder diffraction patterns. It is further discussed how the observed layer faults are related to the supposed formation of this C36 phase from an initial C14 phase by the synchroshear mechanism involving synchro-Shockley partial dislocation dipoles. Similar data on TiCr₂ and NbCo₂ is presented in this chapter for comparison.

In chapter 5, high-resolution transmission electron micrographs obtained from synchro-Shockley dislocation dipoles in C36-NbCr₂ and C36-HfCr₂ are presented. In case of NbCr₂, an isolated dipole has been observed, whereas in HfCr₂ an arrangement of synchro-Shockley partial dislocation dipoles has been observed, which constitutes an “anti-phase boundary” between two impinged C36 domains.

In chapter 6, the occurrence of different polytypes as a function of temperature and phase composition for the HfCr₂-Laves phase has been investigated in order to validate the heterogeneous data in literature concerning polytypism of this Laves phase. It has been found that the C14 modification is stable from the melting point down to at least 1420°C. This modification can be retained at room temperature by fast cooling down. By

annealing at various temperatures, it has been found that C15 is the room temperature modification, but also a C36 modification is stable at intermediate temperatures (probably between about 1200°C and 1400°C, also depending on composition). Further, two tracing parameters are suggested, which can be used to trace phase transformations between the different polytypes.

In chapter 7, these tracing parameters are used to evaluate the kinetics of the C14 to C15 phase transformation of HfCr₂ in a temperature range from 1050°C to 1150°C. A value for the effective activation energy of this transformation has been obtained.

1.6 References

- [1] F. Stein, M. Palm and G. Sauthoff, *Intermetallics* 12 (2004) 713.
- [2] F.C. Frank and J.S. Kasper, *Acta Cryst.* 11 (1958) 184.
- [3] F.C. Frank and J.S. Kasper, *Acta Cryst.* 12 (1959) 483.
- [4] J.B. Friauf, *J. Am. Chem. Soc.* 49 (1927) 3107.
- [5] J.B. Friauf, *Phys. Rev.* 29 (1927) 34.
- [6] F. Laves and H. Witte, *Metallwirtschaft* 14 (1935) 645.
- [7] F. Laves and H. Witte, *Metallwirtschaft* 15 (1936) 840-842.
- [8] G.E.R. Schulze, *Zeitschrift fuer Elektrochemie und Angewandte Physikalische Chemie* 45 (1939) 849.
- [9] C.W. Allen, P. Delavignette and S. Amelinckx, *Phys. Status Solidi A* 9 (1972) 237.
- [10] P.M. Hazzledine and P. Pirouz, *Scr. Metall. Mater.* 28 (1993) 1277.
- [11] P. Hazzledine, *Twinning in Advanced Materials* (1994) 403.
- [12] K.S. Kumar and P.M. Hazzledine, *Intermetallics* 12 (2004) 763.
- [13] G. Leitner and G.E.R. Schulze, *Krist. Tech.* 6 (1971) 449.
- [14] A. von Keitz, G. Sauthoff and P. Neumann, *Z. Metallkd.* 89 (1998) 803.
- [15] R.L. Johnston and R. Hoffmann, *Z. Anorg. Allg. Chem.* 616 (1992) 105.
- [16] F. Stein, M. Palm and G. Sauthoff, *Intermetallics* 13 (2005) 1056.
- [17] M.L. Kronberg, *Acta Met.* 5 (1957) 507.
- [18] J.D. Livingstone and E.L. Hall, *J. Mater. Res.* 5 (1990) 5.

- [19] F. Chu and D.P. Pope, *Mater. Sci. Eng. A* 170 (1993) 39.
- [20] A.L. Kazantzis, M. Aindow, I.P. Jones, G.K. Triantafyllidis and J.T.M. De Hosson, *Acta Mater.* 55 (2007). 1873.
- [21] M.F. Chisholm, S. Kumar and P. Hazzledine, *Science* 307 (2005) 701.
- [22] Z. Nishiyama, "Martensitic Transformations" (1978), New York, Academic Press.
- [23] T. Waitz and H.P. Karnthaler, *Philos. Mag. A* 73 (1996) 365.
- [24] H. Heinrich, H.P. Karnthaler, T. Waitz and G. Kostorz, *Mater. Sci. Eng. A* 272 (1999) 238.
- [25] K.S. Kumar and P. Hazzledine, *Mater. Res. Soc. Symp. Proc.* 364 (1995) 1383.
- [26] W. Baumann, A. Leineweber and E.J. Mittemeijer, (2010). *To be published*.
- [27] T.B. Massalski, "Binary Alloy Phase Diagrams" (1990-1996), Metals Park, Ohio, ASM International.
- [28] E.M. Savitskii and Y.V. Efimov, *Monatsh. Chem.* 103 (1972) 270.
- [29] D.J. Thoma and J.H. Perepezko, *Mater. Sci. Eng. A* 156 (1992) 97.
- [30] W. Baumann, Dissertation. "Phase transformation kinetics of the TiCr₂ Laves Phase" (2010), Institute for Materials Science. University of Stuttgart
- [31] V.M. Pan, *Fiz. Met. Metalloved.* 12 (1961) 455.
- [32] I.I. Kornilov, K.I. Shakhova, N.B. Budberg and N.A. Nedumov, *Dokl. Akad. Nauk SSSR* 149 (1963) 1340.
- [33] L.N. Guseva, *Inorg. Mater.* 1 (1965) 1581.
- [34] Y.A. Kocherzhinskiy, V.Y. Markiv and V.V. Pet'kov, *Russian Metallurgy* 1 (1973) 134.
- [35] O. Vedmedenko, F. Rösch and C. Elsässer, *Acta Mater.* 56 (2008) 4984.

2. The absence of a stable hexagonal Laves phase modification (NbCr₂) in the Nb-Cr system

Jochen Aufrecht, Andreas Leineweber, Anatoliy Senyshyn and Eric Jan Mittemeijer

High-temperature differential thermal analysis and neutron diffraction have been employed to investigate the previously proposed polytypic phase transformation C14-NbCr₂ \rightleftharpoons C15-NbCr₂ at around 1600°C. It could be shown that for high-purity alloys and high-purity conditions, the phase transformation does *not* occur. However, small amounts of atmospheric contaminations induce the formation of an η -carbide type phase, which melts (partially) in a temperature range around 1600°C. This has led to the erroneous, former conclusion of the occurrence of a thermodynamically stable high-temperature modification of NbCr₂.

2.1 Introduction

For several binary Laves-phase systems, polytypic phase transformations between the different Laves-phase structures C14 (hexagonal, $P6_3/mmc$), C36 (di-hexagonal, $P6_3/mmc$) and C15 (cubic, $Fd\bar{3}m$) as function of temperature have been reported [1]. Classical examples are provided by the group IV-VI Laves phases, $TiCr_2$, $ZrCr_2$ and $HfCr_2$. Also for the group V-VI Laves phases, $NbCr_2$ and $TaCr_2$ (the V-Cr system does not exhibit a Laves phase but reveals solid solubility over the entire composition range), such temperature dependent, polytypism has been reported. Besides a C15 low-temperature modification, the existence of a C14 high-temperature modification has been reported for both alloys [2,3]. The high-temperature modification can be retained in samples solidified from the melt: the $TaCr_2$ alloy thus produced is 100% C14 and transforms only incompletely to C15 even upon very prolonged annealing at a temperature in the range where the C15 modification is stable [4]. Arc-melted or rapidly solidified $NbCr_2$ alloys are reported to consist partly of C14 and partly of C15 [5] and the C14- $NbCr_2$ modification completely transforms to C15 readily upon heating to 1000°C [5]. Occasionally, an intermediate C36 phase or other polytypes have been observed after casting or during subsequent annealing [5-7], cf. chapter 3. These experimental observations for the Nb-Cr and Ta-Cr systems have been attributed to very different transformation velocities for the C14 \rightarrow C15 transformation in the C15 phase field (very fast in case of $NbCr_2$ and very sluggish in case of $TaCr_2$). This is puzzling, for $NbCr_2$, because of the chemical similarity of Nb and Ta. Also the polytypic phase transformations of Laves phases, especially those forming the cubic C15 phase from hexagonal modifications (C14 or C36), are usually extremely sluggish, as observed for $TaCr_2$.

Nevertheless, the nature of C14- $NbCr_2$ as a stable high-temperature phase, which forms at around 1600°C, rather than as a metastable phase, seems to have been supported by high-temperature differential thermal analysis (HT-DTA) [8,9]: in the temperature range around 1600°C a thermal effect has been detected, which was endothermic upon heating and exothermic upon cooling. This thermal effect was interpreted as evidence for a reversible polytypic C14 \rightleftharpoons C15 transformation. As additional evidence for the

stability of the C14 structure at higher temperatures it can be mentioned that a stable C14 phase has been found for ternary Nb-Cr-Me alloys: e.g if Cr in NbCr₂ is partially replaced by Ni or Al or if Nb is partially replaced by Ti, Mo or W [9-11]. However, no *direct* evidence for the existence of a C14-NbCr₂ phase has been given up to now. Thus, the polytypic phase transformation between the hexagonal and the cubic modification, although commonly taken for granted, has been indicated as only preliminarily in the assessed phase diagrams (e.g. [2]).

Direct evidence for a stable C14 phase in NbCr₂ could be obtained by in-situ structure determination (i) above the (postulated) phase-transformation temperature or (ii) after solid quenching of C14-NbCr₂ from above the (postulated) phase-transformation temperature. Up to now, C14-NbCr₂ was only reported for samples quenched from the liquid state. On this basis in the present work, results obtained by application of high-temperature neutron powder diffraction (HT-NPD) and by new, elaborate HT-DTA measurements convincingly show that C14-NbCr₂ is no thermodynamically stable high-temperature phase. The thermal effects occurring at the proposed phase-transformation temperature arise instead from a secondary phase formed due to sample contamination.

2.2 Experimental details and results

Three C15-NbCr₂ alloys (cf. Fig. 2.1a), of different compositions, Nb_{31.0}Cr_{69.0}, Nb_{33.2}Cr_{66.8} and Nb_{34.8}Cr_{65.2} (specimen compositions as weighted-in and validated by lattice-parameter measurements [12]), were produced by arc-melting from high-purity elements. The samples were flipped and remelted several times to ensure chemical homogeneity. Then the samples were homogenized at 1500°C for 62 h in an induction furnace with high purity argon atmosphere, where the sample container as well as the susceptor were covered with Zr getter sheets. After homogenization and as evaluated by X-ray powder diffraction, the Cr-rich specimen was two-phased, i.e. dominantly C15-NbCr₂ with a very small amount of Cr-rich solid solution as secondary phase, whereas the two other alloys were single-phase C15-NbCr₂.

HT-NPD measurements were performed at SPODI (structure powder diffractometer) at the FRM-II neutron source (Garching, Germany), using a resistance

furnace under vacuum. As sample container, for the first experiment with the Nb-rich sample ($\text{Nb}_{34.8}\text{Cr}_{65.2}$) a non gas-tight Ta tube was employed, which led to chromium evaporation due to the high vapour pressure of Cr and the high temperatures, changing the sample composition such that it entered the two-phase field $\text{NbCr}_2 + \text{Nb}$ solid solution. This problem was fixed by using a gas-tight Ta tube in a second experiment. In the second experiment, the stoichiometric single-phase $\text{Nb}_{33.2}\text{Cr}_{66.8}$ specimen and the two-phase Cr-rich $\text{Nb}_{31.0}\text{Cr}_{69.0}$ specimen were used. Ta contamination did not occur as shown by energy-dispersive X-ray spectroscopy (EDX) for specimens which remained solid during the whole experiment. Specimens which (partially) attained a liquid state during the treatment contained several at% of Ta after the experiment. Thus only results obtained before any melting of the specimen occurred are relevant for investigating the stability of a C14- NbCr_2 phase.

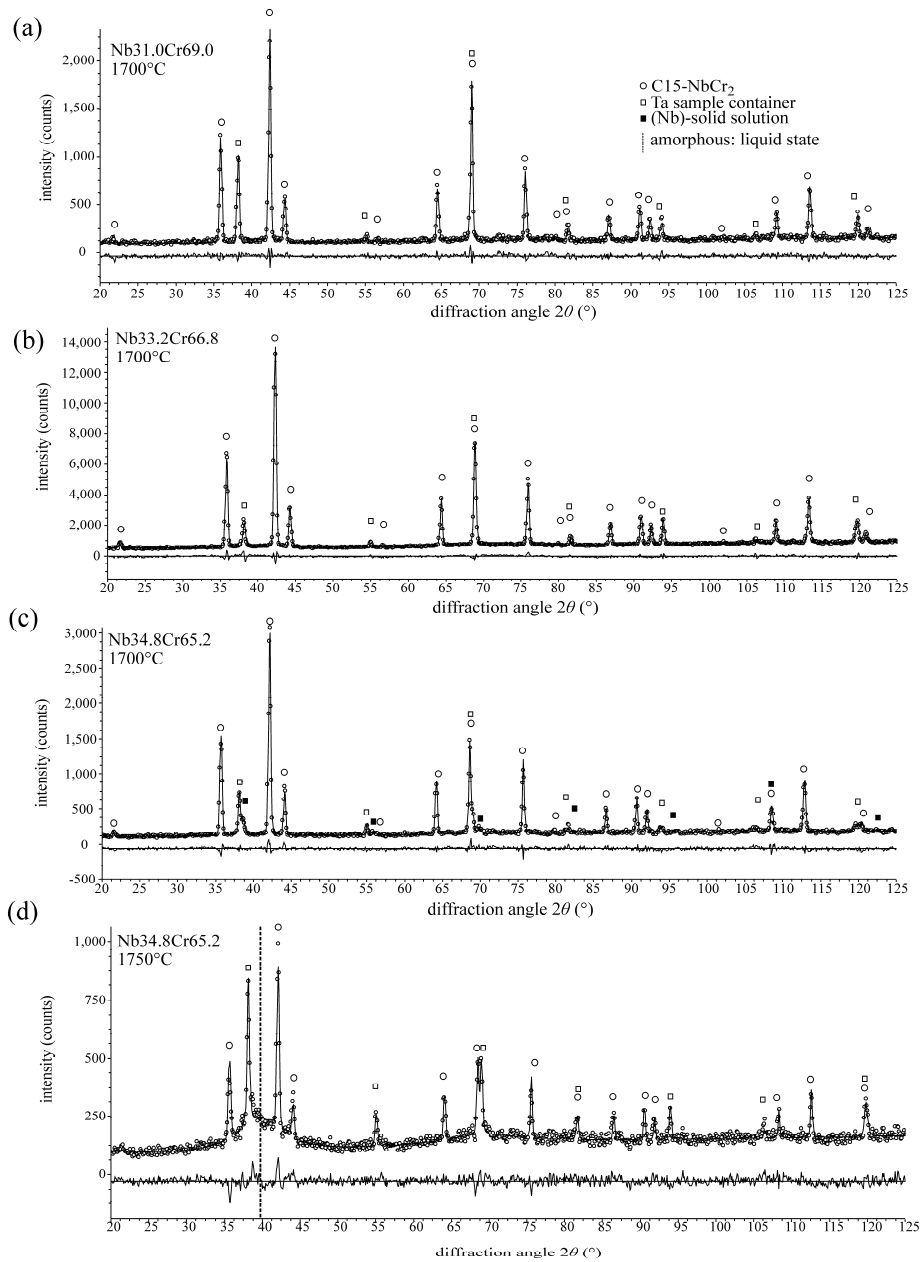


Fig. 2.1: High-temperature neutron diffraction patterns of NbCr₂ samples: (a) initial composition Nb_{31.0}Cr_{69.0} at 1700°C, (b) initial composition Nb_{33.2}Cr_{66.8} at 1700°C. (c) initial composition Nb_{34.8}Cr_{65.2} at 1700°C, where chromium evaporation changed the specimen composition causing formation of a Nb-rich (bcc) solid solution. (d) same sample as (c) at 1750°C, where a broad maximum in intensity (position indicated by the vertical dashed line) corresponds to a liquid phase. In all cases, no other Laves phase modification of NbCr₂ then C15 can be detected. The small circles represent experimental data points, whereas the black solid line corresponds to the best Rietveld fit.

In case of all three compositions, no structural changes have been detected during heating from room temperature to 1700°C (Fig. 2.1). The crystal structure of NbCr₂ remained C15, although for temperatures above around 1600°C, C14 would be expected according to the literature as stable modification. In case of the first experiment, the specimen was heated until partial melting started. Even in this case the C15 structure appears to be in equilibrium with the melt. These results are obviously incompatible with the occurrence of a C15 → C14 transformation above about 1600°C as deduced from the earlier DTA works.

Therefore, new HT-DTA experiments were performed using a Netzsch DTA 409 CD apparatus. W crucibles, coated with Y₂O₃ were used. The measurement chamber was evacuated and back-filled with argon three times. During the experiment, a constant argon flow of 50 ml/min was established. In a first series of experiments, argon of purity 5N was employed as well as thin W sheets to cover the crucibles. Three heating/cooling cycles were performed between 1200°C and 1620°C applying a heating/cooling rate of 20 K/min. At around 1560°C a peak was detected which is endothermic upon heating and exothermic upon cooling (Fig. 2.2a), similar as reported in [8,9]. To identify this thermal effect with the polytypic C15→C14 phase transformation of NbCr₂, as in the previous works [8-10], is invalidated by additional observations:

- (1) The initial powder sample had a droplet shape after the HT-DTA experiment, which yet did not reach the nominal melting temperature, 1730°C, of NbCr₂.
- (2) An evaluation of the area of the peak in the HT-DTA scan (after calibration of the instrument using Pd) yielded enthalpy values which increased from 8 kJ/mol (first cycle) to 18 kJ/mol (third cycle). This rather is the magnitude of melting enthalpies than the magnitude of reaction enthalpies associated with solid-solid phase transformations. Moreover, in the latter case, the reaction enthalpy should remain constant for all cycles.
- (3) A post-mortem XRD pattern (Fig. 2.3) revealed the appearance of a new cubic phase (lattice parameter $a = 11.523 \text{ \AA}$), which appears to be an η -carbide type phase (Ti₂Ni related) [13].

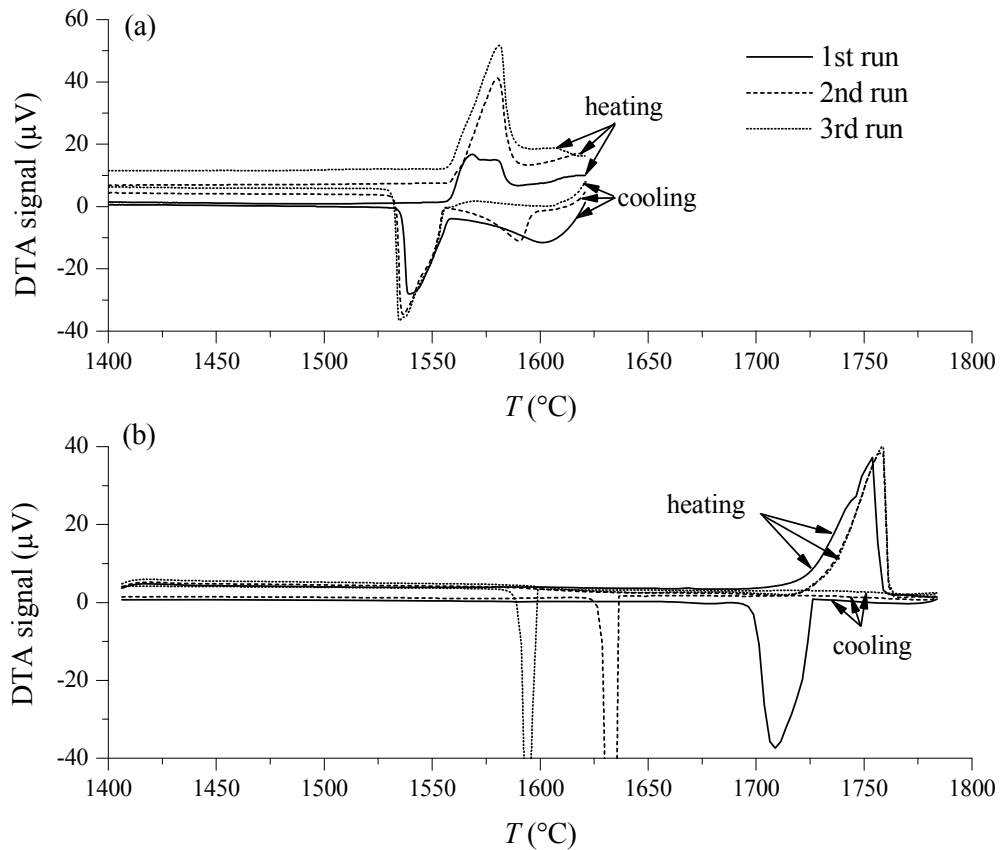


Fig. 2.2: DTA curves taken during three heating/cooling cycles with a stoichiometric NbCr_2 sample: (a) experiencing formation of the η -carbide type phase due to sample contamination, showing thermal effects which are attributed to melting/re-solidification of this phase. (b) without formation of the η -carbide type phase. The only thermal effects in this measurement are attributed to melting/re-solidification of the C15-Laves phase. Due to undercooling of the melt, the peaks corresponding to solidification are shifted towards lower temperatures in the 2nd and 3rd cooling cycle (nucleation of the solid phase became more difficult with each cooling cycle). No thermal effect at around 1600°C, where the $\text{C14} \rightleftharpoons \text{C15}$ phase transformation has been reported to occur, can be detected.

An η -carbide type phase, mentioned under (3) above, has been frequently encountered in investigations of the Nb-Cr system (e.g. [12,14])¹. However, this phase was not detected during the present HT-NPD experiments. Therefore, this phase is likely an impurity-stabilized phase with O or N taking the role of carbon. Rietveld analysis performed in this work [17] (not being sensitive to the presence of interstitial O/N atoms) revealed that within the space group $Fd\bar{3}m$ Cr occupies the $16c$ and $32e$ Wyckoff sites and Nb occupies the $48f$ Wyckoff sites in the crystal structure of the η -carbide type phase. Thus the formula of the phase may be Nb_3Cr_3X ($X = N, O$) or Nb_6Cr_6X ($X = N, O$), i.e. η_{66} or η_{33} adopting a nomenclature for η -carbide type phases proposed in Ref. [13]². The higher Nb content (compared to the Laves-phase composition) in the η -carbide type phase explains also the observed formation of a Cr-rich solid solution next to the η -carbide type phase (see Fig. 2.3b).

Next, the experimental setup was modified in order to avoid even small specimen contaminations: 6N argon was used instead of 5N, the standard plastic tubes for gas supply were replaced by stainless steel tubes, and the thin W cover sheets were replaced by thick W discs (thickness: 2.5 mm). With this new setup, while performing three heating/cooling cycles between 1400°C and 1780°C, no peak was detected in the HT-DTA scans between 1550°C and 1600°C (Fig. 2.2b). The endothermic peak occurring at 1760°C upon heating can be identified with the melting of $NbCr_2$. During cooling, corresponding exothermic peaks caused by solidification occur, which are in case of the second and third cycle shifted to lower temperatures due to undercooling. After the experiment, no η -carbide type phase could be identified in the diffraction pattern (Figs. 2. 3a,b).

¹ Also in recent works, diffraction patterns have been presented, where, upon inspection, this η -carbide type phase clearly is present to a large fraction. However, in the papers concerned, the reflections corresponding to the η -carbide type phase were erroneously attributed to C14-NbCr₂, C36-NbCr₂, Nb or Cr [15,16].

² These formulas assume full occupancy of either type of octahedral interstitial sites present in the metallic framework of the η -carbide type phase. The present investigations do not allow quantitative statements on the occupancies of these sites and thus on the interstitial content, except that this phase occurs in the Cr-Nb system only upon contamination.

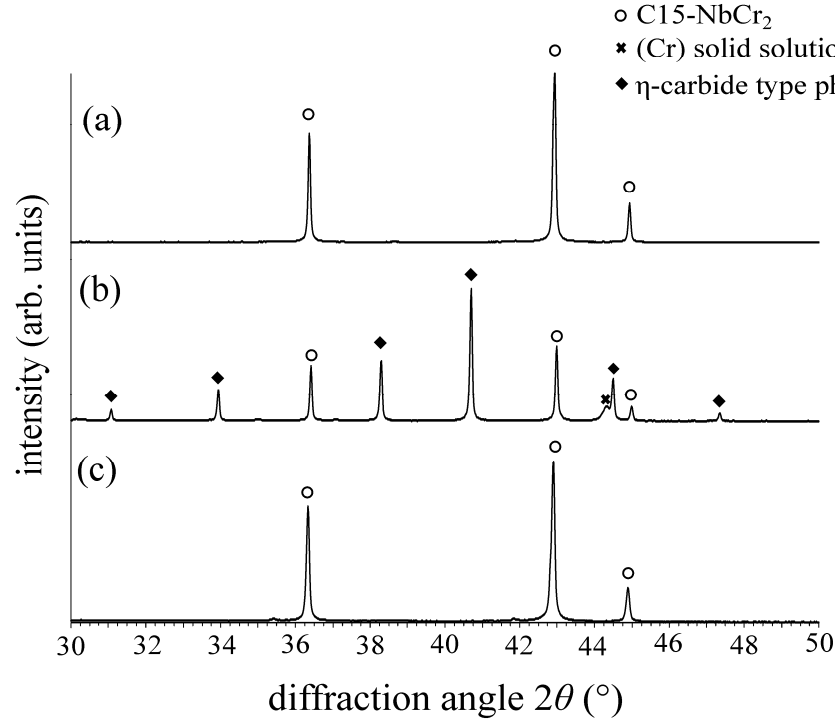


Fig. 2.3: X-ray diffraction patterns (Cu-K α_1 radiation) recorded at room temperature of the stoichiometric NbCr₂ sample (a) before the experiments, (b) after three heating/cooling cycles between 1200°C and 1620°C using the initial experimental setup, leading to formation of the η -type phase and (c) after three heating/cooling cycles between 1400°C and 1780°C using the modified, high-purity experimental setup

2.3 Conclusions

Hence, it is concluded that oxygen (maybe also nitrogen) contamination of the alloy during high-temperature experiments promotes the formation of a η -carbide type phase, which melts at temperatures between 1550°C and 1600°C. In the past, this has led to the erroneous conclusion of the occurrence of a polytypic (C15→C14) transformation of NbCr₂ at (and above) about 1600°C. HT-NPD and HT-DTA experiments, during which the formation of this secondary phase could be avoided by establishing very clean conditions did not give any evidence of such a polytypic phase transformation of NbCr₂. C14-NbCr₂ is *not* a stable high-temperature modification of NbCr₂. The formation of

C14-NbCr₂ during (rapid) solidification is not challenged by this finding; this phase is likely a metastable, non-equilibrium phase [7], cf. chapter 3.

The existence of stable C14-high temperature modifications in the other group IV-VI or group V-VI Laves-phase systems, especially TaCr₂, is not challenged by this finding. The difference to these other systems could be that temperature (range) of a virtual C14 \rightleftharpoons C15 equilibrium is above the melting point of the structure. The present finding indeed also explains the apparent differences between NbCr₂ and TaCr₂ regarding C14 \rightleftharpoons C15 phase transformation kinetics and the impossibility to obtain pure C14 upon (rapid) solidification from the melt, which have been discussed in literature [5,14].

This work has been performed within the framework of the Inter-Institutional Research Initiative "The Nature of Laves Phases" funded by the Max Planck Society.

2.4 References

- [1] F. Stein, M. Palm, G. Sauthoff, *Intermetallics* 13 (2005) 1056.
- [2] M. Venkatraman, J.P. Neumann, *Bull. Alloy Phase Diagr.* 7 (1986) 462.
- [3] M. Venkatraman, J.P. Neumann, *Bull. Alloy Phase Diagr.* 8 (1987) 112.
- [4] K.S. Kumar, P.M. Hazzledine, *Intermetallics* 12 (2004) 763.
- [5] D.J. Thoma, J.H. Perepezko, *Mater. Res. Soc. Symp. Proc.* 194 (1990) 105.
- [6] A.L. Kazantzis, T.T. Cheng, M. Aindow, I.P. Jones, *Inst. Phys. Conf. Ser.* 147 (1995) 511.
- [7] J. Aufrecht, A. Leineweber, E.J. Mittemeijer, *Mater. Res. Soc. Symp. Proc.* 1128 (2009) 481.
- [8] V.M. Pan, *Fiz. Met. Metalloved.* 12 (1961) 455.
- [9] I.I. Kornilov, K.I. Shakhova, N.B. Budberg, N.A. Nedumov, *Doklady Akademii Nauk SSSR* 149 (1963) 1340.
- [10] V.N. Svechnikov, V.M. Pan, *Issled. po Zharoproch. Splavam, Akad. Nauk SSSR, Inst. Met.* 8 (1962) 47.
- [11] T. Takasugi, M. Yoshida, *J. Mater. Res.* 13 (1998) 2502.
- [12] D. Grüner, PhD-Thesis, "Untersuchungen zur Natur der Lavesphasen in Systemen der Übergangsmetalle" (2006) Dresden University of Technology.

- [13] P. Ettmayer, R. Suchentrunk, *Monatsh. Chem.* 101 (1970) 1098.
- [14] L.N. Guseva, *Inorg. Mater.* 1 (1965) 1581.
- [15] X.W. Nie, S.Q. Lu, K.L. Wang, *Mater. Char.* 59 (2008) 816.
- [16] S.Q. Lu, H.Z. Zheng, M.W. Fu, *Scripta Mater.* 61 (2009) 205-207.
- [17] R.A. Young, Ed., *The Rietveld method*, Oxford Univ. Press, Oxford, 1995.

3. Metastable hexagonal modifications of the NbCr₂ Laves phase as function of cooling rate

Jochen Aufrecht, Andreas Leineweber and Eric Jan Mittemeijer

In as-cast ingots produced by arc-melting, several metastable polytypic modifications of NbCr₂ were found additional to the cubic C15 phase stable at room temperature: C14, C36 and 6H-type structures, often highly faulted and/or intergrown. Strikingly, these phases had formed at locations of the specimen which had experienced a relatively low cooling rate, whereas the C15 phase was formed preferentially in regions which had experienced the highest cooling rates.

3.1 Introduction

In the binary Nb-Cr system, the Laves phase NbCr₂ exhibits the cubic C15-type structure (prototype: MgCu₂) at room temperature [1]. Nevertheless, in as-cast ingots, other Laves-phase polytypes of NbCr₂ have been found: Guseva found a “hexagonal structure” [2]. Thoma et. al. reported hexagonal C14 and C36 modifications (prototypes: MgZn₂ and MgNi₂) in as-cast ingots prepared by arc-melting, together with the stable C15 phase [3, 4]. The amount of the metastable phases was reported to depend on the location within the ingot: more metastable phase at locations adjacent to the water-cooled copper hearth (i.e. the ground plate) of the arc-melting furnace, i.e. at locations where relatively high cooling rates occurred. Splat-quenched NbCr₂ samples contained an even larger fraction of C14, but always together with the C15 modification [3]. Kazantzis et al. [5] reported various Laves-phase polytypes in solidified arc-melted alloys together with the C15 modification: Besides C14 and C36 also more complex polytypes (Ramsdell symbols 6H, 8H and 9R) were suggested to be present.

The occurrence of a C14 modification seems to be in agreement with the commonly accepted phase diagram [1], which incorporates a C14-type high-temperature modification of NbCr₂ stable between about 1600°C and the congruent melting point at 1770°C. It has thus been supposed that NbCr₂ solidifies into this crystal structure, in the first stage of cooling upon solidification, which structure is only partially retained upon continued cooling to room temperature. The high cooling rates occurring after arc-melting or during splat-quenching necessitate very fast kinetics to complete the C14 → C15 transformation, while this type of transformation has been reported to be very sluggish in Laves phases like TaCr₂, HfCr₂ and TiCr₂ [6]. The transformation is assumed to proceed by the “synchro-shear” process, involving mediation by a certain type of complex partial dislocations, changing the stacking sequence of the Laves-phase structures [6, 7]. On this basis the occurrence of stacking sequences of longer period than corresponding with C14 and C15, as 4H (= C36), 6H, 8H and 9R, which could represent intermediate stages, might be understood. Contamination with O and N has also been suggested as possible reason for the formation of these longer-period stacking variants [5].

However, recent work by our group indicates that a reverse C15 \rightarrow C14 transformation does not occur at high temperatures upon heating [8]; C15 appears to melt directly. Thus, the C14 phase should be of metastable nature at all temperatures, which invalidates the above interpretation as presented in Refs. [2-5]. In the present work, NbCr₂ ingots produced by arc-melting were examined using X-ray powder diffraction (XRPD), electron-backscatter diffraction (EBSD), in combination with energy-dispersive X-ray spectroscopy (EDX) and high-resolution transmission electron microscopy (HR-TEM). The occurrence of metastable phases was demonstrated and an alternative explanation for their formation is presented.

3.2 Experiment

NbCr₂ ingots within the compositional range from 32.4 at% Nb to 34.5 at% Nb were prepared from high-purity niobium and high-purity chromium (Nb: non-metallic impurities < 10 ppm, Ta \sim 50 ppm, other metallic impurities \sim 80 ppm; Cr: non-metallic impurities 34 ppm, other metallic impurities \sim 20 ppm). Ingots of about 5 g were produced by arc-melting appropriate amounts of chromium and niobium under a titanium-gettered argon atmosphere. Six-fold flipping and remelting of the ingots ensured chemical homogeneity (in the liquid state). In the furnace, the samples were placed in moulds on a water-cooled copper hearth, thus the cooling rate was very high in the arc-melting furnace. However, note that by dedicated rapid solidification techniques (e.g. splat quenching [3]), considerably higher cooling rates are achieved.

For XRPD investigations, the ingots were crushed into several pieces, such that the original locations within the ingots of the obtained single pieces were known. From these pieces, powders were produced by grinding in a mortar; each powder was suspended in isopropanol and sedimented on a (510)-cut Si crystal plate (wafer) using a supporting brass ring during evaporation of the liquid. XRPD patterns were obtained using a “Philips X’Pert MPD” diffractometer equipped with a germanium single crystal monochromator in the incident beam, thus using Cu-K _{α 1} radiation.

Metallographic samples for EBSD and EDX analyses were produced by embedding large pieces (about one fourth) of an ingot into a conductive mould and by

subsequent grinding and polishing, using a dispersion of colloidal silicon oxide (OPS) for the final polishing step to remove any deformed surface-adjacent material. EBSD analysis was performed using a Zeiss scanning electron microscope (LEO 438VP) equipped with an EBSD system (TSL, EDAX Inc.) and using the software OIM 4.5.

For HR-TEM analysis using a Philips CM 30 (300kV) apparatus, a coarse powder was produced from a piece taken from the top of one of the ingots (initial sample composition of $\text{Nb}_{34.5}\text{Cr}_{65.5}$). The powder was sedimented on a copper mesh. Due to the brittle nature of the investigated materials, the edges of the powder particles were thin enough to be electron transparent.

3.3 Results

The XRD patterns taken from the top part and from the bottom part of ingot obtained by arc-melting of initial composition $\text{Nb}_{33.3}\text{Cr}_{66.7}$ (see Fig. 3.1) show that besides reflections from the stable C15 room-temperature modification, also reflections pertaining to hexagonal modifications as C14 or C36 are present. Those reflections of these latter structures with the indices $h-k = 3N$ ($N = 0, \pm 1, \pm 2, \dots$) coincide with the C15 reflections. Some of the C36 reflections ($h-k \neq 3N$ and $l = 4M \pm 1$, ($M = 0, \pm 1, \pm 2, \dots$)) are severely broadened, so that they are only with difficulties discernible against the background. This selective broadening of reflections can be attributed to specific types of stacking faults occurring in the hexagonal modifications. A quantitative estimation of the relative amount of C14 and C36 is very difficult from the XRPD patterns, since all non-broadened reflections of C36 (reflections with $h-k = 3N$ as well as with $h-k \neq 3N$ and $l = 4M \pm 2$) occur at same locations as C14-type reflections.

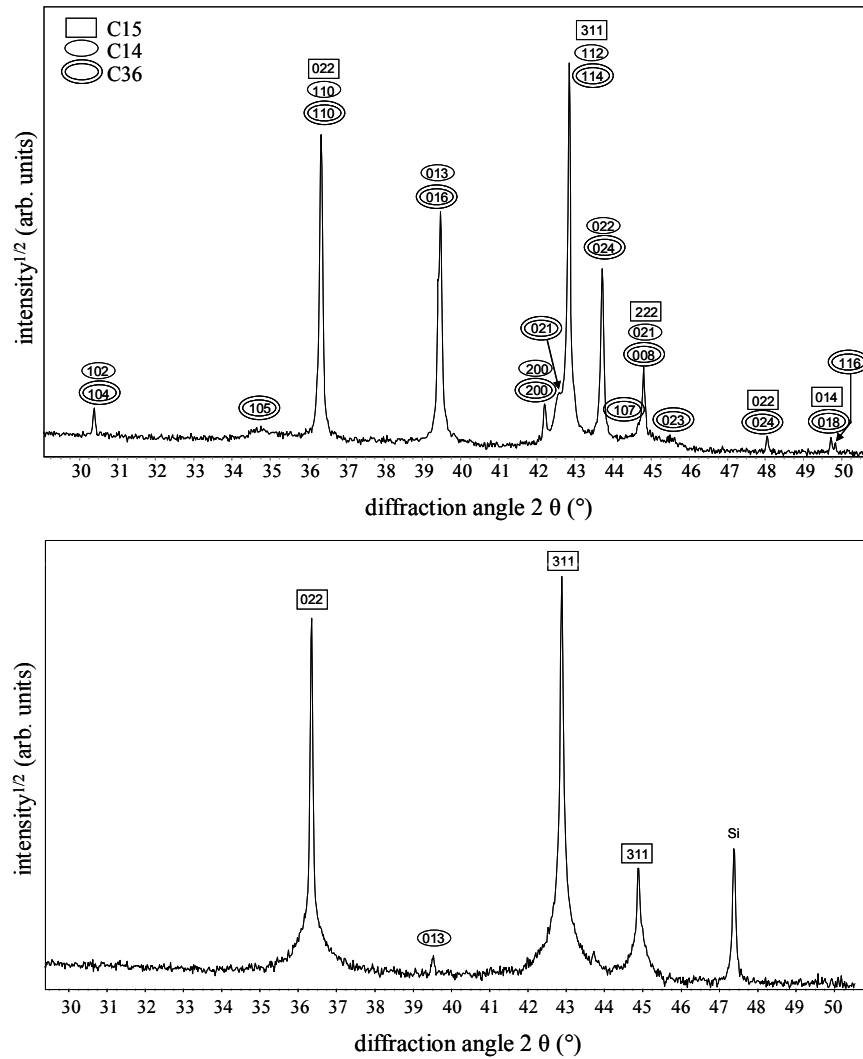


Fig. 3.1: XRPD patterns of material taken from the top (left) and the bottom (right) parts of an NbCr₂ ingot upon arc-melting. Whereas the material taken from the bottom part consists predominantly of the C15 modification, the material taken from the top part of the ingot is relatively rich of the hexagonal C14 and C36 modifications. Note that the C36 modification exhibits strongly hkl-dependent broadening of the reflections.

Very remarkably, according to the XRD pattern from the bottom part of the ingot, where it was in contact with the water-cooled copper hearth of the arc-melting furnace, a much smaller amount of these hexagonal C14/C36 phases is present at the bottom part, which was found to be the case in this work for all investigated ingots, irrespective of

their composition. This is in striking contradiction with results reported in Refs. [3,4], where C14 was found to occur preferably in the bottom parts of the ingots.

Phase distinction by EBSD is difficult: The Kikuchi patterns pertaining to C14 and C36 are very difficult to distinguish and, moreover, the C15 phase often exhibits very fine twins so that patterns originating from two twin variants within one crystallite may overlap, leading to incorrect assignment of C15 regions to C14/C36. Nevertheless, the occurrence of the hexagonal non-C15 modifications preferentially in the top part of the ingot, rather than in the bottom part, could be confirmed by EBSD (Fig. 3.2a). Additionally, the grain size in the top part of the ingot could be shown to be much larger than in the bottom part: The hexagonal crystallites appear to be larger than the cubic C15-type crystallites (Fig. 3.2b). Accompanying EDX measurements did neither reveal a detectable composition gradient from top to bottom of the ingot, nor differences in composition between hexagonal and C15 crystallites.

In a HR-TEM investigation of material taken from the top part of an as-cast ingot (Fig. 3.3), a total of 15 different crystallites were investigated. For only one crystallite, the pure C14 structure could be observed. For two crystallites, the C14 type structure occurred together with the C36 type structure. The latter structure type was the most frequently observed one: In 9 crystallites it occurred exclusively and in two others it occurred together with the C15 modification. The pure C15 modification was found in only one crystallite. Stacking faults occurred in most of the observed structure types (and additionally twins in the C15 structure type). The stacking fault density was highest in the C36 structures type, where as a consequence of the faulting 6H-type stacking sequences (...cchcch..., "6H1") were found. Sometimes, intergrowth structures consisting of sequences of C14, C36 and 6H-type stacking units were observed. Stacking faults found in C14 usually involved intergrowths of C36-type sequences.

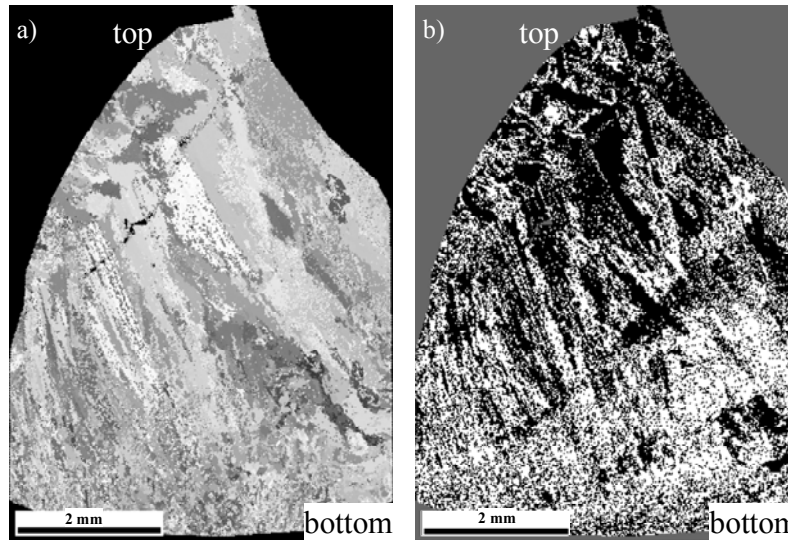


Fig. 3.2: EBSD orientation (a) and phase map (b). In the phase map, dark areas correspond to the C14 or the C36 structure types; white areas were indexed as C15 structure type. In the orientation map, different grey shades correspond to different crystallite orientations. The crystallite size is much larger in areas the top part of the ingot, where also the hexagonal C14 and C36 modifications occur preferentially.

3.4 Discussion

Employing three different techniques it has been shown in this work that additionally to the C15 modification, also C14 and C36 modifications of NbCr_2 occur in as-cast ingots. The assumption of C14 being a high-temperature modification stable above around 1600°C has been disproven recently [8], cf. chapter 2. The appearance of the hexagonal C14/C36 modifications in the top part of the arc-melted ingots is especially surprising, as one would expect that non-equilibrium phases are formed during solidification preferentially at locations where the cooling rate is very high. For samples produced upon arc-melting, the cooling rate in the bottom part of the ingots, where they are in contact with the water-cooled copper hearth, is expected to be significantly higher than in the top part. However, no or only small quantities of C14 or C36 could be detected in the bottom part. Thus, two questions have to be answered: why do metastable hexagonal modifications form from the melt during solidification and why do these structures form preferentially in regions experiencing relatively low cooling rates (top of ingots)?

For the following considerations, two assumptions are made: (i) the Gibbs energies of formation of the competing Laves structures are very similar [10], and (ii) the C36 phase does not crystallize from the melt but forms from an initially solidified C14 phase. Instead of the direct transformation of C14 to equilibrium C15 upon continued cooling, which transformation is supposed to be sluggish as observed in similar systems [6], a (kinetically more favoured) transformation to C36 might occur. In view of Gibbs energy of formation, C36 may be intermediate between C14 and C15. The high density of stacking faults in C36 found in the present investigations can be taken as indication that C36 has been formed from C14 by the

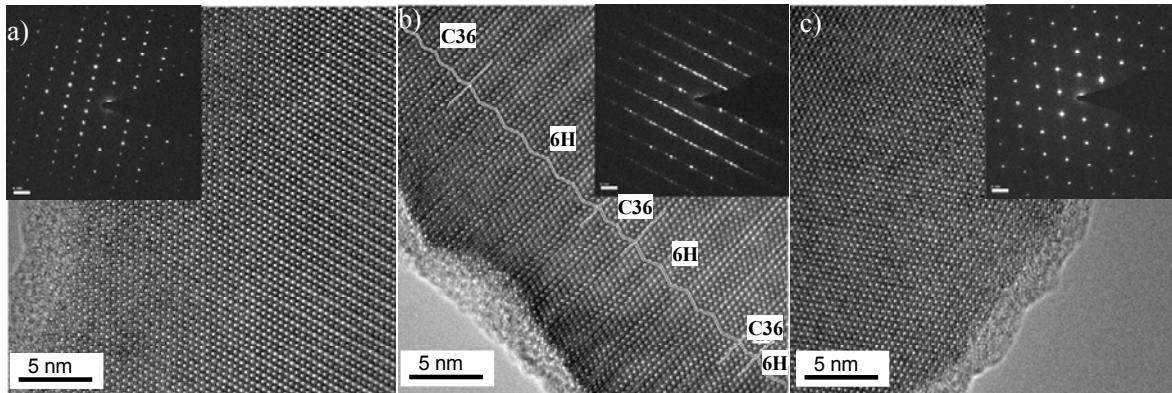


Fig. 3.3: HR-TEM images and corresponding selected-area diffraction patterns (SADPs) obtained from material taken from the top part of an ingot upon arc-melting. In a), a C14 crystallite without stacking faults is shown ([010]-zone). In b), an intergrowth structure consisting of C36 and 6H-type stacking is present ([010]-zone). The faulting gives rise to streaking in the SADPs, i.e. appearance of diffuse intensity along the $h0l$ lattice rows. In c), an image of a C15 crystallite is shown (110-zone).

synchro-shear mechanism rather than by direct crystallization from the melt [9], cf. chapter 4. Further, the only type of stacking fault found in C14 involves C36-type stacking sequences.

If the C14 phase would be a stable high-temperature modification (i.e. have the lowest Gibbs energy of formation directly below the melting point) of NbCr_2 , as proposed before [1], the retention of this phase and the formation of C36 from C14 could be understood easily in view of the sluggish $\text{C14} \rightarrow \text{C15}$ transformation. In the bottom

part of the ingot, a higher cooling rate can lead to undercooling of the melt down to temperatures where C15 is the (much more) stable phase, and thus, this phase is present in this part of the ingot. However, such an interpretation is in contradiction with the recent results presented in [8], cf. chapter 2, which invalidate C14 as stable high-temperature phase. (An only very small possible stability range of C14, of some Kelvin below the melting point of NbCr₂, could be beyond detectability by the methods as used in [8], cf. chapter 2).

If C14 is an unstable phase at all temperatures (i.e. has a slightly higher (less negative) Gibbs energy of formation than C15 at all temperatures below the melting point), it could nevertheless be formed during solidification because due to the very similar Gibbs energies of the competing Laves phase structures below the melting point, phase selection upon solidification may be determined by nucleation. A smaller value for the solid/liquid interface energy in case of C14, as compared with C15 could favour nucleation of C14. This will apply especially, when crystallization occurs at temperatures near the melting point, so that nucleation occurs at relatively low undercooling, i.e. in regions experiencing relatively small cooling rates. In the bottom part of the ingot, the melt may be undercooled very fast and thus much more pronouncedly than in the top part of the ingot. At large undercooling the difference between the Gibbs energy of formation of the stable C15 and the metastable C14 will be larger than at small undercooling. Hence, C15 is formed preferentially in the bottom part of the ingot and C14 (and thus C36) is formed preferentially in the top part of the ingot.

As a final note, it is pointed out that no information on solidification at very low cooling rates (“equilibrium solidification”) can be given, since the cooling rate also in the top region of the ingot is still high (cooling to room temperature is achieved within some seconds). The present work deals with the significant differences in cooling rate within a solidifying ingot in an arc-melting furnace, for the case of an overall relatively high cooling rate, but smaller than in case of rapid solidification techniques as e.g. splat quenching.

3.5 Conclusions

XRPD, EBSD and HR-TEM characterization of as-cast ingots of the Laves phase NbCr_2 produced by arc-melting have shown the occurrence of hexagonal C14 and C36 modifications of NbCr_2 . These metastable phases were shown to be present, together with the stable cubic C15 equilibrium modification, predominately in the top part of the arc-melted ingots, whereas in the bottom part, which had been in contact with a water-cooled copper hearth, only very small amounts of these metastable phases occur. XRPD and HR-TEM analysis showed that at room temperature (i.e. after completed cooling) the major part of the hexagonal modifications is represented by the heavily faulted C36 phase, and that the C14 phase is a minority phase. The faulting in C36 suggests that this phase had formed from initially crystallized C14 by the synchro-shear mechanism.

The appearance of the metastable C14 phase (and subsequently the C36 phase within the originally C14 phase) is most likely if the undercooling upon solidification is rather small, i.e. in the top part of the ingot where the relatively lowest cooling rates occur. At large undercooling, i.e. in the bottom part of the ingot where the relatively highest cooling rates occur, the difference in Gibbs energy (of formation) of the C15 and the C14 phases can be relatively large, thereby promoting the formation of the C15 phase.

3.6 Acknowledgements

The authors wish to thank Mrs. Viola Duppel, Max Planck Institute for Solid State Research, Stuttgart for HR-TEM analysis and Mr. Ewald Bischoff, Max Planck Institute for Metals Research, Stuttgart for EBSD analysis.

This work has been performed within the framework of the Inter-Institutional Research Initiative “The Nature of Laves Phases” funded by the Max Planck Society.

3.7 References

- [1] M. Venkatraman and J.P. Neumann, *Bull. of Alloy Phase Diagr.* 7 (1986) 462.
- [2] L.N. Guseva, *Inorg. Mater. (USSR)* 1 (1965) 1581.
- [3] D.J. Thoma and J.H. Perepezko, *Mater. Res. Soc. Symp. Proc.* 194 (1990) 105.
- [4] D.J. Thoma and J.H. Perepezko, *Mater. Sci. Eng. A* 156 (1992) 97.
- [5] A.L. Kazantzis, T.T. Cheng, M. Aindow and I.P. Jones, *Inst. Phys. Conf. Ser.* 147 (1995) 511.
- [6] K.S. Kumar and P.M. Hazzledine, *Intermetallics* 12 (2004) 763.
- [7] C.W. Allen and K.C. Liao, *Phys. Status Solidi A* 74 (1982) 673.
- [8] J. Aufrecht, A. Leineweber, A. Senyshyn and E.J. Mittemeijer, *Scripta Mater.* 62 (2010) 227.
- [9] J. Aufrecht, W. Baumann, A. Leineweber, V. Duppel and E.J. Mittemeijer, *Phil. Mag.* 90 (2010) 3149.
- [10] O. Vedmedenko, F. Rösch and C. Elsässer, *Acta Mater.* 56 (2008) 4984.

4. Layer-stacking irregularities in C36-type Nb-Cr and Ti-Cr Laves phases and their relation with polytypic phase transformations

Jochen Auffrecht, Wolfgang Baumann, Andreas Leineweber, Viola Duppel and Eric Jan Mittemeijer

Specific layer-stacking irregularities have been identified in C36 (4H) Nb-Cr and Ti-Cr Laves-phases on the basis of X-ray diffraction line-profile analysis and high resolution transmission-electron microscopy. Domain boundaries and transformation errors within domains could be distinguished. The layer-stacking irregularities in both C36-NbCr₂ and C36-TiCr₂ can be associated with a preceding C14 (2H) → C36 (4H) phase transformation carried out by glide of mobile synchro-Shockley partial dislocation dipoles in an ordered fashion. The stacking irregularities observed can be interpreted as deviations from such perfect “ordered glide”. The interpretation is supported by the observation that in case of C36-NbCo₂, where no preceding C14 → C36 transformation occurs, different layer-stacking irregularities are observed.

4.1 Introduction

4.1.1 Laves phases; layer-stacking rules

In the last ten years the interest in Laves phases (general formula AB_2 ; A, B : metal atoms) has grown pronouncedly. From a practical point of view, Laves phases have been proposed as candidates for structural materials, but also for functional materials, like magnetic, superconducting materials and as hydrogen-storage materials [1]. From a scientific point of view, the Laves phases constitute the largest group of intermetallic phases occurring in a very large number of binary and ternary systems [2, 3], which makes it possible to study specific properties as function of the elemental constituents of the Laves phase. Such information allows tailoring the properties for specific applications.

Laves phases are characterised by their specific crystal structures, which are tetrahedrally close-packed structures and thus belong to the so-called Frank-Kasper phases [4, 5]. The different Laves-phase crystal-structure types can be conceived as polytypes generated by stacking several types of atomic layers subject to some particular stacking principles (Fig. 4.1). These crystal structures imply that the atomic-radius ratio of the A and B atoms, r_A/r_B , equals $(3/2)^{1/2} \approx 1.225$, regarding the atoms as hard spheres.

Different descriptions of stacking rules leading to the Laves phases are available in the literature. For the current purposes it suffices to focus on the stacking of *layer-sandwich units*, each composed of a specific stack of three atomic layers, AB_3A (this notation refers to the composition of this stacking unit; called layer triplets in Ref. [6]; not identical with the triple layers considered in some other works [7, 8]). Between these layer-sandwich units additional *single-layer units*, B are located (see Fig. 4.1). With respect to a given two-dimensional hexagonal unit mesh defined by the lattice-structure basis vectors \mathbf{a} and \mathbf{b} perpendicular to the stacking direction, the A atoms of the *layer-sandwich units* and the B atoms of the *single-layer units* can each assume three different relative positions, i.e. at fractional coordinates either $(0, 0)$, or $(1/3, 2/3)$ or $(2/3, 1/3)$.³ Representing the position of the layer-sandwich units by X, Y , and Z , and of the single-layer units by x, y , and z , depending on which of the former three positions is assumed by

³Use of the symbols A, B , and C to indicate the relative layer positions is prevented to avoid confusion with the symbols A and B used for the two different metals constituting the Laves phase AB_2 .

the layer concerned (i.e. (0, 0): X, x; (1/3, 2/3): Y, y; and (2/3, 1/3): Z, z), the layer-stacking sequence of a Laves phase can be represented by an alternate sequence of these upper- and lower-case letters. The following rules apply additionally:

(i) Taking first only into account the upper-case letters, a given letter, say X, may only be followed by a different other upper-case letter, in this case Y or Z, i.e. an X cannot be followed by an X (Y not by Y; Z not by Z).

(ii) A *single-layer unit* located between two *layer-sandwich units* is represented by a lower-case letter different from the upper-case letters representing the adjacent *layer-sandwich units*. Consequently, a z-type single layer is located between X and Y, i.e. the corresponding part of the stacking sequence reads ...XzY.. or ..YzX...

Table 4.1: The most important Laves-phase stacking types described as polytypes (see text)

stacking sequence	stacking sequence, "reduced"	Jagodzinski symbol ^a [9]	Ramsdell symbol [10]	Strukturbericht symbol [11]	prototype	space group
XzYxZy	XYZ	c	3C	C15	MgCu ₂	$Fd\bar{3}m$
XzYz	XY	h	2H	C14	MgZn ₂	$P6_3/mmc$
XzYxZxYz	XYZY	ch	4H	C36	MgNi ₂	$P6_3/mmc$
XzYxZyXyZxYz	XYZXZY	cch	6H ^b	--	--	$P6_3/mmc$

^a The Jagodzinski symbol indicates the stacking transition associated with a certain layer-sandwich unit: "h", if the layer-sandwich units above and below the respective layer are both at the same position and "c" if they are at different positions. The respective crystal structures are built up by infinite repetition of the stacking transitions given by the Jagodzinski symbols. To obtain one single, complete unit cell in stacking direction of the respective crystal structure, the number of layers given by the Ramsdell symbol is necessary; i.e. ...ccc... for 3C, ...hh... for 2H, ...chch... for 4H and ...cchcch... for 6H.

^bThis 6H-type structure is often referred to as 6H₁. The 6H₂ structure with the Jagodzinski symbol hchhc is not considered here.

Since the positions of the single layer units are unambiguously prescribed by the positions of the adjacent layer-sandwich units (see above), it is sufficient for most purposes to consider only the upper-case letters to indicate the stacking sequence, as done at most places in the present paper. In terms of only the X, Y, and Z symbols describing the stacking sequences following the rules given above, the possible polytypes of Laves phases constitute one-to-one analogues of the polytypes possible for closed-packed structures of pure elements, and also of the polytypes possible for SiC, CdI₂ etc. Against this background, see also Table 4.1 summarizing the most important Laves-phase polytypes.

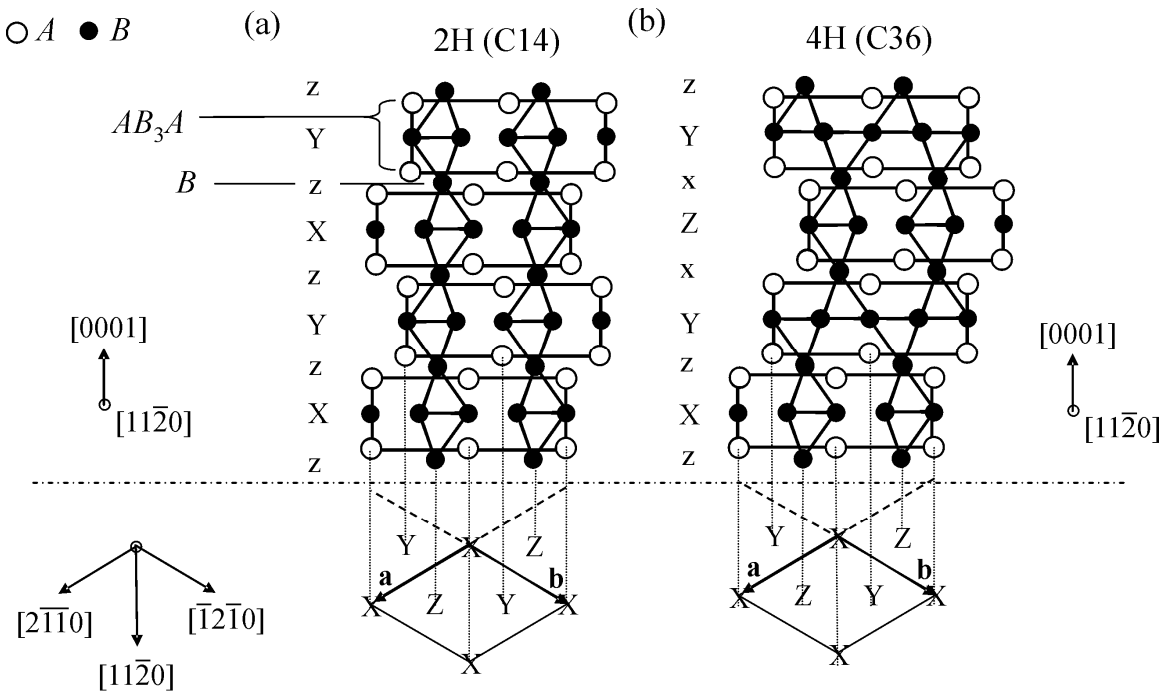


Fig. 4.1: Schematic crystal structure of (a) C14 type Laves phase and (b) C36 type Laves phase, built up by alternate stacking of AB_3A layer-sandwich units and B single-layer units. In the upper part of the figure, the layer-stacking sequences have been displayed in a $[11\bar{2}0]$ projection, i.e. the $[11\bar{2}0]$ direction is perpendicular to the plane of drawing. In the lower part of the figure, the stacking positions have been indicated in $[0001]$ projection. The basis vectors **a** and **b**, perpendicular to the stacking $[0001]$ direction, span a two-dimensional hexagonal unit mesh.

4.1.2 Partial-dislocation dipole mechanism for polymorphic transformations in Laves phases

The phase diagrams of many binary and ternary systems comprise several Laves-phase polytypes. The stability of a particular polytype can vary as function of composition or temperature (at constant pressure). A transformation from one to another polytype is in principle possible without need of long-range diffusion. A number of works have been dedicated in the past to the problem how such a polymorphic transformation can occur [7, 8, 12-15]. One main idea is that the layer-stacking sequences, considering only the layer-sandwich units, are changed by glide of partial dislocations, with six different Burgers vectors $\pm\mathbf{b}_1 = \pm\frac{1}{3}[10\bar{1}0]$, $\pm\mathbf{b}_2 = \pm\frac{1}{3}[\bar{1}100]$, and $\pm\mathbf{b}_3 = \pm\frac{1}{3}[0\bar{1}10]$ (Fig. 4.2; employing Miller-Bravais indices for hexagonal crystal structure lattices, where the basis vectors \mathbf{a} and \mathbf{b} correspond to those used for the unit mesh mentioned in section 4.1.1; cf. Fig. 4.1), along the basal (0001) plane between two (assumedly rigid) *layer-sandwich units*. Thereby the relative position of the layer-sandwich unit, say “above” the (0001) glide plane becomes changed with respect to that of the layer-sandwich unit “below” the (0001) glide plane (Fig. 4.3). Note that, as consequence of stacking rule (ii) indicated above, this glide process requires that the *single-layer unit* between the two *layer-sandwich units* has to move synchronously in another direction, but also within the glide plane. Thus the shear process associated with one of the above-mentioned Burgers vectors is actually a synchroshear process, which has been discussed in more detail elsewhere [7, 8, 14, 15]. The corresponding *partial* dislocations are, therefore, called synchro-Shockley partial dislocations [14].

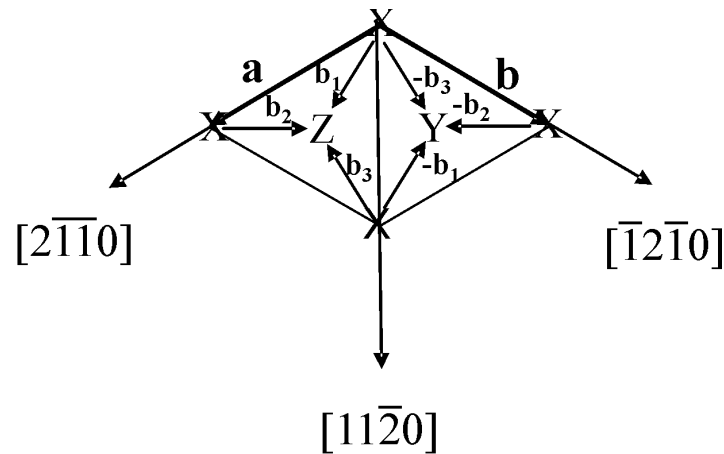


Fig. 4.2: Stacking positions and Burgers vectors of partial dislocations in a (0001) plane of a Laves phase.

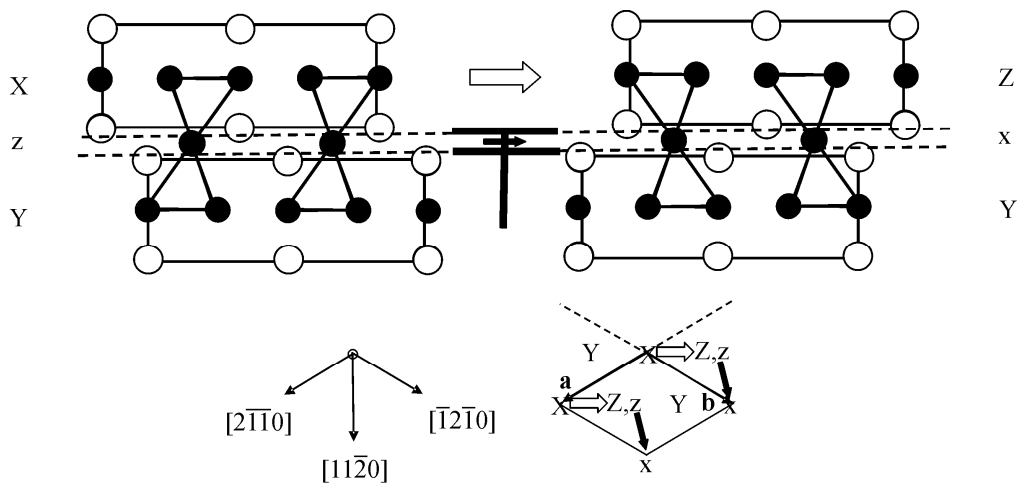


Fig. 4.3: Change of layer-stacking sequence by glide of a single synchro-Shockley partial dislocation. The *layer-sandwich unit* AB_3A , denoted by X in the left part of the figure, and the *single-layer unit* B, denoted by z in the left part of the figure, are shifted along the (0001) glide plane according to different Burgers vectors, as indicated in the [0001] projection in the bottom part of the figure: the white arrows correspond to the Burgers vector associated with the shift of the *layer-sandwich unit*; the black arrows correspond to the Burgers vector associated with the shift of the *single-layer unit*. The symbols \perp and \perp denote single synchro-Shockley partial dislocations with Burgers vectors of opposite sign. The symbols \perp or \perp do *not* specify whether the dislocation is of edge-, screw- or mixed character.

It has been proposed [14, 15], supported by some experimental evidence (see below), that in case of a C14 (2H) \rightarrow C36 (4H) transformation, such synchro-Shockley partial dislocations as described above do not glide through the crystal independently. Instead they glide as *dislocation dipoles*, where the two dislocations comprising the dipole have Burgers vectors of opposite sign (e.g. \mathbf{b}_1 and $-\mathbf{b}_1$) and with one dislocation travelling above and one dislocation travelling below a given *layer-sandwich unit*. As net effect, only the middle layer-sandwich unit and accordingly the two adjacent single layer units are shifted with respect to the initial stacking sequence, whereas the upper layer-sandwich unit remains at its original position. Hence, such dislocation dipoles do not lead to a macroscopic shear of the crystal (see Fig. 4.4) and thus can occur under the constraint of conservation of shape of the crystal. Thus, simple, ordered (i.e. periodic) sequences of such dislocation dipoles can bring about the 2H (C14) \rightarrow 4H (C36) (Fig. 4.5) and the 2H (C14) \rightarrow 6H transformation, which have been frequently observed in real systems. Early high-resolution electron microscopy (HRTEM) studies on TiCr_2 , in which a C14 \rightarrow C36 transformation proceeds, revealed C36 domains growing parallel to the (0001) plane into the C14 matrix [13]. This observation is compatible with the glide of synchro-Shockley partial dislocation dipoles as transformation mechanism. In the same work [13] it was indicated that the apparent sluggishness of formation of 3C (C15)- TiCr_2 from 2H (C14)- TiCr_2 (in contrast to that of formation of 4H and also 6H) might be ascribed to the impossibility to accomplish the 2H \rightarrow 3C transformation by a partial dislocation dipole mechanism as discussed above; the 2H \rightarrow 3C transformation has to involve macroscopic shear for the crystal considered, which can be difficult to realize in a polycrystalline specimen.

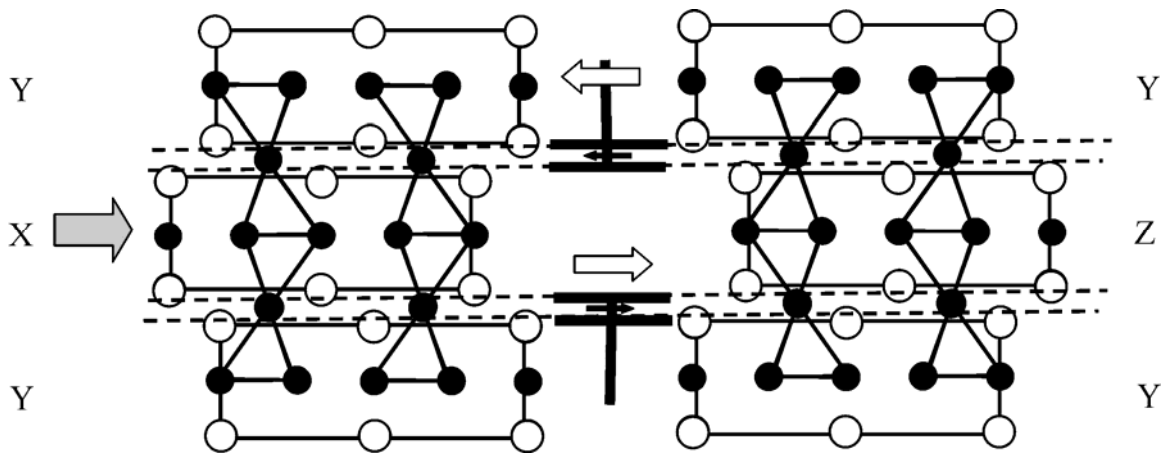


Fig. 4.4: Change of stacking sequence in a Laves-phase crystal (as indicated by the layer-sandwich units) by passage of a synchro-Shockley partial dislocation *dipole*, in order to preserve the external shape of the crystal: note the absence of *macroscopic* shear for the crystal concerned, in contrast with the situation realized by passage of a single synchro-Shockley partial dislocation as sketched in Fig. 4.3. For white and black arrows, see Fig. 4.3. The grey arrow indicates the effective shift of the middle layer-sandwich upon passage of the dipole.

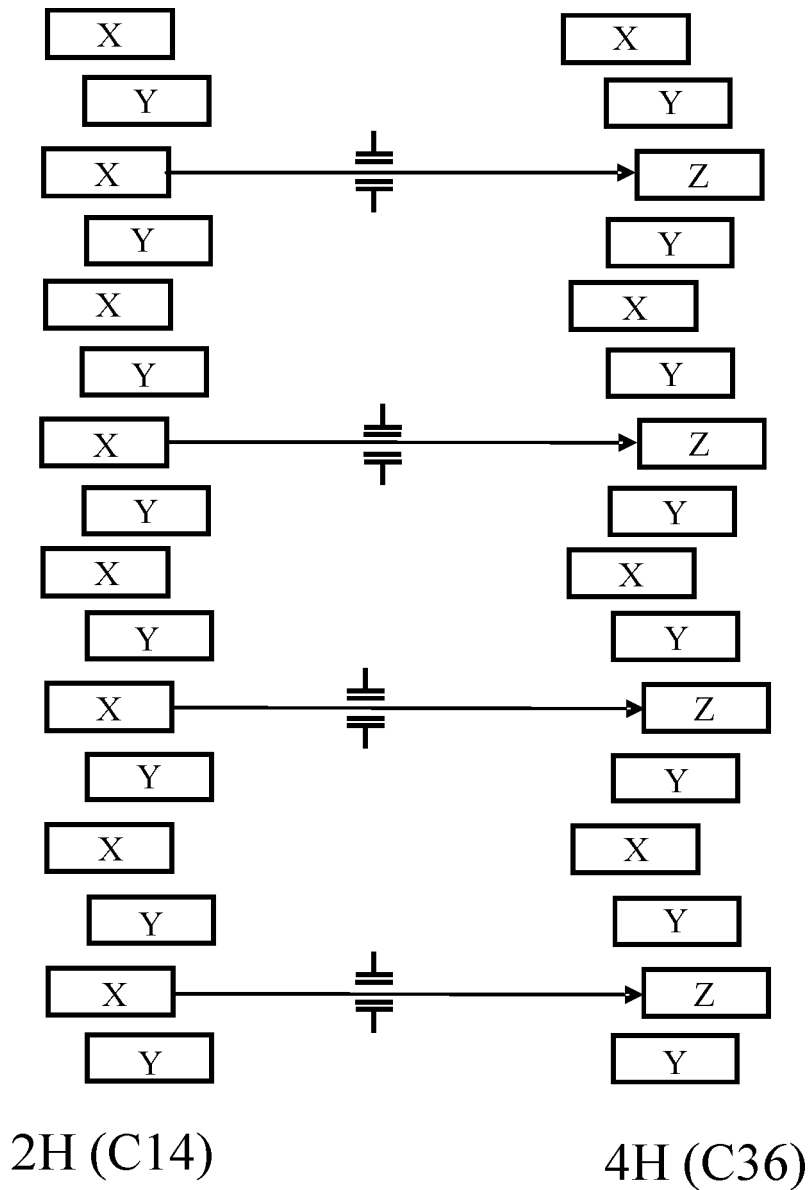


Fig. 4.5: Formation of the 4H stacking sequence of C36 from the 2H stacking sequence of C14 by passage by glide of an ordered sequence of synchro-Shockley partial dislocation dipoles (the symbols $\overline{\perp}$ and \perp denote single synchro-Shockley partial dislocations with Burgers vectors of opposite sign).

In the present publication layer faulting in three C36-type Laves phases ($NbCr_2$, $TiCr_2$, $NbCo_2$; see the phase diagrams provided by Fig. 4.6) have been studied by transmission electron microscopy and X-ray powder diffraction. It was found that the investigated C36- $NbCr_2$ and C36- $TiCr_2$ Laves phases contain specific stacking

irregularities. These are compatible with the occurrence of specific irregularities in the periodic passage of the synchro-Shockley partial dislocation dipoles in the course of the 2H (C14) \rightarrow 4H (C36) transformation, experienced by the NbCr₂ and TiCr₂ specimens. In contrast with these observations, the C36-NbCo₂ Laves phase does not contain such layer-stacking faults: a 2H (C14) \rightarrow 4H (C36) transformation does not occur during formation of C36-NbCo₂ (cf. Fig. 4.6c).

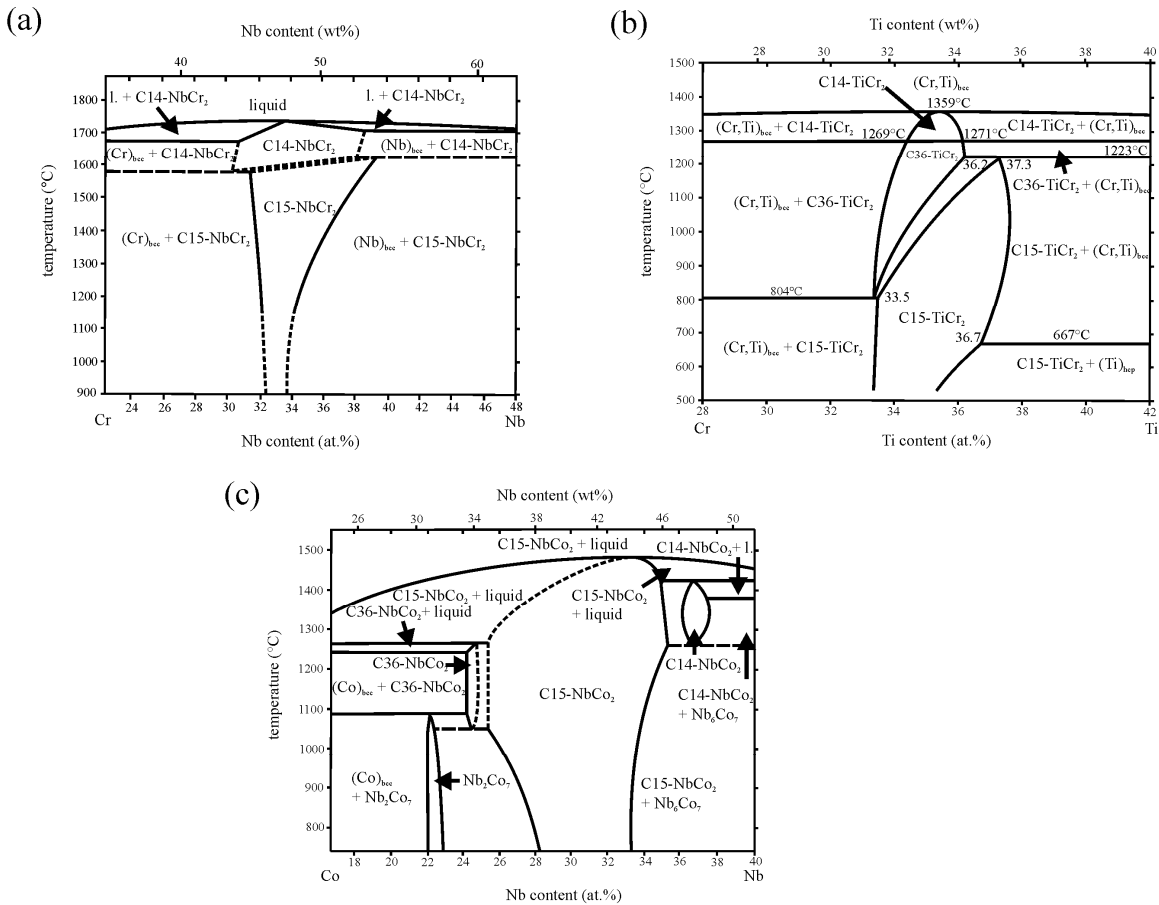


Fig. 4.6: Laves-phase containing composition ranges of the phase diagrams of the systems (a) Nb-Cr [16], (b) Ti-Cr [17, 18] and (c) Nb-Co [19]. Note that in case of NbCr₂ the C14-NbCr₂ Laves phase (and also the C36-NbCr₂ Laves phase) is no equilibrium phase, as shown recently in Ref.[20] (cf. chapter 2).

4.1.3 Diffraction from layered hexagonal structures containing stacking irregularities

The effect of a stacking irregularity like a single stacking fault, and also of a combination of stacking faults, in a layered structure on its diffraction pattern can be understood recognizing that a single stacking irregularity separating two halves of a crystal (Fig. 4.7) displaces one half of the crystal with respect to the other half by a *displacement vector* $\Delta\mathbf{r} = u'\mathbf{a} + v'\mathbf{b} + w'\mathbf{c}$ with real-valued u' , v' , and w' , and \mathbf{a} , \mathbf{b} , \mathbf{c} as the basis vectors of the translation lattice. Non-integer u' , v' and w' imply that for certain (some, all or most) diffraction vectors $\mathbf{g} = h\mathbf{a}^* + k\mathbf{b}^* + l\mathbf{c}^*$, with h , k and l as integer-valued Miller (actually Laue) indices and \mathbf{a}^* , \mathbf{b}^* and \mathbf{c}^* as the reciprocal basis vectors of the crystal, a phase shift occurs between the diffraction waves emanating from the two halves of the crystal, which phase shift can be shown to amount to $2\pi\mathbf{g}\cdot\Delta\mathbf{r} = 2\pi(u'h + v'k + w'l)$. No phase shift will occur for certain hkl if $\mathbf{g}\cdot\Delta\mathbf{r} = u'h + v'k + w'l$ assumes an integer value, and thus the reflections pertaining to these hkl do not broaden and do not shift (in reciprocal space). If $\mathbf{g}\cdot\Delta\mathbf{r}$ assumes an arbitrary, non-integer value, the otherwise delta-function shaped diffraction peak (in absence of other line-broadening contributions) gets broadened and possibly shifted in reciprocal space into a direction perpendicular to the fault plane. For predicting how such broadening in reciprocal space will show up in an (X-ray) powder-diffraction pattern, it has to be considered that the line broadening in reciprocal space then gets projected onto the diffraction vector. For example, considering one crystal, if the stacking direction is parallel to \mathbf{c}^* and thus the fault plane is perpendicular to \mathbf{c}^* , the line broadening in reciprocal space leads to a large line broadening in the X-ray diffractogram if $\mathbf{g} \parallel \mathbf{c}^*$. If $\mathbf{g} \perp \mathbf{c}^*$, no line broadening in the X-ray diffractogram results.

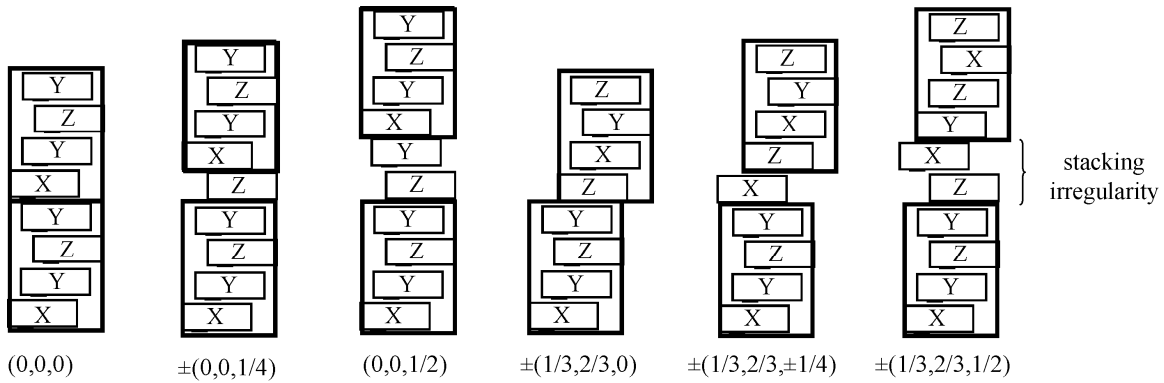


Fig. 4.7: Graphical illustration of the five different stacking-fault displacement vectors between two halves of a C36 crystal separated by a stacking irregularity. The actual, here arbitrarily chosen atomistic structure of the irregularity itself has no or negligible influence on the line broadening in reciprocal space. Because of the periodicity of the crystal structure, the two displacement vectors $+(0, 0, 1/2)$ and $-(0, 0, 1/2)$ are identical, whereas displacements as $+(0, 0, 1/4)$ and $-(0, 0, 1/4)$ are not identical but equivalent with respect to the resulting line broadening.

The actual line broadening in case of an ensemble of crystals (a polycrystal or powder) containing many stacking faults will depend on the probability (distribution) of the (different types of) faults. Corresponding calculations have been performed for many types of layered structures, and computer programs are available to predict for general layered structures the layer-fault induced line broadening [21]. The line broadening (and the line shift) depends on the relative phases of the diffracted waves emanating from the two crystal parts separated by a stacking irregularity. Thus, for the Laves-phase crystal structures considered here, it suffices to refer to previously worked out predictions on line broadening in similar (simple close packed) layered crystal structures in which same types of displacement vectors occur upon varying the layer-stacking sequence. For 4H-type structures, as the C36-type Laves phase with its XYXZ stacking sequence, such results have been presented in Refs. [22, 23]. The different types of stacking faults considered in these works can be ascribed to only five types of displacement vector $\Delta \mathbf{r}$ (indicated in the following by its coefficients (u', v', w')): $\pm(0, 0, 1/4)$, $(0, 0, 1/2)$, $\pm(1/3, 2/3, 0)$, $\pm(1/3, 2/3, \pm 1/4)$, $\pm(1/3, 2/3, 1/2)$; see Fig. 4.7. Because of the translational symmetry of the crystals, all components u', v', w' of $\Delta \mathbf{r}$ are equivalent to $u' \bmod 1$, v'

mod 1 and $w' \bmod 1$, respectively. The occurrence of one of these displacement vectors leads to a specific characteristic hkl dependence of the line broadening (and the line shift) in reciprocal space. The hkl dependence of the line broadening can be systematised by considering six classes of hkl reflections, depending on the values of $h - k$ and of l . Of these classes, one (with $h - k = 3N$ and $l = 4M$, with integer N, M) shows no line broadening for any of the five $\Delta\mathbf{r}$. Two further classes (with $h - k = 3N$ and $l = 4M \pm 1$, and with $h - k = 3N$ and $l = 4M + 2$) are irrelevant because their reflections have an integrated intensity of exactly or close to 0 (these classes were not considered explicitly in Refs. [22, 23]). Three further classes show line broadening characteristic for the corresponding type of $\Delta\mathbf{r}$, see Table 4.2. Note that the appearance of a “0” in a cell in Table 4.2 means that the reflections of that reflection class remain unbroadened for the type of displacement vector considered, which implies that $\mathbf{g} \cdot \Delta\mathbf{r} = u'h + v'k + w'l$ is an integer.

Table 4.2: Extent of line broadening for a 4H-type crystal (as C36) along \mathbf{c}^* in reciprocal space as function of the displacement vector for four of the six reflection classes^a. The width in reciprocal space units (here not specified) is proportional to the indicated numbers, as well as to the specimen-dependent probability for the occurrence of the corresponding displacement vectors. N and M are integers.

reflection-class; conditions for hkl	displacement vector, $\Delta\mathbf{r} = (u', v', w')$				
	$\pm(0,0, 1/4)$	$(0, 0, 1/2)$	$\pm(1/3, 2/3, 0)$	$\pm(1/3, 2/3, \pm 1/4)$	$\pm(1/3, 2/3, \pm 1/2)$
$h - k = 3N$ $l = 4M$	0	0	0	0	0
$h - k \neq 3N$ $l = 4M$	0	0	3	3	3
$h - k \neq 3N$ $l = 4M \pm 1$	2	4	3	2	1
$h - k \neq 3N$ $l = 4M + 2$	4	0	3	1	3

a) The two additional reflection classes indicated by $h - k = 3N$ and $l = 4M \pm 1$, and $h - k = 3N$ and $l = 4M + 2$ are irrelevant due to the zero or negligible integrated intensity of the corresponding hkl reflections.

4.2 Experimental

4.2.1 Preparation of alloys

The NbCr₂ (target composition 34.5 at.% Nb) and the TiCr₂ (target composition 35.8 at.% Ti) alloys were prepared by arc melting high-purity metals (niobium 99.99 wt%, titanium 99.999 wt%; chromium 99.999 wt%) under a titanium-gettered argon atmosphere. To ensure chemical homogeneity, the samples were flipped, remelted and subsequently

cooled down on a water-cooled copper hearth for several times. Although samples of various compositions were prepared, the observations presented here were found to be composition-independent and can be discussed by considering, exemplarily, specimens of the two compositions indicated above.

The NbCr₂ ingot was used as obtained after arc-melting because C36 material can only be obtained in as-cast conditions [20, 24] (cf. chapters 2 and 3). The TiCr₂ ingot was subjected to further heat treatments. First, the sample was annealed for 50 h at 1395 °C (in the bcc-solid solution region; cf. Fig. 4.6b) to ensure chemical homogeneity, i.e. to eliminate the chemical inhomogeneity inherent to the dendritic as-cast structure. Thereafter, the specimen was annealed for 50 h at 1200 °C (in the C36 Laves-phase region; cf. Fig. 4.6b). These heat treatments were carried out in an induction furnace under a high-purity argon atmosphere. To this end, the sample was placed into an Y₂O₃ crucible which was covered with three Ti-getter sheets. Before starting the annealing the furnace was evacuated and back-filled with argon for several times. After the annealing, the specimens were rapidly cooled down by switching off the furnace.

For preparation of the C36-type Nb-Co Laves phase (25.0 at.% Nb) powder, considered here on the sole basis of its X-ray powder diffraction pattern, see Ref. [25].

Both the as-cast NbCr₂ alloy and the as-cast and heat treated TiCr₂ alloy were characterised by optical microscopy, scanning electron microscopy (SEM), and energy/wavelength dispersive X-ray analysis (EDX/EPMA-WDX electron microprobe analysis), X-ray powder diffractometry (XRPD) and high resolution transmission-electron microscopy (HRTEM).

For the TEM and XRPD measurements powders of the NbCr₂ (material taken from the top of the ingots containing predominantly C36 phase [24], cf. chapter 3) and TiCr₂ alloys were produced within a mortar. In case of TiCr₂, for the XRPD both a fine and a coarse powder batch were produced. For the SEM and EDX/EPMA-WDX analyses metallographic cross sections were prepared which were manually ground and polished. A Cameca SX100 microprobe was employed for the EPMA-WDX measurements, applying an acceleration voltage of 15 kV and a current of 40 nA. Elemental standards (Nb, Ti, Cr) were employed for quantification according to the $\Phi(\rho z)$ approach [26]. The electron backscattering diffraction (EBSD) measurements were conducted using a Zeiss

LEO 438 VP scanning electron microscope equipped with an EBSD system (TSL, EDAX, Inc.) and the software OIM 4.5.

Chemical analysis by carrier-gas hot extraction (ELTRA ONH 2000), combustion technology (ELTRA CS-800) and Inductively Coupled Plasma Optical Emission (Spectro – CIROS CCD) showed that no uptake of metallic or non-metallic impurities had occurred during sample production and treatment.

4.2.2 High resolution transmission electron microscopy (HRTEM)

Due to the brittle nature of the investigated coarsely ground NbCr₂ and TiCr₂ powders, the edges of the powder particles were thin enough for electron transmission. The powder was suspended in n-butanol. Afterwards, a holey-carbon covered copper net was covered with that suspension leaving behind, after evaporation of the liquid, wedge-shaped crystallites in random orientation transparent for electrons. HRTEM was performed using a Philips CM 30 with an accelerating voltage of 300 kV.

4.2.3 X-ray powder diffraction (XRPD)

XRPD was performed using a “Philips X’Pert MPD” diffractometer equipped with a germanium-monochromator in the incident beam, selecting Cu-K α_1 radiation.

In case of the TiCr₂ powder specimen, for correction of instrumental broadening, the instrumental line-profile contributions were determined using a LaB₆ powder sample (NIST standard reference material, SRM660a) using TOPAS [27]. These instrumental contributions were then convoluted with pseudo-Voigt functions which were fitted to the reflections of the experimental TiCr₂ diffraction patterns by least squares minimization. The fitting parameters were the reflection-maximum position, $2\theta_{\max}$ and the full width at half maximum (FWHM) of the only structurally broadened line profiles; the line-shape parameter η was fixed to a value of 1.2 for all reflections⁴. Similar fits using pseudo-Voigt functions were conducted for NbCr₂, however, without separate consideration of

⁴ Fixing the peak-shape parameter η to a certain, reasonable value, removes the possible correlation of the FWHM and η in a fitting procedure and thereby the hkl dependency of the FWHM is more clearly exhibited. This procedure was necessary for the TiCr₂ powder specimen and for also the Nb-Co alloy powder specimen.

the instrumental contribution (because of the considerably larger structural line broadening in case of NbCr₂) and with η as an additional fit parameter.

Diffraction patterns of the Nb-Co alloy powder specimen were recorded using a Huber G670 Guinier camera equipped with an incident-beam germanium monochromator, selecting Co-K α_1 radiation. The powder was put as a thin layer on a Kapton foil. Like for NbCr₂, because of the relative large structural line broadening, without making separate consideration of the instrumental contribution, the reflection positions and widths were determined by fitting Lorentzian functions (corresponding to pseudo-Voigt functions with fixed $\eta = 1$; see also footnote 4) to each reflection.

4.3 Results

4.3.1 Nb-Cr

4.3.1.1 Phase analysis and composition

For the as-cast NbCr₂ specimens, a majority of crystallites of the hexagonal C36 modification occur at the top of the arc-melted ingot, together with a minor amount of (retained; cf. Fig. 4.6a) hexagonal C14-type crystallites (see Fig. 4.10a) and cubic C15 type crystallites [24] (cf. chapter 3). The bottom part of the ingot mainly consists of the C15 modification. Recent research performed in the present project has demonstrated that the C14 and C36 modifications are metastable at all temperatures and form only upon solidification from the melt at the top of the initially arc-melted ingots, with the C36 phase forming by solid state transformation from the initially crystallized C14 (see Refs. [20, 24], chapter 2 and 3). The powder used for the present study was taken from the top of the arc-melted ingot (cf. section 4.2.1). Because, in order to maintain the C36 modification, the sample could not be homogenized rigorously (this would have led to transformation of the C14/C36 crystallites to C15; cf. Fig. 4.6a) compositional inhomogeneities as a result of the solidification process are possible. The average niobium content of the sample was determined by WDX-EPMA to be equal to 34.9 ± 0.2 at.%. A niobium content somewhat higher than the target composition (34.5 at.%) can be ascribed to chromium evaporation during arc-melting.

4.3.1.2 XRPD

Although the powder taken from the top part of the as-cast specimen contains C14- and C15-type crystallites additional to the C36 majority phase crystallites (cf. section 4.3.1.1), separate reflections of these minority phases are not visible in the X-ray diffraction pattern (Fig. 4.8a) because they are superimposed on the C36 reflections occurring at the same values of the diffraction vector Q . In view of the tiny amounts of C14 and C15 phase, for the current purpose the diffraction patterns can yet be conceived as characteristic for the C36 phase.

The recorded diffraction pattern exhibits a distinct hkl -dependent broadening of reflections: The broadening occurs for (and is restricted to; see later) reflections with $h-k \neq 3N$ and $l = 4M \pm 1$ (see Figs. 4.8a and 4.9a), as it is expected for layer-faulting induced line broadening for the C36 modification (cf. Table 4.2). The extent of the line broadening for these reflections increases with l (Fig. 4.9a), leading to almost complete undetectability of reflections of high l values (see e.g. the 105 and 107 reflections in Fig. 4.8a). All other reflections exhibit no appreciable broadening. Hence, $(0,0,1/2)$ is the predominant displacement vector (cf. Table 4.2). This conclusion is supported by the observation that in particular the 106 reflection (belonging to the $h-k \neq 3N$ and $l = 4M \pm 2$ reflection class) is narrow, whereas it would have broadened by the occurrence of all types of displacement vectors, in particular as promoted by its high l value, except for the occurrence of $(0,0,1/2)$ as displacement vector (Table 4.2).

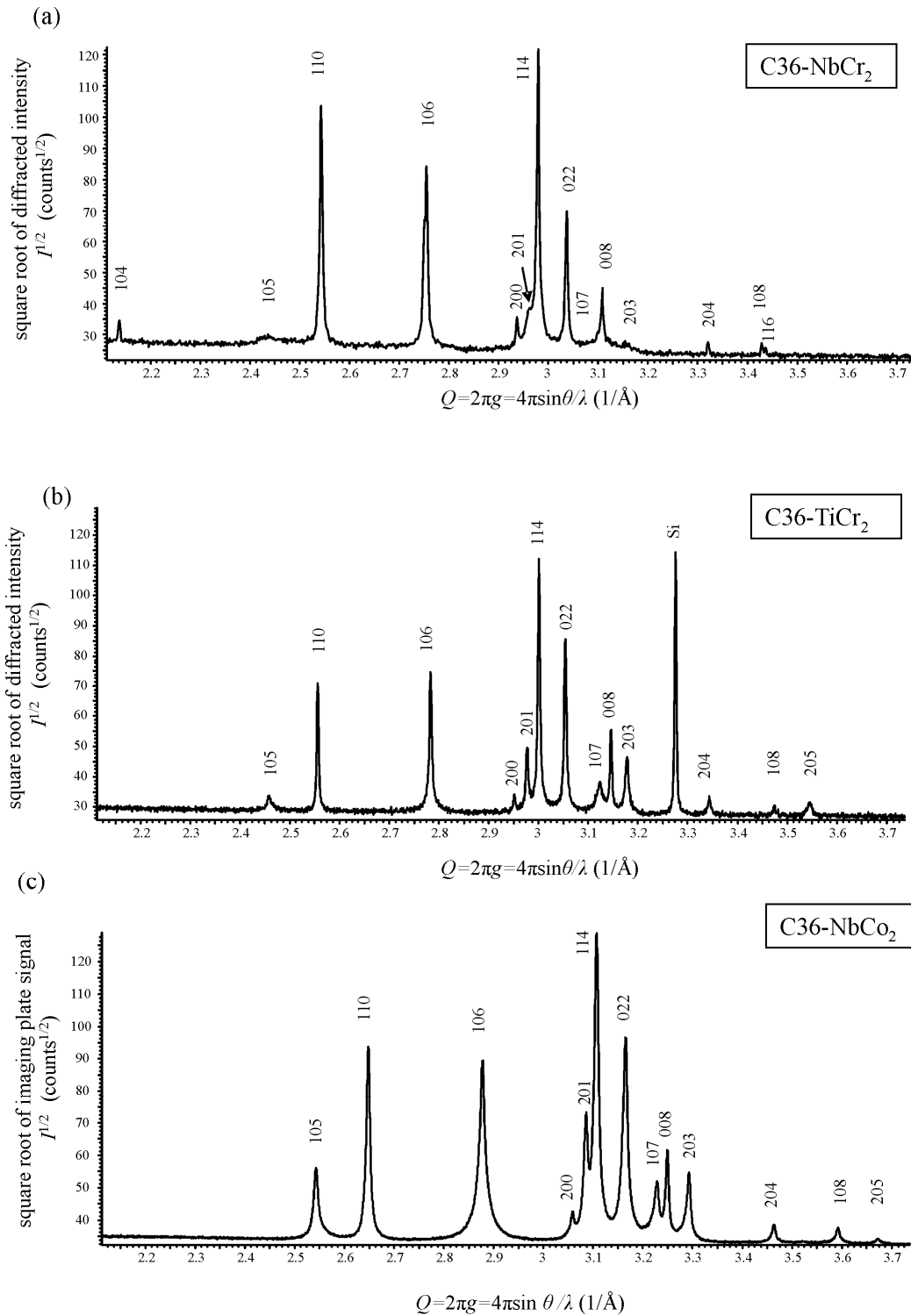


Fig. 4.8: X-ray powder diffraction patterns: (a) C36-NbCr₂, powder as obtained from top of the arc-melted, solidified ingot (Cu-K α_1 radiation); (b) C36-TiCr₂ produced by solid-state annealing for 50 h at 1200°C (coarse powder; Cu-K α_1 radiation); (c) C36-NbCo₂ (Co-K α_1 radiation). The Laue indices have been indicated.

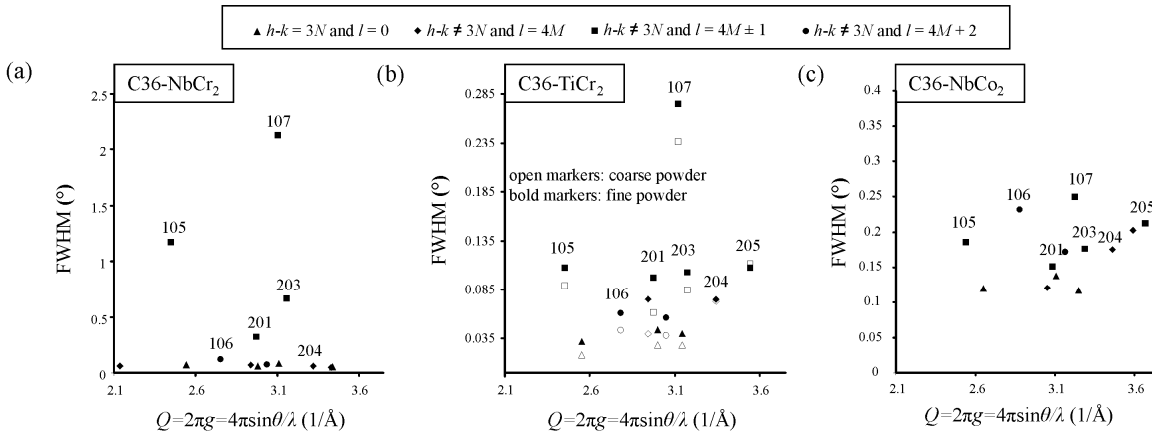


Fig. 4.9: FWHM values of the reflections in the XRPD patterns of (a) C36-NbCr₂ as obtained from top of the arc-melted, solidified ingot (Cu-K α_1 radiation), (b) C36-TiCr₂ produced by solid-state annealing for 50 h at 1200°C (coarse powder and fine powder, Cu-K α_1 radiation) and (c) C36-NbCo₂ (Co-K α_1 radiation).

4.3.1.3 HRTEM

A total of 15 crystallites from the NbCr₂ powder obtained from the top part of the as-cast ingot was examined by HRTEM. The C36 structure was found in 13 crystallites; in two cases together with some regions exhibiting the C14 modification and in two other cases together with some regions exhibiting the C15 modification. Only one crystallite was fully of the C14 modification, and one other crystallite was fully of the C15 modification. In many crystallites, a high density of layer-stacking irregularities was found, in association with streaks along the (hexagonal) $\langle 0001 \rangle$ direction in the selected area diffraction (SAD) patterns (Fig. 4.10).

Single faults (i.e. only one isolated “incorrect” *transition* between two layers (actually, two layer-sandwich units) with respect to the C36 layer-stacking sequence; cf. Fig. 4.3)) were generally not found in the hexagonal C36 crystallites: instead, combinations of successive faults were observed which led to the emergence of intergrowth-type irregularities within the dominant C36 modification (Figs. 4.10 a-c). Similarly, intergrowth-type irregularities were observed within the minor retained C14 modification as well (Fig. 4.10d).

With reference to Table 4.1, in case of the C36 modification (stacking sequence ...chch...), one or multiple *2H*-type (C14-type) sequences (with stacking sequence -hh-) are observed (Fig. 4.10a) and one or multiple *6H*-type sequences (with stacking sequence -cchcch-; Figs. 4.10b,c).

In case of the C14 modification (stacking sequence ...hh...), frequently one or multiple *4H*-type (C36-type) sequences (with stacking sequence -chch-) are found (Fig. 4.10d). For distinction between the periodic Laves-phase crystal structure matrices and the local stacking irregularities, the Ramsdell notation is used for the stacking irregularities and the Strukturbericht designation for the matrices. Further, the periodic stacking sequences of the crystal structures will be enframed by the symbol "...", whereas the local stacking irregularities will be enframed by the symbol "-" to distinguish between the periodic stacking sequences of the matrices and the local layer configuration at the layer-stacking irregularities.

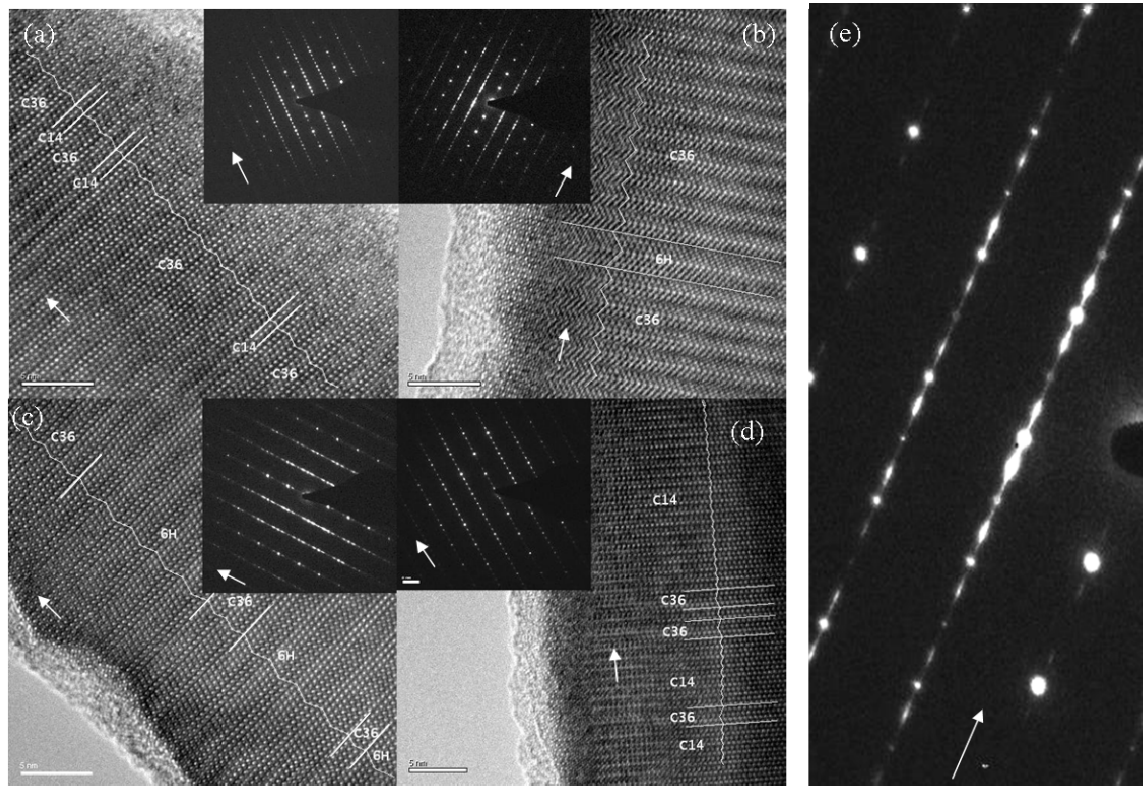


Fig. 4.10: HRTEM images (C36 zone axis: $\langle 11\bar{2}0 \rangle$) of material taken from the top of an as-cast NbCr₂ specimen: (a-c) C36 crystallites with (a) *2H-type* stacking irregularities; single (b) or an accumulation of (c) *6H-type* stacking irregularities and (d) a retained C14 crystallite exhibiting *4H-type* stacking irregularities; (e) enlargement of a part of the SAD pattern shown as insert in (b), revealing the streaking along the (hexagonal) $\langle 0001 \rangle$ direction. The arrows indicate the $\langle 0001 \rangle$ direction.

4.3.2 TiCr₂

4.3.2.1 Phase analysis and composition

The as-cast and heat treated (cf. section 4.2.1) specimen consisted fully of C36-Laves phase (as determined by X-ray diffraction). According to wavelength dispersive X-ray analysis (WDX-EPMA) the composition of the Laves phase obeys (35.6 ± 0.3) at.% Ti and (64.4 ± 0.3) at.% Cr in agreement with the target composition (section 4.2.1).

By optical microscopy and SEM the presence of a minority phase was detected (volume fraction approx. 1 % as determined by area analysis). The phase was identified by EBSD as a bcc phase. Standardless EDX analysis revealed that the minority phase is a Ti-rich phase. In view of the Ti-Cr phase diagram this suggests that this phase is the β -Ti solid solution.

4.3.2.2 XRPD

The diffraction pattern of the coarse powder (cf. section 4.2.1) of the C36 phase is shown in Fig. 4.8b. The FWHM of the reflections (shown in Fig. 4.8b), after correction for instrumental broadening (see section 4.2.3), has been plotted as function of the diffraction vector Q in Fig. 4.9b.

The 110 reflection belongs to the class of reflections with $h - k = 3N$ and $l = 4M$. These reflections show no peak broadening due to layer-stacking irregularities (see Table 4.2), so that only broadening due to finite crystallite size and due to microstrains, caused by defects or composition variations, is possibly exhibited by these reflections. Assuming that the whole broadening of the 110 reflection is due to microstrain-like broadening caused by composition variations, an upper boundary for the width of the composition distribution equal to $B_\xi = 0.56$ at.% was calculated from the FWHM of the 110 reflection according to the method given in Ref. [28]. This B_ξ is the FWHM of a super-Lorentzian ($\eta = 1.2$, see section 4.2.3) probability density function of the composition on the at.%-scale. Thus the maximum compositional variation was determined to be ± 0.28 at.%. This value is within the standard deviation of the WDX-EPMA analysis (cf section 4.3.2.1): such compositional variation cannot be exposed by WDX-EPMA analysis.

The peak broadening is affected by the grinding procedure: the peaks of the fine powder (more severely ground) are somewhat broader than the peaks of the coarse powder (less severely ground; see Fig. 4.9b). This includes the reflection class with $h - k = 3N$ and $l = 4M$, as well. Since the $h - k \neq 3N$ reflections (which should show peak broadening due to (also) the layer-stacking irregularities, in addition to microstrains, as discussed above (cf. Table 4.2)) of the fine powder, as compared to the coarse powder, reveal extra broadening to about the same extent as reflections of the reflection class with

$h - k = 3N$ and $l = 4M$, it can be concluded that the grinding procedure does not influence the layer-stacking irregularity density.

The powder-diffraction pattern of the C36 phase exhibits a distinctly hkl -dependent broadening of reflections, which is of the same type as observed for C36-NbCr₂ (see section 4.3.1.2): The reflections with $h - k \neq 3N$ and $l = 4M \pm 1$ show a considerable peak broadening. This means that in the case of TiCr₂ also $(0,0,1/2)$ is the predominant displacement vector. However, in contrast to C36-NbCr₂, the $h - k \neq 3N$ and $l = 4M$ reflections (e.g. 204) and $h - k \neq 3N$ and $l = 4M + 2$ reflections (e.g. 106) show a slightly larger peak broadening than the $h - k = 3N$ and $l = 4M$ reflections. This indicates that in case of TiCr₂ also layer-stacking irregularities with displacement vectors different from $(0,0,1/2)$ occur.

4.3.2.3 HRTEM

A total of eight crystallites were investigated by HRTEM. All crystallites are dominantly composed of the C36 modification. In one crystallite within the C36 phase a $2H$ -type (C14-type) stacking irregularity was found and in another a $6H$ -type stacking irregularity was found. Furthermore in one crystallite both an accumulation of three consecutive $2H$ -type (-hh-) and a $6H$ -type (-cchcch-) stacking irregularity was found (see Fig. 4.11a). In addition one crystallite contained a “split” $6H$ -type stacking sequence (i.e. two -cch-stacking sequences separated by a larger C36 block; see Fig. 4.11b). In general, in the investigated C36-TiCr₂ specimens much fewer stacking irregularities occur than in the investigated C36-NbCr₂ specimens.

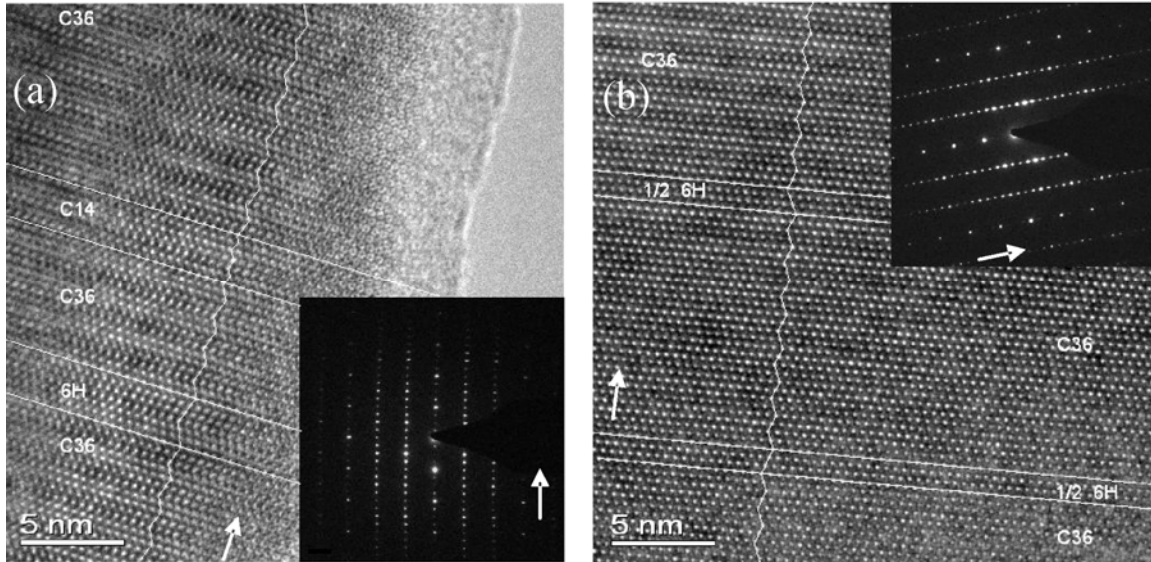


Fig. 4.11: HRTEM images (C36 zone axis: $\langle 11\bar{2}0 \rangle$) of annealed C36-TiCr₂ specimens containing stacking irregularities. (a) A *2H*-type (C14-type) and a *6H*-type stacking irregularity, (b) a “split” *6H*-type stacking irregularity. The arrows indicate the $\langle 0001 \rangle$ direction.

4.3.3 NbCo₂

The line broadening visible in the XRPD data of C36-NbCo₂ differs distinctly from that observed for the NbCr₂ and TiCr₂ analogues (Figs. 4.8a,b vs. Fig. 4.8c). The reflections pertaining to all reflection classes with $h - k \neq 3N$ experience considerable line broadening (Fig. 4.9c), in particular the prominent 106 reflection (belonging to the $h - k \neq 3N$ and $l = 4M + 2$ class of reflections) which is only marginally broadened in the case of the C36-TiCr₂ specimens (Fig. 4.9b) and not broadened at all for the C36-NbCr₂ specimens (Fig. 4.9a). Moreover, distinctly asymmetric diffraction-line broadening occurs for the $h - k \neq 3N$ and $l = 4M + 1$ class of reflections, which has been reported in Ref. [23] as representative for stacking-layer faulting not characterized by the $(0,0,1/2)$ displacement vector.

4.4 Discussion

4.4.1 Stacking irregularities and associated displacement vectors

Two predominant types of stacking irregularities are found in the equilibrated C36-TiCr₂ specimen and in the as-cast C36-NbCr₂ specimen by HRTEM: *single* and/or *multiple 2H-type* and *6H-type* (intergrowth-type) stacking irregularities. Insertion of a *2H-type* irregularity in a perfect C36 (4H) crystal leads to a displacement vector of (0,0,1/2) (cf. section 4.1.2); insertion of a *6H type* irregularity requires a displacement vector of (0,0,3/2), which is equivalent to the displacement vector (0,0,1/2) due to the translational symmetry of the C36 (4H) crystal structure, comprising four layer-sandwich units (cf. Table 4.1). Further, because of this translational symmetry, accumulations of multiple *2H-type* or *6H-type* stacking irregularities, as frequently observed in the HRTEM images (e.g. Figs. 4.10c, 4.11a), can only add up to a displacement vector equivalent to (0,0,0), which causes no peak broadening, or (0,0, 1/2) which leads to broadening of reflections of the class with $h - k \neq 3N$ and $l = 4M \pm 1$. Then also reflections of the class with $h - k \neq 3N$ and $l = 4M + 2$ remain narrow, which would be not the case for (all) other possible displacement vectors (cf. Table 4.2).

Exactly these above-indicated broadening characteristics are observed in the XRPD patterns of C36-NbCr₂ and in those of C36-TiCr₂ (where the broadening was less pronounced).

A special case is the “split” *6H-type* irregularity observed in TiCr₂ (cf. Fig. 4.11b). The displacement between the middle 4H (C36) part, which is bounded by the two -cch-stacking irregularities, which can be regarded as a split-up 6H (-cchcch-) stacking sequence, and the two adjacent parts of the 4H crystal is of type $\pm(1/3, 2/3, +1/4)$; the displacement vector between the two adjacent parts of the 4H crystal separated by the whole “split” *6H-type* irregularity is again of type (0,0,1/2).

HRTEM and XRPD line-profile analysis give complementary results: HRTEM reveals the detailed structure of individual stacking irregularities, whereas XRPD provides data pertaining to the average microstructure. It thus follows that the *2H-type* and *6H-type* stacking irregularities are the dominating layer-stacking defects in C36-type NbCr₂ and TiCr₂ Laves phases.

4.4.2 Relation with phase-transformation mechanism

4.4.2.1 General remarks

The similarity of the stacking irregularities occurring in C36-TiCr₂ and C36-NbCr₂ (i.e. the occurrence of the same type of displacement vector; cf. section 4.4.1) suggests that the origin of these stacking irregularities is the same for both Laves phases. A very remarkable feature of the stacking irregularities with a displacement vector of (0,0,1/2), is that no shear displacement of the part of the crystal above the irregularity occurs with respect to the part of the crystal below the irregularity: i.e. $u' = v' = 0$ (see Fig. 4.7). It can thus be concluded that these stacking irregularities are not induced by plastic deformation processes possibly occurring during sample preparation, e.g. by thermal stresses. Indeed, as demonstrated in section 4.3.1.3, the grinding procedure has no influence on the density of the stacking irregularities.

It is supposed that both C36 Laves phases, NbCr₂ and TiCr₂, have been formed from a C14-type structure, which evolves in case of NbCr₂ as a metastable state (cf. section 4.3.1.1) during solidification at certain locations in the ingot [20, 24] (cf. chapters 2 and 3) and in case of TiCr₂ as a stable state during the decrease of annealing temperature from 1395°C (bcc-solid solution) to 1200°C (cf. phase diagram, Fig. 4.6b); in this temperature range, the C14 phase field of TiCr₂ is passed. In section 4.1.2 it has been discussed how a C14 crystal can transform into C36 by passage of a periodic series of synchro-Shockley partial dislocation dipoles (“ordered glide”, Figs. 4.4, 4.5). The passage of one synchro-Shockley partial dislocation dipole within a C14 structure (as shown in Fig. 4.4), generates a layer-stacking irregularity of 4H-type (C36-type) – YZYX- (-chch-) into the ...XYXY... (...hh...) stacking sequence of C14. Due to the opposite sign of the Burgers vectors of the partial dislocations forming the dipole, the overall Burgers vector associated with this defect is zero, and thus no macroscopic displacement will be induced between the parts of the C14 crystal adjacent to such a defect (see Fig. 4.4). Such 4H-type layer stacking irregularities are experimentally observed in the retained NbCr₂-C14 crystallites (Fig. 4.10d). Only “ordered glide”, i.e. glide of a synchro-Shockley partial dislocation dipole on (i.e. above and below) every fourth layer-sandwich unit over a certain range of the C14 crystal, generates the C36 modification. This “ordered glide” requires coordination of the gliding partial-dislocation

dipoles in order to produce C36. If this order is kept perfectly over the whole crystal, a defect-free, perfect C36 crystal would result, and hence no layer-stacking irregularities (with respect to the C36 layer stacking) and no corresponding reflection broadening would occur.

Irregularities in the passage of the synchro-Shockley partial dislocation dipoles (i.e. deviations from “ordered glide”) can be the origin of the layer-stacking irregularities in the C36-Laves phases as observed by HRTEM and XRPD in this work. Two mechanisms, which can occur simultaneously, are proposed in the following to explain the observed deviations. The first mechanism (section 4.4.2.2) derives from the recognition that four different but energetically equivalent modes for formation of C36 are possible, depending on which of the four possible layers within two consecutive C14 unit cells (i.e. XYXY) is shifted to produce C36 (cf. Fig. 4.4). If more than one of these modes is operative within one parent C14 crystal, initiating from different locations within the crystal, different C36 *domains* form, and layer-stacking irregularities occur upon impingement of these domains (Fig. 4.12). Yet, this first mechanism involves perfect, “ordered glide” within each domain. The second mechanism (section 4.4.2.3) involves the occurrence of local deviation from “ordered glide”, i.e. within a domain, leading to breaking up of the domain into *regimes*.

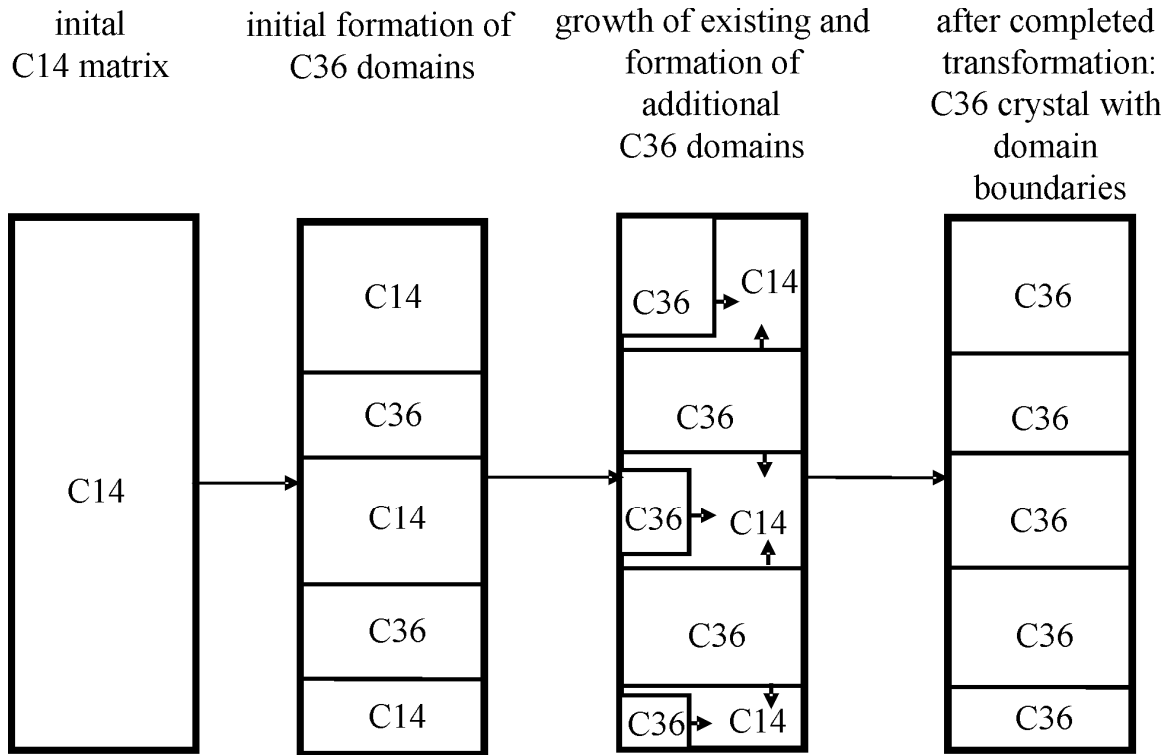


Fig. 4.12: Formation of a C36 crystal by formation, growth and impingement of C36 domains

4.4.2.2 Domain formation

The requirement that every fourth layer-sandwich unit has to be displaced for the formation of C36 from C14 necessitates to distinguish between every two adjacent layer-sandwich units in C14, which is done here by introducing Roman numerals as subscript (see Fig. 4.13); the stacking sequence of a C14 crystallite would thus be ...X_IY_IX_{II}Y_{II}.... A C36 stacking can then be formed by shifting either all X_I to Z or all X_{II} to Z or all Y_I to Z or all Y_{II} to Z (cf. Fig. 4.5). Taking the initial C14 structure as reference, four different C36 product domains can thus be formed (similar to the domains found e.g. in ordered substitutional intermetallics/phases). In the first two cases, the shift is realized by a dipole consisting of the synchro-Shockley partial-dislocation pair $\mathbf{b}_i/-\mathbf{b}_i$, while in the last two cases, the pair of synchro-Shockley partial dislocations is $-\mathbf{b}_i/\mathbf{b}_i$ (cf. Fig. 4.2) Note that the first Burgers vector of the pair indicates the shift of the layer-sandwich unit with respect to the, say, bottom part of the crystal concerned, while the second Burgers vector is necessary to shift (reversely) the, say, top part of the crystal back to its original position,

thereby avoiding macroscopic shear of the crystal (see Fig. 4.4). The four possible C36 structures formed by the four layer-shift options are not identical, but displaced with respect to each other by the displacement vectors indicated in Fig. 4.13 and provided by Table 4.3⁵. The C36 domains thus formed either grow in *c* (stacking) direction by “ordered glide” of more synchro-Shockley partial-dislocation dipoles shifting the same type of layer-sandwich unit, or new domains form between the existing ones, which is shown schematically in Fig. 4.12. Growth of existing domains and formation of new domains may also occur simultaneously. The crystal can be regarded as completely transformed from C14 to C36 after impingement of these domains.

⁵ The layer-stacking irregularity occurring between a pair of such domains can be conceived as an anti-phase boundary.

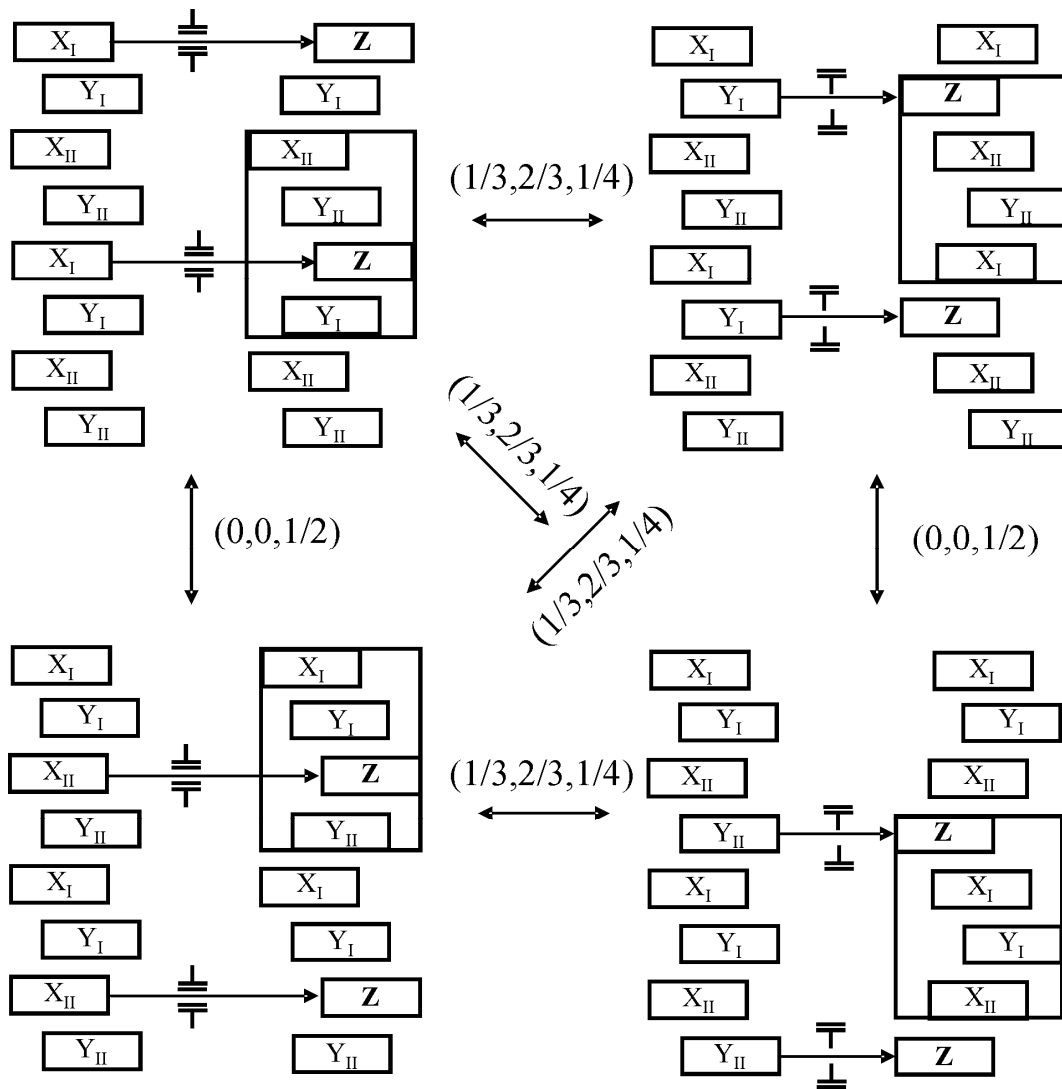


Fig. 4.13: The four different C36 domains which can evolve from the same C14 crystal by shifting layer-sandwich units and the single (B atom) layer in-between by the ordered passage (glide) of synchro-Shockley partial dislocation dipoles (see Figs. 4.4 and 4.5). The difference in Burgers vectors for the dipole pairs ($\mathbf{b}_i/\mathbf{b}_i$ if X is shifted to Z and $-\mathbf{b}_i/\mathbf{b}_i$ if Y is shifted to Z) has been indicated by using the symbols $\frac{\perp}{\tau}$, and $\frac{\tau}{\perp}$. The corresponding displacement vectors between the resulting C36 domains have been indicated too. Note that for random occurrence of all four types of displacements (i.e. all four types of domains), the vector $(1/3,2/3,1/4)$ occurs twice as frequently as the vector $(0,0,1/2)$. The latter displacement occurs exclusively, if within a transformed crystal, only X layers or only Y layers have been displaced, i.e. either only the two domains shown on the left or only the two domains shown on the right, occur.

A perfect (i.e. stacking-fault or layer-stacking irregularity free) C36 crystal can only result from a parent C14 crystal if *only one* of the above four layer-sandwich unit shift options is adopted throughout the crystal. In this case, for transitional stages as well as for the end stage of the transformation, the displacement vectors between the various C36 domains would always be (0,0,0), and thus no phase shift of diffracted waves and hence no reflection broadening of reflections originating from the C36 domains in the XRPD pattern can occur. In this case, after impingement of the growing domains, a perfect C36 stacking sequence over the whole initial C14 crystallite results.

If the four types of domains shown in Fig. 4.13 would occur randomly within a parent C14 crystal, the impingement (of the domains growing in the *c*-direction) between different domains, will lead to “anti-phase boundaries” (see footnote 5) because of the displacement between two impinging C36 structures: stacking irregularities occur associated with corresponding broadening of XRPD reflections according to the theoretical considerations in section 4.1.3. Two types of displacement vectors can be indicated: (1/3,2/3,1/4) and (0,0,1/2), with the first one occurring statistically twice as frequently as the latter one if all four types of domains occur randomly (see Fig. 4.13). This last phenomenon is not compatible with the present observations for the C36-NbCr₂ and C36-TiCr₂ specimens, revealing a predominant broadening of the reflections of the class with $h - k \neq 3N$ and $l = 4M \pm 1$, which implies that the (0,0,1/2) displacement vector is dominant, i.e. only X or only Y layer-sandwich units have been displaced within a parent C14 crystal (cf. Fig. 4.13). In the case of TiCr₂, also $h - k \neq 3N$ reflections not pertaining to $l = 4M \pm 1$ are slightly broadened suggesting a minor mixed occurrence (i.e. both X and Y) of layer-sandwich unit displacements within a parent C14 crystal. The “split” *6H-type* irregularity (Fig. 4.11b; see section 4.3.2.3) can thus be conceived as the outcome of impingement of three C36 domains: The upper and lower one are formed by e.g. shifts of X layers (e.g. X_I in the lower and X_{II} in the upper domain), whereas the middle domain is formed by e.g. shifting Y_{II} layers.

Table 4.3: Displacement vectors between C36 domains, produced in a parent C14 crystal by the synchro-Shockley partial dislocation dipole mechanism, by shifting for each domain one of the four different layer-sandwich units of the ...X_IY_IX_{II}Y_{II}... sequence in the parent C14 structure to Z position (see Fig. 4.13).

	X _I to Z	X _{II} to Z	Y _I to Z	Y _{II} to Z
X _I to Z	(0,0,0)	(0,0,1/2)	(1/3,2/3,1/4)	(1/3,2/3,1/4)
X _{II} to Z	(0,0,1/2)	(0,0,0)	(1/3,2/3,1/4)	(1/3,2/3,1/4)
Y _I to Z	(1/3,2/3,1/4)	(1/3,2/3,1/4)	(0,0,0)	(0,0,1/2)
Y _{II} to Z	(1/3,2/3,1/4)	(1/3,2/3,1/4)	(0,0,1/2)	(0,0,0)

4.4.2.3 Transformation errors

The “ordered glide” of synchro-Shockley partial dislocation dipoles is induced and controlled by the associated decrease in Gibbs energy of the transforming Laves phase (cf. section 4.4.2.1). The “ordered glide” and thus the stacking sequence of the resulting C36 crystal will be practically perfect, if the energy “penalty” for deviations from this perfectly ordered glide is high compared to the decrease of Gibbs energy achieved by the transformation from C14 to C36. In case of Laves phases, the Gibbs energies of the different layer-sandwich unit stacking modifications differ only slightly (e.g. [29]) and hence the stacking fault energy is also low. Thus, deviations from perfect “ordered glide” are likely.

Irrespective of the precise origin of deviations from perfect “ordered glide”, the most likely deviations are those which correspond most closely to the state of perfect order. Such most likely deviations are those which, nevertheless, satisfy the following characteristics of the *perfect* phase transformation:

- Glide of only synchro-Shockley partial dislocation *dipoles* is required to realize the irregularity
- Within one transforming domain, either only X or only Y layers are shifted to Z.

The last point involves that glide is realized by either only dipoles with the Burgers vectors $\mathbf{b}_i/-\mathbf{b}_i$ or only dipoles with the Burgers vectors $-\mathbf{b}_i/\mathbf{b}_i$.

Under these constraints, disorder in the passage of synchro-Shockley partial dislocation dipoles during the transformation occurs by a change of either X_I to X_{II} or Y_I

to Y_{II} for the shifting layer-sandwich unit (Fig. 4.14). Such changes can occur if (i) one (say, either X_I or Y_I) layer, which should have shifted according to perfect “ordered glide”, remains immobile and “ordered glide”, supposed to proceed in the c -direction (i.e. stacking direction) is continued by shifting the other representatives of the layers of the same stacking position (i.e. either X_{II} or Y_{II} , Fig. 4.14a), or (ii) a change of shifting layer (from either X_I to X_{II} or Y_I to Y_{II}) occurs without such preceding immobilisation, i.e. the distance between two shifted layers is two instead of four layers (Fig. 4.14b). Both such local deviations from perfect “ordered glide” are accompanied by the introduction of $2H$ -type layer-stacking irregularities; the displacement vector between the different $4H$ (C36) regimes is $(0,0,1/2)$.

Another possibility to introduce stacking irregularities in the product C36 crystal is that some of the synchro-Shockley partial dislocation dipoles are not separated by only one (cf. Fig. 4.4) but by three layer-sandwich units (see Fig. 4.15a). Such deviations also bring about a change of shifted layer type from either X_I to X_{II} or Y_I to Y_{II} , or vice-versa. The local stacking irregularity formed by such an “expanded” dipole is of $6H$ type, the corresponding displacement vector between the adjacent $4H$ (C36) regimes is $(0,0,1/2)$.

Formation of $6H$ -type layer-stacking irregularities (Fig. 4.15) may be a way to lower the energy increase associated with the introduction of the $2H$ -type layer-stacking irregularities described above (Fig. 4.14). This could occur upon further cooling (i.e. after completion of the $C14 \rightarrow C36$ transformation, assuming that (for some temperatures range) below the $C14 \rightarrow C36$ transformation temperature, a $6H$ stacking sequence has a lower Gibbs energy than a $2H$ stacking sequence. This process is shown in Fig. 4.15b. It requires (with respect to Burgers vector pair) passage of the type of synchro-Shockley partial dislocation dipole with Burgers vectors of opposite signs as compared to those operating upon formation of the C36 structure from the parent C14 structure.

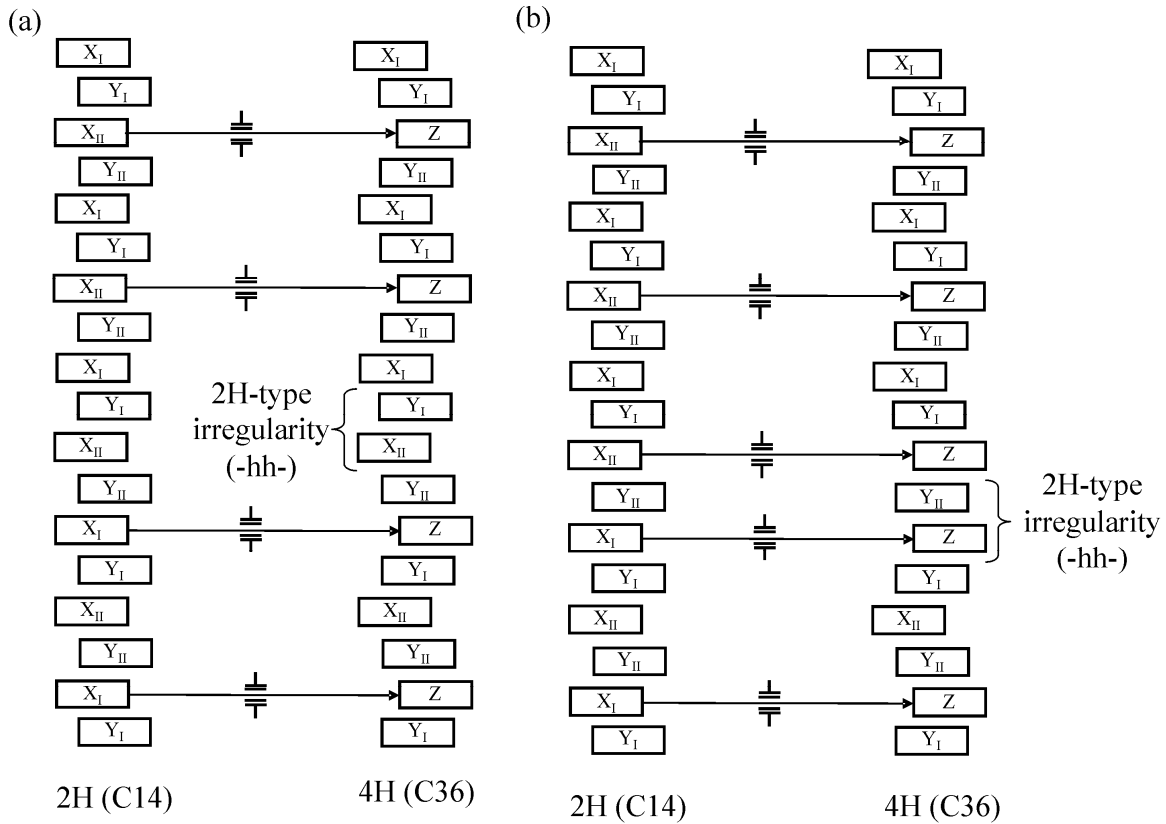


Fig. 4.14: Possible deviations from perfect “ordered glide” of synchro-Shockley partial dislocation dipoles during a C14 \rightarrow C36 transformation, subject to the constraint that only one type of synchro-Shockley partial dislocation dipoles is involved in the phase transformations, i.e. either only X or only Y layers are shifted to Z positions (cf. Fig. 4.13). For both cases shown in the figure, the layer shift switches from X_I to X_{II} , contrarily to the occurrence of perfect “ordered glide” in the parent C14 crystal, where every second X layer is shifted to Z, either one X layer to be shifted becomes immobilized (a), or two adjacent X layers (i.e. an X_I layer *and* an X_{II} layer) are shifted to Z (b). In both cases, a 2H-type stacking irregularity occurs.

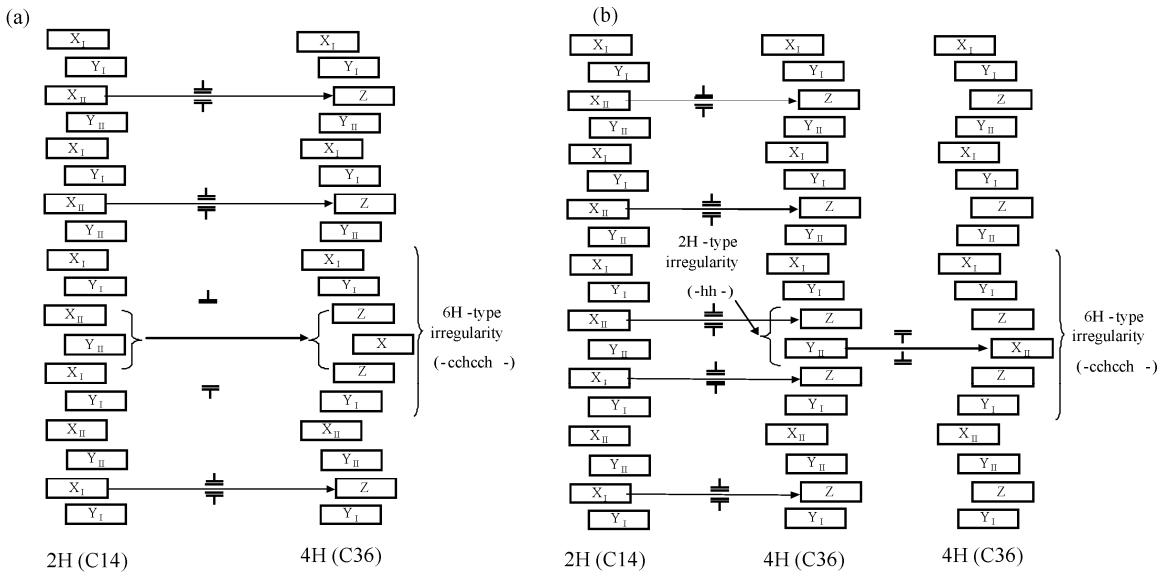


Fig. 4.15: Formation of 6H-type stacking irregularities (a) during or (b) subsequent to a C14 \rightarrow C36 phase transformation: (a) glide of a synchro-Shockley partial dislocation dipole with a three-layer spacing between the two partials (instead of the regular single-layer spacing; cf. Fig. 4.4) and (b) transition of a 2H-type layer-stacking irregularity, to a 6H-type layer-stacking irregularity within the defective C36 structure after the C14 \rightarrow C36 transformation (cf. Fig. 4.14b); formation of the 6H-type irregularity requires glide of a synchro-Shockley partial dislocation dipole with Burgers vectors of sign opposite from those of the synchro-Shockley partial dislocation dipoles which have formed the C36 structure to the C14 structure.

4.4.2.4 Overall discussion

In the two preceding sections, two mechanisms have been presented which induce stacking irregularities into a C36 product structure formed from a C14 parent structure by otherwise perfect “ordered glide” of synchro-Shockley partial dislocation dipoles. According to the first mechanism (section 4.4.2.1) four different types of domains can be formed, which are not “in phase” with respect to each other, causing layer-stacking irregularities upon impingement of the domains. Within each domain perfect “ordered glide” of synchro-Shockley partial dislocation dipoles takes place and thus no layer-stacking irregularities occur within the domains. Two different displacement vectors occur between the different domains in this model: $(1/3, 2/3, 1/4)$ and $(0, 0, 1/2)$. In case of

random occurrence of all four domain types the first displacement vector $(1/3, 2/3, 1/4)$ occurs statistically twice as often as the displacement vector $(0, 0, 1/2)$. The experimentally observed dominance of the $(0, 0, 1/2)$ displacement vector thus is ascribed to the presence of *2H*- and *6H*-type irregularities, induced by the second mechanism to generate stacking irregularities, i.e. by deviations from perfect “ordered glide” of synchro-Shockley partial dislocation dipoles during the transformation in a single domain (section 4.4.2.2), leading to regime formation within the domains. It is shown that the smallest possible and simplest deviations lead to the *2H*- and *6H*-type layer-stacking irregularities as observed by HRTEM, associated with a displacement vector between the adjacent C36 crystal regimes of $(0, 0, 1/2)$, as deduced from XRPD-line profile analysis.

The two mechanisms for generating stacking irregularities can operate jointly. Domain formation and impingement can occur *together* with flawed “ordered glide” during the transformation *within* the forming domains (transformation errors). The case that regime boundaries occur more frequently than domain boundaries has been schematically illustrated in Fig. 4.16. In this case, using HRTEM, the probability of finding a *2H*-type or *6H*-type layer-stacking irregularity would be much higher than finding a domain boundary. Also the line broadening in XRPD patterns originating from such C36 structures would be dominated by the displacement vector $(0, 0, 1/2)$, inducing pronounced broadening of reflections of the class with $h-k \neq 3N$ and $l = 4M \pm 1$. These predictions regarding the HRTEM and XRPD data agree fully with the corresponding observations made on C36-NbCr₂. Domain boundaries associated with a displacement vector of $(1/3, 2/3, 1/4)$ would also induce some minor broadening of reflections of the classes $h-k \neq 3N$ with $l = 4M$ and $h-k \neq 3N$ with $l = 4M + 2$, in addition to broadening of reflections of the class $h-k \neq 3N$ and $l = 4M \pm 1$. This is in agreement with the experimental observations made on C36-TiCr₂.

The C36-NbCo₂ structure does not form by a C14 \rightarrow C36 transformation. Although a C14-NbCo₂ Laves phase exists at high Nb content, it is separated from the C36-phase field in the Nb-Co phase diagram by a C15-NbCo₂ phase [16] (see Fig. 4.6c). Thus, the preferential formation of stacking irregularities with a $(0, 0, 1/2)$ displacement vector, based on formation of C36 from (fault-free) C14, cannot pertain to C36-NbCo₂. The discussion of possible origins for the stacking-layer irregularities in C36-NbCo₂

(associated with only a minor occurrence of the displacement vector $(0,0,1/2)$, but with major occurrence of other displacement vectors as listed in Table 4.2; see results reported in section 4.3.1) is beyond the scope of the present paper.

C36-crystal formed
from C14

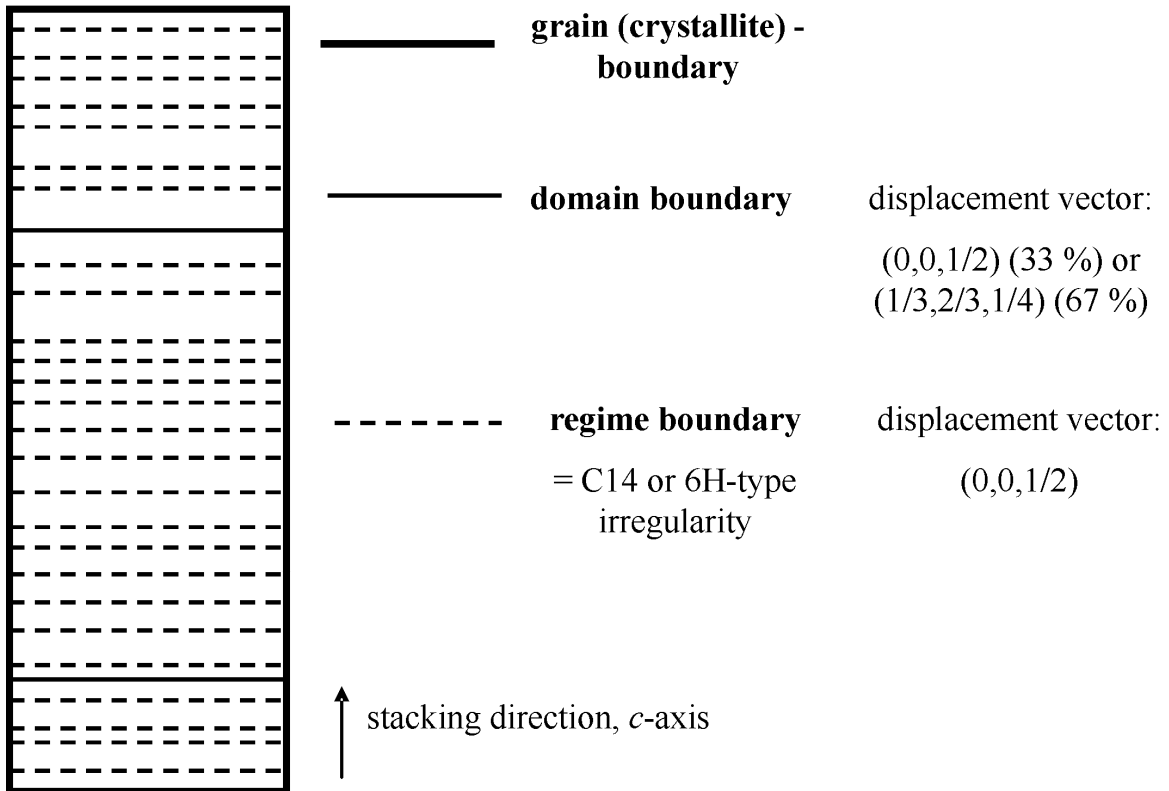


Fig. 4.16: Hierarchy of stacking irregularities in a C36 crystal, as deduced from the results of the present XRPD and HRTEM investigations. The C36 crystallite has formed from a C14 crystal by glide of synchro-Shockley partial dislocation dipoles. The displacement vectors between the crystal parts adjacent to the various irregularities have been indicated, including the probabilities for the displacement vectors associated with the domain boundaries for the case that the four layer-sandwich unit shift possibilities (X_I , X_{II} , Y_I , Y_{II}) contribute equally.

4.5 Conclusions

- i. Irregularities in the layer-sandwich unit stacking sequences of C36 Laves phases (TiCr_2 and NbCr_2), which form from C14-type precursors, have been exhibited by HRTEM and XRPD-line profile analysis. The occurrence of such faulting provides validation of the proposed mechanism for the C14 \rightarrow C36 phase transformation by glide of a series of ordered synchro-Shockley partial dislocation dipoles (“ordered glide”).
- ii. Two mechanisms bringing about the (layer-sandwich unit) stacking irregularities have been identified:
 - Domain formation: Four different types of perfect C36 domains, which are displaced with respect to each other, occur simultaneously within one parent C14 crystal, leading to layer-stacking irregularities upon impingement of the growing domains.
 - Transformation errors: Deviations occur from perfect “ordered glide” during the transformation within a domain.
- iii. The predominant layer-stacking irregularities are *2H*- and *6H*-type stacking sequences within a domain, as evidenced by HRTEM and XRPD (selective broadening of the class of XRPD reflections with $h - k \neq 3N$ and $l = 4M \pm 1$ implying that stacking faults with a displacement vector of $(0,0,1/2)$ are dominant): The transformation errors are the dominating layer-sandwich unit stacking irregularities for the investigated C36- NbCr_2 and C36- TiCr_2 Laves phases. The contribution of domain boundaries is negligible compared to that of the regime boundaries in case of C36- NbCr_2 , but less so in case of C36- TiCr_2 .
- iv. C36- NbCo_2 , which is not formed from a C14 precursor, (indeed) shows faulting distinctly different from C36- TiCr_2 and C36- NbCr_2 .

4.6 Acknowledgements

The authors are grateful to Mr. Thomas Meisner (Max Planck Institute for Metals Research) for indispensable collaboration during alloy preparation. The diffraction pattern

of NbCo₂ was kindly provided by Dr. Daniel Grüner and Dr. Guido Kreiner (Max Planck Institute for Chemical Physics of Solids, Dresden, Germany). This work has been performed within the framework of the Inter-Institutional Research Initiative “The Nature of Laves Phases” funded by the Max Planck Society.

4.7 References

- [1] Sauthoff, G. (1995). "Intermetallics". Weinheim, VCH.
- [2] Stein, F., Palm, M. and Sauthoff, G. (2004). *Intermetallics* 12: 713-720.
- [3] Stein, F., Palm, M. and Sauthoff, G. (2005). *Intermetallics* 13: 1056-1074.
- [4] Frank, F. C. and Kasper, J. S. (1958). *Acta Crystallographica* 11(3): 184-190.
- [5] Frank, F. C. and Kasper, J. S. (1959). *Acta Crystallographica* 12(7): 483-499.
- [6] Allen, C. W., Delavignette, P. and Amelinckx, S. (1972). *Phys. Status Solidi A* 9: 237.
- [7] Hazzledine, P. M. and Pirouz, P. (1993). *Scr. Metall. Mater.* 28: 1277-1282.
- [8] Kumar, K. S. and Hazzledine, P. M. (2004). *Intermetallics* 12: 763-770.
- [9] Jagodzinski, H. (1949). *Acta Crystallogr., Sect. A: Found. Crystallogr.* 2: 201-207.
- [10] Ramsdell, L. S. (1947). *Am. Mineral.* 32(1-2): 64-82.
- [11] Barrett, M. A. and Massalski, T. B. (1966). "The structure of metals", McGraw-Hill, New York.
- [12] Allen, C. W. and Liao, K. C. (1979). *Proceedings of the ICOMAT Boston 1979*: 124-129.
- [13] Liao, K. C. and Allen, C. W. (1981). *Proceedings of the International Conference of Solid-Solid Phase Transformations*: 1493-1497.
- [14] Allen, C. W. and Liao, K. C. (1982). *Phys. Status Solidi A* 74: 673-681.
- [15] Chisholm, M. F., Kumar, S. and Hazzledine, P. (2005). *Science* 307: 701-703.
- [16] D.J. Thoma and J.H. Perepezko, *Mater. Sci. Eng. A* 156 (1992) 97.
- [17] Z. Zhuang, J. Shen, Y. Liu, L. Ling, S. Shang, Y. Du and J.C. Schuster, *Z. Metallkunde* 91 (1000) 121.
- [18] H. Okamoto, *J. Phase Equil.* 23 (2002) 382.

- [19] F. Stein, D. Jiang, M. Palm, G. Sauthoff, D. Grüner and G. Kreiner, *Intermetallics* 16 (2008) 785.
- [20] J. Aufrecht, A. Leineweber, A. Senyshyn and E.J. Mittemeijer, *Scripta Mater.* 62 (2010) 227.
- [21] M. Leoni, *Z. Kristallogr.* 223 (2008) 561.
- [22] B. Prasad and S. Lele, *Acta Crystallogr. Sect. A: Found. Crystallogr.* 26 (1970) 54-64.
- [23] E. Michalski, S. Kaczmarek and M. Demianiuk, *Acta Crystallogr. Sect. A: Found. Crystallogr.* 44 (1988) 650.
- [24] J. Aufrecht, A. Leineweber and E.J. Mittemeijer, *Mater. Res. Soc. Symp. Proc.* 1128 (2009) 481.
- [25] D. Gruener, F. Stein, M. Palm, J. Konrad, A. Ormeci, W. Schelle, Y. Grin and G. Kreiner, *Z. Kristallogr.* 221 (2006) 319.
- [26] J.L. La Pouchau and F. Pichoir *Recherche Aerospatiale* 3 (1984) 167.
- [27] Topas, General Profile and Structure Analysis Software for Powder Diffraction Data, Version 3 (2003) Bruker AXS GmbH, Karlsruhe.
- [28] A. Leineweber and E.J. Mittemeijer, *J. Appl. Crystallogr.* 37 (2004) 123.
- [29] O. Vedmedenko, F. Rösch and C. Elsässer, *Acta Mater.* 56 (2008) 4984.

5. Transformation-dislocation dipoles in Laves phases: a high-resolution transmission electron microscopy analysis

Jochen Aufrecht, Andreas Leineweber, Viola Duppel and Eric Jan Mittemeijer

Images of synchro-Shockley partial dislocation arrangements in the Laves phases NbCr₂ and HfCr₂ have been obtained by high-resolution transmission electron microscopy. These defects enable the polytypic C14 → C36/6H phase transformation, which occurs in both alloys. In NbCr₂ a single synchro-Shockley partial dislocation dipole, consisting of two synchro-Shockley partials with Burgers vectors of opposite sign, has been identified. An atomistic picture of the core structure of this defect has been proposed. The ordered passage of a series of this type of line defects brings about the C14 → C36 transformation. The occurrence of stacking faults due to locally disordered passage of the line defects has been demonstrated. In HfCr₂ a complex synchro-Shockley partial dislocation configuration has been revealed. It can be regarded as an “anti-phase boundary” between two C36 domains in a common matrix consisting of an irregular stacking sequence of the so-called layer-sandwich units building up the Laves-phase polytypes, which are displaced with respect to each other by half of the unit cell’s c-axis. It has been made likely that this defect structure has formed by impingement of two domains of C36 growing perpendicular to the stacking direction by glide of synchro-Shockley partial dislocation dipoles.

5.1 Introduction

For many binary and multinary Laves phases, polytypism, i.e. the occurrence of different layer-(sandwich unit; see section 4.4.2) stacking variants, is a frequently observed phenomenon [1]. Phase transformations from one to another polytype are established by periodic changes in the stacking sequence (i.e. they are not reconstructive). This recognition led to the proposal that these transformations proceed by ordered passage of (specific) partial dislocations, leaving the changed stacking sequence in the wake of the moving partial dislocations [2]. Due to the complex crystal structure of the Laves phases, such a shear process and the corresponding structure of the partial dislocations is more complicated than in case of e.g. Co or Co-based alloys, where similar polytypic (e.g. fcc \rightarrow hcp) transformations on the basis of a change in layer-stacking sequence are observed [3]. For the case of Laves phases the partial dislocation is composed of two dislocations on two adjacent planes, having different Burgers vectors; such a combination is called a “*synchro-Shockley partial dislocation*”. This type of combined partial dislocations has been imaged using high-resolution electron microscopy in Mg-based Laves phases [4, 5]. The first atomic-resolution image of this type of (combined) dislocation (pair) obtained by Z-contrast electron microscopy has been presented recently [6].

For the particular case of the C14 \rightarrow C36 transformation occurring in some Laves phases it has been proposed that this transformation proceeds by ordered passage of pairs (dipoles) of synchro-Shockley partial dislocations with Burgers vectors of opposite sign, with one dislocation of the dipole (the synchro-Shockley partial dislocations constituting a dipole have parallel line vectors) travelling above and one dislocation of the dipole travelling below a given layer-sandwich unit [7]. Conventional transmission electron microscopy images of an TiCr₂ Laves phase alloy transforming from C14 to C36 were obtained previously indicating the growth of C36 lamellae into a C14 matrix [2, 8] and it was argued that the C36 lamellae should be bounded by *synchro-Shockley partial dislocation* dipoles. Further, a high-resolution electron microscopy image of *synchro-Shockley partial dislocation* dipoles in a Mg(Cu_{0.535}Al_{0.465})₂ Laves phase was presented in Ref. [9], although the defects (called *N* type and *P* type defects there, cf. section 5.4.1)

were not identified as dislocation dipoles. Moreover it was not made clear whether the occurrence of these observed defects is related with a polytypic phase transformation.

In the present work, a high-resolution transmission electron microscopy analysis of a *synchro-Shockley partial dislocation* dipole promoting a C14 to C36 transformation in the NbCr₂ Laves phase is presented. Further, it is shown that an antiphase-boundary type interface can be formed by “collision” of gliding *synchro-Shockley partial dislocation* dipoles in a transforming HfCr₂ Laves-phase.

5.2 Theoretical considerations: layer-stacking sequences and their changes by glide of synchro-Shockley partial dislocations

Laves phases (general formula AB_2) belong to the tetrahedrally close-packed Frank-Kasper phases [10, 11]. The ratio of the atomic radii of the constituents in the Laves phases has to be close to $r_A/r_B = \sqrt{3/2} = 1.225$. A fraction of the relatively small B atoms form a so-called Kagomé net, the relatively large A atoms are situated in the “holes” above and below such a Kagomé layer (Fig. 5.1a), forming an AB_3A layer-sandwich unit (Fig. 5.1b). Between these layer-sandwich units additional *single-layer units*, B are located (Fig. 5.1c). With respect to a given two-dimensional hexagonal unit mesh spanned by the lattice basis vectors \mathbf{a} and \mathbf{b} perpendicular to the stacking direction, the A atoms of the layer-sandwich units and the B atoms of the single-layer units can each assume three different relative positions, i.e. at fractional coordinates either $(0, 0)$, or $(1/3, 2/3)$ or $(2/3, 1/3)$.⁶ Representing the position of the layer-sandwich units by X , Y , and Z , and of the single-layer units by x , y , and z , depending on which of the former three positions is assumed by the layer concerned (i.e. $(0, 0)$: X , x ; $(1/3, 2/3)$: Y , y ; and $(2/3, 1/3)$: Z , z), the layer-stacking sequence of a Laves phase can be represented by an alternate sequence of these upper- and lower-case letters. The following rules apply additionally:

⁶Use of the symbols A , B , and C to indicate the relative layer positions is prevented to avoid confusion with the symbols A and B used for the two different metals constituting the Laves phase AB_2 .

(i) Taking first only into account the upper-case letters, a given letter, say X, may only be followed by a different other upper-case letter, in this case Y or Z, i.e. an X cannot be followed by an X (Y not by Y; Z not by Z).

(ii) A *single-layer unit* located between two *layer-sandwich units* is represented by a lower-case letter different from the upper-case letters representing the adjacent *layer-sandwich units*. Consequently, a z-type single layer is located between X and Y, i.e. the corresponding part of the stacking sequence reads ...XzY.. or ..YzX....

For the most common Laves-phase structures, the corresponding stacking sequences have been given in Table 5.1.

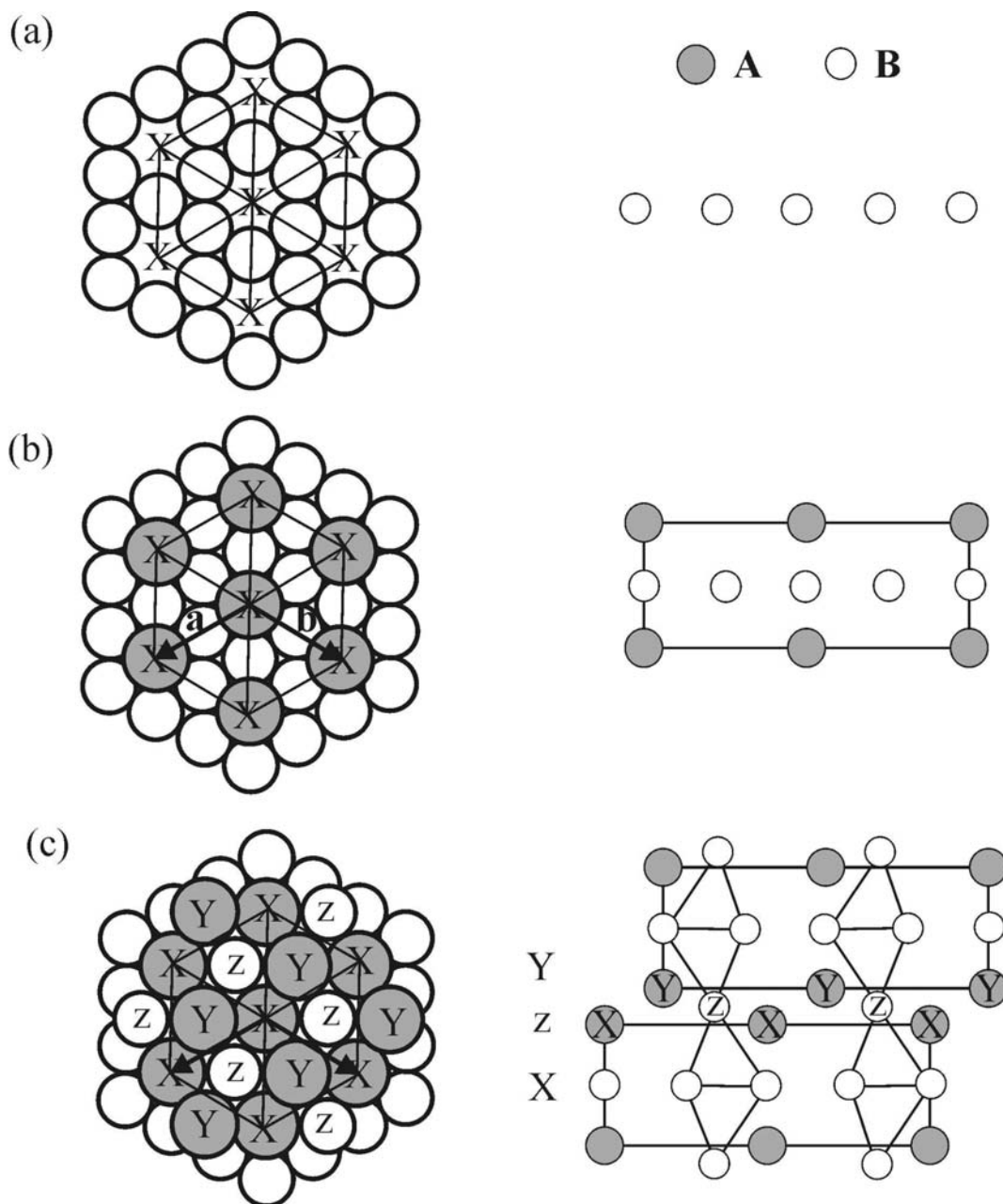


Fig. 5.1: Elementary layers of Laves phases, viewed in $[0001]$ direction (left) and $[11\bar{2}0]$ direction (right). The relatively large A atoms have been represented in grey, the relatively small B atoms in white. (a) Kagomé layer with holes on X positions, (b) AB_3A layer-sandwich unit, (c) stacking of two layer-sandwich units with a single B -layer unit in-between; in the $[0001]$ projection not all atoms of the upper layer-sandwich units have been drawn: only those labeled with a "Y" are shown.

Table 5.1: Stacking sequences of Laves-phase polytypes

stacking sequence	stacking sequence, “reduced”	Ramsdell notation	Strukturbericht designation	prototype	space group	Hägg notation
XzYxZy	XYZ	3C	C15	MgCu ₂	$Fd\bar{3}m$	+++ or ---
XzYz	XY	2H	C14	MgZn ₂	$P6_3/mmc$	+ - + -
XzYzXyZy	XYXZ	4H	C36	MgNi ₂	$P6_3/mmc$	+ + - -
XzYxZyXyZxYz	XYZXZY	6H (6H ₁) ^a	--	--	$P6_3/mmc$	+ + + - - -

^a This 6H-type structure is often referred to as 6H₁. The 6H₂ structure with the stacking sequence XYZYZY is not considered here.

As a consequence of rules (1) and (2) only one position is allowed for the single-layer unit B between the two adjacent layer-sandwich units AB_3A . Therefore, it is sufficient for many purposes to describe layer-stacking sequences of Laves phases by only giving the relative positions of the layer-sandwich units. With this simplified, “reduced” notation (see Table 5.1), the relationship with other close-packed structures as simple close-packed metals or compounds (e.g. SiC or CdI₂) is emphasized. However, for considerations of shear processes and associated changes in the layer-stacking sequence, as in the course of polytypic transformations, at least on the atomistic level, it is crucial to take account of the single-layer units located between the layer-sandwich units as well.

To describe the stacking sequence of layer-sandwich units AB_3A also the Hägg notation can be used [12], which will be of some importance in the present paper. In this notation, a symbol is not associated with a layer-sandwich unit, but with the local layer-stacking sequence of two consecutive layers-sandwich units. The three structurally equivalent pairs XY, YZ and ZX are denoted by a “+”, whereas the three “mirrored” pairs YX, ZY and XZ are denoted by a “-“ (see also Tables 5.1 and 5.2). A graphical indication of the Hägg notation can be a zig-zag line in the $[11\bar{2}0]$ projection, where (the Kagomé layers of) two adjacent layer-sandwich units are connected by / in case of a “+” transition and \ in case of a “-” transition (Fig. 5.2).

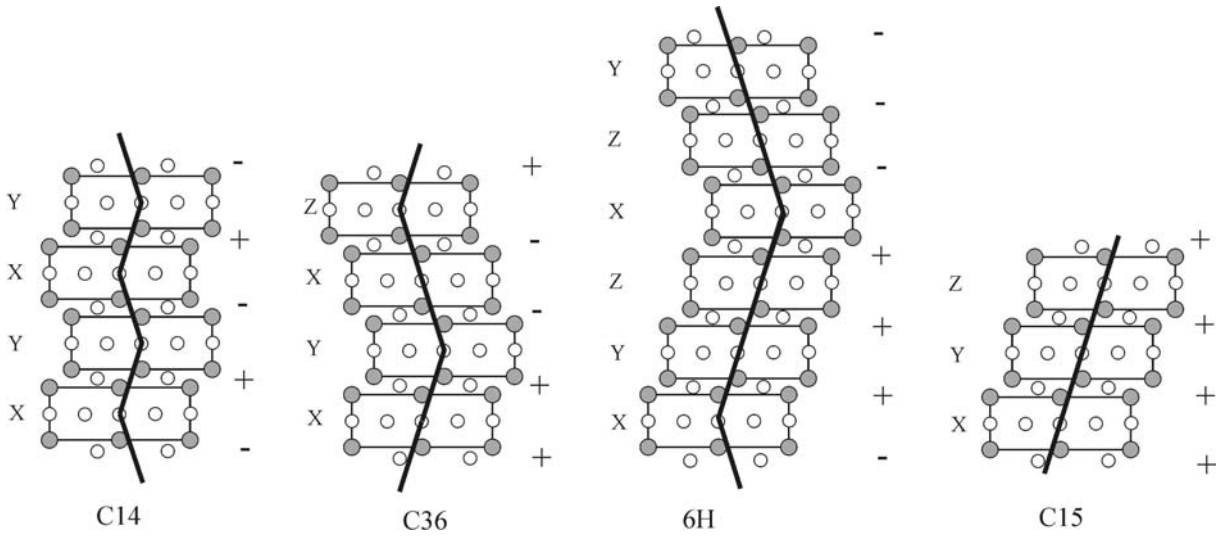


Fig. 5.2: Stacking variants, Hägg notation (“+”, “-“) and zig-zag notation (black line; “+” = “/”; “-“ = “\”, viewed in $[11\bar{2}0]$ direction.

A change in stacking sequence associated with phase transformations of one Laves-phase polytype into another one can be realized by passage of partial dislocations analogous to the Shockley partial dislocations in close-packed metals (Fig. 5.3). Because of the more complex crystal structure of Laves phases, these analogous partial dislocations have a more complex structure. Consider two layer-sandwich units AB_3A with one intermediate single layer unit B , with the stacking sequence YzX . By passage of a partial dislocation along the basal (0001) plane, the upper layer-sandwich unit can be shifted to “Z”. Because rule (ii) applies, the single-layer unit in-between the two layer-sandwich units then has to be shifted *simultaneously*, in another direction but also within the glide plane considered, to position “x”, so that the new stacking sequence becomes “YxZ”. This change in stacking sequence is thus described by two synchronous shear processes along the plane between the upper layer-sandwich unit and the single-layer unit *and* along the plane between the single-layer unit and the lower layer-sandwich unit (in different crystallographic directions). Thereby, this process of combined glide of two partial dislocations is called “synchro-shear” [2] (originally proposed for deformation of sapphire [13]) and the partial dislocation pair associated with this change in stacking sequence is called “synchro-Shockley partial dislocation” [14]. It can be characterized by two Burgers vectors, one referring to the shift of the upper layer-sandwich unit with

respect to the lower layer-sandwich unit and one referring to the shift of the single-layer unit with respect to the lower layer-sandwich unit. The six possible Burgers vectors⁷ are $\pm\mathbf{b}_1 = \pm\frac{1}{3}[\bar{1}100]$, $\pm\mathbf{b}_2 = \pm\frac{1}{3}[10\bar{1}0]$, and $\pm\mathbf{b}_3 = \pm\frac{1}{3}[0\bar{1}10]$ (cf. Fig. 5.4). In the following, only the Burgers vector corresponding to the shift between the upper layer-sandwich unit and the lower layer-sandwich unit will be referred to when a synchro-Shockley partial dislocation is characterized.

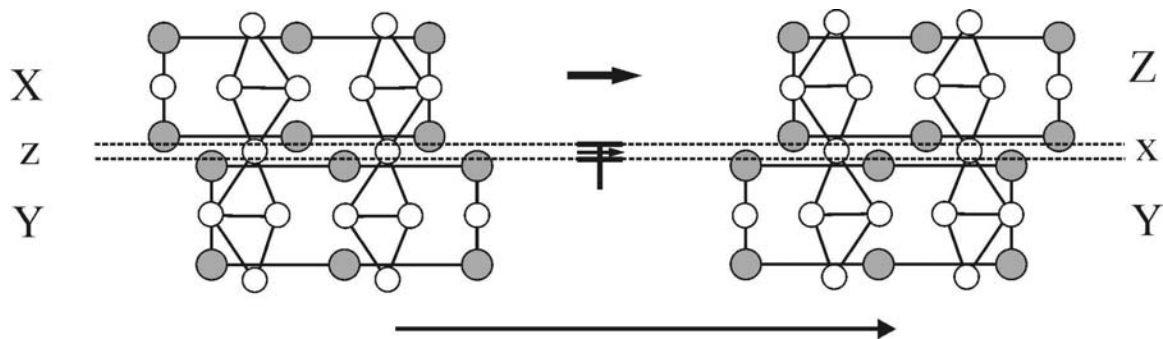


Fig. 5.3: Change of stacking sequence by synchroshear involving a synchro-Shockley partial dislocation, viewed in $[11\bar{2}0]$ direction.

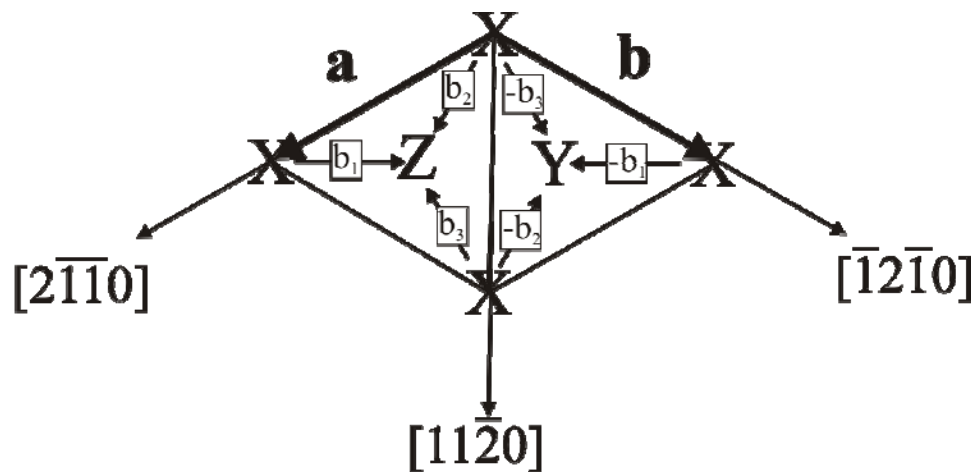


Fig. 5.4: Possible Burgers vectors for synchro-Shockley partial dislocations (considering only the layer-sandwich units) in a Laves-phase layer-stacking sequence to change the layer-sandwich unit stacking sequence (exemplified for shifts of X layer-sandwich units to either Y or Z stacking positions); $[0001]$ projection.

⁷ The Burgers vector is here defined as the displacement of the part of the crystal *above* the glide plane with respect to the part of the crystal *below* the glide plane.

If two AB_3A layer-sandwich units form a local “+” sequence (i.e. XY, YZ or ZX), (rule (i)), only synchro-Shockley partial dislocations with a Burgers vector of type $-\mathbf{b}_i$ ($i = 1, 2, 3$) can glide between them. The pair of layer-sandwich units is then changed to a local “-” sequence. Glide of synchro-Shockley partial dislocations with Burgers vector of type $+\mathbf{b}_i$ would lead to the local stacking sequences XX, YY or ZZ, which are not allowed according to rule (i). Complementarily, if two AB_3A layer-sandwich units are connected via a “-” transition (i.e., YX, ZY and XZ), only dislocations with a Burgers vector of $+\mathbf{b}_i$ can glide between them, establishing a local “+” sequence (cf. Table 5.2).

Table 5.2: Hägg symbols for local stacking sequences of two adjacent layer-sandwich units in Laves phases and the Burgers vectors of the synchro-Shockley partial dislocations (considering only the layer-sandwich units) which can glide between the two layer-sandwich units. The local stacking sequences resulting from such glide and the associated Hägg symbol are also listed.

transition	sign in Hägg notation	allowed Burgers vectors	resulting transition	resulting sign in Hägg notation
XY or YZ or ZX	+	$-\mathbf{b}_i$	XZ or YX or ZY	-
YX or ZY or XZ	-	$+\mathbf{b}_i$	YZ or ZX or XY	+

Stacking sequences and irregularities thereof in Laves phases are best identified/visualized in a $[11\bar{2}0]$ projection of the crystal structures (cf. Fig. 5.1 (right part) and, accordingly, Fig. 5.5) in HRTEM images with the $\langle 11\bar{2}0 \rangle$ direction parallel to the incident electron beam. In this projection, dislocations can be observed edge-on if their line vector \mathbf{l} is parallel to this direction and the Burgers vector is not parallel to the line vector as is the case here. Because of the three possible directions for the Burgers vectors (see above), such dislocations can either be of pure edge character (the angle between Burgers vector and line vector is 90° ; see Fig. 5.4) or of mixed (edge/screw) character (the angle between Burgers vector and line vector is $\pm 30^\circ$, see Fig. 5.4).

If an HRTEM image of atomic resolution is available, the character of the observed dislocation, out of the set of possible ones (edge or mixed), can be determined by drawing Burgers circuits around them as shown in [6] for a Laves phase and in [15, 16] for Co-Fe alloys, where similar shear transformations occur (but in that case by glide of “single” Shockley partials).

The change of stacking sequence which is necessary for the transformation of a C14 structure into a C36 structure can be conceived to be realized as follows: Consider the ...XYXY... sequence of C14 (Fig. 5.5). Every fourth layer-sandwich unit has to be displaced individually (without changing the stacking sequence of the other layer-sandwich units and thus without macroscopic shear of the crystal) to obtain the ...XYZY... sequence of C36 (Fig 5.5a). Taking into account also the single-layer units, the local change in stacking sequence would be of the type (see Fig. 5.5b and cf. rule (ii) above):

$$zXz \rightarrow xZx.$$

Passage of a partial with Burgers vector $-\mathbf{b}_i$ between two layer-sandwich units constituting a local “+” layer-stacking sequence leads to change of this local layer-stacking sequence to “-“ whereas change of a local “-“ layer-stacking sequence to a local “+” layer-stacking sequence requires passage of a partial with Burgers vector $+\mathbf{b}_i$. Thus, to realize the transformation ...XYXY... \rightarrow ...XYZY, under the avoidance of macroscopic shear, the corresponding local changes of stacking require the passage of synchro-Shockley partial dislocation *dipoles*. Such dipoles consist of two synchro-Shockley partial dislocations of opposite sign, with the Burgers vectors \mathbf{b}_i and $-\mathbf{b}_i$ (or vice-versa, $-\mathbf{b}_i$ and \mathbf{b}_i), travelling above and below the to be displaced layer-sandwich unit (Fig. 5.5b). Note that in a cubic layer-stacking sequence (...XYZXYZ...), where all local layer-stacking sequences are of the same sign, the formation of partial dislocation dipoles is impossible, because only one type of local layer-stacking sequences exists (either “+” or “-“) and thus only either synchro-Shockley partials with Burgers vector $-\mathbf{b}_i$ or only synchro-Shockley partials with Burgers vector $+\mathbf{b}_i$, but no pairs of partials with opposite sign, can glide through such stacking sequences. The overall displacement between the parts of the crystal above and below the layer-sandwich unit which is displaced by the dipole (i.e. the sum of both Burgers vectors) equals nil; hence there are

no long-range lattice distortions away from the dislocation dipole. The dipole defect could be regarded as a single line defect rather than as a combination of two separate line defects and is thus treated as a special type of defect (N-type and P-type in [9]). The lattice distortion is restricted to the very “core” of the defect. This could make formation of this type of defect energetically more favourable than formation of “unpaired” single synchro-Shockley partials and may also enhance mobility of the dipoles as compared to single, unpaired synchro-Shockley partial dislocations, facilitating the polytypic phase transformations in Laves phases, which proceed by ordered passage of such dipoles, in contrast with other polytypic transformations (e.g. C14 \rightarrow C15), which proceed by ordered passage of single, unpaired synchro-Shockley partial dislocations.

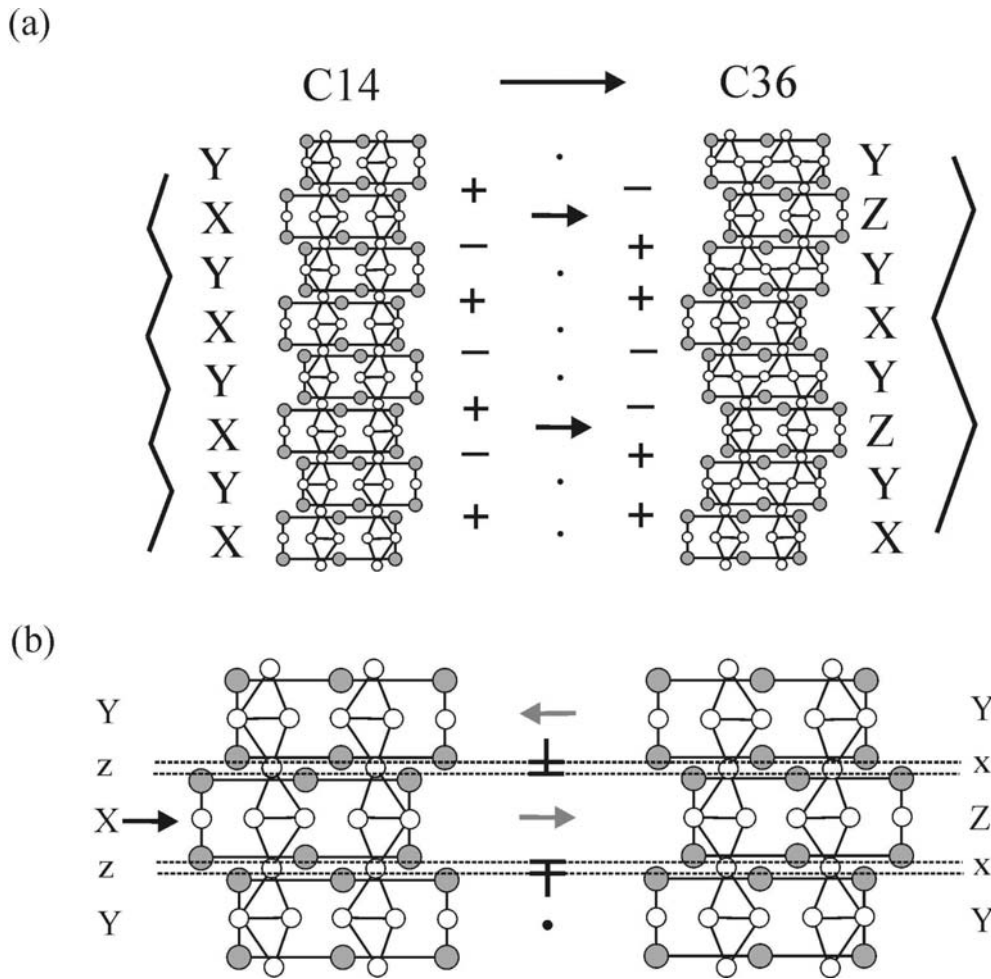


Fig. 5.5: (a) Layer-stacking sequences of a parent C14-type (left) and a product C36-type (right) Laves phase, $[11\bar{2}0]$ projection. The relative stacking positions of the layer-sandwich units AB_3A have been indicated by X,Y,Z and the corresponding local layer-stacking sequences have been indicated by the Hägg notation (Table 5.1 and Fig. 5.2). The stacking sequence of the layer-sandwich units in the microstructure has been indicated in the image using the zig-zag notation: “+” = “/” and a “-“ = “\”. (b) Schematic depiction how the above local layer-displacement (of every fourth layer, here X layer) is realized under avoidance of macroscopic shear by a synchro-Shockley partial dislocation *dipole*; in this example a $\mathbf{b}_1/\mathbf{-b}_1$ dipole (the same change in stacking sequence can also be realized by $\mathbf{b}_2/\mathbf{-b}_2$ or $\mathbf{b}_3/\mathbf{-b}_3$ dipoles). The displacements of the layer-sandwich units relative to each other occurring upon formation of C36 from C14 have been indicated by the grey arrows. The black arrow indicates the resulting shift of the central layer-sandwich unit.

5.3 Experimental

The NbCr₂ (target composition 34.5 at% Nb) and the HfCr₂ (target composition 33.4 at.% Hf) alloys were prepared by arc melting high-purity metals (Nb: 99.99 wt%, Cr: 99.999 wt%; the Hf contained 0.87 wt% Zr, 40 ppm Fe and 40 ppm O) in a titanium-gettered argon atmosphere. Ingots of about 5 g mass were produced. To ensure chemical homogeneity, the samples were flipped, remelted and subsequently cooled down on a water-cooled copper hearth for several times.

Specimens of the NbCr₂ alloy were taken from the top of the arc-melted ingot. During solidification, initially the metastable C14-Laves phase crystallizes at the top of the ingot, which then transforms to (also) metastable C36 upon further cooling [17, 18] (cf. chapters 2 and 3). Due to the high cooling rate, an intermediate stage of the transformation is frozen in. The NbCr₂ ingot was used as obtained after arc-melting, because the C36 phase can only be obtained in as-cast state of the alloy [17] (cf. chapter 3).

The as-cast HfCr₂ alloy was homogenised for 60 h at 1420°C in a high-purity argon atmosphere in an induction furnace, at a temperature at which the C14 phase is stable [19]. That C14 phase was retained by fast cooling from annealing to room temperature. Subsequently, the sample was annealed for 66 h at 1300°C to induce the phase transformation to the lower-temperature modifications C36 and C15.

For HRTEM investigations, using a Philips CM 30 microscope operating at an accelerating voltage of 300 kV, coarse powders were produced from the ingots by pestling within a mortar. Due to the brittle nature of the materials, these powders could be used as-obtained, as the edges of the individual particles were thin enough to be electron-transparent. The powder was sedimented on a holey-carbon covered copper mesh to be inserted into the electron microscope. All images and selected-area diffraction (SAD) patterns presented in this study were obtained for the case of the hexagonal $[11\bar{2}0]$ direction of the C14/C36 modifications parallel to the incident electron beam. The images were Fourier-filtered applying a mask on the Fourier transform (FFT) of the image, which suppressed the contribution of the strong (0,0,0) spot to the image. The HRTEM images shown in Figs. 5.12b and 5.13 were additionally “Fourier-filtered” by a line filter

selecting only the $hk0$ rods for image reconstruction to reduce contribution of diffuse scattering.

5.4 Results and discussion

5.4.1 Stacking faults and the structure of a single synchro-Shockley partial dislocation dipole

An isolated synchro-Shockley partial dislocation dipole was found in the as-cast NbCr₂ alloy specimen. First, the microstructure of the specimen will be discussed.

In as-cast NbCr₂ specimens, a microstructure consisting of multiple Laves-phase polytypes (C14, C36, 6H, C15) was found [17, 20] (cf. chapters 3 and 4). Most of the crystallites show a defective C36-based microstructure (Fig. 5.6a). Several crystallites show in some areas a mixed microstructure comprising regimes exhibiting C14 and C36 layer-stacking sequences (Fig. 5.7); such a microstructure can be interpreted as resulting from a (partial) C14 → C36 transformation.

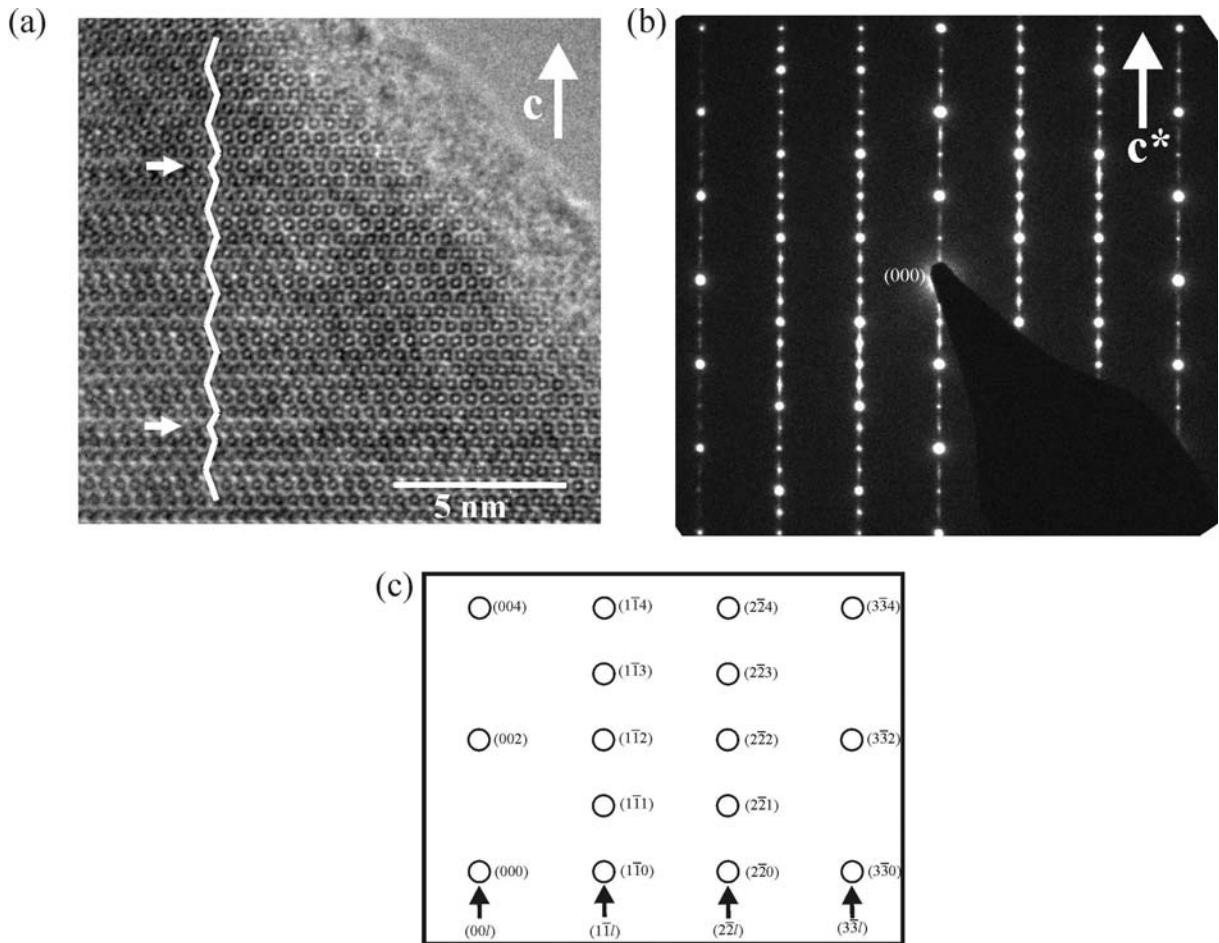


Fig. 5.6: (a) HRTEM image of a (largely) C36 crystallite in as-cast NbCr₂ containing two regions exhibiting “stacking faults” in the C36 layer-stacking sequences (indicated by arrows, see Fig. 5.9 and text), (b) corresponding SAD pattern, $[11\bar{2}0]$ zone axis and (c) schematic indexing of spots in the SAD pattern. The $[0001]$ stacking direction is indicated by **c** (in (a)) and **c*** (in (b)).

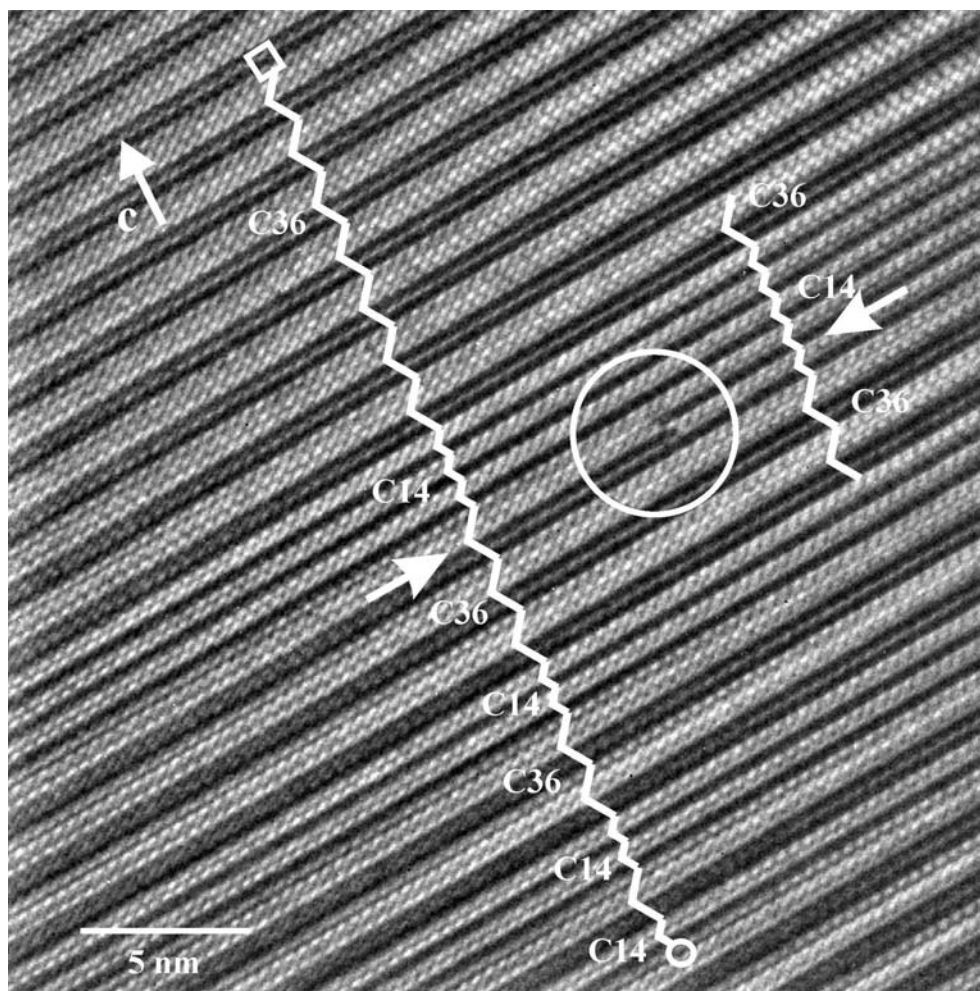


Fig. 5.7: HRTEM image of the same crystallite as shown in Fig. 5.6, but from a different area. A mixture of blocks of C14 and C36 layer-stacking sequences is observed. The stacking sequence of the layer-sandwich units in the microstructure has been indicated in the image using the zig-zag notation: a “+” (= “/”) local stacking sequence has been associated with a bright stripe and a “-“ (= “\”) local stacking sequence has been associated with a dark stripe (see text). At one location, a change (swap) of contrast of two adjacent layers can be observed (circle). The corresponding stacking sequence has been indicated at the right. From the stacking sequences left and right of the contrast change, it can be concluded that the layer-sandwich unit marked by the arrows has different stacking positions left and right of the contrast change. A synchro-Shockley partial dislocation dipole thus is located at the location of the contrast reversal (cf. Fig. 5.5). $[11\bar{2}0]$ zone axis; the $[0001]$ stacking direction has been indicated by **c**.

The two polytypes can be distinguished in Fig. 5.7 from the black/white stripe contrast, which derives from the local stacking sequences, “+” or “-“, as follows. If the stacking sequence of two neighbouring layer-sandwich units is of the “+” type, e.g. a bright (white) stripe results. In case that the stacking sequence of two neighbouring layers is of the “-“ type, then a dark (black) stripe occurs (see Fig. 5.8). This correlation is ambiguous: the bright stripes could also arise from “-“ stacking sequences and (then) the dark stripes from “+” stacking sequences. From the image presented in Fig. 5.8, a “bright-dark” decision cannot be obtained, because, due to the too large foil thickness at the imaged location, the contrast does not comprise enough details (in contrast to other images presented in this work, see discussion of the results obtained from the HfCr₂ specimen). For graphical illustration in Figs. 5.7, 5.8 and 5.9, one of both possibilities has been arbitrarily selected. The “mirrored” version (each “+” of the sequence is converted to “-“ and vice versa) is thus equally possible. Because the ...XYXY... layer-sandwich unit stacking sequence of the C14 structure involves alternation of “+” and “-“ sequences (cf. Figs. 5.5a and 5.8a), a pattern of alternating *single* dark and bright stripes occurs. Because the ...XYXZXYXZ... layer-sandwich unit stacking sequence of the C36 structure involves alternation of “++” and “--“ sequences, a pattern of alternating two dark and two white stripes occurs. In accordance with this discussion, the layer-sandwich unit stacking sequence in the crystallite has been indicated by the zig-zag lines in the experimental images shown in Figs. 5.6-5.8.

The layer-sandwich unit stacking sequence between the markers “□” and “○” in Fig. 5.7 has been reproduced in Fig. 5.9 (black line), together with the original parent C14-type layer-sandwich unit stacking sequence (grey line). At the locations of the arrows in Fig. 5.9 the C36 type of stacking sequence is realized by synchro-Shockley partial dislocations, which pass above and below every fourth layer-sandwich unit (i.e. a synchro-Shockley partial dislocation dipole) as indicated in Fig 5.5. Untransformed parts of the parent sequence have been marked by braces in Fig. 5.9. If, consecutively, some of those layers, say N , which should have shifted to obtain a continuous, perfect C36 structure in the parent crystal, would not have shifted, a number of $(4N-1)$ layers maintain the C14-type of stacking between the two bordering shifted layers. Such a case occurs for braces b and b' with $N = 2$ (Fig. 5.9). However, in the case of braces a and c in Fig. 5.7

and Fig. 5.9, a number of 9 and 5, thus $(4N-3)$ with $N=3$ and 2, respectively, maintain the C14-type stacking sequence between two bordering shifted layers. Thereby a “phase change” for the resulting C36 structure is induced: the crystal lattices of adjacent C36 blocks in the parent crystal are displaced with respect to each other by $\frac{1}{2}\mathbf{c}_{\text{C36}}$. In this sense, the transformation is not only incomplete, but also defective, because even if the transformation would now proceed to completion, the displacement between C36 domains as described immediately above is preserved and as a consequence, defects (“stacking faults”) between such domains occur, as observed (see above: arrows in Fig. 5.6). The effect of such “stacking faults” on the diffraction patterns of C36-Laves phases has been discussed rigorously elsewhere [20] (cf. chapter 4).

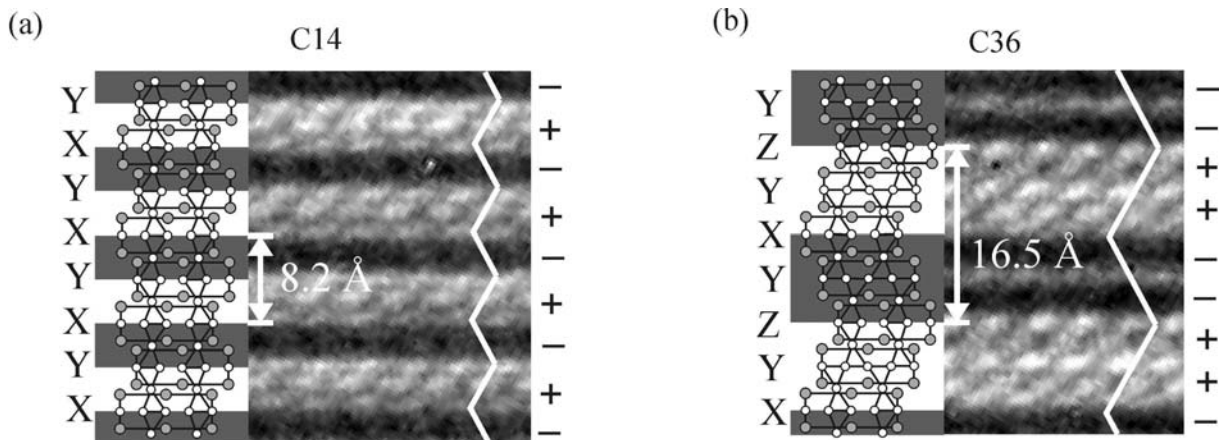


Fig. 5.8: The relation between bright-dark stripe contrast and crystal structure in the HRTEM image shown in Fig. 5.7. Regions exhibiting the stacking sequence of layer-sandwich units according to the C14 (a) and C36 (b) modifications, as observed in parts of the HRTEM image can be compared with idealized structure images, where the dark- and bright contrast has been overlaid. The periodicity of the stripe pattern equals in both cases that of the stacking sequences. $[11\bar{2}0]$ -zone axis. Here, a bright stripe has been attributed to a “+” (“/”) stacking sequence, a dark stripe has been associated with a “-“ (“\”) stacking sequence.

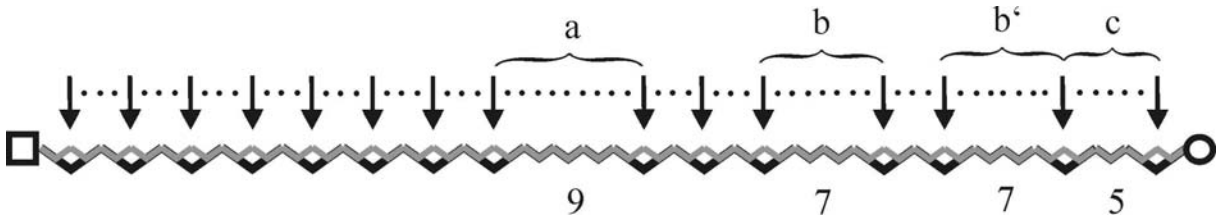


Fig. 5.9: The zig-zag line of the stacking sequence from Fig. 5.7 (between “□” and “○”; black line). The (hypothetical) parent C14 structure has been superimposed (grey line). The arrows indicate which layers of the hypothetical, parent C14 structure have to be displaced to form the observed product C36 stacking sequence. The braces highlight blocks where the C14 structure has been preserved. See text for discussion of these blocks.

A reversal in contrast within each of two neighbouring stripes can be observed in Fig. 5.7 in the area enclosed by the circle. Comparing the structures left and right of the contrast reversal, it follows that this contrast reversal is brought about by a change of stacking position of one single layer-sandwich unit (marked by the arrows in Fig. 5.7). Such relative displacement is realized by passage of and thus is bounded by a synchro-Shockley partial dislocation dipole, as schematically indicated in Fig. 5.5b. The following structural analysis of this single synchro-Shockley partial dislocation dipole is possible.

As described in section 5.2, six Burgers vectors are possible for the synchro-Shockley partial dislocations (here again referring to the shift of layer-sandwich units only, cf. section 5.2 and Fig. 5.4): $+\mathbf{b}_1 = +\frac{1}{3}[\bar{1}100]$, $+\mathbf{b}_2 = +\frac{1}{3}[10\bar{1}0]$, $+\mathbf{b}_3 = +\frac{1}{3}[0\bar{1}10]$ and $-\mathbf{b}_1 = -\frac{1}{3}[\bar{1}100]$, $-\mathbf{b}_2 = -\frac{1}{3}[10\bar{1}0]$, $-\mathbf{b}_3 = -\frac{1}{3}[0\bar{1}10]$. These six Burgers vectors can be combined into six possible pairs of Burgers vectors for the synchro-Shockley partial dislocation *dipoles*: $+\mathbf{b}_1/-\mathbf{b}_1$, $+\mathbf{b}_2/-\mathbf{b}_2$, $+\mathbf{b}_3/-\mathbf{b}_3$, $-\mathbf{b}_1/+\mathbf{b}_1$, $-\mathbf{b}_2/+\mathbf{b}_2$, $-\mathbf{b}_3/+\mathbf{b}_3$. Other combinations would not be associated with an overall displacement of zero. Note that the dipoles with $+\mathbf{b}_2/-\mathbf{b}_2$ and $+\mathbf{b}_3/-\mathbf{b}_3$ are structurally equivalent, This holds for the dipoles with $-\mathbf{b}_2/+\mathbf{b}_2$ and $-\mathbf{b}_3/+\mathbf{b}_3$ as well.

Consider Figs. 5.2 and 5.4: The $[\bar{1}1\bar{2}0]$ direction is parallel to the line vector of the dislocation and also represents the zone axis of the discussed HRTEM images. For this viewing direction, possible structures of the core of the synchro-Shockley partial

dislocation dipole have been drafted in Figs. 5.10 and 5.11 for the (four) possible non equivalent dislocation dipoles indicated above: the structures left and right of the dislocation dipole, and the proposed connection of these two structures are all compliant with the HRTEM images and satisfy the structural requirements (stoichiometry, little distortion of the crystal structure). Now, the two possible variants regarding “+” and “-“ transitions are treated separately. The dislocation dipoles with the Burgers vector pairs $-\mathbf{b}_1/\mathbf{b}_1$ (Figs. 5.10a and 5.11a) and $+\mathbf{b}_1/-\mathbf{b}_1$ (Figs. 5.10b and 5.11b) are of edge character (cf. Fig. 5.4), whereas the dislocation dipoles with the Burgers vector pairs $+\mathbf{b}_2/-\mathbf{b}_2$ and $+\mathbf{b}_3/-\mathbf{b}_3$ (Figs. 5.10c and 5.11c) as well as $-\mathbf{b}_2/\mathbf{b}_2$ and $-\mathbf{b}_3/\mathbf{b}_3$ (Figs. 5.10d and 5.11d) are of mixed 30° character (cf. Fig. 5.4). As shown in Figs. 5.10 and 5.11, the 30° dislocations are associated with less distortion and may therefore be energetically favoured and thus may be more probable.

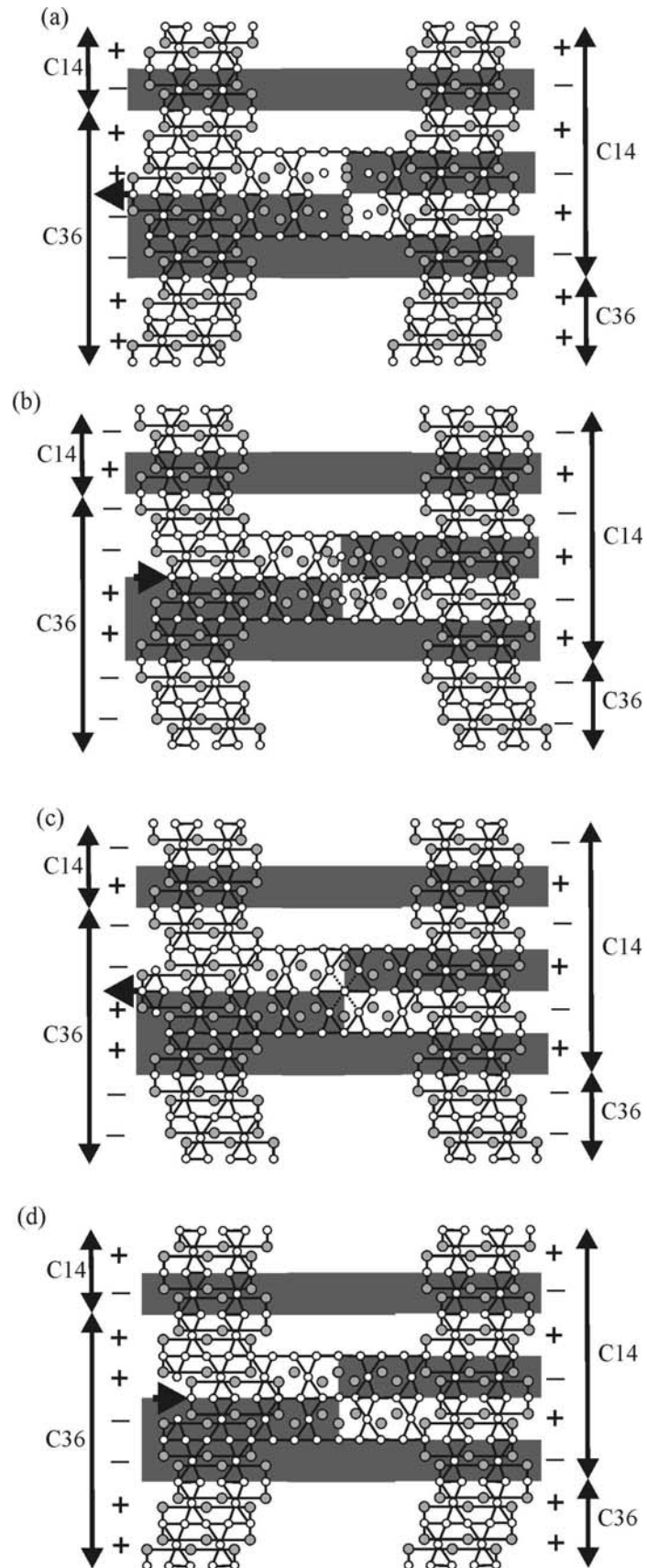


Fig. 5.10 (previous page): Possible core structures of the synchro-Shockley partial dislocation dipole detected in the HRTEM image shown in Fig. 5.7. The black-white stripe background at and adjacent to the defect mimics the contrast in Fig. 5.7. Atomistic models of possible layer-stacking sequences, shown in the appropriate projection parallel to the $[11\bar{2}0]$ zone axis, which are compliant with the contrast in the corresponding HRTEM image, have been indicated left and right of the defect in the HRTEM image. The proposed core structures have been obtained by connecting the atomistic models left and right of the synchro-Shockley partial dislocation dipole. The black arrows indicate the shift of the central layer-sandwich unit according to the Burgers vector pairs (a) $-\mathbf{b}_1/+\mathbf{b}_1$, (b) $+\mathbf{b}_1/-\mathbf{b}_1$, (P-type in [9]) and (c) $+\mathbf{b}_2/-\mathbf{b}_2$ or $+\mathbf{b}_3/-\mathbf{b}_3$, (d) $-\mathbf{b}_2/+\mathbf{b}_2$ or $-\mathbf{b}_3/+\mathbf{b}_3$ (N-type in [9]).

As revealed by the HRTEM images, the strain field of the synchro-Shockley partial dislocation dipole is concentrated within a very restricted region of the crystal; no long-range strain field around the defect (associated with pronounced contrast variation) is present, in agreement with the above presented, theoretical consideration. From the HRTEM images and the structure models for the possible atomistic configuration at the core of the synchro-Shockley partial dislocation dipole it can be suggested, that this type of defect cannot be considered as a pair of neighbouring synchro-Shockley partial dislocations; it has rather to be treated as a singular defect.

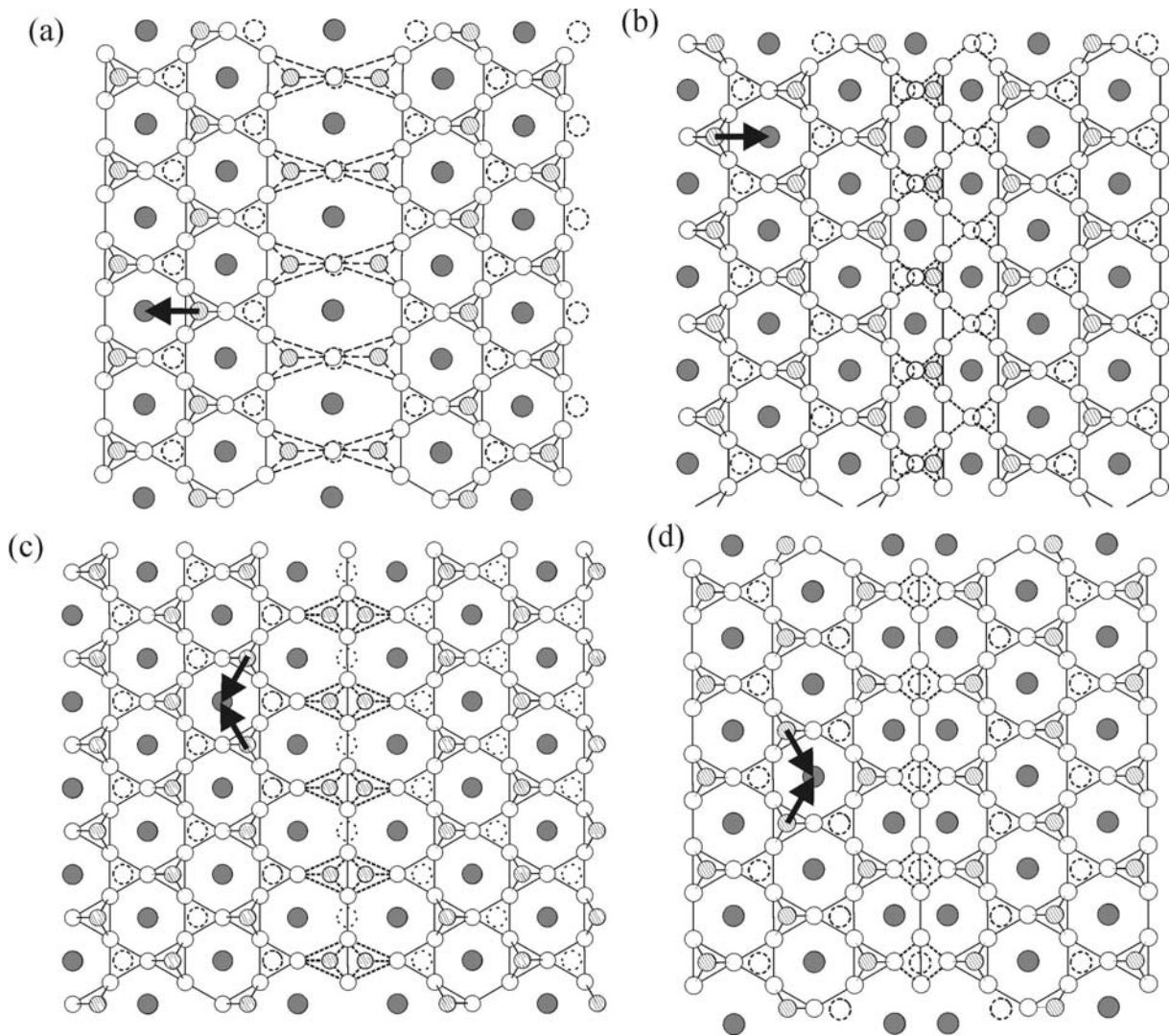


Fig. 5.11: Top view (i.e. in $[0001]$ -direction; cf. Fig. 5.1) of the layer-sandwich AB_3A unit encompassed by the singular synchro-Shockley partial dislocation dipole (cf. Fig. 5.5b). The large A atoms have been indicated by grey circles, the small B atoms by small white circles. The positions of the atoms of the adjacent single layers of B atoms (above and below the layer-sandwich unit) have been indicated as hatched circles, the positions of the large A atoms of the adjacent undistorted layer-sandwich units (above and below the distorted layer-sandwich unit) have been indicated by the large white circles. The black arrows indicate the shift of the central layer-sandwich unit (cf. Fig. 5.5b) according to the Burgers vector pairs (a) $-\mathbf{b}_1/\mathbf{b}_1$, (b) $+\mathbf{b}_1/\mathbf{b}_1$, (P type in [9]) and (c) $+\mathbf{b}_2/\mathbf{b}_2$ or $+\mathbf{b}_3/\mathbf{b}_3$, (d) $-\mathbf{b}_2/\mathbf{b}_2$ or $-\mathbf{b}_3/\mathbf{b}_3$ (N type in [9]).

The observed microstructure with its synchro-Shockley partial dislocation dipole is the result of an incomplete $C14 \rightarrow C36$ transformation. A further motion (glide) of this dipole (to the right in the figure) would result in ledge-wise growth of the $C36$ phase below the plane of the dipole. Motion of further synchro-Shockley partial dislocation dipoles on every fourth plane above the plane of the dipole considered would transform the $C14$ material into $C36$. The immobilization of the observed dipole and the untransformed $C14$ material are the result of the quenching of the sample (cf. section 5.3).

5.4.2 “Anti-phase boundary”, constituted by a synchro-Shockley partial dislocation dipole configuration

In the case of the $HfCr_2$ -Laves phase, the microstructure as developed from an initial $C14$ structure established by fast cooling from 1420°C and subsequent annealing at 1300°C for 66 h is more complicated than that of $NbCr_2$ considered before. The periodicity of the black/white line-contrast changes in the dark-field image shown in Fig. 5.12a reveals layer-sandwich unit stacking sequences corresponding to four Laves-phase polytypes: Besides $C14$ and $C36$, two variants of $C15$ (in twin orientation) and also a $6H$ -type stacking sequence can be observed. For formation of the $C15$ structure from the parent $C14$ crystal, not dislocation dipoles, but individual synchro-Shockley partial dislocations have to pass (glide) through the initial $C14$ structure [7].

For the HRTEM image shown in Fig. 5.12b it is possible to distinguish between local “+” and “-” stacking sequences (in contrast with the HRTEM image shown in Fig. 5.7 and discussed in section 5.4.1), i.e., to deduce the “sense” of the layer-sandwich unit stacking sequences from the image. To this end, the $C15$ lamellae in twin orientation at the bottom of Fig. 5.12b can be used, as follows.

The distance between two AB_3A layer-sandwich units (calculated from the lattice constants of the $C14$ - $HfCr_2$ Laves phase, as published e.g. in [19]) has been indicated in the enlarged view of the high-resolution image (Fig. 5.12c): 4.12 nm. It can be seen that this distance comprises two rows of points in the image, which are perpendicular to the stacking direction c . This suggests that every second row corresponds to an AB_3A layer-sandwich unit, whereas the rows in-between are associated with the single-layer units B .

The layer directly at (i.e. constituting the) twin boundary has to be an AB_3A layer-sandwich unit, because the layers directly above and beneath this layer are at the same lateral position, which is only possible if they are single-layer units B , not AB_3A layer-sandwich units (rule (i), section 5.2). All layers assume one of three different lateral positions. In case of the layer-sandwich units, these positions can be identified by the stacking positions X, Y and Z, in case of the single layer units by the stacking positions x,y and z (cf. section 5.2). Every third layer-sandwich unit in the [0001] direction is at the same position, which indicates cubic stacking. The stacking sequence of the AB_3A layer-sandwich units has been indicated by a single zig-zag line in Fig. 5.12c. Now, by comparing Figs. 5.12a and c, the local “+” sequences can be attributed to the bright blocks, whereas the local “-” sequences can be attributed to the dark blocks.

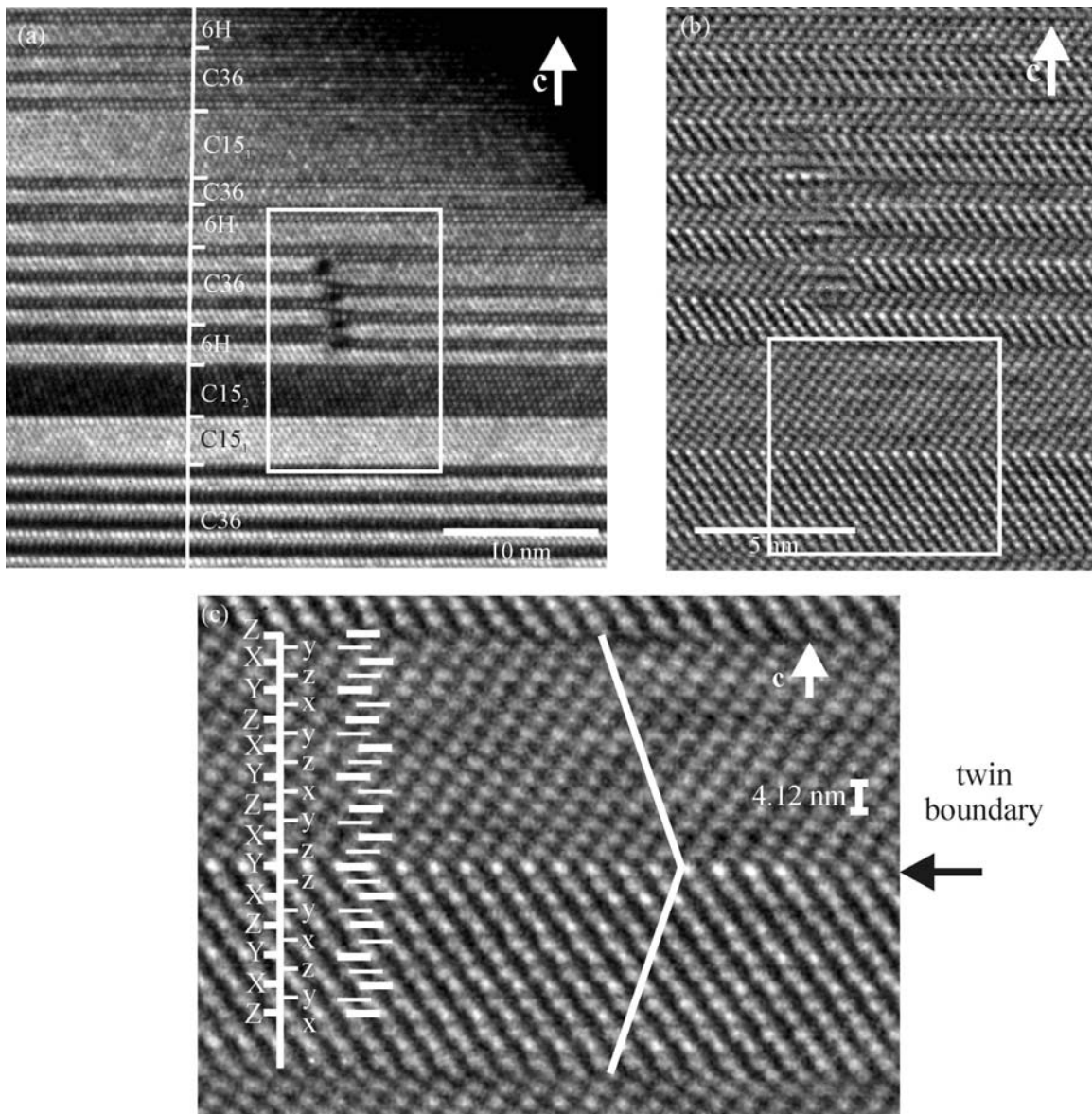


Fig. 5.12: (a) Dark-field image of a HfCr_2 crystallite transformed from C14 to a C36/6H/C15 microstructure. The dark field image has been obtained using the diffracted intensity of multiple spots close to each other on the $1\bar{1}l$ rod (cf. Fig. 5.6c). In the middle, a defect structure is visible, which can be regarded as an anti-phase boundary. (b) HRTEM image of the box indicated in (a). An enlarged view of the C15 twin lamellae within the rectangle in (b) is shown in (c). The box in (b) has been enlarged in (c), allowing determination of the layer-stacking sequence (see text), which has been indicated by the single zig-zag line in (c). $[11\bar{2}0]$ zone axis, the $[0001]$ stacking direction has been indicated by **c**.

In the middle of Fig. 5.12a, a defect structure is visible, which is associated with a contrast reversal for several consecutive layers. A close-up of the dark-field TEM image of this structure is provided by Figs. 5.13a. The stacking sequences have been indicated by a zig-zag line (Fig. 5.13b and c) and the corresponding Hägg notation (cf. section 5.2). The sequences left and right of the defect structure consist of one 6H sequence and three C36 sequences, which have formed from the initial C14 sequence. The arrangement of these sequences is different at either side of the defect structure: at the left-hand side, the 6H-type sequence is at the bottom and at the right-hand side, it is at the top. As a consequence, the units of three C36 sequences are shifted by $\frac{1}{2}\mathbf{c}_{\text{C36}}$. The two units of three C36 sequences adjacent to the defect can thus be regarded as different C36 *domains*, which developed in the same parent crystal, and consequently, the defect between them can be denoted as an anti-phase domain-boundary.

This anti-phase boundary constitutes a change in the (layer-sandwich unit) stacking sequences by a lateral shift on certain planes, as brought about by synchro-Shockley partial dislocations at the location of the defect. From the stacking sequences left and right of the anti-phase boundary a dislocation arrangement as schematically shown in Fig. 5.13b can be deduced. It consists of four synchro-Shockley partial dislocation dipoles constituting the anti-phase boundary, and two synchro-Shockley partial dislocation dipoles (one at the top and one at the bottom), which have a separation of two layer-sandwich units between the individual synchro-Shockley partial dislocations of the dipole. These last two, “extended”, dipoles are necessary to realize the boundary between the C36 and the 6H regions. Comparison with the experimental image shown in Fig. 5.13a (see Fig. 5.13c) shows that such a dislocation configuration is compatible with the observation. Layer-sandwich units which are at a different stacking position on either side of the boundary are expected to be subjected to large stain/distortion at the location of the synchro-Shockley partial dislocation dipoles (these layer-sandwich units have been indicated by dashed lines in Figs. 5.13b and c); dark areas (indicating the local presence of severe lattice strain) occur at these locations in the dark-field TEM image, which is compatible with the presence of synchro-Shockley partial dislocation dipoles. Layers which are at the same stacking position left and right of the anti-phase boundary are not

subjected to such high strain at the location of the anti-phase boundary and, indeed, no such pronounced dark areas are visible in case of these layers.

The likely origin of the anti-phase boundary is the impingement of two different C36 domains which had grown from two different locations within the same, initial C14 crystal. The stacking sequences of the two domains and that of the possible C14 parent structure have been indicated in Fig. 5.14a. Also the directions of synchro-Shockley partial dislocation glide and the associated displacement of layer-sandwich units (arrows) have been indicated for the case of 30° mixed dislocations (dislocation dipoles with the Burgers vector pairs $+\mathbf{b}_2/-\mathbf{b}_2$ and $+\mathbf{b}_3/-\mathbf{b}_3$ (Fig. 5.10c) as well as $-\mathbf{b}_2/+\mathbf{b}_2$ and $-\mathbf{b}_3/+\mathbf{b}_3$ (Fig. 5.10d)), which is considered as more probable than the case of 90° dislocations (see section 5.4.1). While above and below the defective region, the synchro-Shockley partial dislocation dipoles glide on the same planes, they glide on different planes inside the area where the antiphase-boundary is located. Upon impingement of the two dislocation fronts, dislocation reactions as shown in Fig. 5.14b will occur. Dislocations of the opposite sign will annihilate. The remaining dislocations will be immobilized, because no structure associated with a lower Gibbs energy would be formed, if the dislocations would glide further. The resulting dislocation configuration is exactly the one which has been deduced from the HRTEM images (Fig. 5.13c) for the experimentally observed anti-phase boundary.

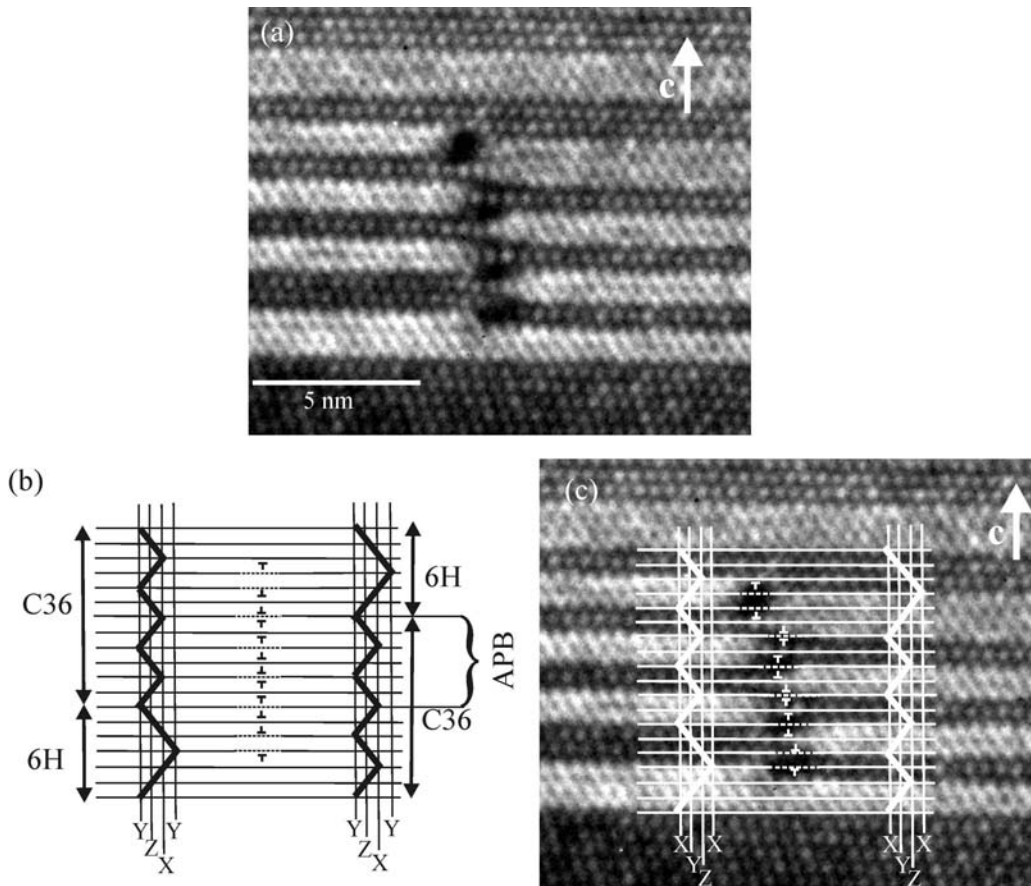


Fig. 5.13: (a) Enlarged view of the location of the defect structure shown in Fig. 5.12a, the corresponding HRTEM image is provided by Fig. 5.12b). (b) Layer-sandwich unit stacking sequences (and corresponding Hägg notation of local stacking sequences) left and right of the defect. Note that the $\dots YZXZ\dots$ stacking sequence of the C36 crystal structures presented here can be written as $\dots ZXZY\dots$, which is equivalent with $\dots XYXZ\dots$. The synchro-Shockley partial dislocation configuration, establishing the transition from the layer-sandwich unit stacking sequence at the left to that at the right of the figure has been indicated. Lattice planes which are expected to be heavily distorted because they are located between two synchro-Shockley partial dislocations constituting a dipole (and thus, the stacking sequence is different on both sides of the dipole) have been marked with dashed lines in (b) and (c). The anti-phase boundary has been indicated by “APB”. (c) Superposition of the proposed defect structure and the observed dark-field TEM image, which shows lattice distortions as dark areas at the predicted locations indicated by the dashed lines. The [0001] stacking direction has been indicated by **c**.

5.5 Conclusions

Direct experimental evidence has been provided demonstrating that the transformation in Laves phases from the C14 structure to the C36 (or 6H) structure is realized by glide of an ordered arrangement of synchro-Shockley partial dislocation dipoles.

Stacking faults, due to locally disordered passage of these line defects, have been identified. Atomistic structures for the cores of all non-equivalent synchro-Shockley partial dislocation dipoles have been proposed for the transformation from C14 \rightarrow C36 (in NbCr₂).

A C36-“anti phase boundary” has been observed for the first time (in HfCr₂). This anti-phase boundary consists of a specific arrangement of synchro-Shockley partial dislocation dipoles. This anti-phase boundary is the result of impingement of two growing C36 domains within the same, initial C14 crystal.

The microstructural situation in HfCr₂ contrasts with that of NbCr₂: whereas in NbCr₂ in principle the isolated dislocation dipole could still glide and therefore continue the C14 \rightarrow C36 transition (which has not been completed), in HfCr₂ the transformation has been completed and impingement of two completely transformed C36 domains has occurred and the dislocation arrangement (of the anti-phase boundary) is thus fixed.

The experimental observations demonstrate the long-range, largely strain-free/deformation-free character of the overall dislocation configurations: the lattice distortion is highly concentrated within the core of the individual synchro-Shockley partial dislocation dipoles. The present results indicate that the synchro-Shockley partial dislocation dipoles, which carry the C14 \rightarrow C36 phase transformations in Laves phases, should be regarded as singular defects.

5.6 Acknowledgements

This work has been performed within the framework of the Inter-Institutional Research Initiative “The Nature of Laves Phases” funded by the Max Planck Society.

5.7 References

- [1] F. Stein, M. Palm, and G. Sauthoff, *Intermetallics* 13 (2005) 1056.
- [2] C.W. Allen, P. Delavignette and S. Amelinckx, *Phys. Status Solidi A* 9 (1972) 237.
- [3] Z. Nishiyama: “Martensitic Transformations” (1978) Academic Press, New York.
- [4] Y. Kitano, M. Takata, and Y. Komura, *Journal of Microscopy* 142 (1986) 181.
- [5] Y. Liu, J.D. Livingstone, and S.M. Allen, *Metal. Mater. Trans. A* 26 (1995) 1441.
- [6] M.F. Chisholm, S. Kumar and P. Hazzledine, *Science* 307 (2005) 701.
- [7] C.W. Allen and K.C. Liao, *Phys. Status Solidi A* 74 (1982) 673.
- [8] C.W. Allen and K.C. Liao, *Proceedings of the ICOMAT Boston 1979* (1979) 124.
- [9] Y. Kitano, Y. Komura, H. Kajiwara and E. Watanabe, *Acta Cryst. A* 36 (1980) 16.
- [10] F.C. Frank and J.S. Kasper, *Acta Cryst.* 11 (1958) 184.
- [11] F.C. Frank and J.S. Kasper, *Acta Cryst.* 12 (1959) 483.
- [12] G. Hägg, *Arkiv för Kemi, Mineralogi och Geologi* 16B (1943) 1.
- [13] M.L. Kronberg, *Acta Metall.* 5 (1957) 507.
- [14] P.M. Hazzledine P. and Pirouz, *Scr. Metall. Mater.* 28 (1993) 1277.
- [15] T. Waitz and H.P. Karnthaler, *Philos. Mag. A* 73 (1996) 365.
- [16] H. Heinrich, H.P. Karnthaler, T. Waitz and G. Kostorz, *Mater. Sci. Eng. A* 272 (1999) 238.
- [17] J. Aufrecht, A. Leineweber and E.J. Mittemeijer, *Mater. Res. Soc. Symp. Proc.* 1128 (2009) 481.
- [18] J. Aufrecht, A. Leineweber, A. Senyshyn and E.J. Mittemeijer, *Scripta Mater.* 62 (2010) 227.
- [19] M. Venkatraman and J.P. Neumann, *Bull. Alloy Phase Diag.* 7 (1986) 570.
- [20] J. Aufrecht, W. Baumann, A. Leineweber, V. Duppel and E.J. Mittemeijer, *Phil. Mag.* 90 (2010) 3149.

6. Polytypic transformations of the HfCr₂ Laves phase – Structural evolution as a function of temperature, time and composition

Jochen Aufrecht, Andreas Leineweber, Viola Duppel and Eric Jan Mittemeijer

HfCr₂-Laves phase alloys of different composition have been produced by arc-melting followed by homogenization by annealing at temperatures at which the C14-high temperature modification is stable. By subsequent annealing at different, lower temperatures for various times, polytypic phase transformations have been induced. The resulting (micro-) structure of the Laves phase has been characterized by X-ray powder diffraction (XRPD) and high-resolution transmission electron microscopy (HRTEM). At temperatures between 1300°C and 1225°C, a microstructure forms, which can be regarded as composed of randomly alternating C36 and C15 lamellae. At lower annealing temperatures (1050°C-1150°C), the C36 stacking sequences do not occur. Instead a lamellar C14/C15 microstructure develops, representing an incomplete C14 → C15 transformation. A phase map for the Laves-phase part of the Hf-Cr system has been constructed. The XRPD patterns are not a superposition of the diffraction patterns corresponding to the different occurring Laves-phase polytypes; instead a common, average diffraction pattern can be discerned which can be ascribed to coherent diffraction of the polytypes constituting the lamellar microstructure. This coherent diffraction by the irregular layer-stacking sequence induces broadening of the reflections corresponding to the specific polytypes, whereas the “fundamental” reflections, occurring for all polytypes, remain unbroadened. From the diffraction patterns two scalar parameters can be obtained, which describe the stage of phase transformation: one based on the intensity of a selected polytype reflection and the other one based on the average unit cell parameter ratio, c/a , of the lamellar microstructure.

6.1 Introduction

Laves phases are promising candidate materials for high-temperature applications [1]. However, basic knowledge on thermodynamic stability, especially of different Laves-phase polytypes, on the corresponding phase transformations and on the mechanisms of plastic deformation is still scarce. From a fundamental point of view, a particularly interesting field of research concerns the transformations between different Laves-phase polytypes. Because these polytypes differ only in stacking sequence of complex, so-called sandwich layers, it has been proposed that phase transformations from one to another of these polytypes occur by passage of (a special type of) partial dislocations [2-5], similar as for e.g. the hcp-Co \rightleftharpoons fcc-Co transformation. Because of the complex Laves-phase crystal structures, a special type of partial dislocation is required for Laves-phases: the “synchro-Shockley” partial dislocation, which is actually composed of a pair of partial dislocations, which move synchronously. These dislocations have also been proposed to realize plastic deformation by slip and twinning [6, 7]. Detailed studies on the kinetics of the polytypic transformations of Laves phases have, not been undertaken up to now.

To study the kinetics and mechanisms of polytypic phase transformations of Laves phases, those alloys are in particular suitable, which exhibit different polytypes within the same composition range as a function of temperature. Candidate systems are especially TM-Cr alloys containing several TMCr_2 Laves-phase polytypes [8], where TM is a transition metal of group IV (Ti, Zr, Hf). Also for Cr-based Laves phases of group V transition metals, Nb and Ta, polytypism has been reported [8]. However, recently it has been shown that only one modification of NbCr_2 (C15) is an equilibrium phase [9] (cf. chapter 2). Several experimental difficulties impede systematic determination of equilibrium phase diagrams and of the phase transformations in these systems:

- (i) small transformation rates of the polytypic phase transformations and low diffusion rates render establishing equilibrium states difficult; thus determination of the equilibrium phase boundaries may be difficult;
- (ii) distinction of polytypes by diffraction methods can be difficult, since many polytypes differ only in low-intensity reflections. Moreover, faulting and the

occurrence of intergrowth structures of several polytypes, in particular as intermediate states of transformation [10-12] (cf. chapter 3), lead to complicated diffraction effects.

Thus it does not come as a surprise that also in case of the Hf-Cr phase diagram [13] (Fig. 6.1), contradictory data have been provided in the literature regarding the homogeneity range of the Laves phase HfCr₂ and the associated temperature-dependent polytypism. At least two stable variants of HfCr₂ exist: C14 (prototype: MgZn₂, *P6₃/mmc*) as high-temperature modification and C15 (prototype: MgCu₂, *Fd $\bar{3}m$*) as room-temperature modification [14, 15]. In some works, the occurrence of a third modification of C36 type (prototype: MgNi₂, *P6₃/mmc*) at intermediate temperatures (1200°C-1500°C) has been reported [16, 17]. The C14 structure was found after solidification of the samples from the melt. The other polytypes (C15 and C36) were formed upon annealing at temperatures lower than about 1335°C. In a detailed study on the phase transformations of HfCr₂, using transmission electron microscopy (TEM) employing selected area diffraction (SAD) for structure identification, it has been reported that, upon annealing at 800 – 1200 °C, C14-HfCr₂ transforms first to long period structures as 16H, 14H and 10H and finally to C36 (4H) [18, 19]. The formation of a C15 phase was not observed, despite long-time anneals. An ab-initio study of ground-state properties of the TMCr₂ Laves phases (TM = group-IV transition metal), using a density functional approach, showed, however, that, at 0 K, C15 is the most stable modification for all TMCr₂ Laves phases, i.e. including HfCr₂ [20].

In the present study, X-ray powder diffraction (XRPD), complemented by high-resolution electron microscopy (HRTEM) has been used to analyse the structural evolution of HfCr₂-Laves phase alloys upon annealing, departing from the (retained upon quenching) C14 polytype, as a function of time, temperature and composition. The relative stability of the different polytypes could be established.

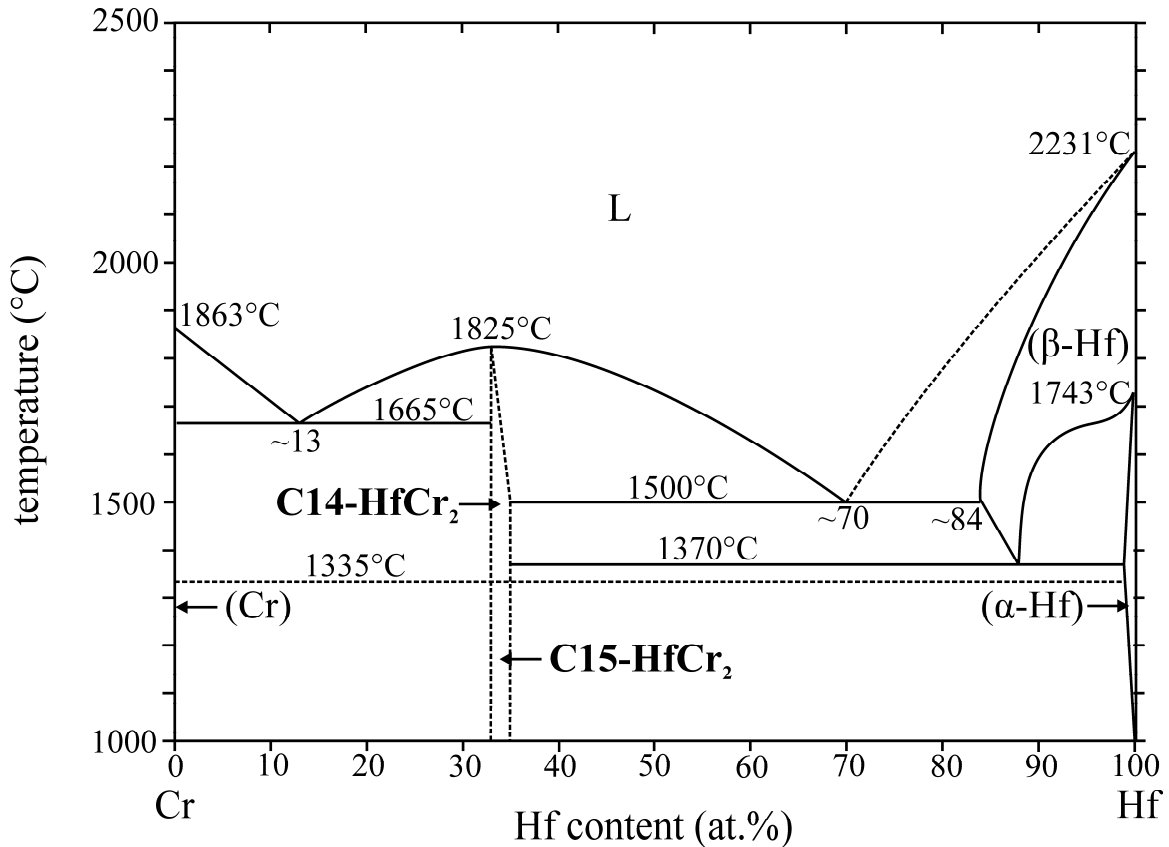


Fig. 6.1: The Hf-Cr phase diagram (after [13]). The homogeneity range of the Laves phase and the temperature of $C14 \rightleftharpoons C15$ phase transformation have been indicated by *dotted* lines, thereby emphasizing the provisional character of this part of the phase diagram.

6.2 Theoretical background

6.2.1 Laves-phase polytypes

The crystal structures of Laves phases (general formula AB_2 , ideal ratio of atomic radii: $r_A/r_B \approx 1.225$ [21]) are built up by stacking of certain complex layers. The relatively small atoms B define a close-packed Kagomé network as indicated in Fig. 6.2a. At the position of the holes, above and below the Kagomé network, the relatively large A atoms are positioned. Thus, a (triple-) layer-sandwich unit AB_3A is formed (Fig. 6.2b). The large A atoms define a two-dimensional hexagonal unit grid with basis vectors \mathbf{a} and \mathbf{b} ; the A atoms are located at positions of type $X(0,0)$. At positions of type $Y(1/3,2/3)$ and $Z(2/3,1/3)$, stacking positions are available for the next atom layers in \mathbf{c} direction. At one

of the two positions, small B atoms are situated which do not belong to the layer-sandwich unit and constitute a single layer; at the other one the large A atoms of the next AB_3A layer-sandwich unit are positioned.

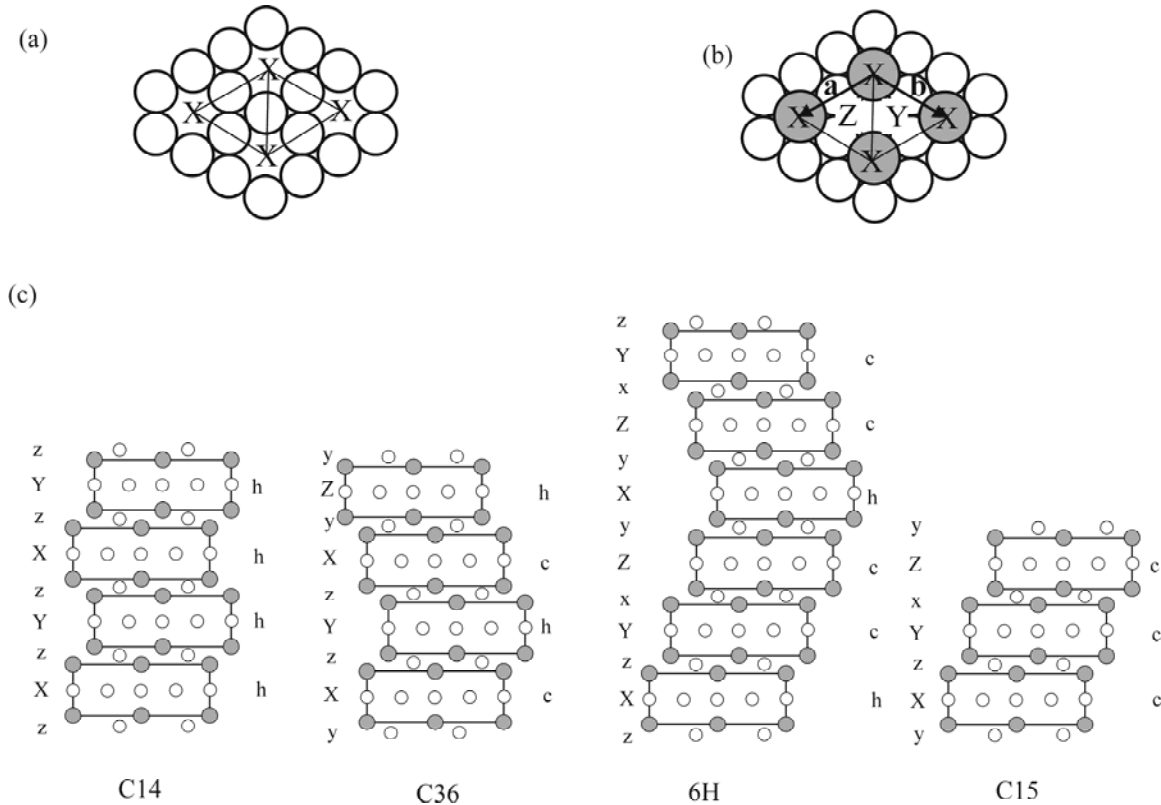


Fig. 6.2: (a) 0001-projection of a Kagomé layer formed by small B atoms; (b) 0001-projection of a layer-sandwich unit AB_3A ; (c) Stacking sequences of the Laves-phase modifications C14, C36, 6H and C15. The upper-case letters X, Y and Z indicate the stacking positions of the layer-sandwich units, the lower-case x, y, and z letters indicate the positions of the single-layer units formed by B atoms, the letters c and h indicate the Jagodzinski symbols associated with the respective layers.

Following this principle, the stacking variants of the Laves-phase polytypes can be constructed. The most common stacking variants have been listed in Table 6.1 and are shown in Fig. 6.2c, where an upper-case letter represents the stacking position of a layer-sandwich unit AB_3A and a lower-case letter indicates the position of a single-layer unit B . Because the stacking position of neither two consecutive AB_3A layers nor of two adjacent

layers AB_3A and B may be identical, the stacking position of a single-layer unit B is determined by the stacking positions of the adjacent layer-sandwich units AB_3A . The following rules apply:

(i) Taking first only into account the upper-case letters, a given letter, say X , may only be followed by a different other upper-case letter, in that this case Y or Z , i.e. an X cannot be followed by an X (Y not by Y ;, Z not by Z).

(ii) A *single-layer unit* located between two *layer-sandwich units* is represented by a lower-case letter different from the upper-case letters representing the adjacent *layer-sandwich units*. Consequently, a z -type single layer is located between X and Y , i.e. the corresponding part of a the stacking sequence reads $\dots XzY..$ or $..YzX\dots$

Table 6.1: Overview of the stacking sequences of common Laves-phase modifications, with corresponding Jagodzinski symbols, Ramsdell symbols, Strukturbericht designation, prototype, space group and fraction f_c of cubic layer-sandwich unit arrangements (see text) and the number N_L of layer-sandwich units per periodic unit along the stacking direction.

stacking sequence	stacking sequence, reduced	Jagodzinski notation [22]	Ramsdell notation [23]	Strukturbericht designation [24]	prototype	space group	f_c	N_L
$XzYxZy$	XYZ	c	3C	C15	MgCu ₂	$Fd\bar{3}m$	1	3
$XzYZ$	XY	h	2H	C14	MgZn ₂	$P6_3/mmc$	0	2
$XzYzXyZy$	$XYXZ$	hc	4H	C36	MgNi ₂	$P6_3/mmc$	0.5	4
$XzYxZyXyZxYz$	$XYZXZY$	cch	6H ^{a)}	--	--	$P6_3/mmc$	0.67	6

a) This 6H-type structure is often referred to as 6H₁. The 6H₂ structure with the Jagodzinski symbol hchhc is not considered here.

Since the positions of the single layer units are unambiguously prescribed by the positions of the adjacent layer-sandwich units (see above), it is sufficient for most purposes (but see below) to consider only the upper-case letters to indicate the stacking sequence.

The local stacking configuration associated with a certain layer-sandwich unit (i.e. as compared with both adjacent layer-sandwich units) can either be hexagonal (if the two adjacent layer-sandwich units are at the same stacking position with respect to each other) or cubic (if the two adjacent layer-sandwich units are at different stacking positions with respect to each other). Layers (i.e. layer-sandwich units) with a hexagonal local arrangement are denoted by a “h” in the notation after Jagodzinski [22]: layers with a cubic local arrangement with a “c”. In case of the C15 structure, all layers are “c”: in case of the C14 structure, all layers are “h”. For C36, “c” and “h” layers are alternating; for 6H always two “c” layers are followed by one “h” layer (Table 6.1). On this basis, one can associate a fraction of cubic layer arrangements, f_c , with each Laves phase (Table 6.1).

6.2.2 Diffraction patterns and distinction between polytypes

The identification of the type of polytype by (X-ray and/or electron) diffraction methods is difficult, also for ideal stacking sequences (i.e. no layer faulting has occurred with respect to the polytype considered), because the diffraction patterns of the various polytypes are rather similar: Certain reflections occur for all polytypic modifications; others occur at least for some of the polytypes. Comparison of the diffraction patterns of various polytypes can most conveniently be made upon adopting a similar crystallographic description of the polytypes. This can be done employing the hexagonal unit cell with basis vectors \mathbf{a} , \mathbf{b} and \mathbf{c} , introduced at the start of section 6.2.1 and with \mathbf{a} and \mathbf{b} as given in Fig. 6.2b. The third basis vector \mathbf{c} is oriented parallel to the stacking direction and has the length

$$c = N_L \times c_0, \quad (6.1)$$

where c_0 is the distance between two layer-sandwich units and N_L is the number of layer-sandwich units in one period of the polytype’s stacking sequence (N_L is identical with the first number appearing in the Ramsdell notation; see Table 6.1). For the face-centred cubic C15 polytype this means that its conventional fcc cubic unit cell vectors \mathbf{a}' , \mathbf{b}' and \mathbf{c}' (all of length a') are transformed into hexagonal-rhombohedral ones, with one set of the body diagonals of the fcc unit cell (corresponding to the stacking directions of layer-sandwich units) becoming the c axis with $c = 3c_0 = 3^{1/2}a'$ and two face diagonals of the fcc unit cell becoming the a and b axes with $a = b = 2^{-1/2}a'$ (Fig. 6.3).

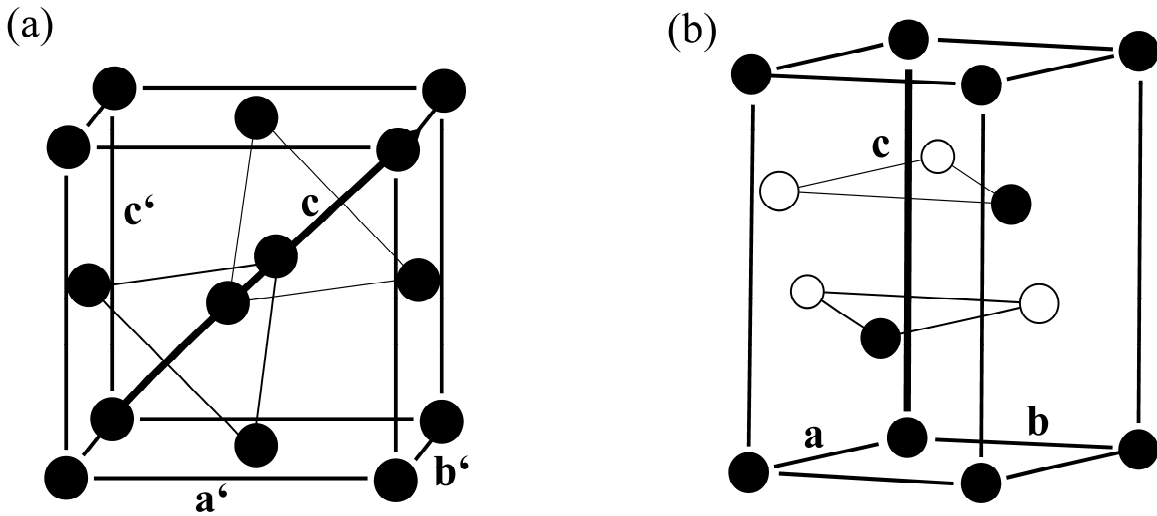


Fig. 6.3: (a) The conventional face-centered cubic unit cell for the Bravais translational lattice of the C15 structure and (b) the hexagonal-rhombohedral unit cell for the same translation lattice as in (a) (white points are situated outside the unit cell).

On the basis of this unit-cell description, with the three basis vectors \mathbf{a} , \mathbf{b} , \mathbf{c} , the reciprocal-lattice basis vectors \mathbf{a}^* , \mathbf{b}^* and \mathbf{c}^* result, with the size of \mathbf{c}^* depending on N_L according to $c^* = (N_L \times c_0)^{-1}$. Because of the dependence of c^* on N_L , reflections from different polytypes but arising from the same sets of layers and thus located at the same spot in reciprocal space will have different indices (e.g. the 002 reflection of C14 corresponds with the 004 reflection of C36). To obtain a standardized, general notation for the Laves-phase polytypes, a standardized basis vector \mathbf{c}_0^* has been defined by: $\mathbf{c}_0^* = N_L \times \mathbf{c}^*$ (thus with polytype-independent $c_0^* = c_0^{-1}$). It can be used together with \mathbf{a}^* and \mathbf{b}^* as a unified coordinate system of reciprocal space for all Laves phases considered here, i.e. independent of the specific polytype. Thus \mathbf{a}^* , \mathbf{b}^* and \mathbf{c}_0^* build up a reciprocal space lattice with lattice points denoted by hkl_0 (corresponding to Laue indices). The thus realized unified indexing of the Laves-phase reflections involves that occurring reflections may have non-integer l_0 values (h and k are integers). These hkl_0 correspond to the reflections hkl (with integer l) for a specific polytype (employing the above-mentioned hexagonal \mathbf{a} , \mathbf{b} , \mathbf{c} basis) with $l = l_0 N_L$.

Using the above introduced hkl_0 indexing scheme it is possible to give the following rules for occurrence of reflections in the diffraction patterns of Laves phases (similar rules hold for close-packed metal polytypes) [25]:

- (a) The reflections with $h - k = 3N$ (N : integer) and integer l_0 pertain to the same structure factor for all Laves-phase polytypes. These reflections will be referred to as *fundamental reflections*. The lattice spacing derived by Bragg's law from the 001 reflection gives c_0 , i.e. the spacing of the layer-sandwich units. Very weak additional reflections with $h - k = 3N$ may result for non-integer values of l_0 , which result from periodic internal distortions of the crystal structure.
- (b) The reflections with $h - k \neq 3N$ (N : integer) and in general non-integer l_0 have different structure factors for different polytypes and therefore differ from polytype to polytype. These reflections will be referred to as *polytype reflections*.

Schematic $h0l/h0l_0$ -sections through reciprocal space which play a role in the work presented here (i.e. corresponding to SADs with [010] parallel to the incident electron beam) are shown in Figs. 4 and 5 for the simplest polytypes C14 (2H), C36 (4H), 6H and two C15 (3C). For C15, two variants in twin orientation, with the basal plane as twinning plane, are shown (presented with cubic and hexagonal (hR – hexagonal-rhombohedral) indices).

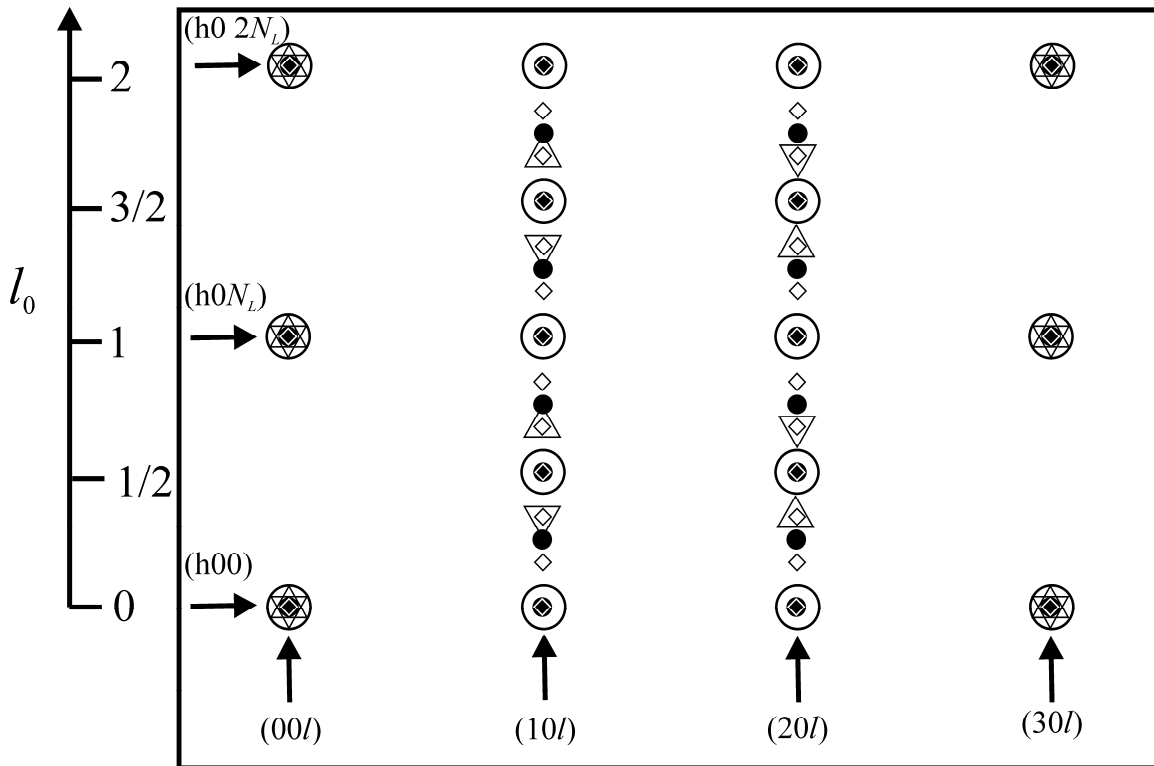


Fig. 6.5: Superimposition of the diffraction patterns ([010]-zone) shown in Fig. 6.4, applying the symbols used in Fig. 6.4 for reciprocal lattice points to identify the different polytypes. The corresponding l_0 scale is given on the left.

Faulting, i.e. occurrence of irregularities in the stacking sequence of the layer-sandwich units of a certain polytype is a frequent phenomenon. The faults can be conceived as boundaries between domains of the Laves phase structure. These domains are thus shifted with respect to each other by a vector $\Delta\mathbf{r} = u'\mathbf{a} + v'\mathbf{b} + w'\mathbf{c}$ with in general real-valued u' , v' and w' . Due to the three distinct positions the layers can assume in the \mathbf{a} - \mathbf{b} plane (see section 6.2.1), it directly follows that $u' = N/3$ and $v' = 2N/3$ or $u' = 2N/3$ and $v' = N/3$ (N : integer). For non-integer values of u' , v' and w' , hkl_0 - and $\Delta\mathbf{r}$ -dependent phase shifts occur between the (X-ray or electron) waves emanating from the coherently diffracting domains, as is well-known for stacking faults or twins of close-packed structures of single metals [26, 27]. For the fundamental reflections these phase shifts are always $2\pi \times M$ (M : integer) due to the restricted values u' and v' can assume. Thus the fundamental reflections are unaffected by the presence of layer-stacking faults. Only for the polytype reflections ($h - k \neq 3N$ (N : integer)) phase shifts different from $2\pi \times M$ (M :

integer) may occur, which leads to hkl_0 -dependent line broadening, line asymmetry and/or line shifts, as well as to diffuse distribution of intensity as a consequence of finite domain size along the \mathbf{c}^* direction. The relation between such hkl_0 -selective broadening and the values u' , v' , and w' has been discussed in some detail for 4H structures [28] and more generally for various hexagonal and rhombohedral polytypes of close-packed structures [29].

In an XRPD pattern the line broadening occurring for polytype reflections along \mathbf{c}^* in reciprocal space is projected onto the diffraction vector \mathbf{g} . Therefore, the line broadening in an XRPD pattern will additionally depend on l_0 : given the same extent of broadening in reciprocal space, reflections with high $|l_0|$ values (and simultaneously small $|h|$ and $|k|$), for which \mathbf{g} is almost parallel to \mathbf{c}^* , will exhibit large broadening in an XRPD pattern, whereas in an XRPD pattern reflections with small values for l_0 (and large $|h|$ and $|k|$), for which \mathbf{g} is almost perpendicular to \mathbf{c}^* , the broadening will not be that pronounced; if $l_0 = 0$ the reflections are not broadened by the effect discussed.

For multiphase Laves-phase samples the (e.g. powder) diffraction pattern in the simplest case (different polytypes occurring in different crystallites) will be a weighted superposition of the diffractions patterns pertaining to the different polytypes. HRTEM studies on Laves phases, e.g. [10-12] (cf. chapter 3), have revealed that occurrence of several polytypes is often realised as a fine intergrowth structure in a single crystallite (see also introduction): Within one crystallite, different regions (domains) occur each exhibiting the typical stacking sequence of a certain polytype. It is this occurrence of different stacking sequences in one crystallite that induces a constant phase difference between the diffracted waves emanating from the different polytypic regions in the crystallite. This will lead to similar diffraction effects as described above for faulting within one polytype: line broadening of the $h - k \neq 3N$ reflections and streaking along the \mathbf{c}^* direction.

The fundamental reflections ($h - k = 3N$) recorded for an intergrowth structure arise by diffraction from a stack of layers with slightly different lattice spacings as a consequence of slightly different values of c_0 for the different polytypes (the lattice parameter a is likely the same for all layers in an intergrowth due the coherent stacking of the layers and some average of the stress-free a lattice parameters pertaining to the

separate polytypes will be established). These fundamental reflections will take some corresponding average position, i.e. the lattice spacings deduced from the peak positions of these reflections represent some average value for all polytypes constituting the intergrowth structure concerned. As a consequence, also the fundamental reflections will be slightly broadened due to the distribution of lattice-spacing parameters in an intergrowth structure, but this broadening is much less pronounced than the broadening of the polytype reflections.

Hence, X-ray diffraction patterns of intergrowth microstructures consisting of stacking sequences of different Laves-phase polytypes are not given by a simple superimposition of the separate diffraction patterns of the individual Laves phase polytypes, but, instead, reveal additional diffraction phenomena; in particular for the non-fundamental, polytype reflections effects occur related to those induced by faulting within one polytype.

6.3 Experimental procedures

The HfCr₂ alloys were prepared from the elements, using chromium of purity 99.999 wt% and hafnium containing 0.87 wt% Zr, 40 ppm Fe and 40 ppm O. Other impurities were below the detection limit (<20 ppm). The alloys were prepared by arc-melting under a high-purity argon-gettered atmosphere. The ingots were flipped and remolten five times to ensure chemical homogeneity. The sample compositions were intended to be as indicated in Table 6.2. Because of the high vapour pressure of chromium, a significant loss of chromium during the casting process was expected. Therefore, the difference of the total mass of the initial material and the as-cast sample was determined and, ascribing the mass loss to solely chromium evaporation, the actual Hf content of the alloys produced was calculated; see Table 6.2.

Table 6.2: The intended Hf content of the HfCr₂ alloys, the weight loss during arc melting of samples, the actual Hf content of the HfCr₂ alloys and the lattice parameters a and c (c_0) of the HfCr₂ alloys after homogenization. Since the specimens were pure C14 polytype after cooling $N_L = 2 = c/c_0 = 2$ (cf. section 6.2.2).

sample	1	2	3	4	5
Intended Hf content (at.%)	32.3	33.1	33.2	34	34.5
mass loss (%)	0.45	0.40	0.37	0.44	0.42
Actual Hf content accounting for chromium loss (%)	32.6	33.3	33.4	34.3	34.8
lattice parameter a (Å)	5.0678	5.0775	5.0790	5.0845	5.0891
lattice parameter c (c_0) (Å)	8.2250 (4.1125)	8.2279 (4.1140)	8.2322 (4.1161)	8.2385 (4.1192)	8.2441 (4.1221)

For homogenization, the samples were annealed for 60 h at 1420°C in an inductive furnace. Inside the furnace, a high-purity argon atmosphere was established. The samples were annealed on Y₂O₃ pads inside Al₂O₃ crucibles. The crucibles were covered by an Al₂O₃ plate, on which a Zr-getter sheet was placed. The samples were heated in a Mo-susceptor, which was also covered by a Zr-getter sheet. The samples were cooled by switching-off the induction current. The initial cooling rate was 45 K/s, and in

about 30 seconds, a temperature of 900°C was reached. As demonstrated in section 6.4.1, this cooling rate was high enough to retain the C14-high temperature modification.

For the subsequent annealing experiments, the ingots were broken into small specimens of 10-50 mg. Annealing at 1225°C-1300°C was also performed in the inductive furnace, using the same experimental setup as for the homogenization. Fast cooling was accordingly achieved by switching of the inductive current. For annealing at 1050°C-1150°C, the material was placed in sealed quartz-tubes filled with argon, together with a Zr-getter sheet. These samples were annealed in a box furnace and subsequently water-quenched.

For X-ray diffraction, a fine powder was produced from the samples using a mortar. The powder was suspended in isopropanol and sedimented on a (510)-cut Si-crystal plate (wafer) using a supporting brass ring during evaporation of the liquid. The measurements were performed using a “Philips X’Pert MPD” diffractometer equipped with a germanium-monochromator in the incident beam, using $Cu-K\alpha_1$ radiation. Silicon powder was used as internal standard for correction of the instrumental shift of the 2θ scale. The Laves-phase lattice parameters a and c_0 (cf. section 6.2.2) were obtained from the diffraction patterns of the Laves phases by calculation of the interplanar spacings d_{hkl_0} from the diffraction angles 2θ of all fundamental reflections using Bragg’s law:

$$d_{hkl_0} = \frac{\lambda}{2 \sin \theta}, \quad (6.2)$$

and subsequent least-square fitting of a and c_0 , minimizing the deviation of the measured lattice spacings d_{hkl_0} and the lattice spacings calculated from

$$\frac{1}{d_{hkl_0}^2} = \frac{4}{3} \frac{h^2 + k^2 + hk}{a^2} + \frac{l_0^2}{c_0^2}, \quad (6.3)$$

for all d_{hkl_0} simultaneously.

The HRTEM investigations were performed using a Philips CM 30 ST microscope with accelerating voltage of 300 kV. For this purpose, coarse powders were produced from the samples by grinding in a mortar. Due to the brittle nature of the materials, these powders could be used as-obtained, as the edges of the particles were thin enough, i.e.

electron-transparent. The powder was suspended in n-butanol. A holey-carbon covered copper mesh was covered by the suspension, allowing the powder to settle on the mesh and the liquid to evaporate. The SAD patterns were recorded using the precession technique enhancing the kinematic diffraction character of the diffraction patterns [30, 31].

6.4 Results

6.4.1 C14-HfCr₂

X-ray diffraction demonstrated that all samples were 100% C14 after homogenization at 1420° and subsequent fast cooling to room temperature (Fig. 6.6). In case of the samples with the highest intended Hf contents (34 and 34.5 at.%), a very small amount of Hf-rich hcp-solid solution is present as a secondary phase. The unit-cell volume and the c/a ratio have been plotted vs. (actual, cf. Table 6.2) composition in Fig. 6.7. If the very small amount of Hf-rich solid solution detected in the two specimens with highest Hf contents would be an equilibrium phase (i.e. the composition of the two specimens would be located in a two-phase field), no increase in the unit-cell volume of the C14-Laves phase with increasing Hf content would be expected for the two specimens of highest Hf content. As this is not the case, the Hf-rich hcp-phase is rather a secondary phase formed during solidification from the melt, which could not be removed by the extended anneals. Therefore, the actual Hf content of the Laves phase in case of these two specimens of highest Hf contents could be slightly lower than as indicated in Fig. 6.7.

A relationship of unit cell volume V (pertaining to the C14 polytype) and Hf content x_{Hf} could be established on the basis of the data shown in Fig. 6.7:

$$V_{\text{HfCr}_2}^{\text{cell}} = [87x_{\text{Hf}} + 155] \text{Å}^3 \quad (6.4)$$

The relationships of the lattice parameters a and c and the Hf content x_{Hf} are given by:

$$a = [0.925x_{\text{Hf}} + 4.768] \text{Å} , \quad (6.5)$$

$$c = [0.885x_{\text{Hf}} + 7.936] \text{Å} . \quad (6.6)$$

These linear relationships are approximations, valid only within the homogeneity range of the Laves phase.

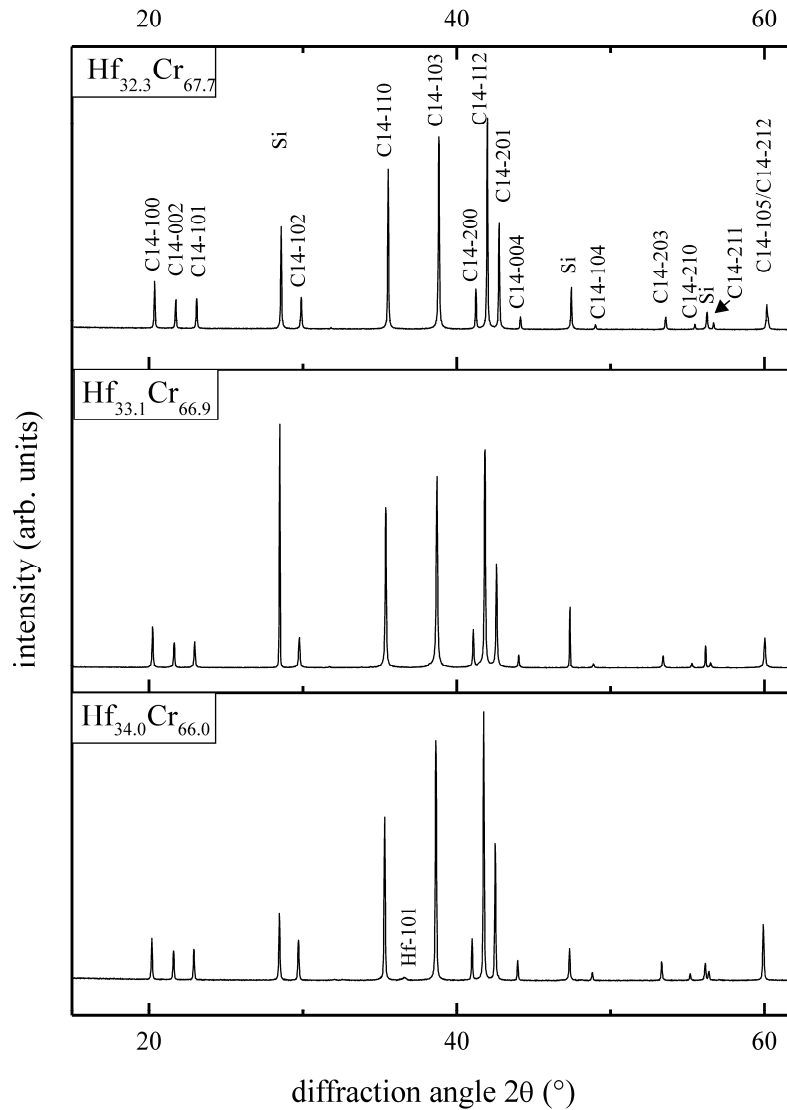


Fig. 6.6: X-ray diffraction patterns (CuK α 1-radiation) of specimen 1 ($\text{Hf}_{32.3}\text{Cr}_{67.7}$), specimen 2 ($\text{Hf}_{33.1}\text{Cr}_{66.9}$) and specimen 4 ($\text{Hf}_{34.0}\text{Cr}_{66.0}$) after annealing for 65 h at 1420°C and subsequent fast cooling to room temperature (the indicated compositions are the intended compositions; see Table 6.2). Silicon has been added as an internal standard (cf. section 6.3). All Laves phases are of C14 type. Note the presence of the minute 101 reflection of the Hf-rich solid solution in case of specimen 4.

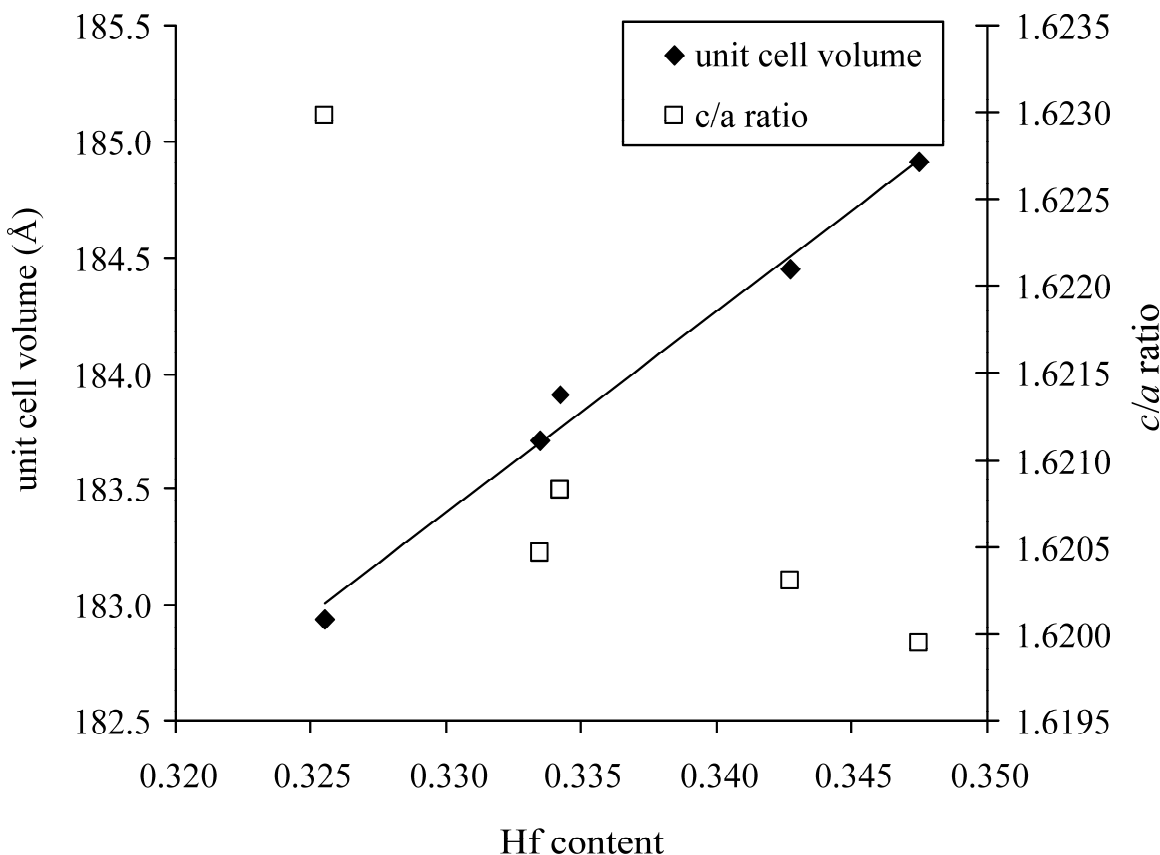


Fig. 6.7: Unit-cell volume and lattice parameter c/a ratio of C14-HfCr₂ specimens annealed at 1420°C and subsequently fast cooled down to room temperature. The composition values have been corrected for mass loss by chromium evaporation (cf. Table 6.2).

6.4.2 Structural evolution upon annealing of C14-HfCr₂ as function of temperature

The diffraction patterns of the stoichiometric specimen (specimen 3; cf. Table 6.2) annealed for 15 h at various temperatures $\leq 1300^\circ\text{C}$ can be compared in Fig. 6.8 with the diffraction pattern of the initial C14 structure (at the bottom of Fig. 6.8).

For the three lowest annealing temperatures, 1050°C, 1100°C and 1150°C, a decrease in height of the reflections pertaining to the hexagonal C14 structure exclusively (i.e. the so-called polytype reflections, $h - k \neq 3N$ and non-integer l_0 , cf. section 6.2.2) is observed. This reflection-height decrease is accompanied by an increase in reflection breadth in case of many of these reflections, so that the integrated diffracted intensity of

these reflections is not reduced considerably. The broadening of the $h - k \neq 3N$ and non-integer l_0 reflections in the XRPD diffraction patterns increases with the index $|l_0|$ (see section 6.2.2). This is compatible with the presence of stacking faults in the C14 structure. No additional reflections, with respect to the original C14 structure, can be detected, so that only formation of C15 from C14 upon annealing is compatible with the XRPD patterns: The C15 reflections coincide with the C14 reflections, except for the C15-004 reflection, which is however too weak to be observed. Further, the intensity of the 100 reflections decreases upon annealing compared to the intensity of the fundamental reflections.

A HRTEM investigation of the specimen annealed at 1150°C for 15 h confirms the conclusions drawn from the XRPD patterns. Intergrowth structures developed upon annealing at 1150°C, containing nanoscale C15 product lamellae in the C14 parent structure (Fig. 6.9). These C15 lamellae have only a thickness of several layer-sandwich units. Domains of C15 in twin orientation occur. In the SAD pattern, also in agreement with the XRPD observations, a broadening of the typical polytype C14-diffraction spots, i.e. with $h - k \neq 3N$ and non-integer l_0 , is observed. The intensity streaking along the rods of constant k in c^* direction is also a consequence of the stacking irregularities. Also spots belonging to the two C15 variants in twin orientation can be observed; these spots overlap with neighbouring C14 spots (cf. Figs. 6.4 and 6.5).

The XRPD patterns of the specimens annealed at 1225°C and 1300°C clearly show reflections pertaining to the C36 modification (Fig. 6.8, $l_0 = N \pm \frac{1}{4}$ (cf. Fig. 6.4b); these reflections did not occur for the specimens annealed at $1050^\circ\text{C} \leq T \leq 1150^\circ\text{C}$; see above). These reflections pertaining to the C36 modification are pronouncedly broadened, so that those with high values for l_0 are practically almost undistinguishable from the background signal. Because of the presence of C36, it is difficult to determine from the XRPD patterns whether C14 and/or C15 are present additionally: the C14 as well as the C15 reflections coincide with reflections pertaining to C36 (cf. Fig. 6.4 in section 6.2.1). Therefore HRTEM of a specimen annealed at 1300°C for 65 h was performed (Fig. 6.10). Stacking sequences corresponding to C36 and C15 crystal structures and to a 6H-type crystal structure were identified within a fine intergrowth structure. No C14-stacking sequences were found. Apparently, the initial C14 crystal had transformed completely to

the intergrowth structure shown in Fig. 6.10. In the corresponding SAD patterns, the broadening of the C36-diffraction spots ($I_0 = N \pm \frac{1}{4}$, cf. Fig. 6.4b) can be observed well.

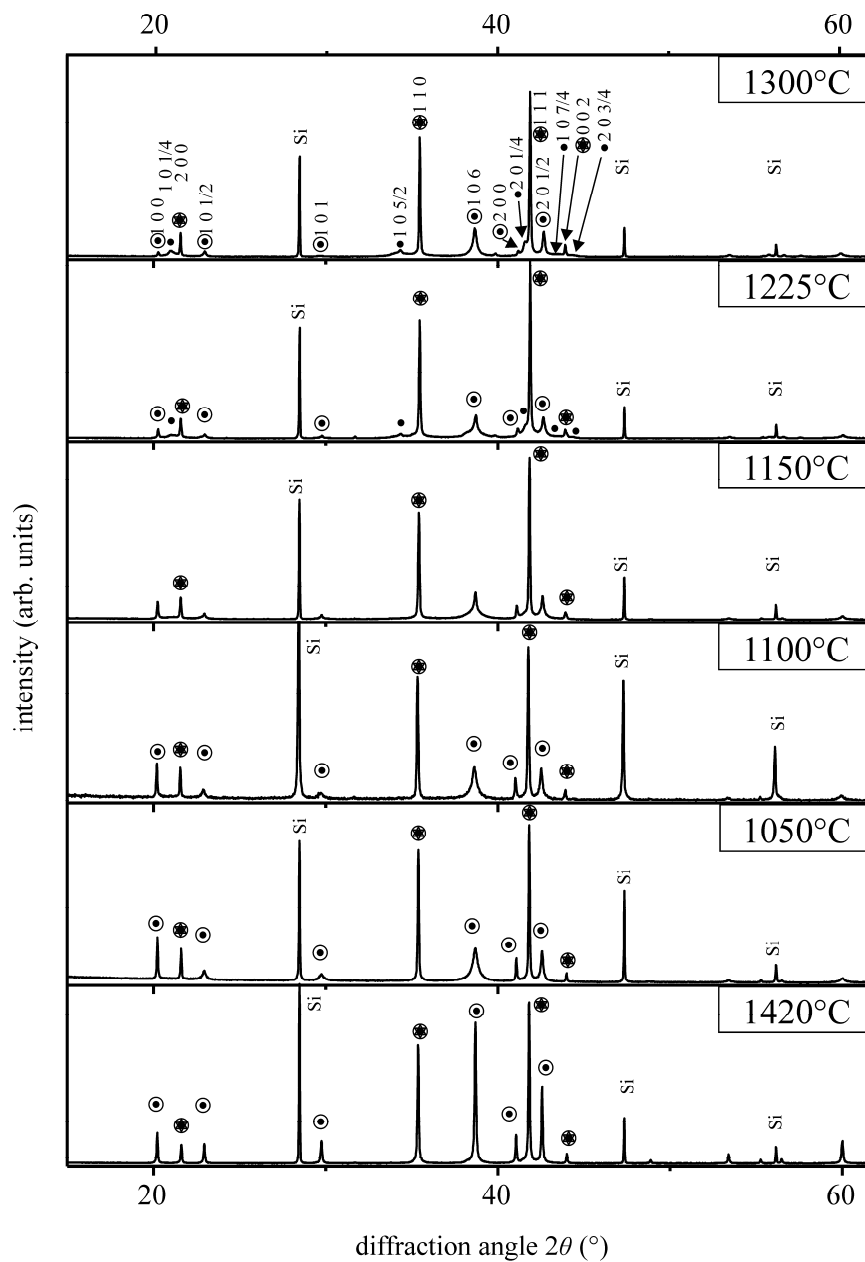


Fig. 6.8: X-ray diffraction patterns (CuK α 1-radiation) of stoichiometric HfCr₂ specimens produced from the C14-HfCr₂ specimen 3 (obtained by annealing at 1420°C for 60 h; diffraction pattern shown at the bottom) by annealing for 15 h at the temperatures indicated at the right. The reflections indices have been given as hkl_0 (see section 6.2.2). The polytype(s) from which the reflections can originate have been indicated by the same symbols as used in Figs. 6.4 and 6.5. Silicon has been added as an internal standard.

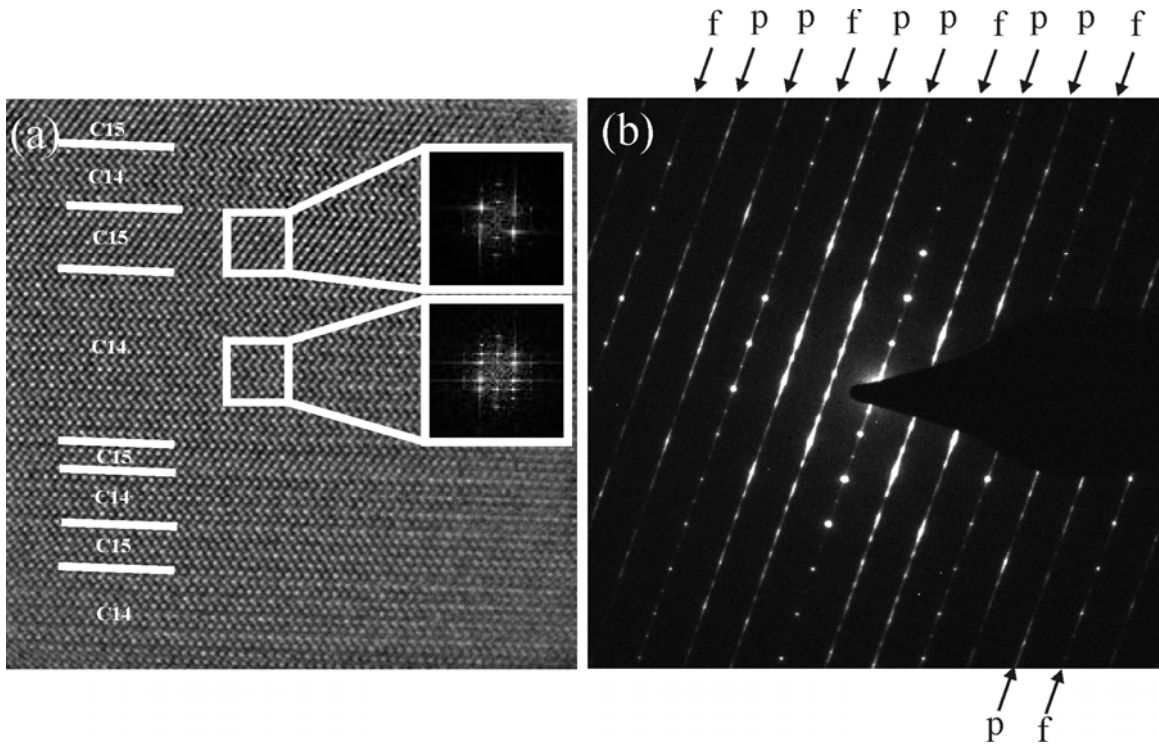


Fig. 6.9: (a) HRTEM image ([010]-zone (incident electron beam) axis) and (b) corresponding SAD pattern obtained from a specimen produced from specimen 3 (cf. Table 6.2) by annealing at 1150°C for 15 h. The Fast Fourier Transforms of the different domains (see insets in (a)) confirm the C14 and C15 crystal structures at the locations concerned. In the SAD pattern, the rods comprising the fundamental reflections ($h - k = 3N$) have been marked with “f”, while the rods comprising the polytype reflections have been indicated with “p” (cf. section 6.2.2 and Figs. 6.4 and 6.5).

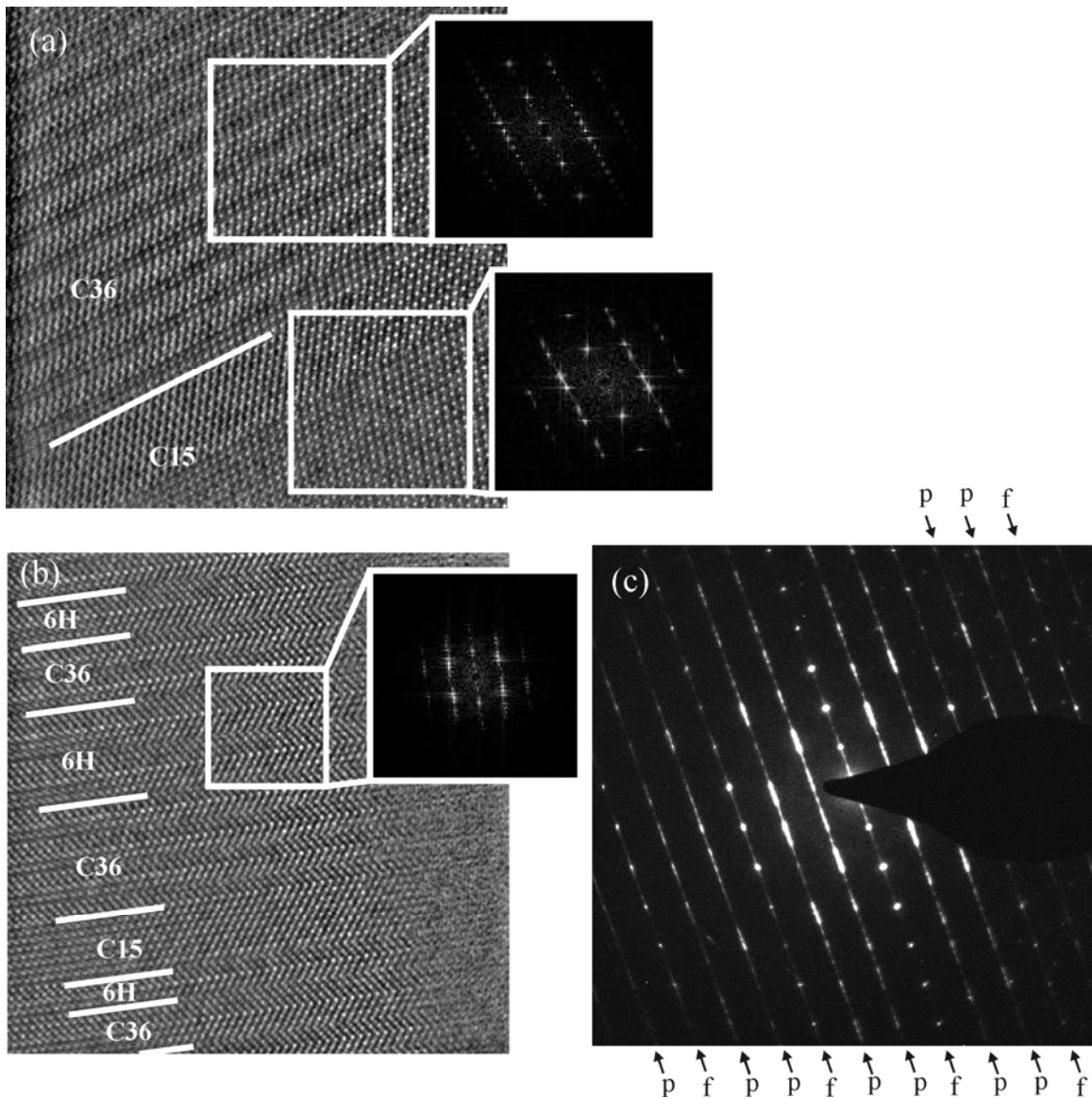


Fig. 6.10: (a,b) HRTEM images ([010]-zone (incident electron-beam) axis) and (c) corresponding SAD pattern obtained from a specimen produced from the stoichiometric specimen 3 (cf. Table 6.2) by annealing at 1300°C for 65 h. Comparison of the Fast Fourier Transforms of the different domains (see the insets in (a) and (b)) with simulated diffraction patterns confirms the presence of the C36, 6H and C15 polytypes. In the SAD pattern, the rods comprising the fundamental reflections ($h - k = 3N$ and integer l_0) have been marked with “f”, while the rods comprising the polytype reflections have been indicated with “p” (cf. section 6.2.2).

6.4.3 Structural evolution upon annealing of C14-HfCr₂ as function of composition

In case of the Hf-poor specimen 1 (cf. Table 6.2), the same product structures are formed upon annealing the parent C14 as in case of the stoichiometric specimen 3 (see section 6.4.2; cf. Fig. 6.11), with the difference that at 1225°C no C36 reflections were observed to emerge, but at 1300°C also C36 reflections were detected. Evidently, the temperature, above which formation of C36 takes place upon annealing, increases with decreasing Hf content.

In the diffraction patterns of the Hf-rich specimen 4 (cf. Table 6.2) C36 reflections are visible after the anneals at 1225°C and 1300°C (Fig. 6.12), similar to the stoichiometric sample. Tiny intensity maxima at the positions of the C36 reflections are even visible already after the anneal at 1150°C. In the diffraction patterns of samples annealed at 1225°C and 1300°C one additional reflection can be found. The appearance of this reflection is accompanied with a strong decrease of the characteristic 101 reflection of the Hf-rich solid solution (cf. section 6.4.1). This could indicate that in this temperature range a new Hf-rich phase is formed. Because no other additional reflections were detected, it is probable that this new phase has a Laves-phase related or Laves-phase type crystal structure. In that case, many reflections of the new phase coincide with reflections of the other Laves phases. The new phase could be the 6H-type Laves-phase polytype, which was already encountered in the HRTEM images of the stoichiometric sample after annealing at 1300°C for 65 h as part of the intergrowth structure (Fig. 6.10b). In that case, however, no reflections corresponding to this phase were present in the XRPD patterns. To identify the unknown phase appearing in the Hf-rich specimen upon annealing in the temperature range 1225°C – 1300°C, a Hf-rich specimen annealed for 15 h at 1300°C was investigated by HRTEM as well. Indeed, in some of the investigated crystallites (Fig. 6.13) relatively long (as compared to Fig. 6.10b) 6H sequences were observed in the intergrowth structures. Yet, most of the specimen consisted of C36; some thin C15 lamella and still untransformed C14 blocks were also observed. The corresponding SAD patterns did not unambiguously provide evidence for the presence of a 6H crystal structure by observation of corresponding discrete diffraction spots. Indeed, such 6H polytype diffraction spots are difficult to observe, because the

strongly broadened C36 (4H) polytype reflections will overlap with possible 6H polytype reflections.

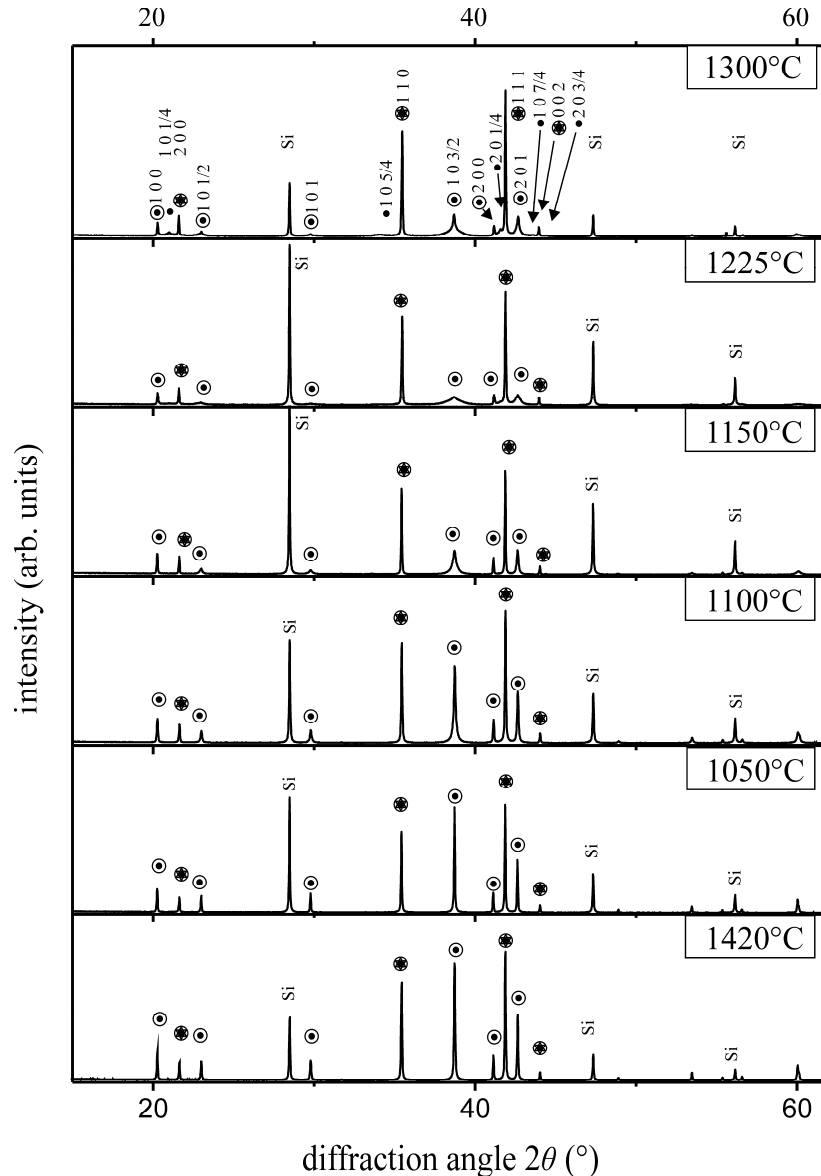


Fig. 6.11: X-ray diffraction patterns (CuK α 1-radiation) of Hf-poor HfCr₂ specimens produced from the C14-HfCr₂ specimen 1 (obtained by annealing at 1420°C for 60 h; diffraction pattern shown at the bottom) by annealing for 15 h at the temperatures indicated at the right. The reflections indices have been given as hkl_0 (see section 6.2.2). The polytype(s) from which the reflections can originate have been indicated by the same symbols as used in Figs. 6.4 and 6.5. Silicon has been added as an internal standard.

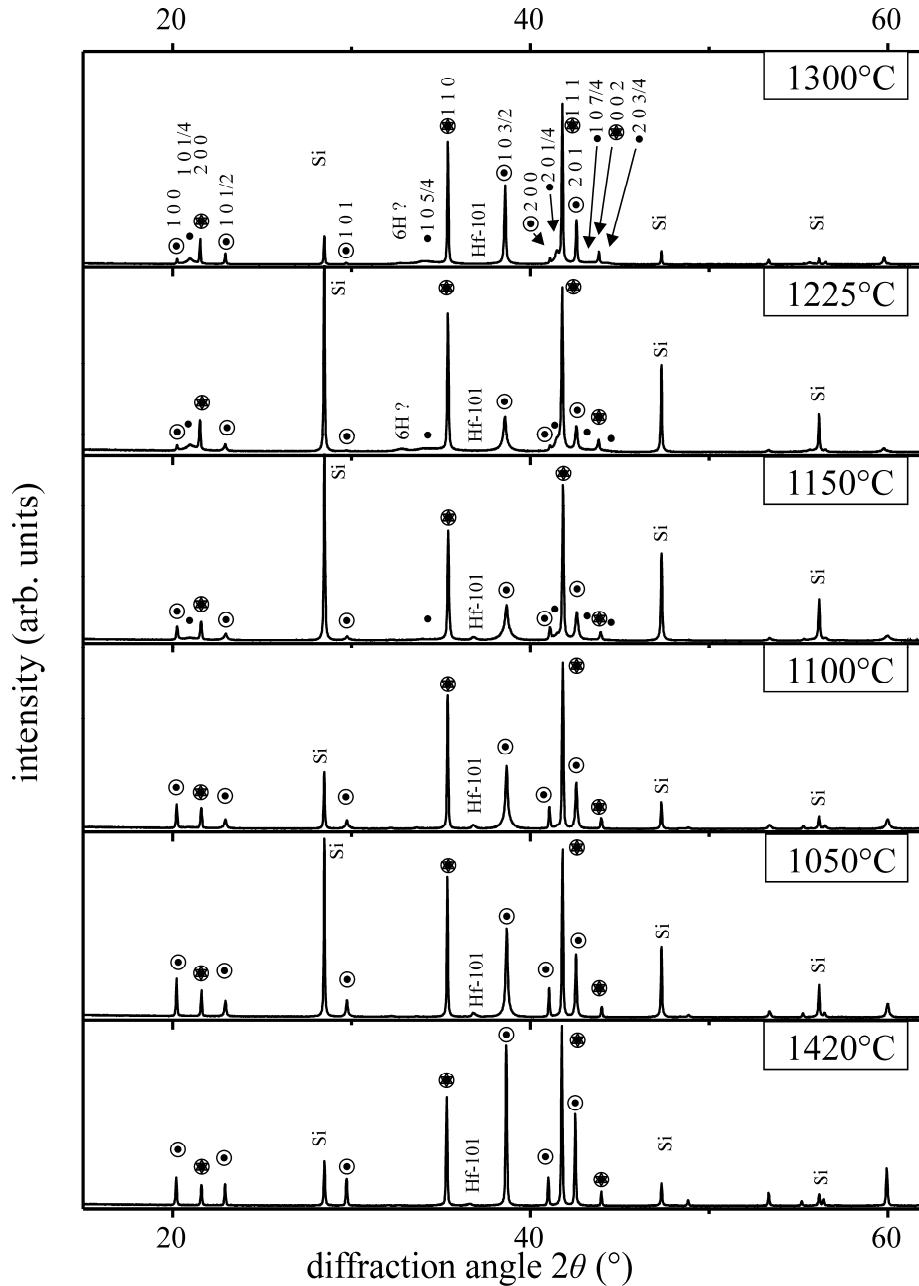


Fig. 6.12: X-ray diffraction patterns (CuK α 1 radiation) of Hf-rich HfCr_2 specimens produced from the C14- HfCr_2 specimen 4 (obtained by annealing at 1420°C for 60 h, diffraction pattern shown at the bottom) by annealing for 15 h at the temperatures indicated at the right. The reflections indices have been given as hkl_0 (see section 6.2.2). The polytype(s) from which the reflections can originate have been indicated by the same symbols as used in Figs. 6.4 and 6.5. Silicon has been added as an internal standard.

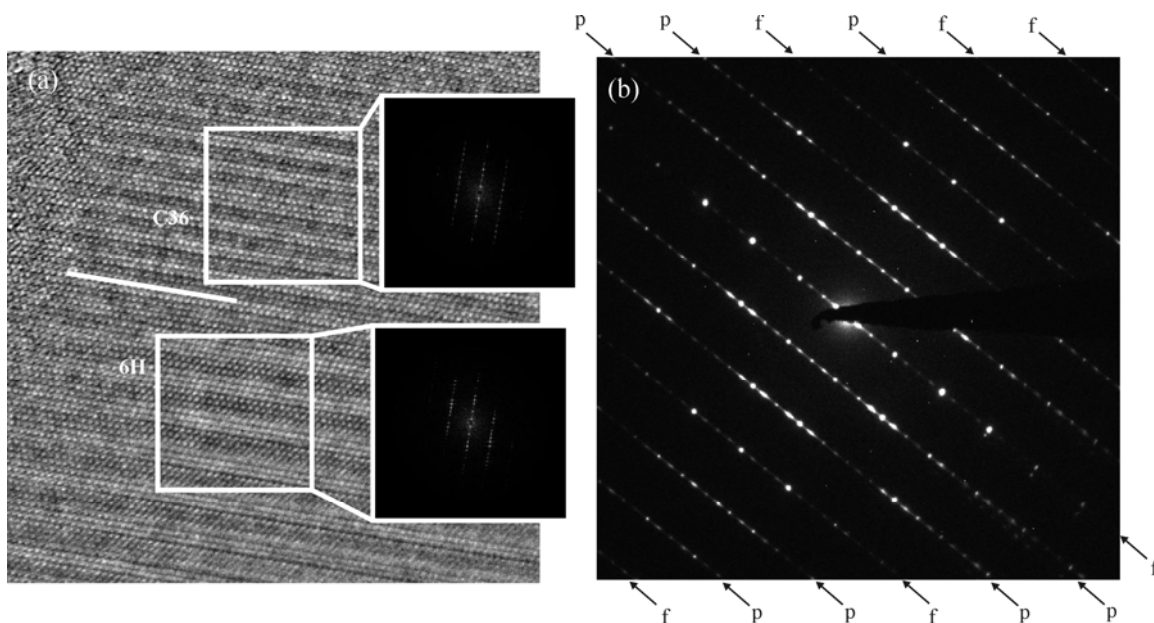


Fig. 6.13: (a) HRTEM image ([010]-zone (incident electron-beam) axis) and (b) corresponding SAD pattern obtained from a specimen produced from the Hf-rich specimen 4 (cf. Table 6.2) by annealing at 1300°C for 15 h. The Fast Fourier Transforms of the different domains (see the insets in (a)) confirm the presence of the C36, 6H and C15 polytypes (cf. sections 6.2.2 and Figs. 6.4 and 6.5). In the SAD pattern, the rods comprising the fundamental reflections ($h - k = 3N$ and integer l_0) have been marked with “f”, while the rods comprising the polytype reflections have been indicated with “p” (cf. section 6.2.2).

6.4.4 Structural evolution upon annealing of C14-HfCr₂ as function of time

To extract quantitative information on the progress of a Laves-phase transformation by HRTEM is difficult: the micrographs provide local information and thus do not represent statistical averages. On the other hand, the XRPD data do provide such statistically assured data. If the polytypic transformation would occur by discontinuous replacement/consumption of the parent crystallites and formation of a new microstructure consisting of product-phase crystallites, instead of by a gradual change in stacking sequence of the parent Laves-phase crystallites, the parent and product phase fractions

would be proportional with the integrated intensities of all corresponding diffraction lines in the XRPD patterns and thus, the “fraction transformed”, varying from 0 to 1, could be determined straightforwardly from intensity ratios of parent and product phase diffraction lines. However, in the present case characterized by intergrowth structures for intermediate stages of transformation, coherency of diffraction effects of related polytypes in the same intergrowth structure of a crystallite (see discussion in section 6.2.2) obstructs quantitative determination of the formation of a certain polytype in the way describes immediately above. In the present work, two simple scalar quantities, the ratio of the integrated intensities of *selected* reflections and the normalized c/a lattice-parameter ratio have been used as measures for the progress of the transformation (see what follows).

6.4.4.1 Ratio of integrated intensities of selected reflections

A possible method to trace a phase transformation is by tracking the (integrated) intensity of a XRPD reflection, which changes its (integrated) intensity during the phase transformation due to change of the amount of phase represented by the diffraction line. In case of the C14 \rightarrow C15 transformation of Laves phases, the $hkl_0 = 100$ reflection (note that in this case $hkl_0 = hkl = 100$) is an interesting candidate, because (i) it occurs for the C14 phase but has nil intensity for the C15 phase, and because it is (hardly) not affected by reflection broadening because $l_0 = 0$ (the line broadening in reciprocal space is perpendicular to the diffraction vector and does not occur in the XRPD patterns, cf. discussion in section 6.2.2). As the total diffracted intensity of an XRPD pattern is scaled by extrinsic factors such as the specimen mass or thickness, it is necessary to normalize the intensity of the 100 reflection. To this end, a fundamental reflection ($h - k = 3N$) can be applied as “internal” standard, because the fundamental reflections do not change their intensity (and remain unbroadened) upon polymorphic transformation between various Laves-phase polytypes (cf. section 6.2.2). To avoid effects of diffraction-angle dependent variations in intensity (e.g. by surface roughness of the specimen and by sample transparency), the internal standard reflection should be located at diffraction angles close to the 100 reflection of the C14 polytype. Thus the $hkl_0 = 001$ fundamental reflection (i.e.

$hkl = 003$ for C14; $hkl = 003$ for C15 (hR unit cell; cf. section 6.2.2 and Fig. 6.3)) seems to be suitable.⁸

Hence, a normalized intensity of the 100-XRPD reflection, \tilde{I}_{100} , is defined by

$$\tilde{I}_{100} = \frac{I_{hkl_0=100}}{I_{hkl_0=001}}, \quad (6.7)$$

with $I_{hkl_0=100}$ as the intensity of the $hkl_0 = 100$ polytype reflection originating from C14 only and $I_{hkl_0=001}$ as the intensity of the $hkl_0 = 001$ fundamental reflection originating from the whole intergrowth structure/crystallite.

If the two phases within a crystallite transforming from C14 to C15 would diffract incoherently, the integrated intensity of the XRPD reflection corresponding to C14 exclusively should decrease linearly with the decrease of C14-phase fraction. However, because such intergrowth structures diffract coherently (as discussed in section 6.2.2), not the integrated intensity but the structure factor associated with the reflection pertaining exclusively to C14 decreases linearly with the C14-phase fraction. Hence, because the intensity of a reflection is proportional to the square of the structure factor, F , the intensity of the C14 reflection decreases parabolically with the phase fraction of C14, f_{C14} :

$$\tilde{I}_{hkl_0=100} \sim F_{hkl_0=100}^2 \sim f_{C14}^2, \quad (6.8)$$

In case in a C14 crystallite C36 phase is formed instead of C15, the 100 reflection does not disappear, but its intensity reduces to $1/4$, as shown by straightforward structure-factor calculations (note that the $hkl_0 = 001$ fundamental reflection, used for normalization (cf. Eq. (6.7)), corresponds with $hkl = 004$ in case of the C36 polytype).

The normalized intensity of the $hkl_0 = 100$ reflection, originating from the C14 phase, $\tilde{I}_{hkl_0=100}$, has been plotted versus annealing time for the different annealing temperatures and the specimens of different composition in Fig. 6.14. Despite some

⁸ In the cubic setting of C15 (cf. section 6.2.2 and Fig. 6.3) there are 8 $hkl = 111$ reflections. Two of these reflections are fundamental reflections: $hkl = 003$ and $hkl = 00\bar{3}$ in the hR setting, or indicated as $hkl_0 = 001$ and $hkl_0 = 00\bar{1}$, respectively. The other six of the 8 $hkl = 111$ (cubic setting) are polytype reflections: $hkl = 102$ -type in the hR setting, or indicated as $hkl_0 = 1\ 0\ 2/3$ -type. These six polytype reflections occur at the same position as the $hkl_0 = 001$ type fundamental reflections. The $hkl_0 = 1\ 0\ 2/3$ -type reflections are pronouncedly broadened ($h - k \neq 3N$; cf. section 6.2.2), so that their contribution to the integrated intensity is eliminated upon removal of the (apparent) background intensity in the procedure for determination of the integrated intensity of the sharp $hkl_0 = 001$ type fundamental reflections.

scatter of the data points, a decrease of $\tilde{I}_{hkl_0=100}$ with annealing time can be observed. This is consistent with the formation of C15 or C36 from C14 upon annealing as observed in the X-ray diffraction patterns and HRTEM micrographs (sections 6.4.2 and 6.4.3). The intensity decrease proceeds more rapidly in case of both the stoichiometric specimen and the Hf-rich specimen as compared to the Cr-rich sample. For the higher annealing temperatures and the longest annealing times, a plateau (minimum) value for $\tilde{I}_{hkl_0=100}$ is approached (the value for the longest annealing time at 1150°C in case of the Hf-rich specimen deviates strongly and may be regarded as an outlier).

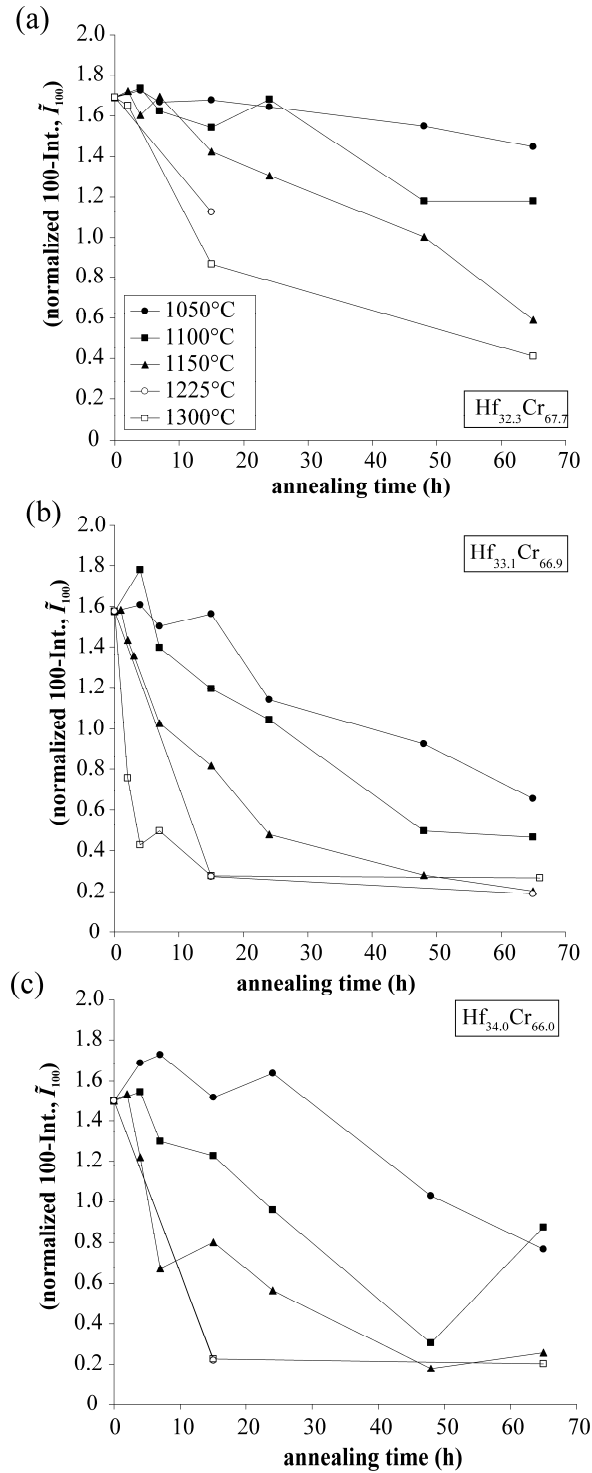


Fig. 6.14: Evolution of the normalized integrated intensity of the $hkl_0 = 100$ -reflection as function of annealing time at the temperatures indicated for the HfCr₂ specimens of initially C14-crystal structure, (a) the Hf-poor specimen 1, (b) the stoichiometric specimen 3 and (c) the Hf-rich specimen 4 (cf. Table 6.2).

6.4.4.2 Normalized c/a ratio

A characteristic quantity for hexagonal structures is the ratio of the height of the hexagonal unit cell, i.e. the lattice parameter c , and the edge length of the hexagonal base of the unit cell, i.e. the lattice parameter a . This c/a ratio equals 1.633 for ideal close packed (single element) hcp structures, where two close packed atomic planes are located within one unit cell. In reality, usually the c/a ratio deviates for hcp structures more or less from this value, which has consequences for the properties, e.g. for the mode of plastic deformation. Also for C14-Laves phases (where, instead of simple close packed mono-atomic layers, the complex layer-sandwich units are stacked on top of each other) the c/a ratio varies around 1.633. In case of C14-HfCr₂, the c/a ratio is smaller than 1.633 (see section 6.4.1).

Also for the polytypes other than C14 a c/a ratio can be calculated. The value of c/a depends on the number N_L of layer-sandwich units per unit cell of the respective polytype (see section 6.2.2 and Table 6.1). In general $c/a = N_L c_0/a$ holds (cf. section 6.2.2). Hence, a general, normalized c/a ratio, r , describing the *ratio of the spacing between the layer-sandwich units and the dimensions of 2D-hexagonal unit mesh of the layer-sandwich units*, is defined by

$$r = \frac{1}{N_L} \frac{c}{a} = \frac{c_0}{a}, \quad (6.9)$$

where c and a are the lattice parameters of the general hexagonal unit cell and c_0 is the spacing between two layer-sandwich units. The cubic symmetry of the C15 polytypes implies that $c/a = 6^{1/2} = 2.4495$ and thus $r = (2/3)^{1/2} = 0.8165$ holds *exactly* (independent of composition; see section 6.2.2 for the relation of the cubic lattice parameter a' with c/c_0 and a), whereas c/a of the other non-cubic Laves-phase polytypes usually deviates from this value (in case of C14-HfCr₂, it is smaller, see section 6.4.1) and depends on composition.

As a consequence, if the stacking sequence of a Laves-phase structure changes gradually from C14 to C15 (gradually in terms of the relative fractions of these phases in an intergrowth structure), a gradual change of r from the characteristic value observed for C14 towards $(2/3)^{1/2} = 0.8165$ is expected, recognizing the coherent nature of the diffraction by an intergrowth structure (cf. section 6.2.2). Also upon formation of C36, or

other polytypes, a change of r upon annealing should be observed. If one attributes the difference between the value of r pertaining to the C14 phase and the value of $r = (2/3)^{1/2}$ pertaining to the C15 phase to the gradual emergence of cubic-type stacking (c) in original C14, characterized by pure hexagonal-type stacking (h , for Jagodzinski symbols and fraction of cubic stacking, see Table 6.1), then the value of r for C36 is expected to assume a value intermediate between those of C14 and C15.

Plots of the normalized c/a axial ratio r (cf. Eq (6.9)) as function of annealing time (for the different annealing temperatures) are shown for the stoichiometric specimen in Fig. 6.15b. Indeed (see above) upon annealing the value of r approaches the value for cubic C15, 0.8165. For none of the annealing temperatures, the ideal value for cubic C15 is reached, which is compatible with the observation in all diffraction patterns of reflections characteristic for hexagonal Laves-phase modifications (C14 and/or C36) remaining/occurring (even) for the longest annealing times. The initial increase of r is faster at the higher annealing temperatures. In case of the annealing at 1225°C and 1300°C, a plateau value is reached quickly. In case of the non-stoichiometric specimens, the general observations are similar to those made for the stoichiometric one (see Figs. 6.15a and c). For the Hf-rich specimen the value of r as function of annealing time/temperature behaves similarly to that observed for the stoichiometric specimen. In case of the Hf-poor specimen, the increase of r occurs much slower.

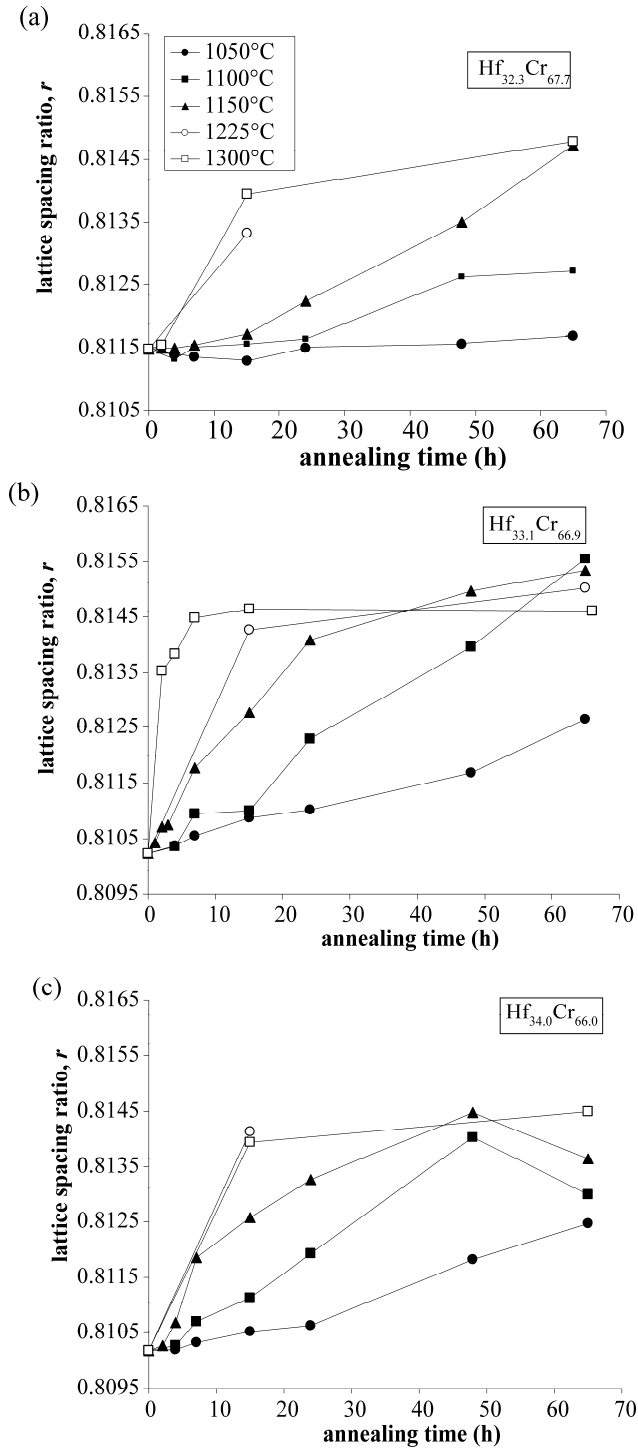


Fig. 6.15: Evolution of the lattice-spacing ratio r as function of annealing time at the temperatures indicated for the HfCr_2 specimens of initially C14- HfCr_2 crystal structure, (a) the Hf-poor specimen, (b) the stoichiometric specimen and (c) the Hf-rich specimen (cf. Table 6.2).

6.5 Discussion

6.5.1 The initial structure: C14-HfCr₂

By annealing of as-cast samples at 1420°C for 60 h and subsequent fast cooling to room temperature, the C14-high temperature modification of HfCr₂ could be retained (Fig. 6.6, section 6.4.1). The increase in unit-cell volume with increasing Hf content, at both sides of the stoichiometric composition (Fig. 6.7, section 6.4.1), is compatible with an antisite-occupation mechanism for accommodating deviations from the ideal HfCr₂ stoichiometry, i.e. the larger Hf atoms replace the smaller Cr atoms on the *B* sublattice for the Hf-rich Laves phase, whereas the smaller Cr atoms replace the larger Hf atoms on the *A* sublattice for the Hf-poor Laves phase (cf. section 6.2.1). Such antisite-occupation mechanisms have been observed for many binary transition-metal Laves phases [32]. The *c/a* ratio decreases with increasing Hf content (Fig. 6.7, section 6.4.1); it is closest to the “ideal” value of 1.633 (cf. section 6.4.4.2) for the Hf-poor specimens. Remarkably, the decrease of *c/a* with increasing Hf content is more pronounced on the Hf-poor than on the Hf-rich side of stoichiometry (Fig. 6.7). The decrease in *c/a* ratio from the Hf-poor side to the Hf-rich side is, however, very small: only about 0.2 %. Note that the change in the normalized *c/a* ratio upon annealing due to the transformation of C14 to other polytypes (sections 6.4.2 – 6.4.4) is considerably larger (up to 0.65 %; see Fig. 6.15)

6.5.2 Structural changes upon annealing; phase map for HfCr₂

The structural changes induced upon annealing of the retained C14-HfCr₂ Laves phase at temperatures of 1300°C and below, as observed in the XRPD patterns, HRTEM images and the SAD patterns, indicate that the polytypic phase transformations do not involve complete consumption of the initial C14 polytype and that the polytypes C36 or C15 do not develop in a reconstructive way, but by gradual changes in the (layer-sandwich unit) stacking sequence within a C14 Laves-phase crystal thereby forming intergrowth structures. The two types of layers (the *AB₃A* layer-sandwich units and the *B* single-layer units; cf. Fig. 6.2) thus remain structurally unchanged upon the transformation. Consequently, in the XRPD patterns and the SAD patterns certain reflections remain

unchanged: the $h - k = 3N$ fundamental reflections. Other reflections (the polytype reflections), in particular those emerging upon transformation, are distinctively broadened as a consequence of the intergrowth structures being composed of lamellae of nanosized thickness. In an intergrowth structure lamellae belonging to the same polytype are laterally displaced with respect to each other, which leads to broadening of the non-fundamental reflections (see section 6.2.2). As already remarked in section 6.4.2, the broadening is different from that observed for product C36 Laves phases in other systems formed from parent C14 phases [33] (cf. chapter 3). In these C36-Laves phases, the C36 polytype formed an intergrowth structure with C14 and 6H stacking sequences, but C15 sequences did not occur [33] (cf. chapter 3): as a consequence, in that case selective broadening of non-fundamental reflections with $l = 4M + 2$ ($l_0 = R/2$, and integer R) has been observed.

A scheme (phase map) summarising the development of phases, as detected by XRPD and HRTEM in the present work upon annealing of C14-HfCr₂ as function of composition and temperature, is presented in Fig. 6.16. The C14 phases (still) found after annealing at 1300°C and below are regarded as residual C14 and thus not shown in the figure. The 6H stacking variant, which occurs upon annealing at 1200°C and 1300°C in case of the stoichiometric and, more pronouncedly, i.e. probably even detectable in XRPD (see discussion in section 6.4.3), in case of the Hf-rich phase, is also not shown in the figure, because, as shown by the present authors in Ref. [33] (cf. chapter 4), this polytype can be regarded as a special type of fault in C36. The phase map shown in Fig. 6.16 should be understood as a precursor of a detailed phase diagram for the temperature/composition range concerned in the Hf-Cr system. It follows that a certain temperature range exists, where the C36 modification of HfCr₂ is formed. Because this C36 phase is only observed together with C15, this C36 phase probably is an off-stoichiometric, Hf-rich phase, compatible with the existence of a C36-C15 two-phase region, which opens towards increasing Hf-content.

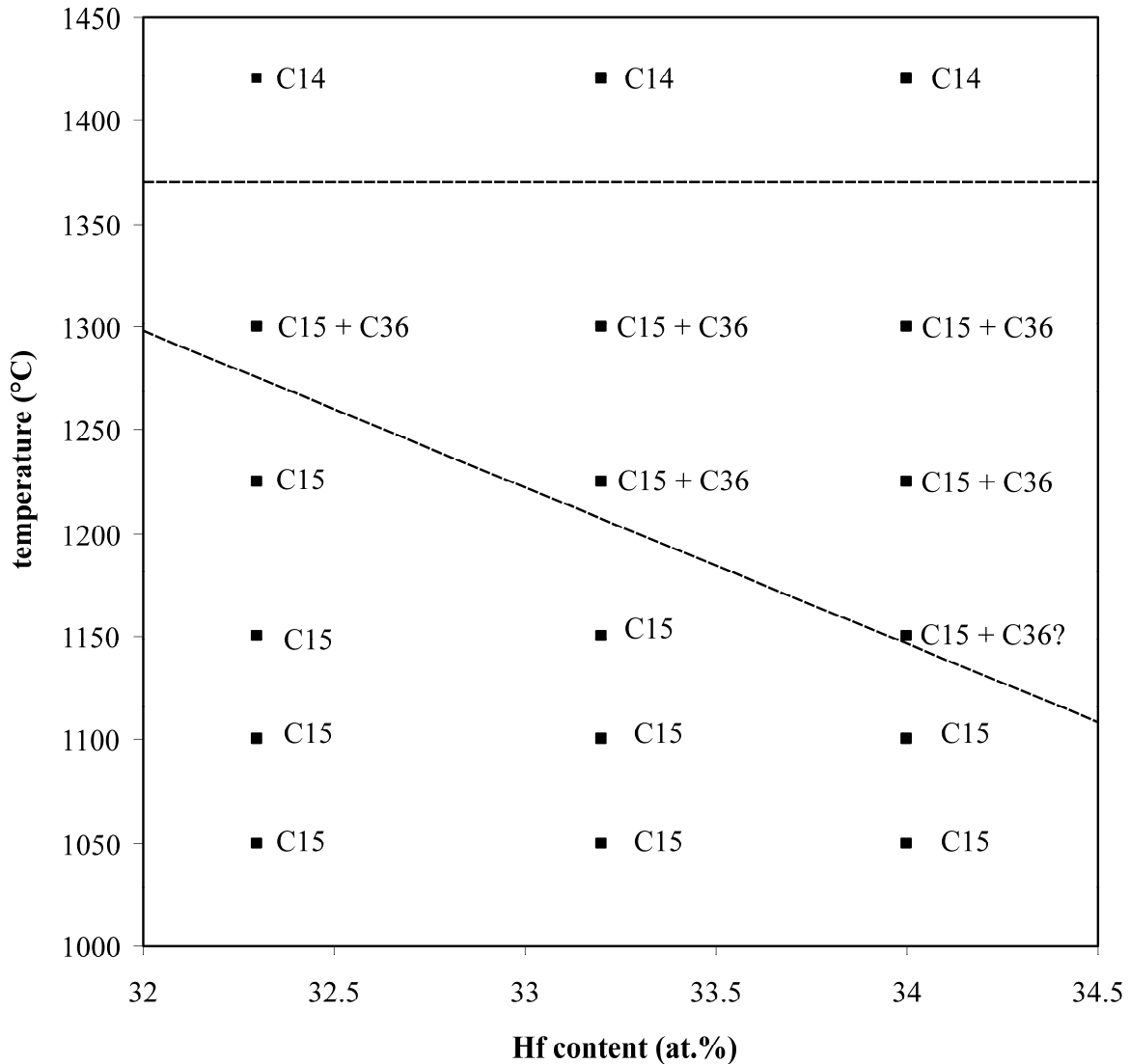


Fig. 6.16: Phase map for the Laves-phase part of the Hf-Cr system, as deduced from the X-ray and HRTEM investigations performed in this work, for C14-HfCr₂ specimens annealed at various temperatures.

The present result partially contradicts an earlier TEM work [19], where, by evaluation of SAD patterns, for the temperature range from 1000°C – 1200°C no C15 phase has been reported, but C36 phase was observed in case of an Hf-poor alloy.

Due to sluggish transformation kinetics, emergence/preservation of metastable phases is possible. Thus the C36 phase, as well as the 6H phase (i.e. faulted C36 [33], cf. chapter 4), could be metastable, forming under the observed conditions, regarding specimen composition and temperature, for kinetic reasons. However, if this would be the

case, formation of C36 would be even more probable at lower annealing temperatures, where formation of metastable phases is more probable. This contrasts with results obtained in the present work: only C15 phase is formed at temperatures below 1150°C. The occurrence of C15 as a stable low-temperature modification, as indicated by the present experimental results, is compatible with results of ab-initio ground-state calculations [20]. The location of the “occurrence fields” for different Laves-phase polytypes of the Hf-Cr system as given in Fig. 6.16 seems reasonable also because the proposed phase map is in qualitative agreement with the well-established phase-stability fields for the C15, C36 and C14 phases of the Ti-Cr system [34].

6.5.3 The degree of transformation

The basic idea behind the approaches to determine a value for the degree of transformation, as proposed in section 6.4.4, is to describe the intergrowth structure constituted of separate Laves-phase polytypes by its average structure, i.e. via F_{100} (Eqs (6.7) and (6.8)) and r (Eq. (6.9)). The results presented in Figs. 6.14 and 6.15 show that the degree of transformation approaches a plateau value at the higher annealing temperatures in case of the stoichiometric and the Hf-rich specimens. The transformation rate appears to be lower in case of the Hf-poor specimen.

It cannot be excluded that different phase constitutions of the intergrowths may correspond to similar values for \tilde{I}_{100} and r . E.g. in case of the stoichiometric sample, similar values for \tilde{I}_{100} and r were obtained for the 65 h anneals at 1150°C and 1300°C, although HRTEM and XRPD clearly showed that the resulting microstructure is C15 + C36 at 1300°C and (residual) C14 + C15 at 1150°C. A kinetic analysis of a specific transformation obviously implies that parent and product phases are nonvariant in the temperature-time window investigated. Thus, in the present case, for the C14 → C15 transformation the temperature range should be restricted to 1050°C – 1150°C. This kinetic analysis is performed in the following chapter, cf. Ref. [35].

6.6 Conclusions

- (1) A (linear) relationship of unit-cell volume of the C14-HfCr₂ Laves phase and composition has been established.
- (2) Annealing of the C14 Laves-phase specimens at temperatures below 1300°C induces phase transformations towards other Laves-phase polytypes, which proceed by gradually changing the layer-sandwich unit stacking sequence within the Laves-phase crystallites, realized by the synchroshear mechanism, leading to intergrowth microstructures (HRTEM and XRPD evidence), i.e. the phase transformations are not of reconstructive nature.
- (3) The thus produced Laves-phase microstructures show an *hkl*-dependent reflection broadening which can be fully explained by coherent diffraction of the entire intergrowths comprising irregularities of the stacking sequences in the intergrowths (constant phase shifts). A unified description of the diffraction by these intergrowth structures is possible departing from an “average” crystal structure for the Laves phases considered.
- (4) In case of the stoichiometric composition, the C15 modification is formed upon annealing at and below 1150°C. At 1225°C and 1300°C, C36 and C15 are formed. The lower-temperature limit for the additional formation of the C36 phase is lower in case of a Hf-rich sample and higher in case of a Hf-poor sample. In some cases, formation of 6H-type stacking sequences (to be conceived as a special type of layer-stacking fault in the C36 phase) is observed. As a result, a phase map for the Laves-phase part of the Hf-Cr system has been proposed.
- (5) To characterize the polytypic transformation, two parameters can be deduced from the diffraction patterns: (i) The intensity of the 100 polytype reflection (observed in the presence of (original or remaining) C14), normalized with respect to the 001 fundamental reflection, and (ii) the ratio of the distance between the Laves-phase layer-sandwich units and the inter-atomic spacing within these layer-sandwich units, i.e. the normalised *c/a* ratio which pertains to the “average” crystal structure of the intergrowth microstructure. The transformed fraction for kinetic evaluation of a phase transformation can thus be obtained also

in the current case, where a simple (e.g. Rietveld-like) phase analysis assuming linear superposition of the X-ray patterns of incoherently diffracting domains is not possible (see (3) above).

6.7 Acknowledgements

The authors are grateful to Mr. Thomas Meisner (Max Planck Institute for Metals Research) for indispensable collaboration during alloy preparation. This work has been performed within the framework of the Inter-Institutional Research Initiative “The Nature of Laves Phases” funded by the Max Planck Society.

6.8 References

- [1] G. Sauthoff, "Intermetallics" (1995) Weinheim, VCH.
- [2] C.W. Allen, P. Delavignette and S. Amelinckx, *Phys. Status Solidi A* 9 (1972) 237.
- [3] C.W. Allen and K.C. Liao, *Phys. Status Solidi A* 74 (1982) 673.
- [4] P.M. Hazzledine and P. Pirouz, *Scr. Metall. Mater.* 28 (1993) 1277.
- [5] K.S. Kumar and P.M. Hazzledine, *Intermetallics* 12 (2004) 763.
- [6] J.D. Livingstone and E.L. Hall *J. Mater. Res.* 5 (1990) 5.
- [7] Y. Liu, J.D. Livingstone and S.M. Allen, *Metall. Trans. A* 23 (1992) 3303.
- [8] F. Stein, M. Palm and G. Sauthoff, *Intermetallics* 13 (2005) 1056.
- [9] J. Aufrecht, A. Leineweber, A. Senyshyn and E.J. Mittemeijer, *Scripta Mater.* 62 (2010) 227.
- [10] A.L. Kazantzis, T.T. Cheng, M. Aindow and I.P. Jones, *Inst. Phys. Conf. Ser.* 147 (1995) 511.
- [11] T. Yokosawa, K. Soederberg, M. Bostroem, D. Gruener, G. Kreiner and O. Terasaki, *Z. Kristallogr.* 221 (2006) 357.

- [12] J. Aufrecht, A. Leineweber and E.J. Mittemeijer, *Mater. Res. Soc. Symp. Proc.* 1128 (2008) 481.
- [13] M. Venkatraman and J.P. Neumann, *Bull. Alloy Phase Diag.* 7 (1986) 570.
- [14] S.P. Alisova, P.B. Budberg and K.I. Shakhova, *Sov. Phys. Crystallogr.* 9 (1964) 78.
- [15] O.N. Carlson and D.G. Alexander, *Journal of less-common metals* 15 (1968) 361.
- [16] Y.A. Kocherzhinskiy, V.Y. Markiv and V.V. Pet'kov, *Russian Metallurgy* 1 (1973) 134.
- [17] N.B. Budberg and S.A. Minaeva, *Krist. Strukt. Svoitva Met. Splavov* (1978) 48.
- [18] K.S. Kumar and D.B. Miracle *Intermetallics* 2 (1994) 257.
- [19] K.S. Kumar and P. Hazzledine, *Mater. Res. Soc. Symp. Proc.* 364 (1995) 1383.
- [20] X.Q. Chen, W. Wolf, R. Podlucky and P. Rogl, *Phys. Rev. B: Condens. Matter* 71 (2005) 174101.
- [21] F. Laves and H. Witte, *Metallwirtschaft* 14 (1935) 645.
- [22] H. Jagodzinski, *Acta Crystallogr. Sect. A: Found. Crystallogr.* 2 (1949) 201.
- [23] L.S. Ramsdell, *Am. Mineral.* 32 (1947) 64.
- [24] M.A. Barrett and T.B. Massalski, "The structure of metals" (1966) McGraw-Hill, New York.
- [25] K. Dornberger-Schiff, *Abh. Dt. Akad. Wiss. C* 3 (1964).
- [26] B.E. Warren, "X-ray diffraction" (1990) New York, Dover.
- [27] M. Leoni, *Z. Kristallogr.* 223 (2008) 561.
- [28] B. Prasad and S. Lele, *Acta Crystallogr. Sect. A: Found. Crystallogr.* 26 (1970) 54.
- [29] E. Michalski, S. Kaczmarek and M. Demianiuk, *Acta Crystallogr., Sect. A: Found. Crystallogr.* 44 (1988) 650.
- [30] C. Own, Dissertation. (2005) Evanston, Illinois, Northwestern University
- [31] A. Kverneland, V. Hansen, R. Vincent, K. Gjonnes and J. Gjonnes, *Ultramicroscopy* 106 (2006) 492.
- [32] J.H. Zhu, L.M. Pike, C.T. Liu and P.K. Liaw, *Acta Materialia* 47 (1999) 2003.
- [33] J. Aufrecht, W. Baumann, A. Leineweber, V. Duppel and E.J. Mittemeijer *Phil. Mag.* 90 (2010) 3149.

- [34] Baumann, W., Leineweber, A. and Mittemeijer, E. J. (2010). *To be published.*
- [35] Aufrecht, J., Leineweber, A. and Mittemeijer, E. J. (2010). *to be published.*

7. Polytypic transformations of the HfCr₂ Laves phase - Kinetics of the polymorphic C14 → C15 transformation

Jochen Aufrecht, Andreas Leineweber and Eric Jan Mittemeijer

The polymorphic phase transformation C14 → C15 of the HfCr₂-Laves phase has been traced using the normalized intensity of the 100 reflection of the C14 phase and, alternatively, using the ratio of the inter-layer spacing and in-planar spacing of the layer-sandwich unit layers as main constituents of the Laves phases, which *tracing parameters* allow determination of the degree of transformation. The effective activation energy of the phase transformation has been determined from isothermal annealing experiments for three alloys of different composition within the homogeneity range of the HfCr₂ phase using the equivalent-time method. For the stoichiometric alloy a value of 235 - 240 kJ/mol for the effective activation energy of the C14 → C15 transformation has been obtained. The corresponding values for the non-stoichiometric alloys vary from 183 kJ/mol to 306 kJ/mol; the activation energy increases with decreasing Hf content. The magnitude of the values obtained for the effective activation energy indicates that jumps of individual atoms determine the kinetics of the polytypic transformation C14 → C15 of the HfCr₂-Laves despite the shear-character (glide of synchro-Shockley partial dislocations) of the transformation mechanism.

7.1 Introduction

Laves phases constitute the largest group of intermetallic phases and are promising candidate materials for high-temperature structural applications [1]. For tuned alloy development it is of crucial importance to understand fundamentally the microstructural evolution upon phase transformations in Laves-phase alloys. Investigations on the kinetics of the polytypic phase transformations, which occur in several Laves phases as a function of temperature and time, are especially interesting: These polytypes differ only in stacking sequence of so-called layer-sandwich units and the polytypic phase transformations are brought about by glide along these layers of an ordered array of a certain type of partial dislocations, the so-called synchro-Shockley partial dislocations [2-6] (cf. chapter 4). Synchro-Shockley partial dislocations are also involved in the plastic deformation of the Laves phases [7]. This role of glide of synchro-Shockley partial dislocations both in realising plastic deformation and establishing the polytypic phase transformations arises special interest as the operating shearing mechanism parallels that governing the hcp \rightleftharpoons fcc (martensitic) transformation in Co, albeit, in that case realized by glide of “normal” Shockley partial dislocations [8].

For the present study, the HfCr₂ Laves phase with its polytypic phase transformations [9] has been selected. The crystal-structure evolution upon annealing of the retained (upon fast cooling) C14 high-temperature modification of HfCr₂, as a function of composition, temperature and time, has been investigated using X-ray powder diffraction (XRPD) and high-resolution electron microscopy (HRTEM) in a first part of this work [10]. In this first part also the extraction of two scalar parameters has been described, which can be identified as parameters characterising the progress (degree) of the phase transformation: (i) the relative intensity of the 001 reflection pertaining to the C14 phase and (ii) a normalized c/a (lattice-spacing) ratio. In the present study the evolution of both these parameters has been traced as a function of time for different annealing temperatures and different alloy compositions. On this basis a quantitative description has been given of the transformation kinetics, in particular the activation energy, of the polytypic C14 \rightarrow C15 phase transformation in HfCr₂.

7.2 Theory

7.2.1 Polytypic transformations of the HfCr_2 Laves phase

By annealing of HfCr_2 specimens of different alloy compositions at 1420°C and subsequent relatively fast cooling, the C14-high temperature modification (hexagonal MgZn_2 type structure) stable at the annealing temperature can be retained at room temperature [10]. Annealing of such specimens at temperatures in the range $1050^\circ\text{C} \leq T \leq 1150^\circ\text{C}$ leads to formation of the C15-low temperature modification (cubic MgCu_2 type). This transformation from a non-equilibrium state to an equilibrium state is associated with a change in (layer-sandwich unit) stacking sequence (see what follows).

The different stacking sequences occurring in Laves phase polytypes (general formula AB_2) can be described on the basis of AB_3A layer-sandwich units and B single-layer units, see section 6.2.1 and chapter 3 (cf. Ref. [6]) for details. The stacking sequence of the C14 polytype is $\dots XzYz\dots$ and the stacking sequence of the C15 polytype is $\dots XzYxZy\dots$, with the upper-case letters indicating the stacking position (three possibilities: X, Y and Z) of the layer-sandwich units and the lower-case letters indicating the stacking positions (three possibilities: x, y and z) of the single-layer units. Since the position of each single-layer unit is unequivocally determined by the position of the two adjacent layer-sandwich units, it suffices for characterizing the Laves-phase ordered structures to indicate the stacking order of only the layer-sandwich units, which will be the policy in the sequel.

The $\text{C14} \rightarrow \text{C15}$ phase transformation is thus given by a change in stacking sequence of the layer-sandwich units from $\dots XY\dots$ to $\dots XYZ\dots$, similar to e.g. the polytypic phase transformation of cobalt [11]. Such a layer-stacking-sequence change can be brought about by glide of partial dislocations, which pass through the crystal on the basal planes (i.e. (001) in C14 and $\{111\}$ in C15). A striking difference with the simple close-packed crystal structure of cobalt is the presence of the single-layer unit B between the layer-sandwich units (see above). The partial dislocations promoting the polytypic phase transformations in Laves phases thus become partial dislocation pairs, which are associated with two different Burgers vectors, travelling, *simultaneously*, between the lower layer-sandwich unit and the single-layer unit and the single-layer unit and the upper layer-sandwich unit. Such a partial dislocation pair is therefore a so-called synchro-

Shockley partial dislocation [2]. Such dislocations have been observed in HfCr₂ by Z-contrast transmission electron microscopy [12]. A C14 crystal can be transformed to a C15 crystal by passage of a periodic array (“ordered glide”) of such synchro-Shockley partial dislocations [3, 6] (cf. chapter 4).

7.2.2 Evaluation of phase-transformation kinetics by XRPD

The progress of a phase transformation can be traced by measuring the value of a characteristic quantity of the transforming sample, which changes monotonously as a function of the progress of the phase transformation. Such quantities will be called *tracing parameters* in the following. As shown in Refs. [13-15] isothermal time-dependent measurement of such tracing parameters x for different annealing temperatures T allows determination of the activation energy of the transformation. This requires isokinetic character of the transformation within the temperature range considered, and an Arrhenius-type temperature dependence of the reaction rate (implying large driving forces, cf. [16]). Then, plots of $x_T(t)$ vs. $\ln(t)$, with t being the annealing time for the different T , yield parallel, isomorphous curves shifted with respect to each other parallel to the $\ln(t)$ axis, with the $\ln(t)$ shifts being characteristic for the activation energy [14]. The activation energy can thus be determined, without recourse to a specific kinetic model, by fitting the x_T vs. $\ln(t)$ curves empirically using polynomials in x , e.g.

$$\ln(t) = A_3^{(x)}x^3 + A_2^{(x)}x^2 + A_1^{(x)}x + A_{0,T}^{(x)} = \ln \tau(x) + \frac{Q}{RT} \quad (7.1a)$$

with $A_i^{(x)}$ ($i = 1, 2, 3$) being T -independent fit parameters and with $A_{0,T}^{(x)}$ a T -dependent fit parameter. Q is the (effective) activation energy of the phase transformation and τ denotes the hypothetical time required to reach a certain value for x in case of $T \rightarrow \infty$. Eq. (7.1a) directly implies that a plot of $A_{0,T}^{(x)}$ vs $1/T$ should be linear with a slope equal to Q/RT .

XRPD patterns obtained from the HfCr₂ samples, which are partly transformed from C14 to C15 upon annealing at $1050^\circ\text{C} \leq T \leq 1150^\circ\text{C}$, are very complex (cf. chapter 6), exhibiting considerable line broadening of (only) specific reflections. These diffraction patterns cannot be interpreted in terms of the presence of two separately, i.e. incoherently, diffracting phases (C14 and C15): coherency of diffraction effects in the occurring intergrowth structures dominates the observed diffraction-line intensity and

shape. Indeed, HRTEM images, for intermediate stages of the C14 → C15 transformation, reveal that the microstructure consists of grains composed of fine lamellae with parts exhibiting the C14-type stacking sequence and other parts exhibiting the C15-type stacking sequence. Coherent diffraction of the C14- and C15-type domains in an intergrowth can occur leading to considerable line broadening for many (polytype) reflections while the other (fundamental) reflections remain narrow.

Careful analysis of the XRPD patterns allows extraction of two different tracing parameters x :

- (1) The normalized intensity I_{hkl_0} of the (hardly broadened) polytype C14- $hkl_0=100$ reflection, $\tilde{I}_{hkl_0=100}$ ⁹:

$$\tilde{I}_{hkl_0=100} = \frac{I_{hkl_0=100}}{I_{hkl_0=001}}, \quad (7.2)$$

with $I_{hkl_0=100}$ being the intensity of the C14- $hkl_0=100$ reflection, which disappears upon the transformation from C14 → C15, and $I_{hkl_0=001}$ being the intensity of the (unbroadened) $hkl_0=001$ fundamental reflection, which also occurs for the cubic C15 modification. Upon C14 → C15 transformation, \tilde{I}_{100} drops from its initial value pertaining to 100 % C14 to 0 for 100 % C15 (for details, see Ref. [10] and footnote 1 therein).

- (2) The ratio r of the distance between the layer-sandwich units and the inter-atomic spacing within these layers, i.e. the normalised c/a ratio [10]

$$r = \frac{1}{N_L} \frac{c}{a} = \frac{c_0}{a}, \quad (7.3)$$

where c and a are the lattice parameters of the general hexagonal unit cell (“normal” for C14; chosen hexagonal setting for cubic C15) and c_0 is the spacing between two layer-sandwich units. N_L represents the number of layer-sandwich units in one

⁹ To allow for a common crystallographic indexing of the different Laves-phase polytypes, the Miller indices are referred to a standardized coordinate system with a c-axis of length $c_0 = c/N_L$, with N_L being the number of layer-sandwich units per unit cell ($N_L = 2$ for C14, $N_L = 3$ for C15). This leads to a normalized Miller index $l_0 = l/N_L$, having the same value for the same spot in reciprocal space, independent of the polytype. See Ref. [10] for details.

period of the polytype's stacking sequence ($N_L = 2$ for C14; $N_L = 3$ for C15). Upon C14 \rightarrow C15, r varies from the value determined for the 100 % C14 starting state to $r = (2/3)^{1/2}$ pertaining to 100 % C15.

As discussed above, the XRPD patterns recorded at some intermediate stage of transformation are characterized by coherence of diffraction phenomena arising from C14-type and C15-type domains present in one stacking sequence/intergrowth. Therefore, (C14 and C15) phase fractions, denoted by α_{C14} and α_{C15} ($\alpha_{C14} + \alpha_{C15} = 1$), cannot be determined by classical quantitative phase analysis by XRPD. Instead, as made plausible in Ref. [10], the two tracing parameters can be related with the fraction of α_{C14} (and thus $\alpha_{C15} (= 1 - \alpha_{C14})$) in the coherently diffracting microstructure. It holds that (i) $\tilde{I}_{hkl_0=100}$ is proportional with the squared fraction of C14-type stacking sequence in the intergrowth structure:

$$\tilde{I}_{hkl_0=100} \sim \alpha_{C14}^2 = (1 - \alpha_{C15})^2, \quad (7.4)$$

and (ii) r varies linearly with α_{C14} and $\alpha_{C15} (= 1 - \alpha_{C14})$.

The “transformed fraction” parameter f commonly considered for quantification of the progress of a transformation [13, 15], running from $f = 0$ for the begin of the transformation to $f = 1$ at the end of the transformation, can here associated with α_{C15} , and it can thus be calculated according to

$$f_x = \frac{x^n - x_{begin}^n}{x_{end}^n - x_{begin}^n} = \frac{(x)^n - (x_{C14})^n}{(x_{C15})^n - (x_{C14})^n}, \quad (7.5)$$

where $n = 1/2$ for $x \equiv \tilde{I}_{hkl_0=100}$ and $n = 1$ for $x \equiv r$. Consequently, $f \equiv f_{\tilde{I}_{hkl_0=100}}$ varies linearly with $\tilde{I}_{hkl_0=100}^{1/2}$ and $f \equiv f_r$ varies linearly with r . x_{C14} corresponds to the value of $\tilde{I}_{hkl_0=100}$ or r pertaining to the original C14 phase state and x_{C15} corresponds to the value of $\tilde{I}_{hkl_0=100}$ or r pertaining to the final C15 phase state (see Table 7.1; note that a final state of 100 % C15 is not reached in practice); in the following, f calculated on the basis of $\tilde{I}_{hkl_0=100}$ is in short denoted as f_I). These f_x values can be substituted for x in Eq. (7.1a), without loss of

generality, to determine the activation energy, since f_x is a bijective¹⁰ function of both tracing parameters x [14]. Thus in the course of the evaluation f_x is plotted vs $\ln(t)$ and fitting is performed using

$$\ln(t) = A_3^{(f_x)} f_x^2 + A_2^{(f_x)} f_x + A_1^{(f_x)} f_x + A_{0,T}^{(f_x)} = \ln \tau(f_x) + \frac{Q}{RT}. \quad (7.1b)$$

The activation energy Q is determined from a plot of $A_{0,T}^{(f_x)}$ vs $1/T$.

Data for $\tilde{I}_{hkl_0=100}$ and r have been determined for C14-HfCr₂ annealed at different temperatures (1050°C, 1100°C and 1150°C, 1225°C and 1300°C) for various times (2 h to 65 h), cf. section 6.3. The above-mentioned requirement of isokinetic character of the phase transformation seems violated comparing data from 1050-1150°C on the one hand and 1225°C and 1300°C on the other hand: At the higher temperatures, upon annealing of C14-HfCr₂, formation of C36 occurred additionally to the formation of C15, and thus a different transformation mechanism exists [10]. Moreover, the two tracing parameters can no longer be used at 1225°C and 1300°C as unambiguous measures for the transformed fraction: pure C36 is associated with the same values for $\tilde{I}_{hkl_0=100}$ and r as hold for a microstructure consisting of 50% C14 and 50% C15, cf. section 6.4.4. Thus the evaluation in the present chapter is restricted to the data pertaining to 1050-1150°C.

Table 7.1: Numerical values of $\tilde{I}_{hkl_0=100}^{1/2}$ and r for the C14 phase (experimentally determined) and the C15 phase (theoretically predicted), cf. chapter 6.

phase	f_x	alloy composition	Hf content	$\tilde{I}_{hkl_0=100}^{1/2}$	r
C14	0	Hf-poor	32.6	1.301	0.81147
		stoichiometric	33.3	1.256	0.81023
		Hf-rich	34.3	1.225	0.81018
C15	1	all	independent	0	0.81650

¹⁰ Each x corresponds to exactly one f_x and vice-versa.

		compositions	of composition		$= (2/3)^{1/2}$
--	--	--------------	-------------------	--	-----------------

7.3 Experimental

XRPD patterns were recorded from the initial C14-HfCr₂ specimens (compositions as indicated in Table 7.1) as well as from these specimens after annealing at 1050°C, 1100°C and 1150°C for various times between 1 h and 66 h. For details on specimen preparation and annealing procedure, see part I [10]. For X-ray diffraction analysis, a powder was produced from the specimens using a mortar. The powder was suspended in isopropanol and sedimented on a (510)-cut Si-crystal plate (wafer) using a supporting brass ring during evaporation of the liquid. Silicon powder (sedimented together with the alloy powder) was used as internal standard for correction of the instrumental shift of the diffraction-angle 2θ scale. The measurements were performed using a “Philips X’Pert MPD” diffractometer equipped with a germanium monochromator in the diffracted beam, using Cu-K α_1 radiation.

The XRPD patterns were analysed by fitting Pseudo-Voigt peak-shape functions [17] to the individual reflections. The fitting parameters were the reflection-maximum position, $2\theta_{hkl}^{\max}$, the full width at half maximum (FWHM), the line-shape parameter η_{hkl} and the integral intensity of the reflections I_{hkl} . $\tilde{I}_{hkl_0=100}$ was obtained from the (integrated) intensities of the C14- $hkl_0=100$ polytype reflection and the $hkl_0 = 001$ fundamental reflection (i.e. $hkl = 002$ for C14; $hkl = 003$ for C15 (hexagonal-rhombohedral unit cell); see Ref. [10]). $r = c_0/a$ was determined from the lattice parameters c and a as described in part I [10].

7.4 Results

Upon annealing at temperatures between 1050°C and 1150°C, the values for both tracing parameters, $x = \tilde{I}_{hkl_0=100}$ and $x = r$, evolve with increasing annealing time from the

characteristic values for the C14 modification towards the characteristic values for the C15 modification (see Fig. 7.1). The values expected for the C15 modification, $\tilde{I}_{hkl_0=100}^{1/2} = 0$ ($f_I = 1$) and $r = (2/3)^{1/2} = 0.8165$ ($f_r = 1$), have not been attained for the largest annealing times applied at the annealing temperatures concerned. This indicates that the transformation has not proceeded to completion at any of the employed annealing temperatures.

Evidently, the progress-of-transformation data provided by the two tracing parameters $\tilde{I}_{hkl_0=100}$ and r are comparable: Indeed, if the transformation is of isokinetic character, such a bijective relation of $\tilde{I}_{hkl_0=100}$ and r should exist, independently of the annealing temperature [14]. If both fraction transformed values as defined by Eq. (7.5), are equal, i.e. $f_I = f_r$, r should linearly depend on $\tilde{I}_{hkl_0=100}^{1/2}$ [14], as indeed observed in Fig. 7.2. For the stoichiometric and the Hf-poor alloys slight deviations from linearity occur for those specimens pertaining to the largest annealing times i.e. for the largest fractions transformed.

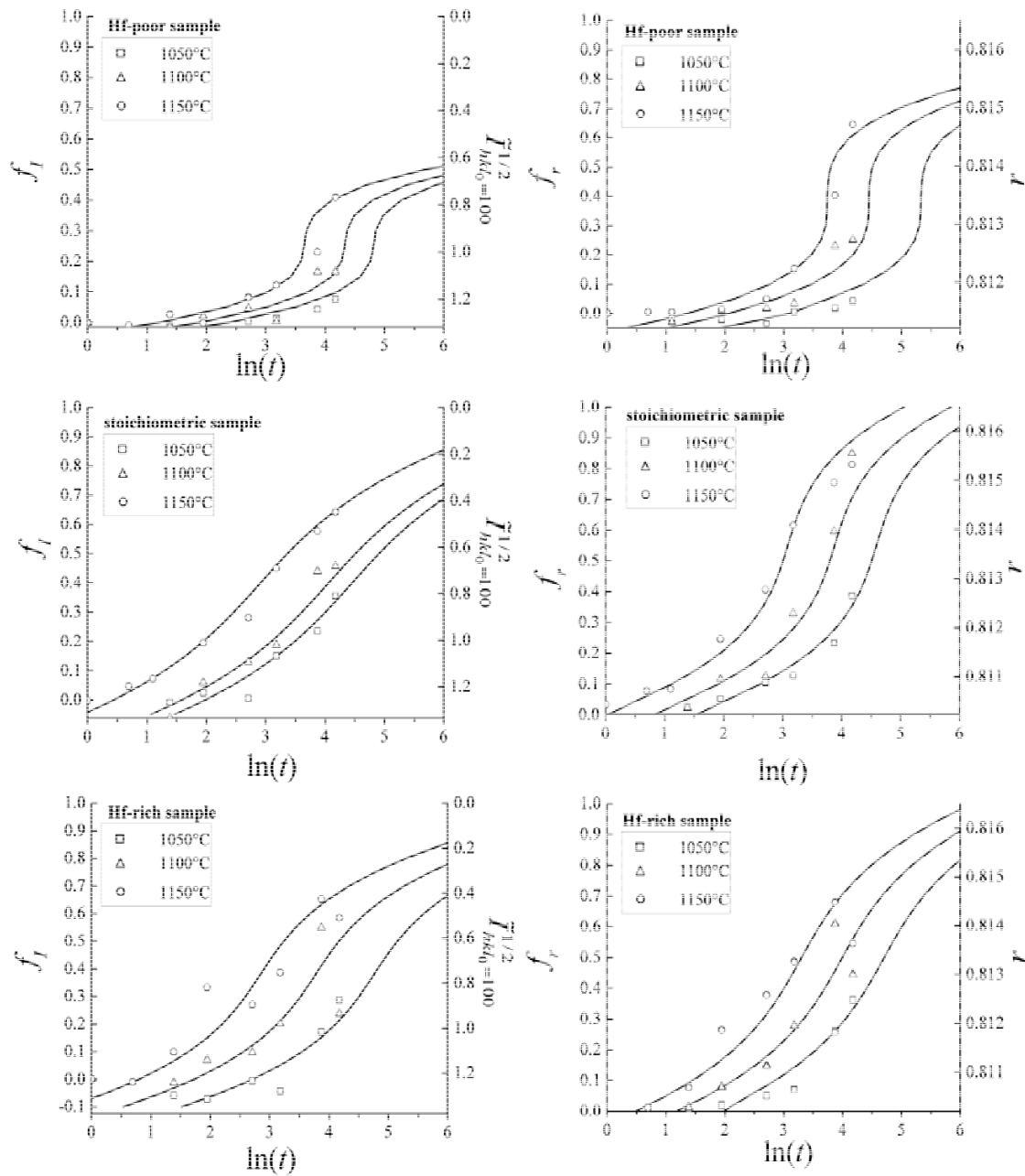


Fig. 7.1: Plots of $\tilde{I}_{hkl_0=100}^{1/2}$ and r and the correspondingly calculated (cf. Eq. (7.3)) transformed fractions, f_I and f_r , vs $\ln(t)$, with t as the annealing time. The best fits of Eq. (7.1b) to these experimental data points are also shown.

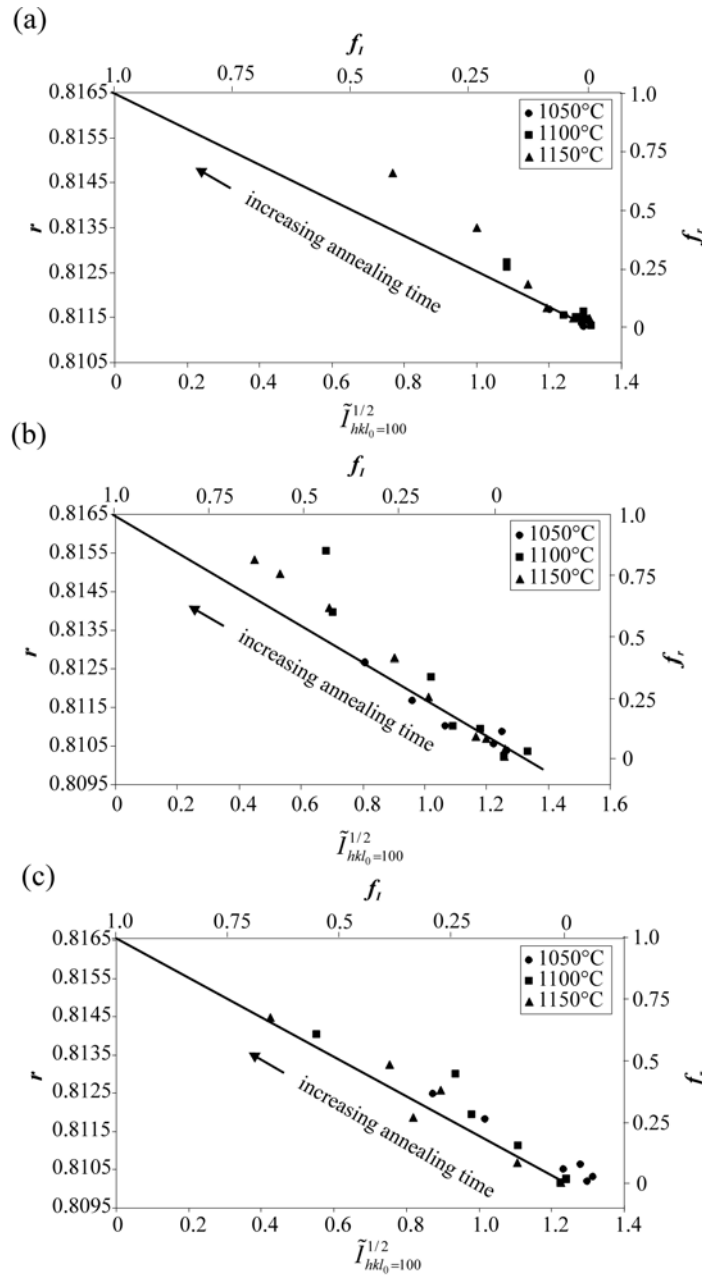


Fig. 7.2: Plots of the lattice-spacing ratio $r = c_0/a$ vs. the square root of the normalized

$hkl_0=100$ -intensity, $\tilde{I}_{hkl_0=100}^{1/2} = \left(\frac{I_{hkl_0=100}}{I_{hkl_0=001}} \right)^{1/2}$, for the HfCr_2 specimens upon transformation

from C14- HfCr_2 to C15- HfCr_2 by annealing at the temperatures indicated, (a) Hf-poor alloy, (b) stoichiometric alloy, (c) Hf-rich alloy (cf. Table 7.1 for compositions). The straight lines drawn indicate the linear trend as expected theoretically (i.e. $f_l = f_r$).

The evolutions of f_x vs. $\ln(t)$, as obtained from both $\tilde{I}_{hkl_0=100}^{1/2}$ and r using Eq. (7.5), are isomorphous for the various T (Fig. 7.1). Fits according to Eq. (7.1b) to these experimental data clearly reveal the relative shifts along the $\ln(t)$ axis. The values obtained for the parameters $A_i^{(f_x)}$ and $A_{0,T}^{(f_x)}$ according to these best fits have been gathered in Table 7.2.

The effective activation energies Q for the C14 \rightarrow C15 phase transformation of HfCr₂ determined on the basis of the $\tilde{I}_{hkl_0=100}^{1/2}$ data and on the basis of the r data, as obtained from Arrhenius-type plots of $A_{0,T}^{(f_x)}$ vs $1/T$ (see Figs. 7.3 and 7.4), have been gathered given in Table 7.3.

Table 7.2: Parameters $A_i^{(f_x)}$ and $A_{0,T}^{(f_x)}$ obtained by fitting Eq. (7.1b) to the experimental data (for compositions of the alloys, see Table 7.1).

transformed fraction calculated on the basis of $x = \tilde{I}_{hkl_0=100}$					
alloy	A_3	A_2	A_1	$A_{0,T}$	T
Hf-poor	133.59	-103.27	133.59	2.39	1050°C
				1.91	1100°C
				1.22	1150°C
stoichiometric	11.35	-13.54	9.76	1.99	1050°C
				1.59	1100°C
				0.44	1150°C
Hf-rich	15.99	-18.29	15.99	2.72	1050°C
				1.73	1100°C
				0.80	1150°C
transformed fraction calculated on the basis of $x = r$					
alloy	A_3	A_2	A_1	$A_{0,T}$	T
Hf-poor ^a	47.81	-54.10	19.36	3.37	1050°C
				2.10	1100°C
				1.42	1150°C
stoichiometric	13.88	-22.89	14.14	1.43	1050°C
				0.72	1100°C
				-0.08	1150°C
Hf-rich	11.48	-17.05	11.30	1.88	1050°C
				1.17	1100°C
				0.48	1150°C

^aThe fitted evolutions of f_r for this specimen were forced to increase monotonously with $\ln(t)$.

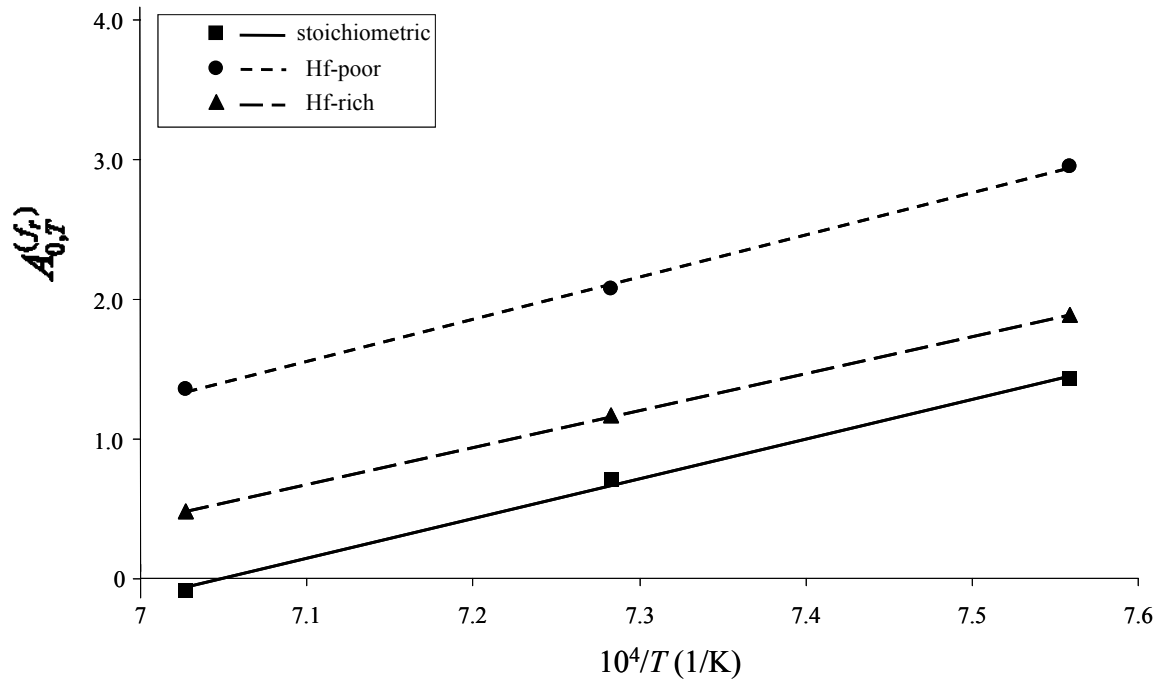


Fig. 7.3: Arrhenius-type plots of $A_{0,T}^{(f_l)}$ as obtained on the basis of f_l .

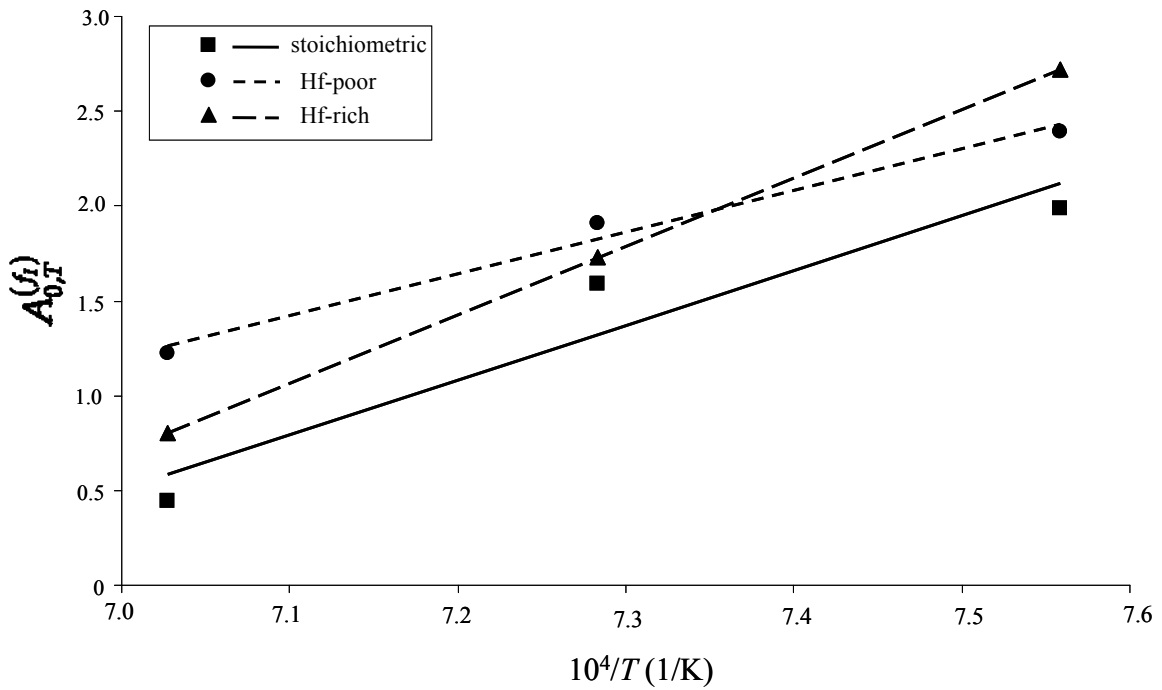


Fig. 7.4: Arrhenius-type plots of $A_{0,T}^{(f_r)}$ as obtained on the basis of f_r .

Table 7.3: Effective activation energies for the C14 → C15 transformation as obtained on the basis of the temperature dependencies of f_i and f_r (cf. Figs. 7.3 and 7.4, respectively).

alloy	activation energy Q determined on the basis of f_i (kJ/mol)	activation energy Q determined on the basis of f_r (kJ/mol)
Hf-poor	180(±20)	250(±10)
stoichiometric	240(±70)	235(±10)
Hf-rich	300(±2)	219(±3)

7.5 Discussion

The experimental data points for the degree of transformation, f_x , scatter around the fitted (on the basis of Eq. (7.1b)) continuous evolutions of f_i and f_r vs $\ln(t)$ in Fig. 7.1. This scatter may be attributed to limited experimental accuracy of the measured values of $\tilde{I}_{hkl_0=100}$ and r used to calculate f_i and f_r . In case of $\tilde{I}_{hkl_0=100}^{1/2}$, the intensity ratio of the $hkl_0=100$ -polytype reflection and the $hkl_0=001$ -fundamental reflection may be affected by artefacts as the surface roughness and the insufficient crystallite statistics of the specimen. Upon C14 → C15 transformation the value of r changes only by less than 1 %, but diffraction-peak positions (and thus lattice-spacing parameters) can be determined with much higher accuracy than integrated intensities. Hence the experimental values of f_r may be more accurate than those of f_i . Indeed, the scatter in the experimental data is less for f_r and in previous studies [14, 18] time-dependent lattice-spacing ratio variations, of similar magnitude and utilized for determination of the activation energy, exhibited little scatter.

A possible source of scatter may be temperature variations during the heat treatment of the specimens, especially at high temperatures. However, this seems unlikely for the present experiments, because this would lead to a generally positive correlation of the deviations, which does not hold: I.e. it would be expected that f_i and f_r pertaining to

the same data point, would simultaneously be too large or too small as compared to the fitted evolution, which is not observed (cf. Fig. 7.1).

The full shapes of the fitted curves for f as $f(t)$ (cf. Fig. 7.1) do not play a role in the present evaluation to obtain the effective activation energy, which depends only on the relative T -dependent shift of the isomorphous curves along the $\ln(t)$ -axis, as described by $A_{0,T}^{(f_x)}$. An Arrhenius-type temperature dependence is observed upon plotting $A_{0,T}^{(f_x)}$ vs $1/T$ (Figs. 7.3 and 7.4): straight lines occur in these plots.

In case of the stoichiometric alloy the values obtained from both data sets (f_l and f_r) for the effective activation energy values of the C14 \rightarrow C15 transformation in HfCr₂ are the same within experimental accuracy. Considerably different values of Q , as determined on the basis of either f_l or f_r , occur for the two non-stoichiometric alloys (cf. Table 7.3). The results based on f_l indicate an increase in activation energy with increasing Hf content; the results based on f_r indicate the opposite. The values determined on the basis of f_r are likely more reliable (see discussion above). Additionally, note that not only the scatter in the experimental data (Fig. 7.1), but also the scatter of the data points in the Arrhenius-type plot (Figs. 7.3 and 7.4; cf. Table 7.3), is considerably smaller in case of the evaluation based on f_r . Hence, the f_r data set is subjected to further discussion. The increase of the activation energy with increasing Hf content, as indicated by the results obtained on the basis of f_r , is consistent with the observation that the phase transformation proceeds particularly slowly in case of the Hf-poor alloy (cf. Fig. 7.1).

The present results have especially significance in view of the until now very small number of experimental data on the kinetics of polytypic transformations of Laves phases. The majority of previous works on kinetic aspects of these transformations was of theoretical character [5, 19, 20]. In a recent experimental work the activation energy for the C14 \rightarrow C36 transformation of TiCr₂ has been reported to be in the range 107 - 112 kJ/mol [21].

The shear character of the transformations, involving motion of synchro-Shockley partial dislocations, suggests the activation energy of the transformations to be dominated by the activation energy for partial dislocation glide in Laves phases. The activation energy for dislocation glide controlled by lattice resistance is smaller than the activation energy for interdiffusion, see Ref. [22]. Self- and interdiffusion data for the HfCr₂-Laves

phase are not available. Self-diffusion data for a transition-metal Laves phase are available for C15-NbCo₂ [23], which has a melting temperature similar to HfCr_2 . The activation energies for Nb and Co diffusion have been reported to be 295 kJ/mol and 292 kJ/mol, respectively. Indeed, the activation energy for the C14 \rightarrow C15 transformation of HfCr_2 is somewhat smaller than the above activation energies for diffusion, which is compatible with the idea that the transformation in HfCr_2 is rate-controlled by glide of synchro-Shockely partial dislocations.

The higher activation energies found in case of the C14 \rightarrow C15 transformation in HfCr_2 as compared to the C14 \rightarrow C36 transformation in TiCr_2 [21], can be understood recognizing that in the first case the transformation proceeds by passage of separate synchro-Shockley dislocations with a long-range strain field, whereas in the latter case, the transformation proceeds by passage of synchro-Shockley dislocation *dipoles*, which possess a strain field concentrated between the two partial dislocations constituting the dipole. As an additional difference between the two transformations, the activation energy decreases with increasing Hf content (i.e. decreasing Cr content) in case of the C14 \rightarrow C15 in HfCr_2 , whereas an increase of the activation energy with increasing Ti content (i.e. decreasing Cr content) has been observed in case of C14 \rightarrow C36 in TiCr_2 [21].

7.6 Conclusions

1. The kinetics of the C14 \rightarrow C15 transformation in HfCr_2 Laves phase can be traced at temperatures as high as 1050-1150°C on the basis of two parameters deduced from XRPD patterns: (i) the ratio of the intensity of a polytype-specific reflection and a fundamental reflection and (ii) a normalized c/a ratio. The two tracing parameters can be employed to calculate the relative fraction of C15 phase in the intergrowth microstructure consisting of C14 and C15 Laves-phase polytype layer-sandwich unit stacking sequences. The data obtained for the degree of transformation from the normalized c/a ratio are considered to be more accurate than those derived from the normalized integrated intensity ratio of a polytype reflection and a fundamental reflection.

2. The activation energies obtained for the C14 \rightarrow C15 phase transformation in HfCr₂, based on the normalized c/a ratio, for the three alloys of different composition, range from 220 kJ/mol (Hf-rich specimen) to 250 kJ/mol (Hf-poor specimen). These values are somewhat smaller than those for the activation energy for self-diffusion of both A and B in related AB_2 transition-metal Laves phases (NbCo₂), which is compatible with the proposed transformation mechanism being controlled by glide of synchro-Schockely partial dislocations.

7.7 Acknowledgements

The authors are much indebted to Mr. Thomas Meisner (Max Planck Institute for Metals Research) for indispensable collaboration during alloy preparation and annealing experiments. This work has been performed within the framework of the Inter-Institutional Research Initiative "The Nature of Laves Phases" funded by the Max Planck Society.

7.8 Literature

- [1] G. Sauthoff, "Intermetallics" (1995) Weinheim, VCH.
- [2] C.W. Allen, P. Delavignette and S. Amelinckx, *Phys. Status Solidi A* 9 (1972) 237.
- [3] C.W. Allen and K.C. Liao, *Phys. Status Solidi A* 74 (1982) 673.
- [4] P.M. Hazzledine and P. Pirouz, *Scr. Metall. Mater.* 28 (1993) 1277.
- [5] K.S. Kumar and P.M. Hazzledine, *Intermetallics* 12 (2004) 763.
- [6] J. Aufrecht, W. Baumann, A. Leineweber, V. Duppel and E.J. Mittemeijer *Phil. Mag.* 90 (2010) 3149.
- [7] A.L. Kazantzis, T.T. Cheng, M. Aindow and I.P. Jones, *Inst. Phys. Conf. Ser.* 147 (1995) 511.
- [8] R. Bauer, E.J. Jägle, W. Baumann and E.J. Mittemeijer, *Phil. Mag. A* (2010) in press.
- [9] M. Venkatraman and J.P. Neumann, *Bull. Alloy Phase Diag.* 7 (1986) 570.

- [10] J. Aufrecht, A. Leineweber, V. Duppel, E.J. Mittemeijer (2010) *To be published*.
- [11] Z. Nishiyama, "Martensitic Transformations" (1978) New York, Academic Press.
- [12] M.F. Chisholm, S. Kumar, and P. Hazzledine, *Science* 307 (2005). 701.
- [13] E.J. Mittemeijer, *J. Mater. Sci.* 27 (1992) 3977.
- [14] A. Leineweber, E.J. Mittemeijer, M. Knapp and C. Baetz, *Phil. Mag. A* 87 (2007) 1821.
- [15] F. Liu, F. Sommer, C. Bos and E.J. Mittemeijer, *Inter. Mater. Rev.* 52 (2007) 193.
- [16] W. Baumann, A. Leineweber and E.J. Mittemeijer, *J. Mater. Sci.* 45 (2010) 6075.
- [17] R.A. Young, Ed., *The Rietveld method* (1995) Oxford, Oxford Univ. Press.
- [18] A. Leineweber, *Acta Mater.* 55 (2007) 6651.
- [19] C.W. Allen and K.C. Liao, *Proceedings of the ICOMAT Boston 1979* (1979) 124.
- [20] O. Vedmedenko, F. Rösch and C. Elsässer, *Acta Mater.* 56 (2008) 4984.
- [21] W. Baumann, A. Leineweber and E.J. Mittemeijer (2010) *To be published*.
- [22] H.J. Frost, M.F. Ashby, "Deformation-Mechanism Maps - The Plasticity and Creep of Metals and Ceramics" (1982) Kronberg-Taunus, Pergamon Press.
- [23] M. Denking and H. Mehrer, *Phil. Mag. A* 80 (2000) 1245.

8. *Summary*

8.1 **Focus of the thesis**

Laves phases form the largest group of intermetallic phases. Especially the transition-metal Laves phases are interesting candidates for high-temperature applications as well as energy storage. In many of such alloy systems, different Laves-phase polytypes, characterized by specific stacking sequences of common building units, exist as a function of composition and temperature. Because of their structural relationship, a special type mechanism for phase transformations between this polytypes, involving changes in stacking sequence by complex partial dislocations, the so-called synchro-Shockley partial dislocations, has been proposed and experimentally proven.

Systematic investigations of the polytypic phase transformations have been obstructed by experimental complications (high temperatures involved, sluggish transformation rates), imprecise and questionable data on phase stability, difficult structure identification from X-ray powder diffraction (XRPD) data and problematic quantification of phase fractions associated with the different Laves-phase polytypes.

In the present work, the Laves phases NbCr_2 and HfCr_2 , which exhibit polytypic transformations as a function of temperature, have been investigated. It has been shown, that the available data on phase stability fields is in part erroneous (NbCr_2).

The microstructures of partly or completely transformed Laves phases have been investigated by combined XRPD analysis and high-resolution transmission electron microscopy (HRTEM). It is shown that such microstructures involving different Laves-phase polytypes consist of intergrowth-like lamellae exhibiting the respective stacking sequence of the polytypes involved. This results in coherent diffraction between regions of different polytypes in XRPD experiments so that XRPD patterns are not a simple superimposition of the patterns corresponding to the particular polytypes. As a consequence, selective line broadening occurs. By line-profile analysis of such XRPD patterns of Laves phases, which were partly or completely transformed from one polytype to another, accompanied by HRTEM studies, details on the transformation mechanism

were revealed. The role of synchro-Shockley dislocation dipoles in the transformation of the hexagonal C14 structure to the dihexagonal C36 structure has been demonstrated. An HRTEM image of such a dipole has been obtained as well as an anti-phase boundary formed upon impingement of ordered arrangements of such dipoles.

Finally, the polytypic phase transformations from the C14-high temperature modification of the HfCr₂ Laves phase, retained upon cooling, to other polytypes like C36 and C15 upon annealing has been studied as a function of temperature, composition and annealing time, employing XRPD and HRTEM. A quantitative kinetic analysis has been performed by extraction of suitable parameters for tracing of the course of the transformations from the XRPD patterns recorded from the different annealed samples. The effective activation energy for the transformation could thus be obtained.

8.2 The absence of a stable hexagonal Laves phase modification (NbCr₂) in the Nb-Cr system

High-temperature differential thermal analysis and neutron diffraction have been employed to investigate the previously proposed polytypic phase transformation C14-NbCr₂ \rightleftharpoons C15-NbCr₂ at around 1600°C. It could be shown that for high-purity alloys and high-purity conditions, the phase transformation does *not* occur. However, small amounts of atmospheric contaminations induce the formation of an η -carbide type phase, which melts (partially) in a temperature range around 1600°C. This has led to the erroneous, former conclusion of the occurrence of a thermodynamically stable high-temperature modification of NbCr₂.

8.3 Metastable hexagonal modifications of the NbCr₂ Laves phase as function of cooling rate

X-ray powder diffraction, electron-backscatter diffraction and high-resolution transmission electron microscopy characterization of as-cast ingots of the Laves phase NbCr₂ produced by arc-melting have demonstrated the occurrence of hexagonal C14 and

C36 modifications of NbCr₂. These metastable phases were shown to be present, together with the stable cubic C15 equilibrium modification, predominately in the top part of the arc-melted ingots. In the bottom part, which had been in contact with a water-cooled copper hearth, only very small amounts of these metastable phases occur. XRPD and HR-TEM analysis showed that at room temperature (i.e. after completed cooling) the major part of the hexagonal modifications is represented by the heavily faulted C36 phase, and that the C14 phase is a minority phase. The faulting in C36 suggests that this phase had formed from initially crystallized C14 by the synchro-shear mechanism.

The appearance of the metastable C14 phase (and subsequently the C36 phase within the originally C14 phase) is most likely if the undercooling upon solidification is rather small, i.e. in the top part of the ingot where the relatively lowest cooling rates occur. At large undercooling, i.e. in the bottom part of the ingot where the relatively highest cooling rates occur, the difference in Gibbs energy (of formation) of the C15 and the C14 phases can be relatively large, thereby promoting the formation of the C15 phase.

8.4 Layer-stacking irregularities in C36-type Nb-Cr and Ti-Cr Laves phases and their relation with polytypic phase transformations

Irregularities in the layer-sandwich unit stacking sequences of C36 Laves phases (TiCr₂ and NbCr₂), which form from C14-type precursors, have been exhibited by HRTEM and XRPD-line profile analysis. The occurrence of such faulting provides validation of the proposed mechanism for the C14 → C36 phase transformation by glide of a series of ordered synchro-Shockley partial dislocation dipoles (“ordered glide”).

Two mechanisms bringing about the (layer-sandwich unit) stacking irregularities have been identified:

- Domain formation: Four different types of perfect C36 domains, which are displaced with respect to each other, occur simultaneously within one parent C14 crystal, leading to layer-stacking irregularities upon impingement of the growing domains.
- Transformation errors: Deviations occur from perfect “ordered glide” during the transformation within a domain, leading to “regime boundaries”.

The predominant layer-stacking irregularities are *2H*- and *6H*-type stacking sequences within a domain, as evidenced by HRTEM and XRPD (selective broadening of the class of XRPD reflections with $h - k \neq 3N$ and $l = 4M \pm 1$ implying that stacking faults with a displacement vector of $(0,0,1/2)$ are dominant): The transformation errors are the dominating stacking irregularities for the investigated C36-NbCr₂ and C36-TiCr₂ Laves phases. The contribution of domain boundaries is negligible compared to that of the regime boundaries in case of C36-NbCr₂, but less so in case of C36-TiCr₂.

C36-NbCo₂, which is not formed from a C14 precursor, (indeed) shows faulting distinctly different from C36-TiCr₂ and C36-NbCr₂.

8.5 Transformation-dislocation dipoles in Laves phases; a high-resolution transmission electron microscopy analysis

Direct experimental evidence has been provided demonstrating that the transformation in Laves phases from the C14 structure to the C36 (or 6H) structure is realized by glide of an ordered arrangement of synchro-Shockley partial dislocation dipoles.

Stacking irregularities, due to locally disordered passage of these line defects, have been identified. Atomistic structures for the cores of all non-equivalent synchro-Shockley partial dislocation dipoles have been proposed for the transformation from C14 → C36 (in NbCr₂).

A C36-“anti phase boundary” has been observed for the first time (in HfCr₂). This anti-phase boundary consists of a specific arrangement of synchro-Shockley partial dislocation dipoles. This anti-phase boundary is the result of impingement of two growing C36 domains within the same, initial C14 crystal.

The microstructural situation in HfCr₂ contrasts with that of NbCr₂: whereas in NbCr₂ in principle the isolated dislocation dipole could still glide and, therefore, continue the C14 → C36 transition (which has not been completed), in HfCr₂ the transformation has been completed and impingement of two completely transformed C36 domains has occurred and the dislocation arrangement (of the anti-phase boundary) is thus fixed.

The experimental observations demonstrate the long-range, largely strain-free/deformation-free character of the overall dislocation configurations: the lattice

distortion is highly concentrated within the core of the individual synchro-Shockley partial dislocation dipoles. The present results indicate that the synchro-Shockley partial dislocation dipoles, which carry the C14 \rightarrow C36 phase transformations in Laves phases, should be regarded as singular defects.

8.6 Polytypic transformations of the HfCr₂ Laves phase – Structural evolution as a function of temperature and time

HfCr₂-Laves phase alloys of different composition have been produced by arc-melting and subsequent homogenization at temperatures, at which the C14-high temperature modification is stable. By annealing at different, lower temperatures for various times, polytypic transformations have been induced and the resulting (micro-) structure of the Laves phase has been characterized by X-ray powder diffraction and high-resolution electron microscopy.

At temperatures between 1300°C and 1225°C, a microstructure forms, which can be regarded as composed of randomly alternating C36 and C15 lamellae. At lower annealing temperatures (1050°C-1150°C), the C36 stacking sequences did not occur. Instead a lamellar C14/C15 microstructure develops, which develops upon incomplete C14 \rightarrow C15 transformation.

The corresponding XRPD patterns are not composed of discrete patterns corresponding to the different Laves-phase polytypes, but a common, average pattern evolves due to coherent diffraction from the polytypes constituting the lamellar structure. This coherent diffraction from the irregular stacking sequence induces a broadening of reflections corresponding to specific polytypes, whereas the “fundamental” reflections present for all polytypes remain unbroadened.

From the diffraction patterns two scalar parameters are obtained, which describe the state of the phase transformation as a function of time, one based on the change of intensity of a selected polytype reflection and the other based on the change of the average unit cell parameter ratio (c/a) of the lamellar structure. In order to treat the lamellar microstructure as one average structure, a standardized crystallographic description for all polytypes has been applied.

8.7 Polytypic transformations of the HfCr₂ Laves phase – Kinetics of the polymorphic C14 → C15 transformation

The polymorphic phase transformation C14 → C15 of the HfCr₂-Laves phase has been traced using the normalized intensity of a selected polytype reflection (indices 100) and, alternatively, using the average unit cell parameter ration (c/a) of the lamellar structure. These two *tracing parameters* provide similar information quantifying the progress (degree) of the transformation.

The effective activation energy of the phase transformations has been determined from isothermal annealing experiments for three alloys of different composition within the homogeneity range of the HfCr₂ phase using the equivalent-time method. The values range from 220 kJ/mol (Hf-rich specimen) to 250 kJ/mol (Hf-poor specimen). The activation energy increases with decreasing Hf content. The values obtained for the effective activation energy are between that for activation energies for self-diffusion of both A and B in AB_2 transition-metal Laves phases and that for (synchro-Shockley) dislocation glide under applied stress. Hence, the mechanism involves both a glide character and single-atomic jumps, which is in agreement with a kink-wise movement of the dislocations.

9. Zusammenfassung

9.1 Fokus der Arbeit

Lavesphasen bilden die größte Gruppe intermetallischer Phasen. Besonders die Lavesphasen der Übergangsmetalle sind potentiell von Interesse für Hochtemperatur-Strukturanwendungen und für die Energiespeicherung. In vielen solchen Legierungssystemen kommen als Funktion der Zusammensetzung und/oder Temperatur verschiedene polytype Modifikationen vor, die sich durch verschiedene Stapelfolgen gemeinsamer Baueinheiten unterscheiden. Wegen der Verwandtschaft ihrer Kristallstrukturen wurde für Phasenumwandlungen zwischen diesen Polytypen ein besonderer Mechanismus vorgeschlagen und experimentell belegt, der auf Änderungen der Stapelfolge durch komplexe Partialversetzungen, den sogenannten synchro-Shockley-Partialversetzungen beruht.

Systematische Untersuchungen dieser polytypen Phasenumwandlungen werden beeinträchtigt von experimentellen Schwierigkeiten (hohe Temperaturen, langsame Umwandlungsgeschwindigkeiten), ungenauen oder sogar fragwürdigen Daten bezüglich der Stabilitätsbereiche verschiedener Polytypen, schwieriger Unterscheidung der Phasen in Röntgenpulverdiffraktogrammen und einer problematischen Quantifizierung von Phasenanteilen der verschiedenen Polytypen.

In der vorliegenden Arbeit wurden die Lavesphasen NbCr_2 und HfCr_2 untersucht, die polytype Phasenumwandlungen als Funktion der Temperatur zeigen. Es konnte gezeigt werden, dass die verfügbaren Daten bezüglich der Stabilitätsbereiche der Polytype zum Teil fehlerhaft sind (NbCr_2).

Die Mikrostruktur von teilweise oder vollständig umgewandelten Lavesphasen wurde mit kombinierter Röntgenpulverdiffraktometrie (XRPD) und hochauflösender Transmissionselektronenmikroskopie (HRTEM) untersucht. Es wurde gezeigt, dass diese Mikrostrukturen teilweise oder vollständig umgewandelter Lavesphasen aus lamellenförmigen Verwachsungen von Blocks mit den jeweiligen Stapelfolgen der beteiligten Polytypen bestehen. Daraus ergibt sich eine kohärente Beugung in XRPD-

Messungen, so dass die Diffraktogramme nicht eine einfache Superpositionen der Diffraktogramme der einzelnen Polytypen sind. Vielmehr tritt ein gemeinsames Diffraktogramm mit einer selektiven Linienverbreiterung auf. Durch Linienprofilanalyse an solchen Diffraktogrammen von Lavesphasen, die teilweise oder ganz umgewandelt wurden, verbunden mit HRTEM-Studien, konnten Details zum Mechanismus der polytypen Phasenumwandlungen aufgedeckt werden. Die Rolle von Dipolen aus synchro-Shockley-Partialversetzungen bei der Umwandlung der hexagonalen C14-Struktur in die dihexagonale C36-Struktur wurde bestätigt. Ein HRTEM-Bild eines solchen Dipols wurde aufgenommen genauso wie eine Anti-Phasengrenze, die sich durch Zusammentreffen von regelmäßigen Anordnungen solcher Dipole gebildet hat.

Schließlich wurde die polytype Phasenumwandlung der durch Abkühlung eingefrorenen C14-Hochtemperaturmodifikation der HfCr_2 -Lavesphase in andere Polytypen wie C36 und C15 durch Tempern mit XRPD und HRTEM untersucht, und dieses als Funktion der Temperatur, der Zusammensetzung und der Auslagerungszeit. Eine quantitative Analyse wurde durchgeführt, indem geeignete Parameter zur Beschreibung des Fortschritts der Umwandlung aus XRPD-Messungen der verschiedenen getemperten Proben extrahiert wurden. Damit konnte die effektive Aktivierungsenergie der Umwandlung bestimmt werden.

9.2 Die Nicht-Existenz einer stabilen hexagonalen Modifikation der Lavesphase NbCr_2 im Nb-Cr-System

Differential-Thermoanalyse (DTA) und Neutronenbeugung (ND) bei hohen Temperaturen wurden verwendet, um die zuvor vorgeschlagene polytypische Phasenumwandlung $\text{C14-NbCr}_2 \rightleftharpoons \text{C15-NbCr}_2$ bei etwa 1600°C zu untersuchen. Es konnte gezeigt werden, dass die Phasenumwandlung für hochreine Legierungen und hochreine Bedingungen *nicht* auftritt. Kleine Verunreinigungen aus der Atmosphäre verursachen allerdings die Bildung einer η -Carbid-artigen Phase, die (partiell) in einem Temperaturbereich um 1600°C aufschmilzt. Dies hat in der Vergangenheit zu der falschen Folgerung geführt, dass eine thermodynamisch stabile Hochtemperaturmodifikation von NbCr_2 existiert.

9.3 Metastabile hexagonale Modifikationen der Lavesphase NbCr₂ in Abhängigkeit von der Abkühlrate

XRPD, Elektronenrückstreubeugung (EBSD) und HRTEM an aus der Schmelze erstarrten Proben der Lavesphase NbCr₂ wiesen das Auftreten hexagonaler C14- und C36-Modifikationen von NbCr₂ nach. Es wurde gezeigt, dass diese metastabilen Phasen zum größten Teil im oberen Teil der erstarrten Probe auftreten, zusammen mit der stabilen Gleichgewichtsmodifikation C15. Dagegen zeigten sich im unteren Teil der Probe, der im Kontakt mit einer wassergekühlten Kupferplatte stand, nur sehr kleine Mengen dieser metastabilen Phasen. XRPD- und HRTEM-Analysen zeigten, dass es sich beim größten Teil der hexagonalen Modifikationen bei Raumtemperatur (also nach erfolgter Abkühlung) um C36-Phase mit einer großen Dichte an Stapelfehlern handelt, und dass C14 nur einen kleinen Anteil einnimmt. Die Stapelfehler in C36 legen nahe, dass diese Phase aus zuvor aus der Schmelze erstarrtem C14 über den Synchronshear-Mechanismus unter Beteiligung von Partialversetzungsdipolen gebildet wurde.

Das Auftreten der metastabilen C14-Phase (und in der Folge der C36-Phase innerhalb der ursprünglichen C14-Phase) ist am wahrscheinlichsten, wenn die Unterkühlung bei der Erstarrung eher gering ist, das heißt im oberen Teil der Probe, wo die relativ gesehen höchsten Abkühlraten auftreten. Bei großen Unterkühlungen, also im unteren Teil der Probe, wo die relativ gesehen höchsten Abkühlraten vorherrschen, kann die Differenz der freien (Gibbs-) Bildungsenthalpien der C15- und der C14-Phase relativ groß sein, was die Bildung der C15-Phase fördert.

9.4 Unregelmäßigkeiten in der Schicht-Stapelfolge bei Nb-Cr- und Ti-Cr-Lavesphasen des C36-Typs und deren Zusammenhang mit den polytypen Phasenumwandlungen

Mit HRTEM und XRPD-Linienprofilanalyse wurden Unregelmäßigkeiten in der Stapelfolge von Sandwich-Schichten (layer-sandwich units) in C36-Lavesphasen (TiCr₂ and NbCr₂), die aus Vorstufen des C14-Typs gebildet wurden, festgestellt. Das Auftreten solcher Stapelunregelmäßigkeiten bestätigt einen vorgeschlagenen Mechanismus für die

Phasenumwandlung von C14 nach C36, der auf dem Gleiten einer Serie von regelmäßig angeordneten synchro-Shockley-Partialversetzungsdipolen beruht („geordnete Gleitung“).

Zwei potentielle Mechanismen, die die Unregelmäßigkeiten in der Stapelfolge verursachen, wurden identifiziert:

- Bildung von Domänen: Vier verschiedene Arten fehlerfreier C36-Domänen, die untereinander verschoben sind, treten gleichzeitig in einem ursprünglichen C14-Kristall auf, was zu Unregelmäßigkeiten in der Stapelfolge als Folge des Aufeinandertreffens wachsender Domänen führt.
- Umwandlungsfehler: Es treten während der Umwandlung Abweichungen von der vollkommen „geordneten Gleitung“ innerhalb einer Domäne auf, was zur Bildung von „Ordnungsregimegrenzen“ führt.

Die vorherrschenden Stapelunregelmäßigkeiten sind Stapelfolgen vom $2H$ - und vom $6H$ -Typ innerhalb einer Domäne, wie durch HRTEM und XRPD gezeigt werden konnte (selektive Linienverbreiterung einer bestimmten Klasse von Röntgenbeugungsreflexen mit $h - k \neq 3N$ and $l = 4M \pm 1$, was bedeutet, dass Stapelunregelmäßigkeiten mit einem Verschiebungsvektor von $(0,0,1/2)$ dominieren): Dies bedeutet, dass Umwandlungsfehler die dominierenden Unregelmäßigkeiten in der Stapelfolge der untersuchten Lavesphasen C36-NbCr₂ und C36-TiCr₂ sind. Im Gegensatz zu C36-TiCr₂ ist der Beitrag der Domänengrenzen bei NbCr₂ im Vergleich zu dem der Ordnungsregimegrenzen vernachlässigbar.

C36-NbCo₂, das nicht aus einer C14-Vorstufe gebildet wird, zeigt (tatsächlich) grundsätzlich andere Stapelfehler als C36-TiCr₂ und C36-NbCr₂.

9.5 Dipole aus Umwandlungsversetzungen in Lavesphasen; eine Analyse mit hochauflösender Transmissionselektronenmikroskopie

Ein direkter experimenteller Beweis wurde erbracht, der zeigt, dass die Umwandlung von C14-Lavesphasen zu C36 (oder der 6H-Struktur) durch Gleitung einer regelmäßigen Anordnung von Dipolen aus Synchro-Shockley-Partialversetzungen realisiert wird.

Es wurden Stapelunregelmäßigkeiten beobachtet, die auf einen Durchlauf von nicht streng periodisch aufeinanderfolgenden Anordnung dieser Liniendefekte hindeuten. Für die Umwandlung von C14 in C36 wurden Vorschläge für die atomistische Struktur der Kerne aller nicht-äquivalenter synchro-Shockley-Partialversetzungsdipole gemacht (im Fall von NbCr₂).

Zum ersten Mal wurde eine C36-„Antiphasengrenze“ beobachtet (in HfCr₂). Diese Antiphasengrenze besteht aus einer speziellen Anordnung von synchro-Shockley-Partialversetzungsdipolen. Sie ist das Resultat des Aufeinandertreffens zweier wachsender C36-Domänen im gleichen C14-Ursprungskristall.

Die Situation bezüglich der Mikrostruktur in HfCr₂ steht im Kontrast mit der von NbCr₂: Während im Fall von NbCr₂ der isolierte Dipol weitergleiten könnte und daher die Umwandlung von C14 in C36 (die nicht vollständig ablief) weiter vorantreiben könnte, war die Umwandlung in HfCr₂ vollständig abgeschlossen und es fand ein Aufeinandertreffen zweier vollständig umgewandelter C36-Domänen statt; damit ist die Anordnung der Versetzungen (an der Antiphasengrenze) fixiert.

Die experimentellen Beobachtungen unterstreichen den langreichweitigen, größtenteils dehnungs-/verformungsfreien Charakter der gesamten Versetzungskonfiguration: Die Gitterverzerrung ist in höchstem Maße im Kern der einzelnen synchro-Shockley-Partialversetzungen konzentriert. Die Ergebnisse zeigen, dass die synchro-Shockley-Partialversetzungen, die die Umwandlung von C14- zu C36-Lavesphasen tragen, als eigene Klasse von Defekten angesehen werden sollten.

9.6 Polytype Umwandlungen der HfCr₂-Lavesphase – Die Strukturentwicklung als Funktion der Temperatur

HfCr₂-Lavesphasenlegierungen verschiedener Zusammensetzung wurden durch Schmelzen im Lichtbogen und anschließendes Homogenisieren bei Temperaturen im Stabilitätsbereich der C14-Hochtemperaturmodifikation hergestellt. Durch Auslagern bei unterschiedlichen tieferen Temperaturen wurden polytype Phasenumwandlungen induziert und die resultierende (Mikro-)Struktur der Lavesphase wurde durch XRPD und HRTEM charakterisiert.

Bei Temperaturen zwischen 1300°C und 1225°C bildet sich eine Mikrostruktur, die aus zufällig wechselnden C36- und C15-Lamellen besteht. Bei niedrigeren Auslagerungstemperaturen trat die C36-Stapelfolge nicht auf. Stattdessen entwickelt sich eine lamellare C14/C15-Mikrostruktur, die ihren Ursprung in einer unvollständigen Umwandlung von C14 in C15 hat.

Die zugehörigen Röntgenpulverdiffraktogramme bestehen aufgrund der kohärenten Beugung ausgehend von den verschiedenen Polytypen nicht aus diskreten Diffraktogrammen, die den jeweiligen Lavesphasen-Polytypen zugeordnet werden können, sondern aus einem gemeinsamen Diffraktogramm, das über die Polytypen einer lamellaren Struktur mittelt. Diese kohärente Beugung, die von der irregulären Stapelfolge ausgeht, verursacht eine Linienverbreiterung bei Reflexen, die ausschließlich zu bestimmten Polytypen gehören („Polytypreflexe“), wohingegen die „Fundamentalreflexe“, die bei allen Polytypen gleich auftreten, unverbreitert bleiben.

Aus den Diffraktogrammen wurden zwei skalare Parameter ermittelt, die den Grad der Phasenumwandlung als Funktion der Zeit beschreiben, von denen einer auf der Änderung der normierten integralen Intensität eines ausgewählten Polytyp-Reflexes (Indizes 100) beruht, und der andere auf der Änderung des mittleren Verhältnisses der Zellparameter der Elementarzelle (c/a) der lamellaren Struktur. Um die lamellare Mikrostruktur als eine Gesamtstruktur behandeln zu können wurde eine standardisierte Beschreibung für alle Polytypen verwendet.

9.7 Polytype Umwandlungen der HfCr₂-Lavesphase – Kinetik der polymorphen C14 → C15 – Umwandlung

Die normierte integrale Intensität eines ausgewählten Polytyp-Reflexes (Indizes 100) und alternativ die Änderung des mittleren Verhältnisses der Zellparameter der Elementarzelle (c/a) der lamellaren Struktur wurden verwendet, um die polymorphe Phasenumwandlung von C14 in C15 der HfCr₂-Lavesphase zu verfolgen. Diese beiden Tracer-Parameter liefern ähnliche Informationen, um den Fortschritt (Grad) der Umwandlung zu quantifizieren.

Die effektive Aktivierungsenergie der Phasenumwandlung wurde anhand isothermer Auslagerungsexperimente für drei Legierungen unterschiedlicher Zusammensetzung innerhalb des Homogenitätsbereichs der HfCr₂-Phase über die Äquivalenz-Zeit-Methode bestimmt. Die ermittelten Werte für die effektive Aktivierungsenergie reichen von 220 kJ/mol (Hf-reiche Probe) bis 250 kJ/mol (Hf-arme Probe). Die Aktivierungsenergie nimmt mit zunehmendem Hf-Gehalt zu. Die ermittelten Werte der effektiven Aktivierungsenergie liegen zwischen denen für die Aktivierungsenergien für Selbstdiffusion sowohl der Spezies A als auch B in AB_2 -Übergangsmetall-Lavesphasen und denen für das Gleiten von (synchro-Shockley-)Versetzen unter äußerer Spannung. Der Mechanismus der Umwandlung beinhaltet somit sowohl einen Gleitungscharakter als auch Sprünge einzelner Atome, was mit einer Bewegung von Versetzungskinken übereinstimmt.

List of publications

A. Leineweber, J. Aufrecht, E.J. Mittemeijer:

Phase Transformations of Iron Nitrides at Low Temperatures (< 700 K) - Application of Mechanical Mixtures of Powders of Nitrides and Iron.

International Journal of Materials Research 97 (2006) 753

J. Aufrecht, A. Leineweber, J. Foct, E.J. Mittemeijer:

The structure of nitrogen-supersaturated Ferrite produced by Ball-Milling

Philosophical Magazine 88 (2008) 1835

J. Aufrecht, A. Leineweber, E.J. Mittemeijer

Metastable hexagonal modifications of the NbCr₂ Laves phase as a function of cooling rate

Materials Research Society Symposium Proceedings 1128 (2009) 481

J. Aufrecht, A. Leineweber, A. Senyshyn, E.J. Mittemeijer

The absence of a stable hexagonal Laves phase modification (NbCr₂) in the Nb-Cr system

Scripta Materialia 62 (2010) 227

J. Aufrecht, W. Baumann, A. Leineweber, V. Duppel, E.J. Mittemeijer

Layer-stacking irregularities in C36-type Nb-Cr and Ti-Cr Laves phases and their relation with polytypic phase transformations

Philosophical Magazine 90 (2010) 3149

J. Aufrecht, A. Leineweber, V. Duppel, E.J. Mittemeijer

Transformation-dislocation dipoles in Laves phases: A high-resolution transmission electron microscopy analysis

Journal of Materials Research 25 (2010) 1983

J. Aufrecht, A. Leineweber, V. Duppel, E.J. Mittemeijer

Polytypic transformations of the HfCr₂ Laves phase – Part I: Structural evolution as a function of temperature, time and composition

Submitted for publication

J. Aufrecht, A. Leineweber, E.J. Mittemeijer

Polytypic transformations of the HfCr₂ Laves phase – Part II: Kinetics of the polymorphic C14 → C15 transformation

Submitted for publication

Danksagung

Die vorliegende Arbeit wurde im Rahmen der institutsübergreifenden Forschungsinitiative „The Nature of Laves Phases“, finanziert von der Max-Planck-Gesellschaft, am Max-Planck-Institut für Metallforschung in Stuttgart und am Institut für Materialwissenschaft der Universität Stuttgart durchgeführt. An dieser Stelle möchte ich allen danken, ohne die die vorliegende Arbeit nicht möglich gewesen wäre.

Herrn Prof. Dr. Ir. E. J. Mittemeijer danke ich für die Möglichkeit, in seiner Abteilung diese Arbeit anzufertigen. Sein ständiges Interesse am Fortgang, die intensive Betreuung und die ausführlichen wissenschaftlichen Diskussionen hatten einen entscheidenden Einfluss auf den erfolgreichen Abschluss und die Qualität dieser Arbeit.

Herrn Dr. Andreas Leineweber danke ich für die tägliche Betreuung der Arbeit. Er war zu jeder Zeit bereit für Gespräche über die Inhalte meiner Arbeit. Auch dank seines unerschöpflichen Fachwissens gelang es, immer wieder neue Zusammenhänge zu erkennen und auf kreative Weise neue Erkenntnisse über das Themengebiet dieser Arbeit zu gewinnen.

Herrn Prof. Dr. J. Bill danke ich für die freundliche Übernahme des Mitberichts und Herrn Prof. Dr. T. Schleid danke ich für die Zusage, den Prüfungsvorsitz zu übernehmen.

Den Mitarbeitern des Max-Planck-Instituts für Metallforschung in Stuttgart danke ich für die gute Zusammenarbeit während dieser experimentell oft schwierigen Arbeit. Insbesondere möchte ich Herrn T. Meisner und Herrn A. Weible von der Probenpräparation danken, die uns mit großem Einsatz und viel Kreativität bei der komplizierten Probenherstellung unterstützt haben.

Frau Viola Duppel vom Max-Planck-Institut für Festkörperforschung in Stuttgart danke ich für die außergewöhnliche Arbeit am HRTEM, sowie Herrn Prof. A. Simon, der diese Zusammenarbeit ermöglichte.

Herrn Dr. A. Senyshyn danke ich für die Möglichkeit, Neutronenbeugungsexperimente am Strukturpulverdiffraktometer (SPODI) am Forschungsreaktor FRM II in Garching durchzuführen. Hierfür stellte er einen Teil seiner persönlichen Messzeit zur Verfügung.

Den Kollegen aus dem Projekt „The Nature of Laves Phases“ danke ich für den wertvollen Gedankenaustausch während der regelmäßigen Treffen, der auch immer eine neue Motivation darstellte.

Allen Kollegen der Abteilung Mittemeijer des Max-Planck-Instituts für Metallforschung danke ich für die Unterstützung und die gute Arbeitsatmosphäre. Es war eine schöne Zeit.

Schließlich danke ich meinen Eltern und meinen Freunden für den Rückhalt und die Unterstützung in dieser Zeit.

Curriculum Vitae

Persönliche Angaben:

Name: Jochen Marc Aufrecht
geboren: am 24. 5. 1980 in Göppingen

Schulbildung:

1986-1990 Schillergrundschule in Göppingen-Faurndau
1990-1999 Freihofgymnasium Göppingen
1999 Abschluss der allgemeinen Hochschulreife

Zivildienst:

1999/2000 Zivildienst in der Klinik am Eichert in Göppingen

Hochschulausbildung

2000 – 2006 Studium der Werkstoffwissenschaft an der Universität Stuttgart mit dem Abschluss Diplom-Ingenieur

2005/2006 Diplomarbeit „Kugelmahlen im System Eisen-Stickstoff“ durchgeführt am Max-Planck-Institut für Metallforschung, Stuttgart.

Promotion

2006 - 2010 Promotion am Max-Planck-Institut für Metallforschung, Stuttgart, und Institut für Materialwissenschaft der Universität Stuttgart,
Thema: Phase Transformations of the NbCr₂ and HfCr₂ Laves Phases
Hauptberichter: Prof. Dr. Ir. E.J. Mittemeijer.

Auszeichnungen

2007 Procter&Gamble Förderpreis 2007 für herausragende Diplomarbeiten im Bereich der Chemie an der Universität Stuttgart